Universidade do Minho
Escola de Engenharia

Ziaaddin Zamanzadeh

Cement based materials reinforced with recycled steel fibres: mechanical, durability and structural performance

março de 2017

Cement based materials reinforced with recycled steel fibres: mechanical, durability and structural performance

Ziaaddin Zamanzadeh

UMinho | 2017

Universidade do Minho
Escola de Engenharia

Ziaaddin Zamanzadeh

Cement based materials reinforced with recycled steel fibres: mechanical, durability and structural performance

Tese de Doutoramento
Programa Doutoral em Engenharia Civil

Trabalho efetuado sob a orientação do
Professor Doutor Joaquim António Oliveira de Barros

e coorientação do
Doutor Lúcio Abel Pereira Lourenço

março de 2017

STATEMENT OF INTEGRITY

I hereby declare having conducted my thesis with integrity. I confirm that I have not used plagiarism or any form of falsification of results in the process of the thesis elaboration.

I further declare that I have fully acknowledged the Code of Ethical Conduct of the University of Minho.

University of Minho, _____

Full name: Ziaaddin Zamanzadeh

Signature: _____

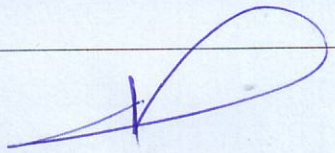

ACKNOWLEDGEMENTS

First, I give thanks to God for all of the blessings.

The research reported in this thesis has been carried out at the Civil Engineering Department of University of Minho, Portugal, under the supervision of Prof. Joaquim Antonio Oliveira de Barros.

I would like to express my sincere gratitude and appreciation to my supervisor professor Joaquim Barros as well as my co-supervisor Dr. Lúcio Lourenço not only for their continuous support, help and encouragement during the making of this thesis, but also for their patience, motivation, enthusiasm, and immense knowledge.

I would like to thank the technicians of the laboratory of the civil engineering department of University of Minho, engineers Marco, Mateus, Jesus Carlos, Pokee and the technicians and staff of CiviTest company, engineers Delfina, Tiago, Dr. Ines Costa and Mr. Inaldo. I also thank the BioSafe and RECIPNEU companies for providing recycled steel fibres and CiviTest company for the contribution on the execution of the beams.

I am also grateful to all my friends living in Portugal and worldwide who assure me that time and distance are not barriers for true friendship.

One of the greatest titles in the world is parent, and one of the biggest blessings in the world is to have parents. Nothing in my life would have been without their strife. Nothing I can say can ever truly convey. Nothing that I do can show my gratitude for them. Mom and dad, you are the best parents by far. Last but not least, my gratitude goes to my brother Nouraddin who I had a great childhood with him.

ABSTRACT

Recent research is showing that the addition of Recycled Steel Fibres (RSF) from post-consumed tyres can decrease significantly the brittle behaviour of cement based materials, by improving its toughness and post-cracking resistance. In this sense, Recycled Steel Fibre Reinforced Concrete (RSFRC) seems to have the potential to constitute a sustainable material for structural and non-structural applications. To assess this potential, experimental and numerical research was performed on the use of RSFRC in elements failing in bending and in shear. The values of the fracture mode I parameters of the developed RSFRC were determined by performing inverse analysis with test results obtained in three point notched beam bending tests. To assess the possibility of using RSF as shear reinforcement in Reinforced Concrete (RC) beams, three point bending tests were executed with three series of RSFRC beams flexurally reinforced with a relatively high reinforcement ratio of longitudinal steel bars in order to assure shear failure for all the tested beams. By performing material nonlinear simulations with a computer program based on the Finite Element Method (FEM), the applicability of the fracture mode I crack constitutive law derived from the inverse analysis was assessed for the prediction of the mechanical behaviour of these beams. The performance of the formulation proposed by RILEM TC 162 TDF and CEB-FIP 2010 for the prediction of the shear resistance of fibre reinforced concrete elements was also evaluated. Furthermore, the use of thin cement based (mortar) panels reinforced with relatively high content of RSF for structural reinforcement was explored. The mechanical properties and the durability performance of this Recycled Steel Fibre Reinforced Mortar (RSFRM) were characterised. The panels were produced by using a mixing technique similar to the one is used in the Slurry Infiltrated Fibre Concrete (SIFCon) technology. Then, their potentialities as a shear strengthening solution for RC beams deficiently reinforced in shear were investigated by performing three point bending tests with RC beams of "I" cross section shape (shear strengthened with this type of panels). Advanced numerical simulations and an analytical study were carried out to contribute for a better understanding of the effectiveness of the shear strengthening technique with RSFRM panels.

Keywords: Recycled steel fibre reinforced concrete, shear reinforcement, durability, FEM analysis, numerical simulation, analytical approach.

Resumo

A investigação desenvolvida no passado recente tem demonstrado que a adição de Fibras de Aço Recicladas (FAR) provenientes de pneus usados pode reduzir, de forma significativa, o comportamento frágil dos materiais de matriz cimentícia, melhorando a sua ductilidade e resistência pós-fendilhação. Neste sentido, o Betão Reforçado com Fibras de Aço Recicladas (BRFAR) apresenta-se como um material de caráter sustentável tanto para aplicações estruturais como não estruturais. Para melhor avaliar este potencial, desenvolveu-se investigação experimental e numérica relativa à utilização do BRFAR em elementos de betão sujeitos a rotura por flexão e por corte. Os parâmetros de fratura tipo I do BRFAR desenvolvido foram obtidos recorrendo a análise inversa dos resultados experimentais de ensaios de flexão, em três pontos, de vigas entalhadas. Para avaliar a potencialidade de utilização de FAR no reforço ao corte de vigas em Betão Armado (BA), foram realizados ensaios de flexão (três pontos) em três séries de vigas em BRFAR reforçadas à flexão com uma elevada percentagem de armadura longitudinal de forma a assegurar uma rotura por corte da totalidade das vigas ensaiadas. Através de simulações numéricas em regime não linear material efetuadas recorrendo a ferramentas baseadas no Método dos Elementos Finitos (MEF), a aplicabilidade das leis constitutivas relativas ao Modo I de fratura, obtidas recorrendo a análise inversa, foi avaliada na previsão do comportamento mecânico dessas vigas. A eficácia das formulações propostas pelo RILEM TC 162 TDF e pelo CEB-FIP 2010 para a previsão da resistência ao corte de elementos em betão reforçados com fibras foi, também, avaliada. Além disso, a utilização de painéis finos constituídos por material de base cimentícia (argamassa) reforçados com uma elevada quantidade de FAR para reforço estrutural foi explorada. As propriedades mecânicas e de durabilidade desta Argamassa Reforçada com Fibras de Aço Recicladas (ARFAR) foram caraterizadas. Os painéis foram produzidos recorrendo à técnica de mistura utilizada no fabrico dos *Slurry Infiltrated Fibre Concrete* (SIFCon). Seguidamente, as potencialidades da sua utilização como solução de reforço ao corte de vigas em BA com défice de reforço ao corte foram avaliadas recorrendo a ensaios de flexão (três pontos) de vigas de betão armado com secção em I (reforçadas ao corte com os painéis desenvolvidos). Paralelamente, realizaram-se simulações numéricas avançadas e um estudo analítico com o intuito de contribuir para um maior conhecimento relativo à eficiência da utilização desta técnica de reforço com painéis finos em ARFAR.

Palavras-chave: Betão reforçado com fibras de aço recicladas, reforço ao corte, durabilidade, análise recorrendo ao MEF, modelo analitíco.

CONTENTS

LIST OF FIGURES

LIST OF TABLES

ABBREVIATIONS

ACI	American Concrete Institute
ASTM	American Standards for Test Method
BS	British Standard
C	Cement
CA	Crushed Aggregates
CFRP	Carbon Fibre Reinforced Polymer
CMOD	Crack Mouth Opening Displacement
COV	Coefficient Of Variation
CRS	Coarse River Sand
CTOD	Crack Tip Opening Displacement
FA	Fly Ash
FEM	Finite Element Method
FRCC	Fibre Reinforced Cement Composites
FRS	Fine River Sand
IP	Integration Points
ISF	Industrial Steel Fibres
ISFRC	Industrial Steel Fibre reinforced concrete
JSCE	Japan Society of Civil Engineers
LF	Limestone Filler
LVDT	Linear Voltage Displacement Transducers
PC	Plain Concrete
PCM	Plain Cementitious Material

PRSF	Pyrolysed Recycled Steel Fibres
RC	Reinforced Concrete
RSF	Recycled Steel Fibres
RSFRC	Recycled Steel Fibre Reinforced Concrete
RSFRM	Recycled Steel Fibre Reinforced Mortar
SFRC	Steel Fibre Reinforced Concrete
SFRSCC	Steel Fibre Reinforced Self-Compacting Concrete
SHCC	Strain Hardening Cementitious Composite
SIFcon	Slurry Infiltrated Fibre Concrete
SIFcon_RSF	Slurry Infiltrated Recycled Steel Fibre Concrete
SMCFT	Simplified Modified Compression Field Theory
SP	Superplasticizer
SRSF	Shredded Recycled Steel Fibre
UPV	Ultrasonic Pulse Velocity
VMA	Viscosity Modifying Admixture
vs.	Versus
VSF	Virgin Steel Fibre
W	Water
WT	Waste Tyres

LIST OF SYMBOLS

A = Cross section of specimen

$A_{F-CMOD}^{\exp}$ = The areas below the experimental $F-CMOD$ curves

A_{F-CMOD}^{num} = The areas below the numerical $F-CMOD$ curves

A_{st} = Cross sectional area of the longitudinal bars

A_c = Area of concrete cross section

a_g = Maximum aggregate size

b_f = Width of the flanges

b_w = Width of the web's cross section

c_0 = Chloride concentration in the catholyte solution

c_d = Chloride concentration at which the colour changes

d = Effective depth of the cross section

$D_{BZ,2,I}^{f}$ = Contribution of steel fibres to the energy absorption capacity mode I

$D_{BZ,2,II}^{f}$ = Contribution of steel fibres to the energy absorption capacity mode II

D_{nssm}= Non-steady-state migration coefficient

$D_{t,1}^{cr}$ = Initial shear fracture modulus

$D_{t,2}^{cr}$ = Crack mode II shear fracture modulus

$D_{t,3-4}^{cr}$ = Crack shear modulus of the unloading and reloading branches

E_c = Concrete Young's modulus

E_s = Modulus of elasticity of longitudinal reinforcement

erf^{-1} = Inverse of error function

f_c = Cylinder compressive strength of concrete

f_{ci} = Individual cylinder compressive test result

f_{ck} = Characteristic value of cylinder compressive strength of the concrete

f_{ctk} = Characteristic tensile strength of concrete

f_{cm} = Mean value of cylinder compressive strength of the concrete

f_{ct} = Tensile strength

f_{ctk} = Characteristic value of the tensile strength

f_{ctms} = Average tensile strength of the test series

f_{eq} = Equivalent residual flexural tensile strength

f_{fct} = Limit of proportionality

$f_{fctk,ax}$ = Uniaxial tensile strength

f_{Ftu} = Ultimate residual strength

f_{Ftuk} = Characteristic value of the ultimate residual flexural tensile strength for FRC

$f_{R,i}$ = Residual flexural tensile strength parameters

$f_{R,1}$ = Residual flexural tensile strength parameter corresponding to CMOD=0.5

$f_{R,2}$ = Residual flexural tensile strength parameter corresponding to CMOD=1.5

$f_{R,3}$ = Residual flexural tensile strength parameter corresponding to CMOD=2.5

$f_{R,4}$ = Residual flexural tensile strength parameter corresponding to CMOD=3.5

$f_{R,1k}$ = Characteristic value of residual flexural tensile strength parameter corresponding to CMOD=0.5

$f_{R,2k}$ = Characteristic value of residual flexural tensile strength parameter corresponding to CMOD=1.5

$f_{R,3k}$ = Characteristic value of residual flexural tensile strength parameter corresponding to CMOD=2.5

$f_{R,4k}$ = Characteristic value of residual flexural tensile strength parameter corresponding to CMOD=3.5

f_c' = Compressive strength of the concrete

G_c = Elastic shear modulus of RSFRC

G_f^I = Fracture energy mode I

$G_{f,s}$ = Shear fracture energy (fracture energy mode II)

h_f = Height of the flanges

h_{panel} = height of the RSFRM panel

h_{sp} = Distance between the tip of the notch and the top of the cross section

I = Second moment of area

K = Factor related to the size effect

K_f = Factor for taking into account the contribution for the shear resistance of the flange in a T cross section beam

K_G = Coefficient of permeability

L= Thickness of the specimen

l_{cs} = Structural characteristic length of the structural element

M_0 = Dry mass of the specimen at 40±5°C

M_{cr} = Cracking moment

M_d = Dry mass

M_h = Hydrostatic mass of the specimen immersed in water

M_i = Mass of the specimen in contact with water for different times of reading

M_s = Saturated mass

n = Number of specimens

P_1 = Absolute pressure gas inlet

P_{max} = Maximum applied load

Q = First moment of area

R = Gas constant

r = Tip radius at notches

s_d = Standard deviation of the results

S_x = Vertical distance between longitudinal reinforcement

s_{xe} = Crack spacing parameter

T = Average value of the initial and final temperatures in the anolyte solution

$t_{10(n-1)}$ = Value of the student distribution for 10% fractile and (n-1) test results

t_{panel} = Thickness of the RSFRM panel

U = Absolute value of the applied voltage

V = Total shear force

V_{ana} = Shear capacity obtained analytically

V_{cd} = Concrete contribution for shear capacity

V_{exp} = Shear capacity obtained experimentally

V_f = Fibre content by volume

V_{Rd} = Shear capacity of the concrete elements

$V_{Rd,F}$ = Shear capacity provided by SFRC

$V_{Rd,s}$ = Shear capacity provided by the steel stirrups

W_c = Water absorbed by capillarity

W_i = Water absorption by immersion

x_d = Average value of the penetration depths

Z= Absolute value of ion valence

α = Angle of notch root

α_1 = Ratio between the stress at the first post-peak point and the tensile strength of the trilinear stress-strain diagram

α_2 = Ratio between the stress at the second post-peak point and the tensile strength of the trilinear stress-strain diagram

α_{th} = Threshold angle

β = Tensile stress factor in the cracked concrete

ε_c = Strain

ε_{c1} = Strain at uniaxial compression peak stress

$\varepsilon_{a,n}$ = Strain corresponding to the $\sigma_{a,n}$

ε_b = Stain corresponding to σ_b

$\varepsilon_{b,n}$ = Strain corresponding to the $\sigma_{b,n}$

$\varepsilon_{n,1}^{cr}$ = Strain at the first post-peak point of trilinear stress-strain diagram

$\varepsilon_{n,2}^{cr}$ = Strain at the second post-peak point of trilinear stress-strain diagram

$\varepsilon_{n,u}^{cr}$ = Ultimate crack strain

ε_x = Longitudinal strain

$\Delta\sigma_n^{cr}$ = Normal stress increment

$\Delta\tau_{nt}^{cr}$ = Shear stress increment

Δ_u = Deflection at loaded section

γ_c = Partial safety factor for concrete

$\gamma_{t,\max}^{cr}$ = Maximum crack shear strain

$\gamma_{t,p}^{cr}$ = Crack shear strain

$\gamma_{t,u}^{cr}$ = Ultimate crack shear strain

ρ_l = Longitudinal reinforcement ratio

ρ_{sx} = Longitudinal steel reinforcement ratio

θ = Inclination of the shear crack

$\sigma_{a,n}$ = Maximum stress level (Young's modulus test)

$\sigma_{b,n}$ = Minimum stress level (Young's modulus test)

σ_{ci}^{r} = Compression stress obtained experimentally

σ_{ci}^{c} = Analytically obtained compressive stress obtained

σ_{cr} = Cracking stress

$\sigma_{\max}$ = Maximum flexural stress

σ_{n}^{cr} = Crack normal stress

$\sigma_{n,1}^{cr}$ = Tensile strength

$\sigma_{n,2}^{cr}$ = Stress at the second post-peak point of trilinear stress-strain diagram

τ = Torque

τ_{avg} = Average shear stress

τ_{cr} = Shear stress at crack initiation

τ_{fd} = Design value of the shear strength provided by the fibre reinforcement

τ_{max} = Average bond stress at maximum pull-out load

τ_{nt}^{cr} = Crack shear stress

$\tau_{t,\max}^{cr}$ = Maximum crack shear stress

$\tau_{t,p}^{cr}$ = Crack shear strength

ν = Gas flow

ν_c = Poisson's ratio

ν_{panel} = Shear strength due to RSFRM panel

Ω_i = Lower surface of the specimen that was in contact with the water

ξ_1 = Ratio between the strain at the first post-peak point and the ultimate strain of the trilinear stress-strain diagram

ξ_2 = Ratio between the strain at the second post-peak point and the ultimate strain of the trilinear stress-strain diagram

Chapter 1

1 Introduction

1.1 Introductory remarks and motivation

Over the last years, the indiscriminate disposal of large amounts of post-consumed tyres into landfills and the illegal burning of tyres have caused serious worldwide environmental damages due to their well-known non-biodegradable nature (Figure 1.1). Consequently, according to the European Commission (European Commission 1999), since July 2006 the disposal of whole or shredded tyres into landfill has become illegal. As a consequence, almost all of the European Governments transposed this directive into national laws and codes, promoting the development of sustainable options for the disposal, recovery, and reuse of tyres (Centonze *et al*. 2012).

Figure 1.1 Illegal dumping and burning of tyres (Bestongroup 2014)

In 2001, about 12M tones of reinforcement bars were used per annum by the EU concrete industry. Steel fibres were utilized in the quantity of l50-200k tonnes per annum as alternative reinforcement in the EU concrete market (SYEP 2001). A research effort has been done in order to replace, at least partially, commercially available steel fibres (herein designated as Industrial Steel Fibres, ISF) or conventional steel reinforcement by steel fibres recovered from used tyres, herein designated as Recycled Steel Fibres (RSF). The applicability of RSF has been explored in specific concrete reinforcement applications like industrial floors, pre-cast concrete, foundations and concrete pavements (Graeff *et al*. 2012, Pilakoutas *et al*. 2004).

At the moment, there are some industrial production processes, like the pyrolysis and shredding, which aim primarily to recover the rubber and steel fibres from the post-consumed tyres. The description of the technological processes to extract RSF from the tyre recycling industry can be found in chapter 2.

1.1.1 Concrete reinforced with industrial steel fibres

Many types of materials have been used as fibre reinforcement in cement based materials, such as steel, glass, polymers, asbestos and ceramics (Kakay *et al*. 2015, Vanaerschot *et*

al. 2015, Drdlová *et al*. 2009, Tlemat 2004). Due to the relatively low elastic modulus (when compared to steel) of some reinforcing materials (glass, polymers, asbestos and ceramics fibres), they can mainly contribute to increase significantly the toughness of the concrete (post-cracking energy absorption capacity and residual strength), but not necessarily its strength. On the other hand, steel has a very high modulus of elasticity, and from the technological point of view, it is a material suitable for providing appropriate mechanical anchorage conditions to produce fibres capable of improving crack control process in concrete elements for accomplishing the serviceability limit state requirements (Kakay *et al*. 2015, Tlemat 2004). Hence, over the past three decades, the potential of using Steel Fibre Reinforced Concrete (SFRC) to improve the performance of statically determinate and indeterminate structures has been investigated (Barros *et al*. 2014, Caggiano *et al*. 2012, De Montaignac *et al*. 2012, Aoude *et al*. 2012, Susetyo *et al*. 2011, Barros and Figueiras 1999, Barros and Figueiras 1998). The crack opening restraint provided by the reinforcement mechanisms of ISF bridging the crack surfaces (Cunha 2010) leads to a significant increase in terms of load carrying capacity and energy absorption performance of concrete structures, mainly those of high redundant support conditions, since stress redistribution provided by fibre reinforcement allows an ultimate load much higher than the cracking load (Zamanzadeh *et al*. 2015, Lee *et al*. 2011, Barros and di Prisco 2009, Voo and Foster 2003). The available bibliography on the subject shows that steel fibre reinforcement can increase significantly the shear (Barros *et al*. 2014, Aoude *et al*. 2012, Susetyo *et al*. 2011), the flexural (Barros *et al*. 2014, Caggiano *et al*. 2012, De Montaignac *et al*. 2012, Barros and Figueiras 1999) and the punching (Barros *et al*. 2015, Ventura-Gouveia *et al*. 2011, Safeer *et al*. 2004) resistance, as well as the durability (Kunieda *et al*. 2014, Lourenço *et al*. 2011, Balouch *et al*. 2010, Granju and Balouch, 2005) of concrete structures.

Reinforced concrete structural elements without adequate transverse reinforcement can fail abruptly in shear before reaching their full flexural capacity when exposed to a combination of flexural and shear forces (Hai 2009). To prevent shear failures, beams are traditionally reinforced with steel stirrups. Since shear failure is brittle in nature, several design codes (ACI Committee 318 2008, Eurocode 2004, NZS4203 1992) recommend a

high quantity of steel stirrups in the critical regions of RC framed structures or in concrete elements of buildings in seismic risk zones (Cucchiara *et al*. 2004). On the other hand the application of high reinforcement ratio in concrete elements can compromise the concrete casting quality (Barros *et al*. 2014). Due to these reasons, the partial or total substitution of steel stirrups by steel fibres has been studied by several researchers. The use of steel fibres in beams reinforced with steel stirrups significantly improves the shear resistance (Centonze *et al*. 2012, Santos *et al*. 2008, Tlemat *et al*. 2004). Experimental results evidenced that even beams reinforced only with steel fibres showed a similar (or even better) post-cracking behaviour than reference beams with the minimum amount of steel stirrups recommended by Eurocode 2 (Meda *et al.* 2005). Steel fibres also reduce the width of shear cracks, leading to improved concrete durability and structural integrity (Meda *et al.* 2005).

1.1.2 Concrete reinforced with recycled steel fibres

Recent research is showing that steel fibres originated from the industry of tyre recycling, RSF, can also be a valuable reinforcement system to decrease significantly the brittle behaviour of cement based materials, by improving their toughness and post-cracking resistance. Recycled Steel Fibre Reinforced Concrete (RSFRC) is, therefore, becoming a promising candidate for some structural and non-structural applications (Aiello *et al*. 2009). The use of RSF as a reinforcement system of concrete elements has also beneficial environmental and economic impacts, since an added commercial value is given to a sub-product of the tyre recycling industry that, in general, is considered a waste product (Graeff *et al*. 2012, Neocleous *et al*. 2006). Although several research studies have already been carried out to enhance the knowledge of both environmental compatibility and sustainability of concrete production in the building industry, further research is still needed for addressing various issues related to the compatibility of recycled materials (such as RSF) in terms of flexural and shear behaviour with the ISF employed in the common concrete production. However, for a wider and reliable use of RSF in concrete construction, important barriers need to be overcome, such are those caused by the lack of knowledge with respect to: i) the technology of producing RSFRC with suitable

properties for concrete construction industry; ii) the characterisation of the relevant mechanical properties of RSFRC; iii) the design of RSFRC structures.

1.2 Aim and objective

The present study aims to contribute for increasing the knowledge on the characterisation of the post cracking properties of RSFRC, on its use as shear reinforcement, and on the design and advanced modelling of RSFRC elements failing in shear and bending. The most recent methodologies for the characterization of FRC properties were applied to the developed RSFRC. The potentialities of RSFRC as a shear reinforcement of relatively shallow beams are also explored.

The data obtained in the experimental investigations was used to evaluate the applicability of stress-strain model developed by RILEM TC 162-TDF, (2003) for ISFRC on the flexural response of RSFRC.

In this thesis also thin cement based mortar panels reinforced with relatively high content of RSF were developed. Two different techniques were examined and the one which is used for fabrication of SIFCon (Slurry Infiltrated Fibre Concrete) was chosen for the production of the Recycled Steel Fibre Reinforced Mortar (RSFRM) panels. In this technique, rather than adding fibres to concrete mixer, steel fibres are placed into a mould in the desired volume fraction. Then, high fluid mortar is poured up to fill the mould. This type of panels can be used in the structural rehabilitation for the shear strengthening of Reinforced Concrete (RC) beams, even those presenting several damages.

1.3 Research method

1.3.1 Tests for the mechanical characterisation of RSFRC

The characterisation of the mechanical properties of RSFRC is essential for evaluating the benefits of fibre reinforcement. Flexural tests are the most used for the characterisation of Steel Fibre Reinforced Concrete (SFRC), by determining the post-cracking performance of this composite. Several international committees have been formed (such as RILEM

2002, ASTM C1018 1995 and JSCESF4 1994) for the development of recommendations for the experimental characterisation of FRC, mainly SFRC, and guidelines of structures made by SFRC.

In this context to evaluate the post-cracking performance of RSFRC, a three point notched beam bending test program was executed according to the recommendations of RILEM TC 162-TDF. Notched beams made by ISFRC were also considered for comparison purposes. To perform a reliable comparison of the mechanical properties, for all the specimens, mixes of similar concrete strength class were used.

1.3.2 Tests for the mechanical and durability characterisation of RSFRM

Recent methodologies for the mechanical and durability characterization of cementitious composites were applied to the developed RSFRM. The specific characterization tests in the experimental program are the following:

- Three point bending test using un-notched specimens were performed to evaluate the cracking moment and flexural strength and also the corresponding deflections. To determine the contribution of the fibres for the post-cracking residual strength of the specimens, three point (centre-point) flexural tests on notched specimens were also carried out;
- Direct uniaxial tensile, direct shear and compressive behaviour of the developed RSFRM were investigated by performing uniaxial tensile, Iosipescu and compressive tests;
- Ultrasonic Pulse Velocity (UPV) measurements were executed for the study of the homogeneity of the used cementitious mortars without RSF and also the influence of different RSF dosages on the UPV;
- Durability performance of the developed RSFRM was investigated.

1.3.3 Testing of prototypes

For assessing the potentialities of RSF as shear reinforcement in RC beams, three point bending tests were executed with series of RSFRC beams flexurally reinforced with a relatively high reinforcement ratio and deficiently reinforced in shear in order to assure shear failure for all the tested beams.

The potentialities of the developed RSFRM panels were investigated as a shear strengthening solution for RC beams deficiently reinforced in shear. For this purpose three point bending tests with RC beams of "I" cross section shape shear strengthened with this type of panels were performed.

1.3.4 Analytical and numerical work

- The applicability of available design recommendations (CEB-FIP2010 2011, RILEM TC 162-TDF, 2003) to predict the shear resistance of RSFRC beams was assessed.
- For the analysis of RSFRC beams failing in shear and also RC beams strengthened with RSFRM panels, material nonlinear simulations were carried out using a smeared crack model available in the FEMIX finite element based computer program.
- After approval of the model's capability in predicting with acceptable accuracy the shear response of the tested beams, the influence of different fibre dosages and using ISFRC instead of RSFRC on shear reinforcement effectiveness for RC beams was evaluated by performing an extensive parametric study.
- The applicability of the analytical formulation developed by Baghi *et al*. (2016) to predict the shear capacity of the beams strengthened with Hybrid Composite Plates (HCP) was assessed for estimating the contribution of RSFRM panels for the shear resistance of RC beams.
- A new analytical approach based on combining the analytical formulation of the simplified modified compression field theory (SMCFT) and the RILEM TC 162-TDF recommendations was proposed for estimating the contribution of RSFRM panel for the shear resistance of RC beams.

1.4 Outline of the thesis

The present thesis is organized in seven chapters as follows:

Chapter one provides introduction, aim, motivation, research methods and the outline of the thesis.

Chapter two is dedicated to the literature review. It is intended to collect data from the most recent work developed in the use of cement based materials reinforced with fibres from the tyre recycling process. The mechanical and chemical processes currently utilised for the recycling of used tyres are described. The recent experimental programs dealing with the mechanical and durability properties of RSFRC and also ISFRC (for comparison purpose) are presented and discussed. Furthermore, recent experimental research carried out by Tlemat (2004), dealing with the characterisation of the mechanical properties of SIFCon reinforced with RSF is briefly presented.

In chapter three, firstly the technological aspects for the production of RSFRC are described. Then, the experimental program carried out to characterise the mechanical properties of the developed RSFRC in terms of compressive and flexural behaviour, and corresponding numerical and analytical study, are detailed and the obtained results are presented and discussed.

Chapter four includes the description of the experimental program and numerical study to assess the shear capacity of RSFRC beams with fibre content of 45 kg, 60 kg and 90 kg per cubic meter of concrete. The experimental program is composed by three series of short-span RSFRC beams longitudinally reinforced with steel bars and deficiently reinforced in shear in order to have shear failure. The contribution of fibre reinforcement for the shear resistance of RC beams is predicted by means of the analytical formulations recommended by RILEM TC 162-TDF and CEB-FIP 2010. For better understanding the shear behaviour of the RSFRC beams failing in shear, numerical simulation of the tested RSFRC beams are performed. Furthermore, the influence of the different fibre dosages (0 kg, 45 kg, 60 kg and 90 kg per cubic meter of concrete) on the shear capacity of RSFRC is assessed by performing a parametric study.

Chapter five presents the experimental program and corresponding numerical study on the development of thin RSFRM panels for the shear strengthening of RC beams. This chapter reports the experimental investigation on RSFRM mechanical properties characterisation associated with flexural, uniaxial compression, uniaxial tension and shear behaviour of RSFRM. Homogeneity of the used mortars is studied by UPV method. Furthermore, the influence of different RSF dosages on the UPV is reported. Durability performance of developed RSFRM in terms of water absorption by immersion and by capillarity, permeability to air, chloride diffusion by migration under non-steady state and drying shrinkage is also studied.

Chapter six reports the experimental program and numerical study associated with the assessment of the effectiveness of the developed RSFRM panels for the shear strengthening of RC beams. Two different procedures are adopted to attach the RSFRM panels on the lateral faces of "I" cross section shape RC beams. In the first case, the RSFRM panels have been attached using an adhesive epoxy, while in the second case the RSFRM panels are bonded using epoxy adhesive and mechanical anchors. For better understanding the shear behaviour of the tested RC beams strengthened with RSFRM panels, numerical simulation of the tested beams is performed. Furthermore, the contribution of RSFRM panels for the shear resistance of RC beams is predicted by means of the analytical formulations based on Simplified Modified Compression Field Theory (SMCFT) and a new analytical approach based on combining the analytical formulations recommended by SMCFT and RILEM TC 162-TDF is proposed.

Conclusions and recommendations for future research are presented in chapter seven.

Chapter 2

2 State of the art

2.1 Introduction

This chapter is organized in six sections and presents a review of the available literature about the most recent work developed in the use of cement based materials reinforced with fibres from the tyre recycling process. After introduction, in the second section, the tyre recycling techniques and the geometric as well as the mechanical properties of RSF are examined, aiming to introduce the sources of fibres used in this investigation. In the third section, the mechanical properties of RSFRC in its fresh and hardened states are reported. In the fourth section, a general presentation of Slurry Infiltrated Fibre Concrete (SIFCon) reinforced with RSF and its mechanical properties are given. In the fifth section, examples of industrial application of RSFRC are presented, and finally in

the last section the author identifies areas on testing, design and modelling of RSFRC that need further investigation.

2.2 Steel fibres from tyre recycling

2.2.1 Industrial process to extract RSF from the tyre recycling

In the present section, the recycling process of fibres recovered from post-consumed tyres is illustrated. Tyre shredding and the cryogenic process can be used to mechanically recover RSF from used tyres. In addition, steel fibres can be recovered by utilizing anaerobic thermal degradation, such as conventional pyrolysis and microwave-induced pyrolysis of tyres (AMAT 2003). The amount of extracted steel fibres depends mainly on the type of tyre. Tyres of light vehicles contain up to 15% steel, whereas truck tyres contain up to 25% steel (Hylands and Shulman 2003).

2.2.1.1 Shredding process

In the shredding process, tyres are reduced into rubber granules and steel fibres in two shredding stages, followed by separation of the steel from rubber by using magnets (Pilakoutas *et al*. 2004). In the first shredding stage, tyres are shredded until they are reduced to rubber pieces of about 50 to 150 mm maximum size dimension (Figure 2.1). To avoid substantial amounts of steel containing rubber, in the second shredding stage, the rubber crumb is subjected to a second re-grinding and is granulated up to approximately 1 to 10 mm size dimensions by using knife or hammer mill (Figure 2.2). Finally, the fragments of tyres containing steel fibres, rubber and textile fibres are sent to an electromagnetic separator, which separates the steel from the rubber. The RSF extracted by using shredding process contains large pieces of rubber, and it is characterised by irregular wrinkles and different diameters, lengths and shapes (Pilakoutas *et al*. 2004).

Figure 2.1 First shredding processes (Charles Lawrence Recycling Ltd. 2003)

a) b)

Figure 2.2 a) Steel and fluff from second stage of shredding (Micelli *et al*. 2015); b) Electromagnetic separation (Micelli *et al*. 2015)

The use of mechanical shredding for extracting RSF from tyres has increased over the years (Used tyre Working Group 2004) as it is considered a commercially mature and technologically reliable process (Pilakoutas *et al*. 2004). However, it can be quite costly. Since the steel fibre in the bead normally is a high strength steel and of a large diameter, therefore the rate of deterioration of the cutting blades is high and the blades

require constant maintenance (Pilakoutas *et al*. 2004).

2.2.1.2 Cryogenic process

The cryogenic process is composed by the four following stages (see Figure 2.3): 1) whole tyre size is initially transformed in pieces of rubber; 2) tyres are then fed into cryo-chamber and frozen with liquid nitrogen to -184 ºC; as a result, they become nearly brittle; 3) hammer mill reduces crumb to particles of various sizes; 4) the steel and textile are removed magnetically, whereas the rubber granules are dried, passed through a steel extraction unit, and finally sieved (INTEC 2003, Kohler 1996)).

a)

b)

c)

d)

e)

f)

Figure 2.3 Overview of the cryogenic process to transform tyres in fibres for using in concrete: a) Tyres to be recycled; b) Tyres transformed in pieces of rubber; c) Stock of pieces of rubber; d) Cryogenic tunnel to put the pieces of tyre in the glassy state; e) Tunnel hammers to break the pieces of rubber in glassy state; f) The fibres are separated by magnetic and collected in a container

The cryogenic process is considered to be energy efficient (Kohler 1996) and the extracted steel fibre is fairly clean (Morris *et al*. 1990). However, the disadvantages of this process are the high cost of liquid nitrogen (Pilakoutas *et al*. 2004) and loss of steel ductility if it is cooled down below its embrittling temperature (Morris *et al*. 1990).

2.2.1.3 Pyrolysis process

2.2.1.3.1 Conventional pyrolysis process

Pyrolysis is a chemical reaction which involves the molecular breakdown of larger molecules into smaller molecules in the presence of heat (see Figure 2.4). The conventional pyrolysis process involves the decomposing of used tyres to their constituents by subjecting the whole or shredded tyre to high temperature of 400° to 450° Celsius in the absence of oxygen. The pyrolysis process produces gases, oil, low grade black carbon and steel (Pilakoutas *et al*. 2004, Rodriguez *et al*. 2001)

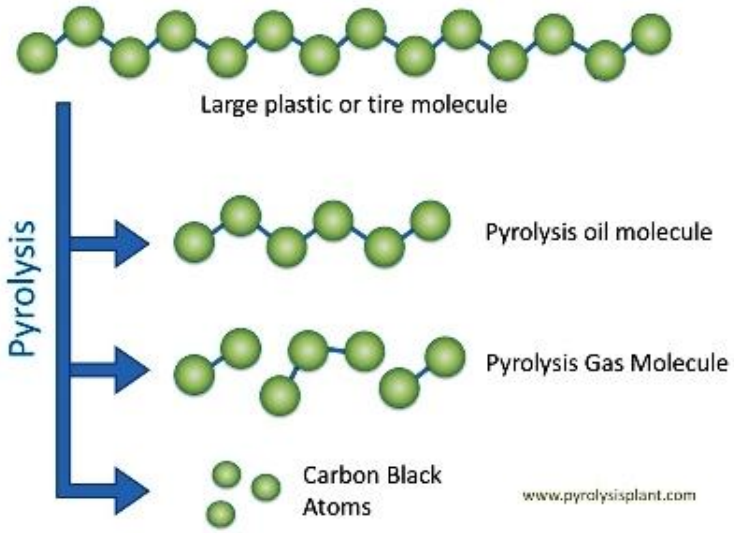

Figure 2.4 Concept of pyrolysis

The RSF extracted by using pyrolysis process is not entirely clean, as it contains a layer of carbon on its surface (Pilakoutas *et al*. 2004). The pyrolysis process is considered to be energy efficient, since the generated gas and oil can be used for the energy demands of the process.

2.2.1.3.2 Microwave induced pyrolysis process

In the microwave induced pyrolysis process, called "Advanced Molecular Agitation Technology" and patented by AMAT-Ltd (2003) the molecular bonds of the long-chain rubber hydrocarbons are excited by microwaves to breakdown into shorter hydrocarbons, which are released as volatile gases around 350° Celsius (AMAT 2003). Figure 2.5a shows the prototype plant developed by AMAT-Ltd. Due to relatively low temperature of the operation of this process, the extracted steel fibre and textile wire remain intact (Figure 2.5b). Similarity to the conventional pyrolysis process, in addition to steel, the microwave induced pyrolysis process produces oil and gases that can be used for the energy requirements of the process (Tlemat 2004).

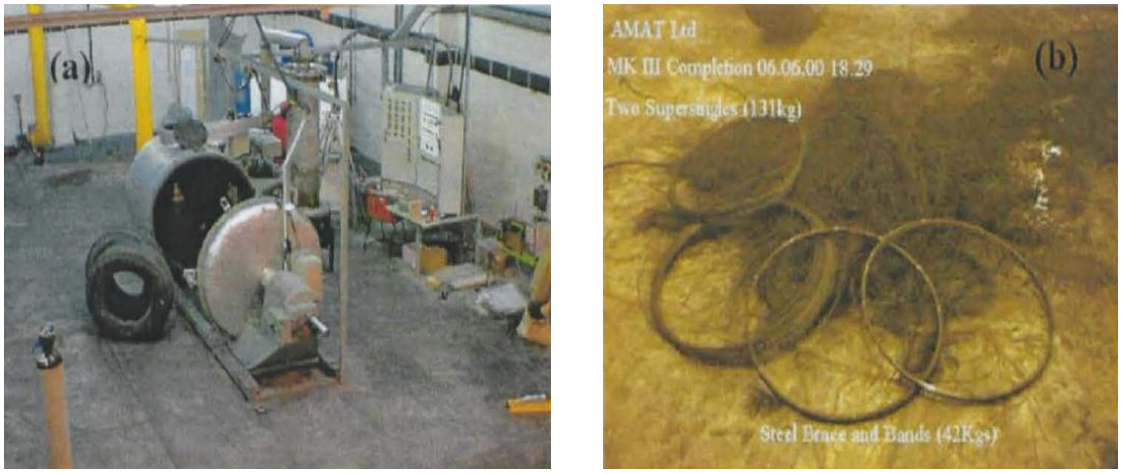

a) b)

Figure 2.5 Pyrolysis process (AMAT-Ltd 2003)

2.2.2 Geometric and mechanical properties of RSF

2.2.2.1 Geometric characterisation and tensile strength of RSF

Recycled steel fibres obtained by any of the processes briefly mentioned in subsection 2.2.1 are generally characterised by a significant variability in geometric parameters, such as length, diameter and aspect ratio (length divided by the diameter). Particularly, due to their tortuous shape, the actual length of fibres is not generally easy to be measured and, then, it is more often described by the distance between the outer ends of the fibres – see Figure 2.6 (CNR-DT 204/2006 2007).

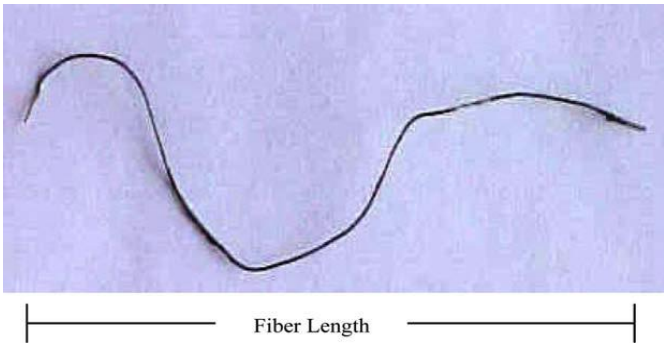

Figure 2.6 Fibre length (Tlemat *et al*. 2006)

The geometric characterisation and tensile strength of RSF was studied by Tlemat *et al*. (2005) by considering the following different types of steel fibres: RSF obtained from shredding process (SRSF); RSF obtained from pyrolysis process (PRSF); steel fibres obtained by cutting industrially available virgin steel tyre-cord to 50 mm pieces (VSF) and also ISF for comparison purposes. Each fibre type is shown in Figure 2.7.

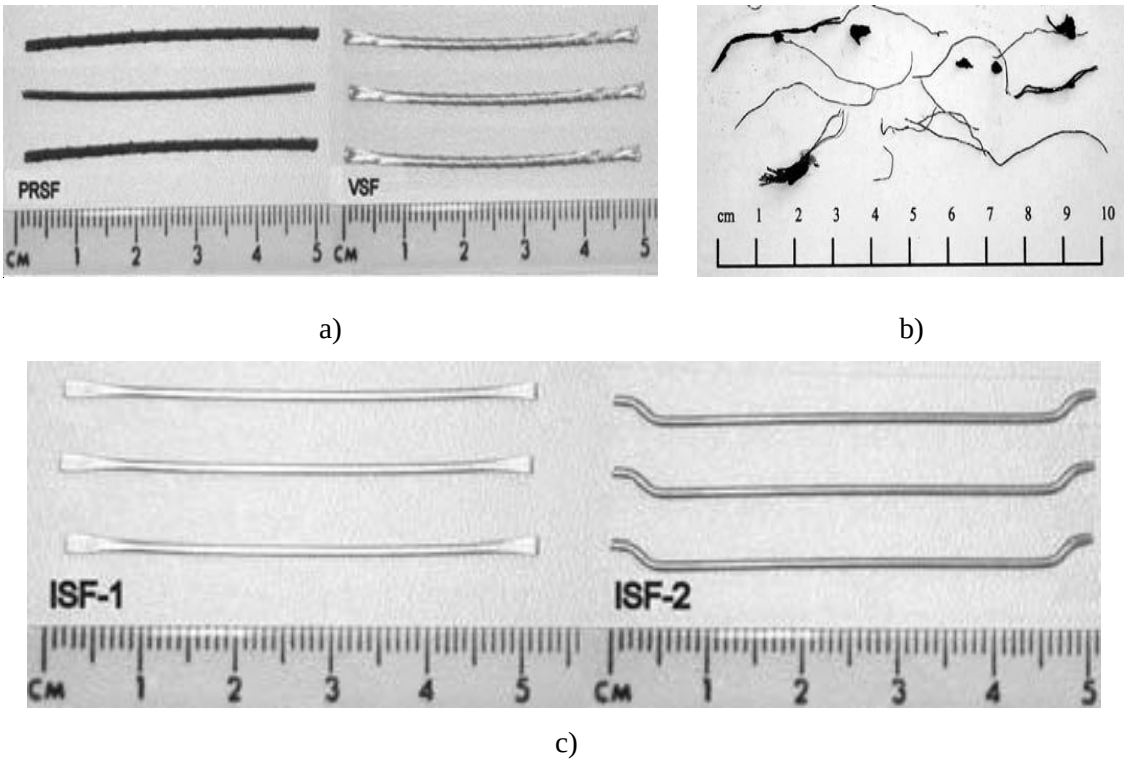

Figure 2.7 a) Pyrolysed and virgin steel fibres; b) Shredded steel fibres; c) Types of industrially produced steel fibres (Tlemat *et al*. 2006)

Tlemat *et al*. (2006) reported that, depending on the type of cord used in the tyre, the used PRSF presented variable diameters (ranging between 0.80 mm to 1.55 mm). The VSF fibres were free from any contaminants with consistent diameter of 1.55 mm. However, the SRF were inconsistent in diameter and shape. Table 2.1 shows a summary of geometry and tensile strength for each type of fibres, that these authors have used.

Table 2.1 Summary of geometry and tensile strength for each type of fibre (Tlemat *et al*. 2006)

Fibre type	Length [mm]	Diameter [mm]	Tensile strength [N/mm^2]
SRSF	20	0.23	~ 2000
PRSF	50	0.80 – 1.55	> 1250
VSF	50	1.55	> 1250
ISF-1	50	1.00	1050
ISF-2	50	1.05	1000

Aiello *et al*. (2009) have used a micrometre for determining the diameter of about 1400 steel fibres that had been taken out after the shredding process. The authors obtained fibre diameters between 0.17 mm and 2.00 mm. The largest number of diameter values (40%) was reported for the class 0.22 mm and 0.24 mm. Figure 2.8 presents the distribution of fibre diameters. The average values of the fibre length and fibre diameter were reported 26 mm and 0.258 mm respectively.

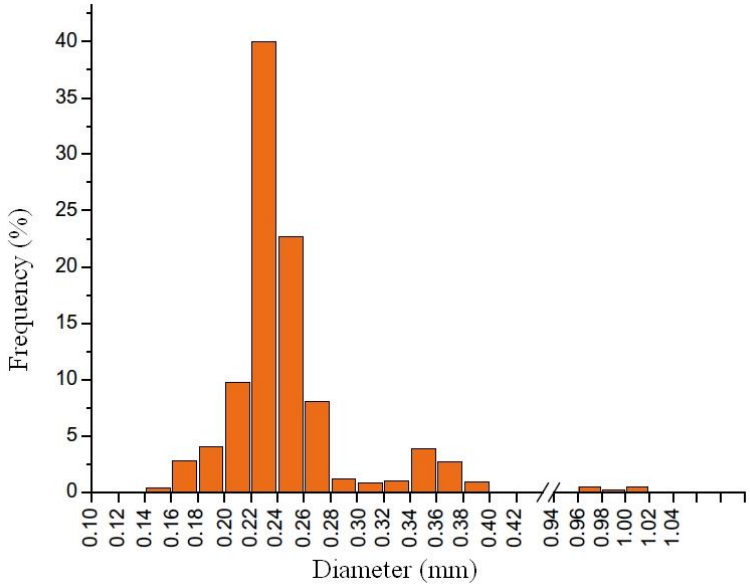

Figure 2.8 Distribution of fibre diameters (Aiello *et al*. 2009)

Moreover, the tensile strength of a RSF sample was determined by Aiello *et al*. (2009) who found values ranging between 2239 MPa to 2314 MPa. From the results reported by Aiello *et al*. (2009) and Tlemat *et al*. (2006), it is possible to conclude that RSF are comparable with ISF in term of tensile strength.

2.2.2.2 Experimental investigations on pull-out behaviour of RSF

To investigate and determine the actual bond interaction (both in terms of bond-slip relationship and maximum bearing capacity), pull-out tests can be carried out on single fibres embedded in concrete matrix. However, no well-established standard test method is currently available in the scientific literature, and several test setups are being used, as indicated by Aiello *et al*. (2009). Figure 2.9 describes two alternative experimental setups to perform pull-out tests on single (recycled) steel fibres.

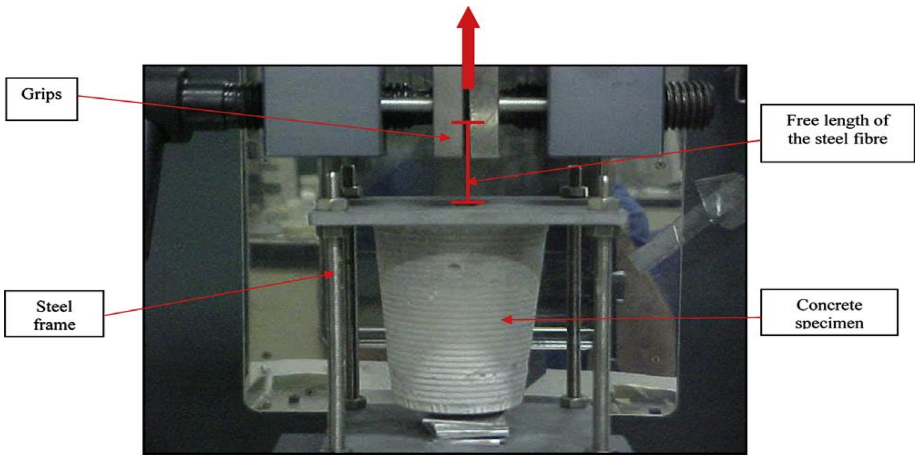

a)

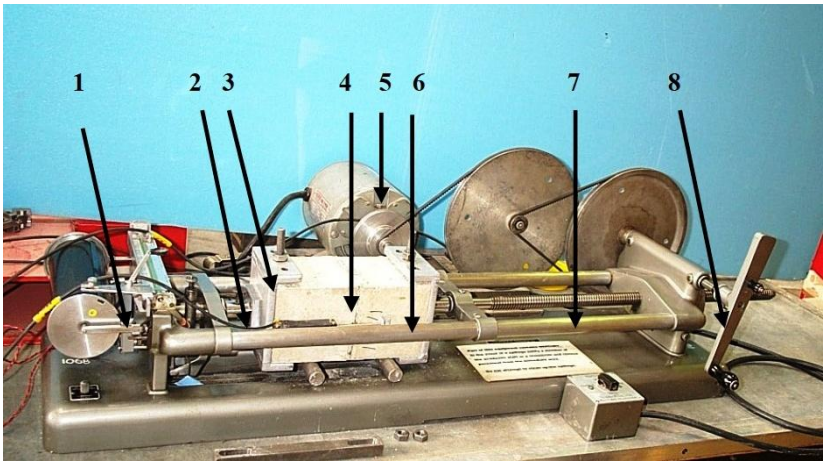

b)

Figure 2.9 Possible pull-out test setups: a) Aiello *et al*. (2009); b) Tlemat *et al*. (2003): 1) Spring beam with two strain gauges; 2) Chuck attached to the clamp with a pin; 3) Metal clamp; 4) Perspex plate with the fibre through its central holes; 5) Electric motor; 6) Pulled part of the specimen; 7) Cross-head attached to motor; 8) Manual handles

Pull-out tests were performed by Aiello *et al*. (2009) for investigating the bond between the RSF recovered by shredding process and the matrix, also to determine the critical embedded length, which is defined as the maximum length that a fibre can be embedded in the matrix without tensile rupturing during pull-out. For this purpose, these authors have used truncated conic concrete specimens with a single RSF embedded within the centre of the concrete specimen. Figure 2.9a shows the used pull-out test setup. Four different values of embedded fibre length (L_b = 15, 20, 30 and 40 mm) were examined for evaluating the critical embedded length.

Figure 2.10 shows the typical load *vs*. slip curve related to a specimen with an embedded fibre length of 15 mm, which failed in the pull-out mode. This curve is composed by the following four regions:

- O-A: the stretching of the part of wrinkled fibre not embedded in concrete makes the first region with null stress;
- A-B: this region is characterised by an almost linear load-slip response until the peak load;
- B-C: a softening zone is observable after peak load;
- C-D: this region is governed by the frictional contribution between fibre and surrounding matrix.

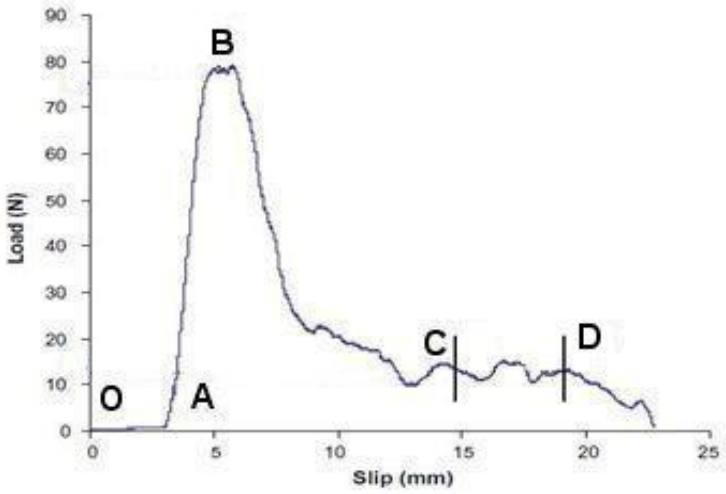

Figure 2.10 Typical applied load *vs*. slip curve for an embedded length of 15 mm (Aiello *et al*. 2009)

Figures 2.11 and 2.12 show the load *vs*. slip curves obtained for embedded length of 15, 20 and 30 mm. In these plots, the initial part of the curves, corresponding to the stretching of the fibres, was removed. All fibres with embedded length of 30 and 40 mm have failed by tensile rupture. In this case only the first two stages (see Figure 2.10) of the load *vs*. displacement curves were observable. Average bond stress at maximum pull-out load (τ_{max}) and Coefficient of Variation (COV) values are reported in Table 2.2. The average bond stress at maximum pull-out load is calculated from the following equation:

$$\tau_{max} = \frac{P_{\max}}{L\pi d} \tag{2.1}$$

where $P_{\max}$ is the maximum applied load, d and L are the fibre diameter and embedded length, respectively.

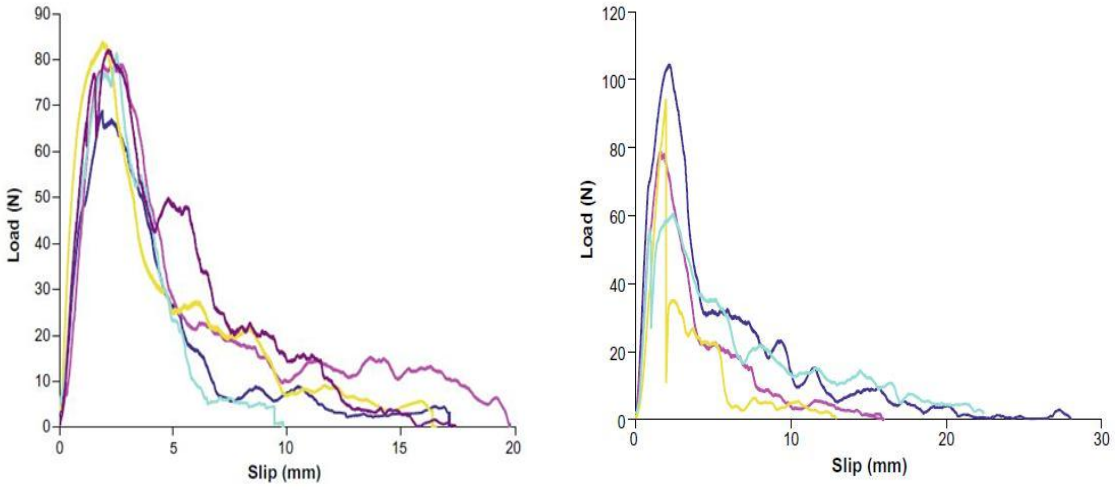

a) b)

Figure 2.11 Load *vs*. slip curves for fibre embedded length of a) 15 mm and b) 20 mm (Aiello *et al*. 2009)

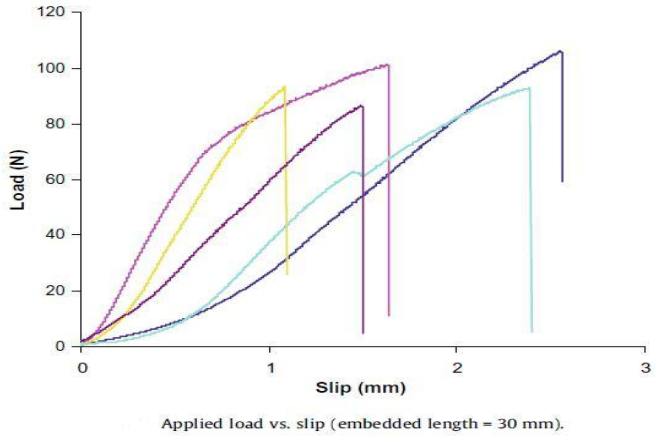

Figure 2.12 Load *vs*. slip curves for fibre embedded length of 30 mm (Aiello *et al*. 2009)

Table 2.2 Average values of bond stress (Aiello *et al.* 2009)

L_b [mm]	Tested specimens	τ_{max} [MPa]	COV [%]
15	15	7.53	14.8
20	12	5.98	19.9
30	15	3.62	18.0
40	8	3.25	19.2

It should be noted that the τ_{max} in Table 2.2 does not represent the maximum shear bond stress along the fibres embedded length, which is calculated based on local shear bond stress (see figure 2.13).

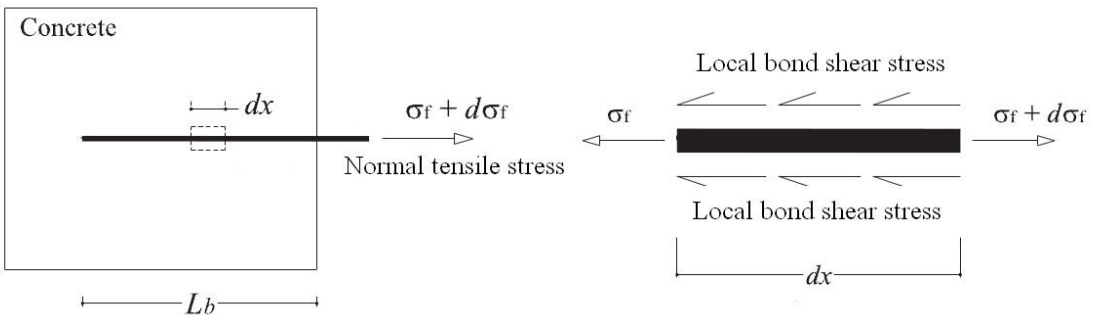

Figure 2.13 Axisymmetric pull-out model, adopted from Cunha (2010)

In fact, the tensile rupture of the fibres with embedded length more than 30 mm confirms that the generated maximum normal tensile stress due to maximum applied load to these fibres has attained the tensile strength of these fibres. So, it could be concluded that the generated maximum normal tensile stress in these fibres is higher than the maximum normal tensile stress generated in fibres with shorter embedded length, since the fibres with shorter embedded length were not failed by tensile rupture. If it is assumed that all the fibres with different embedded lengths have the same geometries, a higher generated maximum normal tensile stress in the fibres with embedded length of 30 mm means that a higher maximum pull-out load was applied to these fibres. Figures 2.11 and 2.12 also show that the fibres with embedded length of 30 mm have failed in the average applied load of around 100 N which is higher than the average value of the maximum applied load for the fibres with shorter embedded length. This could be interpreted by higher maximum shear bond stress along 30 mm fibre embedded length in comparison with the maximum shear bond stress along shorter embedded length of the fibres. A higher maximum shear bond stress leads to a higher pull-out load (Cunha 2010) generating a higher normal tensile stress in the fibre.

In comparison with the pull-out tests that have been executed for industrial steel fibres by Tlemat *et al*. 2004, irregular wrinkles, characterising RSF, confer an effective mechanical contribution to bond performance (Aiello *et al*. 2009). However, relatively high COV values (more than 15%) were obtained for RSF compared to the values obtained by Cunha *et al*. (2010) for both straight and hooked ISF (Table 2.3), which could be justified on the basis of the irregularities of the fibres (Aiello *et al*. 2009). Finally, Aiello *et al*. (2009) suggested the range of 20 mm to 30 mm for embedded critical length.

Table 2.3 COV values of the ISF pull-out tests obtained by Cunha et al. (2010)

Fibre type	L_b **[mm]**	**COV [%]**
Straight ISF	20	11.8
Straight ISF	30	14.4
Hooked ISF	20	9.4
Hooked ISF	30	11.0

2.3 Properties of RSFRC in fresh and hardened state

The key findings about the influence of steel fibres (with emphasis on recycled ones) on the relevant properties of fibre reinforced cementitious composites are summarised in the following subsections.

2.3.1 Workability of RSFRC

One of the main problems when mixing RSF in fresh concrete is the tendency of the fibres for balling (Pilakoutas *et al*. 2004). Several researches were dedicated to the evaluation of the ideal fibre content that gives the best performance without segregation and balling of the fibres in RSFRC, and also for estimating the influence of RSF on the concrete workability (Centonze *et al*. 2012, Bdour and Al-Khalayleh 2010, Aiello *et al*. 2009, Papakonstantinou and Matthew 2006, Tlemat *et al*. 2006). The results of slump tests on RSFRC are listed in Table 2.4.

A negative effect on the concrete workability with the increase of the fibre percentage was reported by Centonze *et al*. (2012), Bdour and Al-Khalayleh (2010) and Papakonstantinou and Matthew (2006). However, the results obtained by Centonze *et al*. (2012) for different content of superplasticizer show that a convenient mix design of RSFRC with enough percentage of plasticizer guarantees the same class of workability obtained for plain concrete.

Tlemat *et al*. (2005) reported slump test results for concrete reinforced with different content and types of recycled steel fibres. Table 2.4 shows slump test results for plain concrete as well as concrete reinforced with Shredded Recycled Steel Fibres (SRSF), Pyrolysed Recycled Steel Fibres (PRSF), Virgin Steel Fibres (VSF) and Industrial Steel Fibres (ISF).

Aiello *et al*. (2009) have assessed the influence of the type of mixer (traditional and planetary) on the workability of RSFRC. By using the traditional mixer, the workability was very small and has decreased significantly with the increase of the fibre content. While, mixing with a planetary mixer of vertical axis has assured much larger slump values and a small reduction of the slump with the increase of the fibre content (in

volume).

Table 2.4 Results of slump tests

Tlemat *et al*. (2006)			
Type	**Content of fibres [%]^{a}**	**Slump [mm]**	**SP [%]**
Plain	0	200	0.10
SRSF	0.5	160	0.20
SRSF	1.0	150	0.40
SRSF	2.0	55	0.75
PRSF	1.5	200	0.20
PRSF	3.0	150	0.40
PRSF	6.0	140	0.75
VSF	1.5	160	0.20
VSF	3.0	90	0.40
VSF	6.0	70	0.75
ISF	6.0	150	0.75

Aiello *et al*. (2009)-(traditional mixer)			
Type	**Content of fibres [%]^{b}**	**Slump [mm]**	**SP [%]**
Plain	0	70	1.00
SRSF	0.13	50	1.00
SRSF	0.15	40	1.00
SRSF	0.19	20	1.00
SRSF	0.26	0	1.00
SRSF	0.19	20	1.20

Centonze *et al*. (2012)			
Type	**Content of fibres [%]^{b}**	**Slump [mm]**	**SP [%]**
Plain	0	215	0.64
PRSF	0.23	220	1.17
PRSF	0.46	210	1.29
ISF	0.46	205	0.60

Papakonstantinou and Matthew (2006)			
Type	**Content of fibres [%]^{b}**	**Slump [mm]**	**SP [%]**
Plain	0	178	The same in the all mixes
Waste tyre steel beads	2	165	
	4	153	
	6	140	
	8	114	

Aiello *et al*. (2009)-(planetary mixer)			
Type	**Content of fibres [%]**	**Slump [mm]**	**SP [%]**
Plain	0	240	1.10
SRSF	0.23	240	1.10
SRSF	0.46	190	1.10
ISF	0.40	240	1.10

Bdour and Al-Khalayleh (2010)			
Type	**Content of fibres [%]^{b}**	**Slump [mm]**	**SP [%]**
Plain	0	171	The same in the all mixes
Waste tyre steel cord	2	160	
	4	146	
	6	137	
	8	116	
	10	102	

[%]^{a} = % of fibres in mass; [%]^{b} = % of fibres in volume; SP [%] = % of Superplasticizer in mass.

2.3.2 Compressive behaviour

The reinforcement provided by fibres can contribute at both micro and macro level. At a micro level, the micro crack development restraint provided by the fibre reinforcement

leads to higher compressive strengths, whereas at a macro level fibres control crack opening, increasing the energy absorption capacity of the composite (Neves and Fernandes 2005). The ability of the fibre to control micro cracking growth depends mainly on the number of fibres, distribution and bond to the matrix (Rossi 1998). A higher number of fibres in the matrix leads to a higher probability of a micro crack being intercepted by a fibre.

The compressive strength of RSFRC was determined by several researchers (Bdour and Al-Khalayleh 2010, Aiello *et al*. 2009, Papakonstantinou and Matthew 2006, Tlemat *et al*. 2006). The results of compression tests on RSFRC specimens are presented in Table 2.5. A negative effect of RSF addition on concrete compressive strength was reported by Bdour and Al-Khalayleh (2010), Tlemat *et al*. (2006), Papakonstantinou and Matthew (2006).

In 2006, Tlemat *et al*. (2006) reported compression test results for concrete reinforced with different contents and types of RSF. Table 2.5 shows compression test results for plain concrete, and concrete reinforced with SRSF, PRSF, VSF and ISF. With the exception of the concrete reinforced with VSF fibres, in all other concretes reinforced with the other types of fibres, the compressive strength had a tendency to decrease with the increase of the fibre content.

The decrease in compressive strength was explained based on the existence of rubber particles on the steel cords recovered from waste tyres (Bdour and Al-Khalayleh 2010). By performing a numerical simulation of the compression test on concrete cubic specimen containing rubber particles (see Annex A), formation of the cracks in the concrete elements surrounding rubber elements confirms the occurrence of stress gradients in these concrete elements.

In fact, rubber particles are much softer than the surrounding cement matrix, which leads to stiffness discontinuity of the microstructure of RSFRC. Due to stiffness discontinuity of the microstructure, the stress gradients might occurs in the concrete medium surrounding these softer particles causing cracking in these concrete elements. These cracks then propagate through the specimen and lead to a loss in the compressive strength.

Table 2.5 Results of compression tests

Tlemat *et al*. (2006)			Papakonstantinou and Matthew (2006)		
Type	**Content of fibres [%]^a**	**Compressive strength (MPa)**	**Type**	**Content of fibres [%]^b**	**Compressive strength [MPa]**
Plain	0	51.5	Plain	0	40.9
SRSF	0.5	49.5	Waste tyre steel beads	2	40.1
SRSF	1.0	50.0		4	35.4
SRSF	2.0	45.0		6	33.4
PRSF	1.5	44.0		8	30.1
PRSF	3.0	38.5	Aiello *et al*. (2009)- (planetary mixer)		
PRSF	6.0	50.0	**Type**	**Content of fibres [%]^b**	**Compressive strength [MPa]**
VSF	1.5	54.1			
VSF	3.0	62.0	Plain	0	32.1
VSF	6.0	66.2	SRSF	0.23	38.5
ISF	6.0	52.9	SRSF	0.46	37.6
Aiello *et al*. (2009)- (traditional mixer)			ISF	0.40	38.6
			Bdour and Al-Khalayleh (2010)		
Type	**Content of fibres [%]^b**	**Compressive strength [MPa]**	**Type**	**Content of fibres [%]^b**	**Compressive strength [MPa]**
Plain	0	39.1	Plain	0	38.8
SRSF	0.13	40.4	Waste tyre steel cord	2	38.1
SRSF	0.15	32.2		4	34.5
SRSF	0.19	34.9		6	32.1
SRSF	0.26	34.6		8	29.4
SRSF	0.19	33.4		10	22.1

[%]^a = % of fibres in mass; [%]^b = % of fibres in volume;

Although there are several reports in the literature indicating reduction of compressive strength of RSFRC due to RSF addition to the concrete mix, Aiello *et al*. (2009) has reported an increase of the compressive strength of the RSFRC with the fibre content when produced in the planetary mixer, while no clear tendency in this respect was observed in the RSFRC produced in the traditional mixer. Moreover, slightly enhancement of compressive strength (2-6%) of RSFRC with different RSF dosages in comparison with control mixture was reported by Lion (2012). This inconsistency in the compressive behaviour of RSFRC reported by several researchers confirms the difficulties of assuring a suitable distribution of the fibres in RSFRC elements and could be justified on the basis of the type of the RSF used in these investigations, and also irregularities of the fibres and negative effect of the balling of fibres on the compressive

behaviour.

2.3.2.1 Compressive post peak response

The main objective of the uniaxial compression tests performed with RSFRC cylinder specimens is to define a stress-strain law to simulate the complete compression behaviour of this composite.

In the literature there are several models to predict the compressive behaviour of plain concrete (Yip 1998, CEB-FIP Model Code 1993, Carreira and Chu 1985). Since SFRC composites have a less steep compression softening branch than plain concrete (Figure 2.14), these models in general cannot be applied for FRC. Some authors (Mansur *et al*. 1999, Hsu and Hsu 1994) have suggested the adaptation of the Carreira-Chu model (1985) to this type of composite. Applicability of the model proposed by Vipulanandan and Paul (1990) for the compressive behaviour of concrete reinforced with ISF has been confirmed by several studies (Barros and Figueiras 2001, Barros 1995). This model might be also applied to RSFRC, but specific researcher in the topic is required.

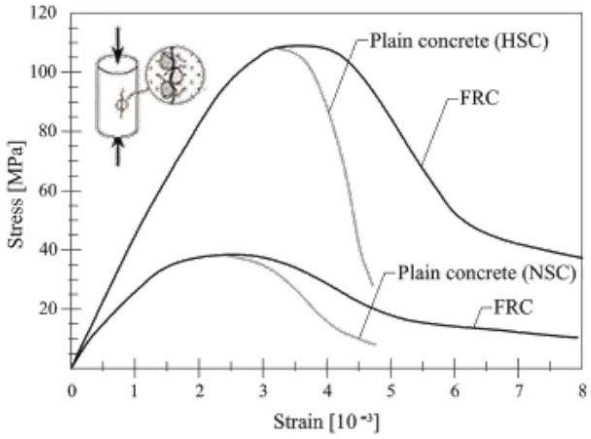

Figure 2.14 Main differences between plain and fibre reinforced concrete in case of normal and high uniaxial compressive strength (adopted from CEB-FIP-2010 2011)

This model was originally proposed by Vipulanandan and Paul (1990) to predict the composite concrete behaviour, by considering the following expression:

$$\sigma_c = \frac{\frac{\varepsilon_c}{\varepsilon_{c1}}}{(1-q-p)+q\left(\frac{\varepsilon_c}{\varepsilon_{c1}}\right)+p\left(\frac{\varepsilon_c}{\varepsilon_{c1}}\right)^{\frac{1-q}{p}}} f_{cm} \tag{2.2}$$

in which p and q are material deformability related parameters to be determined, and should satisfy the following conditions:

$$p+q = 1-\frac{f_{cm}}{E_c \varepsilon_{c1}} \tag{2.3}$$

$$p+q \in]0,1[\tag{2.4}$$

$$\frac{1-q}{p} > 0 \tag{2.5}$$

where ε_{c1} is the strain corresponding to the compressive strength (f_{cm}). Knowing the Young's modulus, the compressive strength and the strain at peak stress, the q parameter can be obtained from p, adopting equation (2.3), thus reducing to 1 the number of parameters to be determined. The parameter p, which takes a value in the range 0 to 1, is obtained by minimizing the following expression:

$$e^2 = \sum_{i=1}^{n}\left(\frac{\sigma_{ci}^r - \sigma_{ci}^c}{f_{cm}}\right)^2 \tag{2.6}$$

where σ_{ci}^r and σ_{ci}^c are the stress obtained in the experiments and calculated form expression (2.2), respectively, and n is the number of scan readings in a test. By adopting the p parameter that minimizes equation (2.6) the other parameters of the model can be obtained.

2.3.3 Flexural behaviour of FRC and RSFRC

The flexural test is widely used to characterise the post-cracking behaviour of fibre reinforced concrete, namely the flexural toughness, which can be represented through one of the following entities: a) absolute energy absorption, b) dimensionless indices related to energy absorption capacity and c) equivalent and residual flexural strength

parameters at prescribed post-cracking deflections or crack mouth opening displacements (Gopalaratnam *et al*. 1995).

Several standard test methods exist in the literature for flexural toughness characterisation of FRC using bending tests (RILEM 2002, ASTM C1018-94b 1995, ACI544 1988, JSCE-SF4 1984,), but to the best of the author's knowledge, no standard recommendations have been proposed specially for flexural toughness characterisation of RSFRC. Hence, in the several researches carried out to evaluate the influence of RSF on the post-cracking behaviour of RSFRC (Centonze *et al*. 2012, Lion Y. 2012, Buratti *et al*. 2011, Olivito and Zuccarello 2010, Neocleous *et al*. 2006, Tlemat *et al*. 2006, Pilakoutas and Strube 2001), the recommendations that are available for FRC were used by the researchers.

As an alternative for toughness characterisation of FRC, the use of notched beams in flexural tests has been investigated (Barr *et al*. 1996, Gopalaratnam *et al*. 1995). This type of test could be controlled by the mid span deflection, Crack Tip Opening Displacement (CTOD) and Crack Mouth Opening Displacement (CMOD). In 2003, Lee and Barr reported that the notched beam provides more stable and reliable tests with lower COV than un-notched beam tests. The following advantages of load-CMOD approach to toughness characterisation were reported by Lee and Barr (2003):

- CMOD measurement automatically excludes all extraneous deformations typically associated with deflection measurements, and is therefore less prone to errors;
- The results can be related to fundamental fracture mechanics and crack propagation behaviour of fibre reinforced concrete of the beam;
- Unlike the un-notched beam, deformation behaviour in notched beams is always localised at the centre of the beam (i.e. at the notch).

2.3.3.1 Notched beam bending tests on RSFRC

Figure 2.15 shows the test setup used by Aiello *et al*. (2009) in the characterisation of the flexural behaviour of RSFRC. The authors adopted a four point bending test setup with notched prismatic specimens (150 mm × 150 mm × 600 mm) reinforced with SRSF, according to UNI 11039 (2003). Plain concrete and ISFRC specimens were also

prepared for comparison purposes. According to these authors, addition of RSF to concrete, satisfactorily contribute to improve the concrete performance.

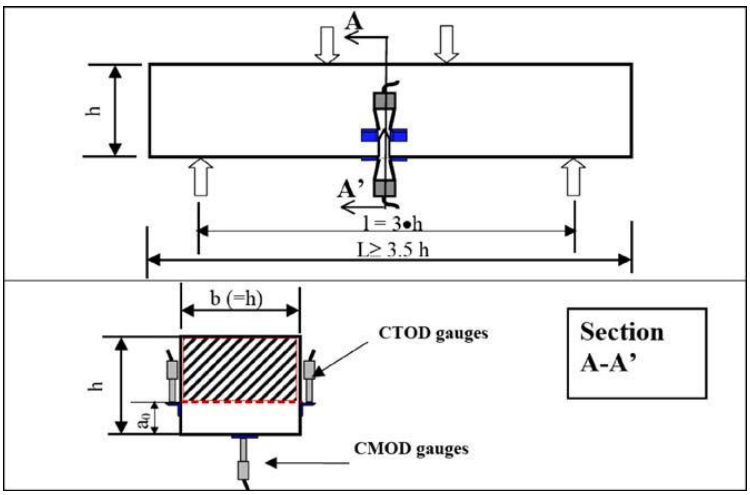

Figure 2.15 Four point bending test setup adopted from Aiello *et al*. (2009)

Figure 2.16 shows the load versus CTOD curves obtained from four point tests. The increase of the fibre percentage in volume has led to an increase of the peak load and post cracking residual strength. Concrete reinforced with 0.4 % in volume of ISF had an almost constant load carrying capacity up to a CTOD = 1.5 mm, while concrete reinforced with 0.46 % in volume of RSF presented a softening deflection.

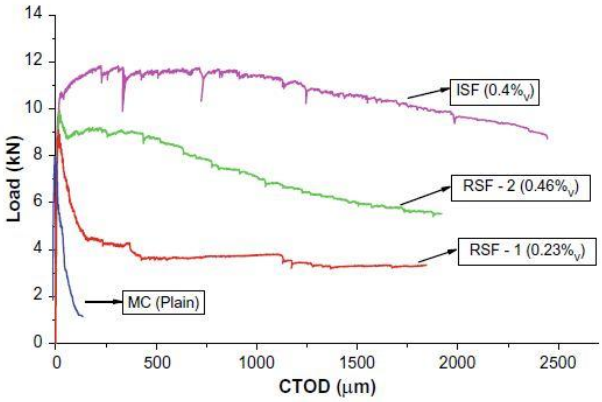

Figure 2.16 Average post-cracking behaviour for each tested mix (Aiello *et al*. 2009)

In the experimental program carried out by Tlemat *et al*. (2005), the effect of carbon black on the surface of RSF on the flexural behaviour of RSFRC was investigated. For

this purpose, four point bending tests were performed on notched prismatic specimens (150 mm × 150 mm × 550 mm) reinforced with VSF and PRSF (see Figure 2.17).

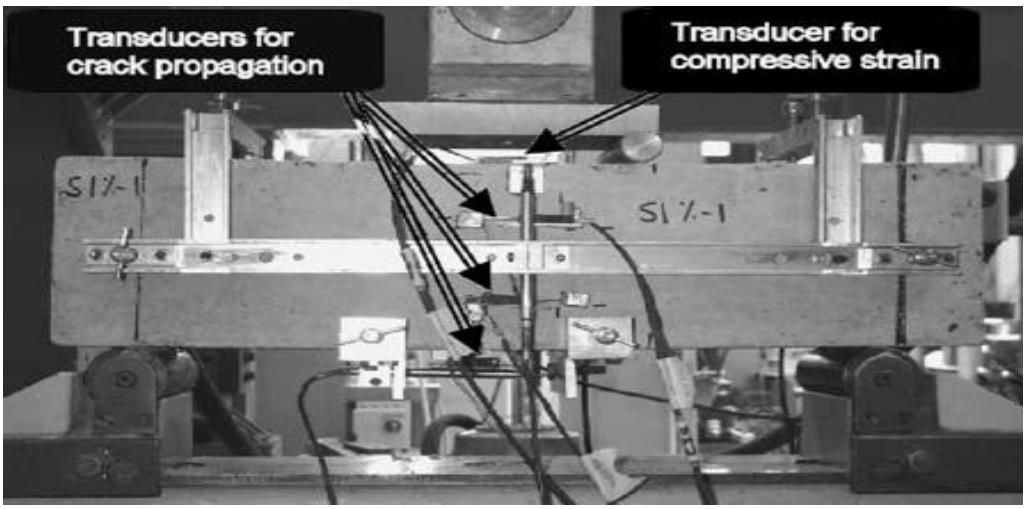

Figure 2.17 Four point bending test setup (Tlemat *et al*. 2006)

Figure 2.18 shows the relationship obtained between the average load and the average mid span deflection for the tested specimens reinforced with 1%, 3% and 6% of two different types of fibres (by mass): PRSF and VSF.

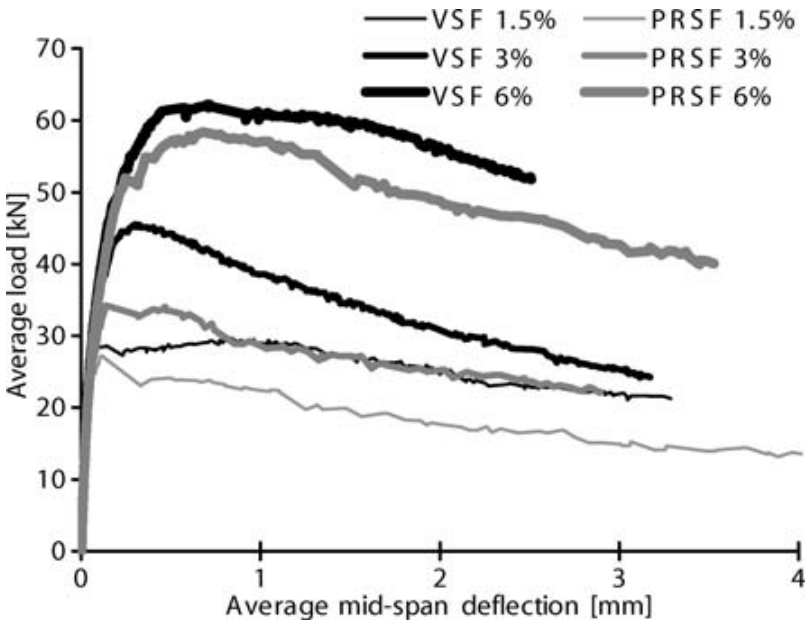

Figure 2.18 Effects of PRSF and VSF fibre ratios on flexural resistance. (Tlemat *et al*. 2006)

A higher flexural strength and energy absorption capacity was observed for the concrete reinforced with virgin fibres. The 20% lower average flexural strength of concrete reinforced with PRSF compared to the concrete reinforced with VSF was justified on the basis of the existence of carbon black on the surface of PRSF. Since the fibres were mixed by weight and the PRSF fibres have carbon black on their surface, this means that less PRSF fibres were used in comparison with VSF. Also, the effect of black carbon on the bond strength of PRSF is not negligible. However, there is no physical evidence to support that.

2.3.4 Tensile behaviour of RSFRC

A fundamental aspect of the mechanical performance of RSFRC is the tensile behaviour. This can be characterised through direct and indirect tensile tests like splitting tensile test. Although the uniaxial tensile test is the most appropriate method to determine the tensile strength of concrete, because of the local stress concentration which can be eliminated only by special precautions (Thomas and Ramaswamy 2007), misalignment of the test specimen and test equipment centrelines causing eccentricities and the difficulties on obtaining a stable post-peak response (Toutanji and EI-Kochi 1994), it is used almost exclusively in research. In the splitting tensile test, a diametrical compressive load is applied to a cylindrical specimen along two opposite generators (Figure 2.19). This creates tensile stress field perpendicular to the loading plane in the central zone of cross section of the specimen and fracture occurs in this plane (Timoshenko and Goodier 1991).

Because of the fact that the splitting tensile test provides exact information only up to first crack (Janusz 1983), therefore, it is not an appropriate test method in the case of FRC, since the material is neither brittle nor isotropic and it is fundamental to derive its post-cracking response.

Figure 2.19 Splitting tensile test (Rossli and Ibrahim 2012)

2.3.4.1 Splitting tensile test on RSFRC

Splitting tensile tests were performed by Rossli and Ibrahim (2012), Bdour and Al-Khalayleh (2010) and Papakonstantinou and Matthew (2006) according to ASTM C496/C496M-04 with cylindrical concrete specimens reinforced with different contents of RSF. Plain concrete cylindrical specimens were also considered for comparison purpose. The results of splitting tensile tests are summarised in Table 2.6.

The results obtained by Bdour and Al-Khalayleh (2010) and Papakonstantinou and Matthew (2006) show that addition of 2% by volume RSF to the concrete slightly decreases splitting tensile strength of concrete. On the other hand, decrease of the splitting tensile strength with the increase of RSF content in the mixture is observable. The decrease of splitting tensile strength was justified on the basis of the existence of rubber particles on the surface of RSF. Air attraction on the surface of the rubber particles due to non-polarity of the rubber reduces the bond with the cementitious matrix (Papakonstantinou and Matthew 2006).

No clear tendency in the splitting tensile strength of RSFRC with different RSF contents

was observed by Rossli and Ibrahim 2012. The values of the splitting tensile strength were ranged between 3.88 to 4.43 MPa. This may be justified by the higher COV of the results due to lower content of the fibres used in the splitting tensile tests performed by this researcher. However, the COV of the results were not reported and a reliable justification is not possible.

Table 2.6 Results of splitting tensile tests

Bdour and Al-Khalayleh 2010			
RSF type	**V_f [%]**	**Cylinder dimension [mm]**	**Splitting tensile strength [MPa]**
Steel cord recovered from waste tyre	0	⌀150×300	2.74
	2	⌀150×300	2.60
	4	⌀150×300	2.54
	6	⌀150×300	2.43
	8	⌀150×300	2.31
	10	⌀150×300	2.01
Papakonstantinou and Matthew 2006			
RSF type	**V_f [%]**	**Cylinder dimensions [mm]**	**Splitting tensile strength [MPa]**
Steel beads recovered from waste tyre	0	⌀ 100×200	2.82
	2	⌀ 100×200	2.75
	4	⌀ 100×200	2.64
	6	⌀ 100×200	2.55
	8	⌀ 100×200	2.47
Rossli and Ibrahim 2012			
RSF type	**V_f [%]**	**Cylinder dimensions [mm]**	**Splitting tensile strength [MPa]**
Generated by the tyre shredding process	0	⌀150×300	3.88
	0.2	⌀150×300	3.39
	0.4	⌀150×300	3.98
	0.6	⌀150×300	3.90
	0.8	⌀150×300	3.50
	1.0	⌀150×300	4.43

The above mentioned results presented only the splitting tensile strength of the RSFRC which was not significantly affected by fibre reinforcement. Therefore, for better

understanding of the post-cracking response of cementitious composites reinforced with RSF and deriving the tensile stress-strain relationship of these materials, it is fundamental to perform direct tensile tests with un-notched specimens.

2.3.5 Energy absorption of RSFRC by square panel tests

The replacement of the traditional reinforcement with ISF in concrete slabs was investigated by Colombo et al. (2009), Cengiz and Turanli (2004) and Ding and Kusterle (1999). As a matter of principle, these studies demonstrated that the addition of fibres may effectively improve the post-cracking behaviour and energy absorption capacity of concrete, and reduce its brittleness. Therefore, the use of RSF in concrete slabs could constitute one of the most interesting applications (Centonze *et al*. 2012).

The post-cracking performance and energy absorption of RFRC slabs were evaluated by Centonze *et al*. (2012) by performing flexural tests on square concrete panels with plant dimensions of 600 mm × 600 mm and the thickness of 100 mm, reinforced with 0.46 % of SRSF by volume of concrete according to EFNARC specification (EFNARC, 1996). For comparison purposes, three concrete samples reinforced with ISF were also tested.

As shown in Figure 2.20 the slabs were simply supported on its four edges by using a rigid steel frame with a span length of 500 mm, and tested under a centre point load through a contact surface of 100 mm × 100 mm. The applied load *vs*. mid span deflection curves for RSFRC and ISFRC slabs obtained from flexural tests on square panels are drawn in Figure 2.21.

Analysing the load vs. mid span deflection curves presented in Figure 2.21, a similar response was observed in all the tested specimens: an almost linear branch until reaching the peak load followed by a deflection softening response, whose load decay was more pronounced in the RSFRC, indicating this material has presented smaller energy absorption capacity than ISFRC.

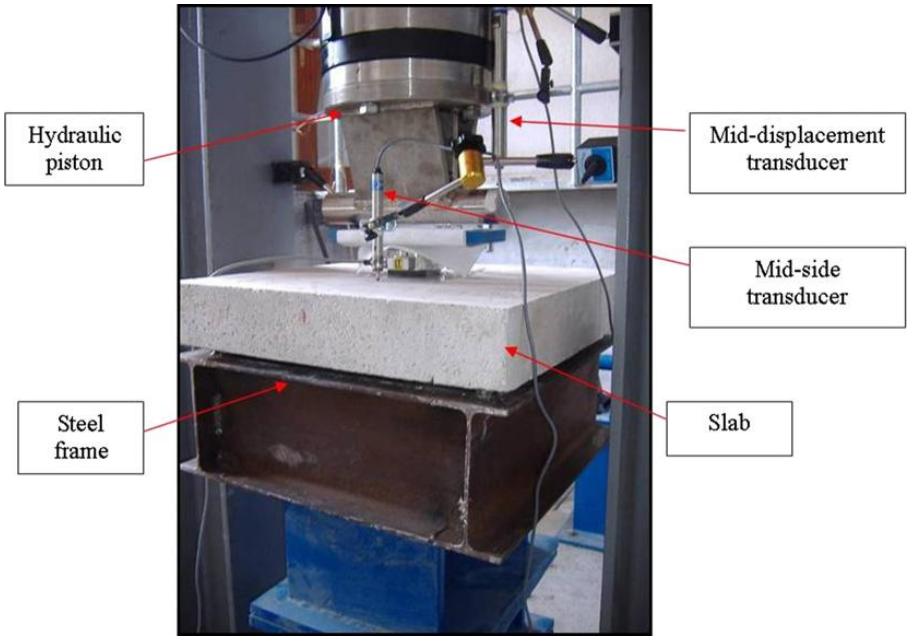

Figure 2.20 Square panel test setup (Centonze *et al*. 2012)

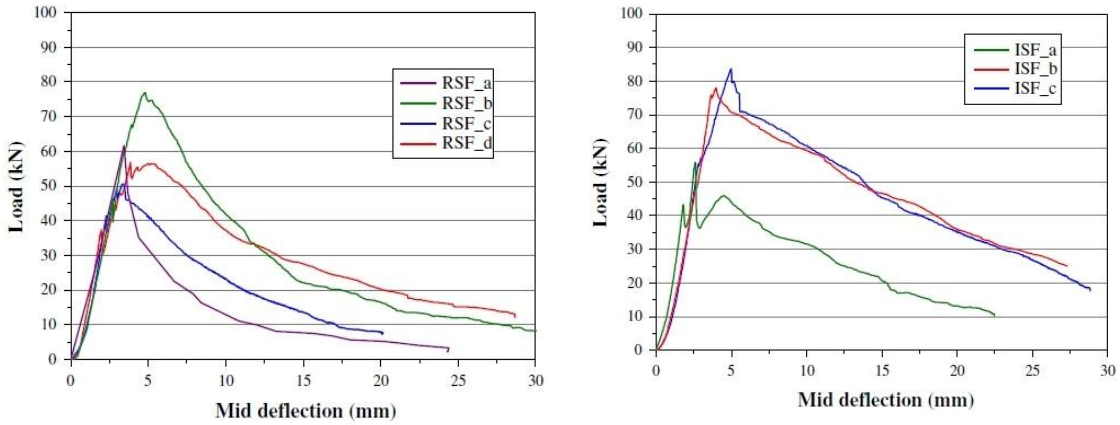

a) b)

Figure 2.21 Applied load *vs*. Mid span deflection for tested square panels of: a) RSFRC, and b) ISFRC (Centonze *et al*. 2012).

A significant scatter in the post-cracking stage of the flexural tests on square panels for both type of materials (RSFRC and ISFRC) was reported. This was explained based on the fact that the fibre distribution in the cracked sections governs the post peak behaviour (Centonze *et al*. 2012).

The average values of toughness (the area under the curve load versus mid span

deflection) for RSFRC and ISFRC were evaluated: 430 kNmm and 551 kNmm, respectively. The obtained values for ISF and RSF specimens confirm the effectiveness of both types of fibre in improving the post-cracking behaviour of concrete (Centonze *et al*. 2012).

RSFRC panels are shown in Figure 2.22a after have been tested. It can be noted that the panels undergone large deflection before the failure, due to the effective contribution given by the RSF on the cracking phenomenon, and maintained integrity even after a central deflection of about 25 mm (L/20). In Figure 2.22b fibres at the cracked section of a RSFRC specimen can be observed: RSF have failed by pull-out, not due to tensile rupture, evidencing the bridging contribution of fibres (Centonze *et al*. 2012).

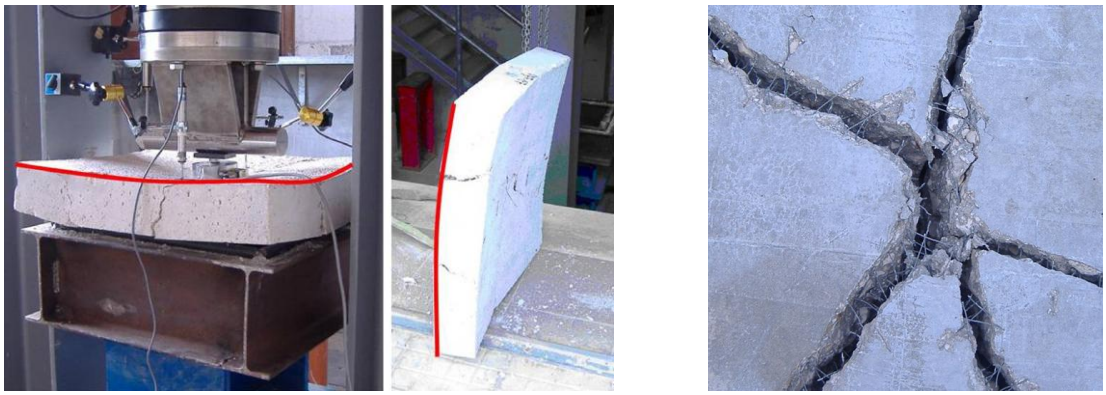

a) b)

Figure 2.22 a) RSFRC panel at the end of the test; b) Detail of the fibres bridging the macro failure cracks (Centonze *et al*. 2012)

2.3.6 Durability issues

2.3.6.1 Susceptibility of RSFRC to fibre corrosion

Corrosion is a very common pathological manifestation occurring in ordinary RC, and also one which causes more damage to structures, and, thus, the analysis of the effects of this phenomenon on durability and mechanical performance of SFRC structures is of paramount importance (Graeff *et al*. 2009). Several researchers have investigated the durability of SFRC (Frazão *et al*. 2015, Granju and Balouch 2005, Kosa and Naaman

1990, Mangat and Gurusamy 1987). The conclusions presented in these works are not still sufficient to attest the susceptibility of SFRC to corrosion resistance and the full understanding of its influence on durability and mechanical performance of SFRC structures (Graeff *et al*. 2009). Thus, the durability of SFRC is still a subject with lack of knowledge, and for a greater acceptation of this composite material, it is fundamental to evaluate durability indicators (Frazão *et al*. 2015)

According to Nordstrom (2000), steel fibres may corrode at a lower rate than conventional reinforcement when both are subjected to the same environmental conditions. The reason for this favourable property of steel fibres is not very well known. However the corrosion of steel fibres at lower rate may be justified by the smaller size of steel fibres in comparison with conventional reinforcement which leads to a better protection by the alkaline environment provided by the concrete. A smaller cathode area compared to the anode area is another argument for better resistance to corrosion (Nordstrom 2000).

Since the concrete reinforced with RSF is still a relatively recent composite material, whose properties and potentialities are being explored, no ample studies can be found in the literature on this aspect.

The influence of corrosion on the mechanical properties of ISFRC, RSFRC and Roller Compacted Concrete (RCC) reinforced with RSF and ISF was investigated by Graeff *et al*. (2009). RCC specimens were compacted by hydraulic hammer after casting, However, ISFRC and RSFRC specimens were compacted by an external vibrating machine. Since corrosion is a long-term process, the authors imposed accelerated corrosion conditions in ISFRC and RSFRC prisms ($150\times150\times550\,mm^3$) and cubes (150 mm edge). In the dry-wet cycle technique which was used to accelerate corrosion, specimens have been immersed in a container with chloride solution (3% of NaCl) for 4 days followed by a period of 3 days of drying at ambient temperature. After the corrosion process was concluded, the flexural and the compressive strength of these specimens were evaluated. Figure 2.23 shows specimens after have been submitted to five months in the accelerated corrosion conditions. It is noted that RSFRC specimens have more superficial corrosion effects. The analysis of the fracture surface of

specimens after have been tested (Figure 2.24) has evidenced that RSF fibres positioned in the specimen's cover layer of a thickness around 10 mm have presented signs of corrosion. In case of ISFRC samples, fibre corrosion only took place in the fibres on the surface, exposed directly to the environmental conditions.

a) b) c)

Figure 2.23 Specimens after 5 months of corrosion accelerating procedures: a) overall view of the samples; b) view of corroded RCC sample with RSF; c) view of corroded RCC sample with ISF (Graeff *et al*. 2009)

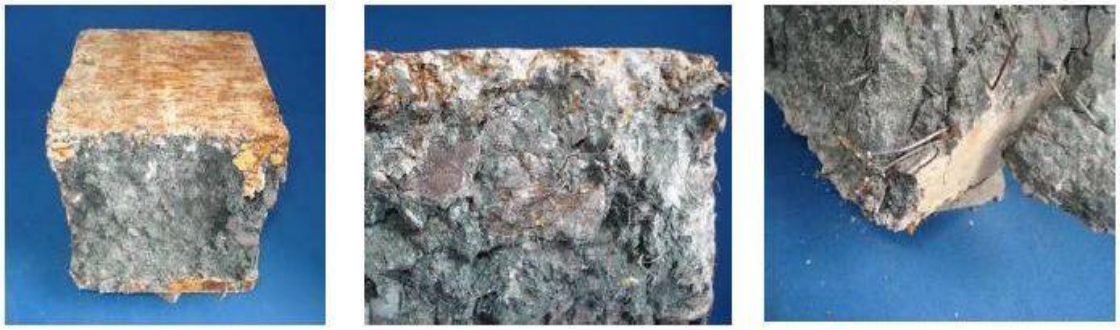

a) b) c)

Figure 2.24 Specimens after 5 months of corrosion accelerating procedures a) RCC sample with RSF after compressive test; b) detail of inside sample's edge – little RSF corroded; c) detail of inside sample's edge – ISF partially corroded (Graeff *et al*. 2009)

Figure 2.25 presents the compressive and the flexural strength of ISFRC of 2% by mass and RSFRC of 6% by mass of fibres, after five months of the corrosion process. The results are compared to those evaluated in the corresponding control SFRC specimens (without corrosion). It is verified that, after five months corrosion, all the specimens

have presented higher compressive and flexural strength than the corresponding specimens, whose properties were evaluated at 28 days. On the other hand, the increase of compressive and flexural strength in the plain concrete specimens after five months confirms that the favourable effect of the curing process on the mechanical properties has hidden an eventual detrimental effect of fibre corrosion. According to Graeff *et al*. (2009), the corrosion process had marginal influence on the post-cracking behaviour of SFRC specimens.

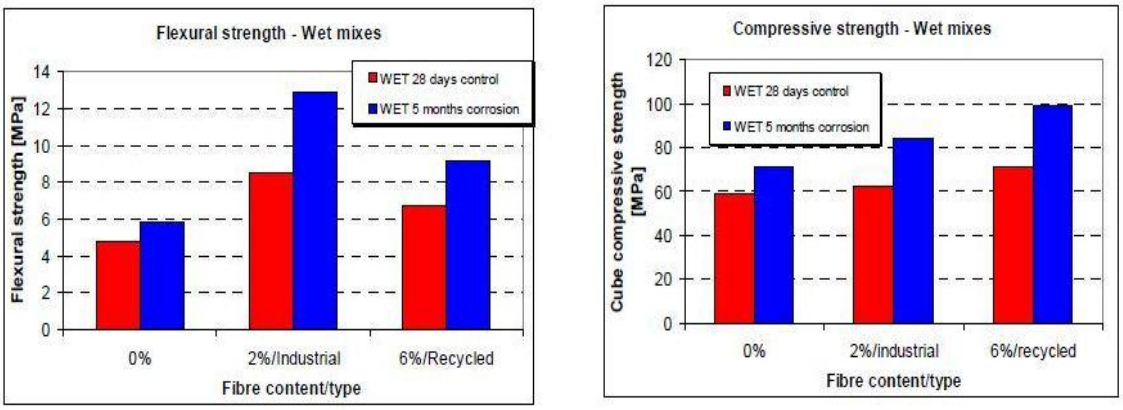

Figure 2.25 Flexural strength and compressive strength of SFRC (Graeff *et al*. 2009)

2.3.6.2 Free and restrained shrinkage of RSFRC

Wu *et al*. (1996a,b, 1994) studied the use of RSF and ISF in concrete to examine their effect on the free and restrained shrinkage cracking behaviour of concrete. The free drying shrinkage test followed the standard test methods of ASTM C596 and ASTM C157. The cracking behaviour due to restrained shrinkage was investigated using ring specimens of 310 mm inner diameter, 356 mm outer diameter, and 152 mm height (Grzybowski and Shah 1990).

The free shrinkage of each composite was measured at different ages of exposure to controlled environmental conditions, and the results are shown in Figure 2.26. The measured free shrinkage of Plain Concrete (PC), RSFRC and ISFRC ranged from 700 to 900 micro strains, agreeing well with other reported data (Mindess and Young 1981). The free shrinkage of ISFRC was about 7% lower than that of PC, and RSFRC

specimens showed about the same free shrinkage as control concrete.

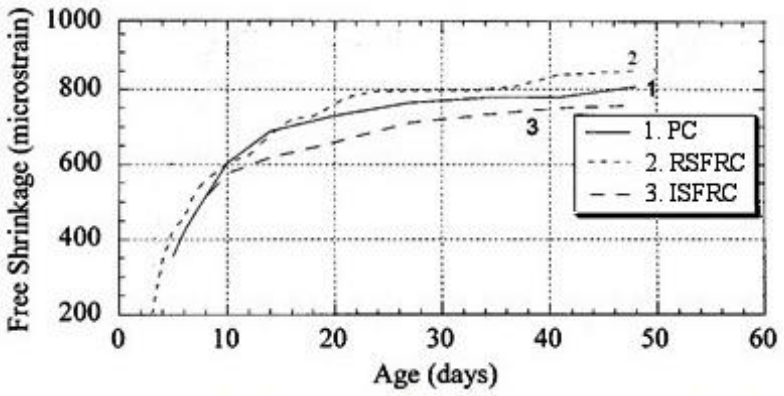

Figure 2.26 Free shrinkage at different ages for PC, RSFRC and ISFRC, adopted from Wang *et al*. (2000)

The cracking behaviour due to restrained shrinkage, evaluated by measuring the total crack width in each ring specimen with respect to time, is shown in Figure 2.27. The total crack width has decreased significantly in the fibre composites including all RSF and ISF reinforced concretes. However, the RSFRC exhibited a larger crack width than that of ISFRC. It was noted that the majority of the RSF was very short (< 6 mm), probably too short to provide adequate bridging for restraining the crack opening (Wang *et al*. 2000).

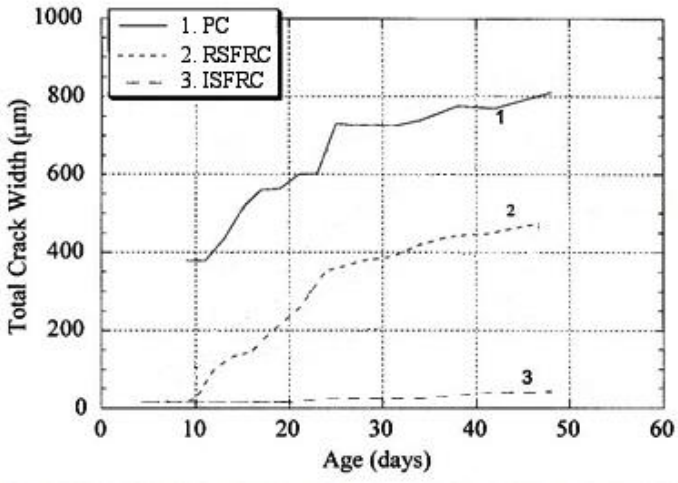

Figure 2.27 Total crack width versus concrete ages in restrained shrinkage test, adopted from Wang *et al*. (2000)

2.4 Slurry infiltrated concrete reinforced with RSF (SIFCon)

Slurry infiltrated fibre concrete (SIFCon) is a type of SFRC made of randomly-orientated steel fibres, placed into a mould in the desired volume fraction (V_f), followed by pouring the high fluid cement paste, or mortar up to filling the mould, rather than adding fibres to concrete mixer (Figure 2.28). During pouring and filling moulds, infiltration is usually assured by gravity flow, aided by light vibration or by pressure grouting (ACI544.2R 1987, Lankard 1985).

The main differences between SIFCon and conventional SFRC are the following ones: 1) unlike SFRC where the percentage, in volume, of steel fibres is generally limited to 2% due to the difficulties of assuring proper fibre distribution, segregation of the mixture constituents and rheological requirements because of workability and mixing issues, SIFCon contains larger volume fraction of fibres as high as 12%; 2) the strength and ductility of SIFCon is much higher than regular SFRC, since the matrix consists of very fine particles with high content of binder materials, which promote more effectively the fibre pull-out mechanisms, and its relatively high fibre volume content favours the occurrence of fibre-to-fibre interlock mechanism (Lee 2003, Van Mier *et al*. 1996).

Although SIFCon has been applied since 1979 in USA, because of its high cost, not justified by the performance of mechanical properties, due to the difficulty of assuring fibre uniform orientation, few commercial applications of this material are being used (Krstulovic-Opara and AI-Shannag 1999).

2.4.1 Flexural and compressive behaviour of SIFCon reinforced with RSF

Flexural and compressive behaviour of SIFCon reinforced with 17% (by weight) of RSF was investigated by Tlemat (2004) by performing four point bending tests on the prisms ($100\times100\times500\,\text{mm}^3$) and compressive tests on cubes ($100\times100\times100\,\text{mm}^3$), respectively. The results were compared with the obtained from flexural and compressive tests on RSFRC specimens. The mix proportions used in this series of tests are shown in Table 2.7.

Figure 2.28 RSF placed into moulds before pouring mortar for the production of SIFCon (Tlemat 2004)

Table 2.7 Mix proportions per concrete cubic meter, adopted from Tlemat (2004)

Mix	OPC [kg]	SP [kg]	SRS [kg]	W [l]	A (10mm) [kg]	S [kg]	WR [%]
RSRFC	236	0.101	48.4	155	1035	844	0.75
SIFCon_RSF	1084	0.464	363	390	0	0	0.81

OPC=Ordinary Portland Cement; SP=Super Pozzolan; SFRF=Shredded Recycled Steel Fibre; W=Water; A (10mm)=Aggregate (10mm); S=Sand; WR=Water Reducer

Figure 2.29 shows the average load mid span deflection curves obtained from four point bending tests. In Figure 2.29 better performance of SIFCon_RSF in comparison with RSFRC in terms of flexural behaviour and energy absorption is obvious. Figure 2.29 indicates that initial load mid span deflection for RSFRC prism is stiffer than that of SIFCcon_RSF, while a higher flexural strength was obtained for SIFCcon_RSF prism in comparison with the one obtained for RSFRC prism (Tlemat 2004).

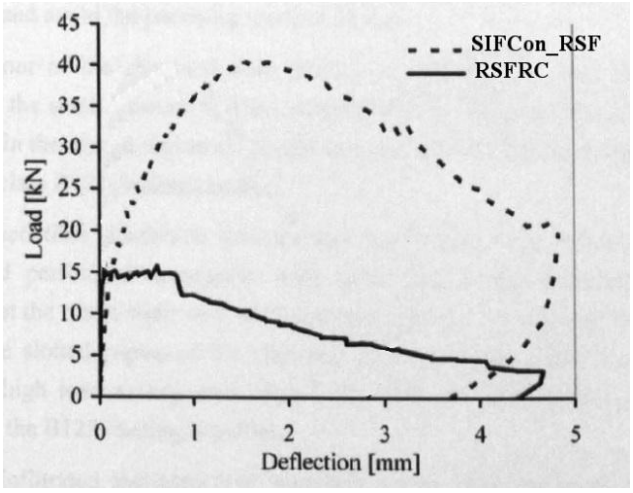

Figure 2.29 Load versus mid span deflection curve for tested RSFRC and SIFCon_RSF beams (Tlemat 2004)

The compressive test of the SIFCon_RSF cubes indicated extremely high axial compression deformability. In fact the cube changed significantly its shape maintaining, however, its integrity without total collapse (Figure 2.30). This can be attributed to the high fibre content and a very good bond between the shredded fibre and the cement paste. The compressive strength of SIFCon_RSF and RSFRC specimens was, respectively, 54.2 MPa and 45.3 MPa (Tlemat 2004).

Figure 2.30 SIFCon_RSF cubes before (right) and after (left) compressive tests (Tlemat 2004)

2.5 Industrial applications of RSFRC

In order to help find a market for the RSF in the field of civil engineering, it is necessary to investigate the performance comparability of the construction products (which utilises RSF for reinforcement) by the ones reinforced with ISF (or even traditional reinforcement), by performing tests on full-scale elements.

The use of RSF as fatigue reinforcement for concrete pavements was investigated by Graeff *et al*. (2010) in which RSFRC prisms were subjected to cyclic flexural loads (Figure 2.31). Two types of mixes, conventional and roller compacted concrete, and two RSF contents, 2.0 % and 6.0 % by mass of concrete were used.

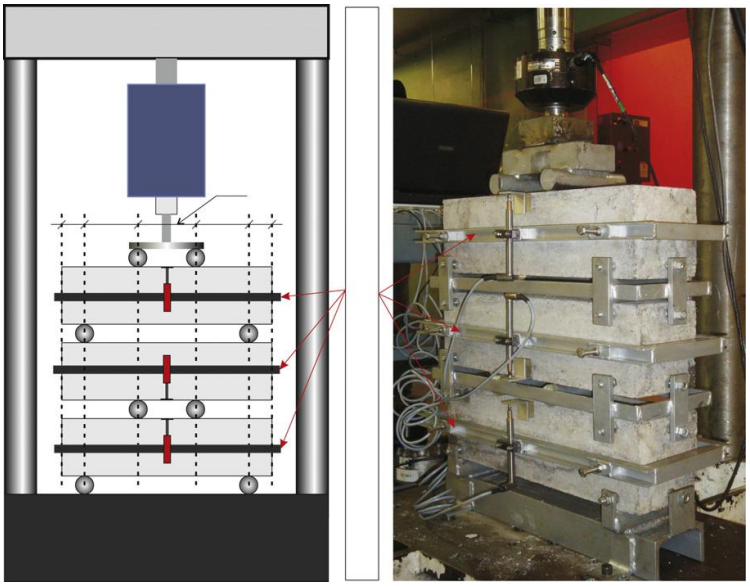

Figure 2.31 setup of specimens (Graeff *et al*. 2012)

According to this investigation, specimens reinforced with RSF can sustain higher stress levels than plain concrete or, for the same stress level, they have longer endurance life. The improvement of the fatigue performance of concrete by addition of RSF to the concrete may lead to a reduction of up to 26 % in the pavement thickness. On the other hand fibre content of 2 % by mass of concrete was reported as an ideal RSF dosage that gives the best fatigue performance.

Precast RSFRC slab (Figure 2.32) used for drainage cover is another practical application that was investigated by Pilakoutas *et al*. (2004). The design of the slab was

based on decathlon reinforced concrete surface-water drainage system so that ordinary steel bars were replaced by RSF.

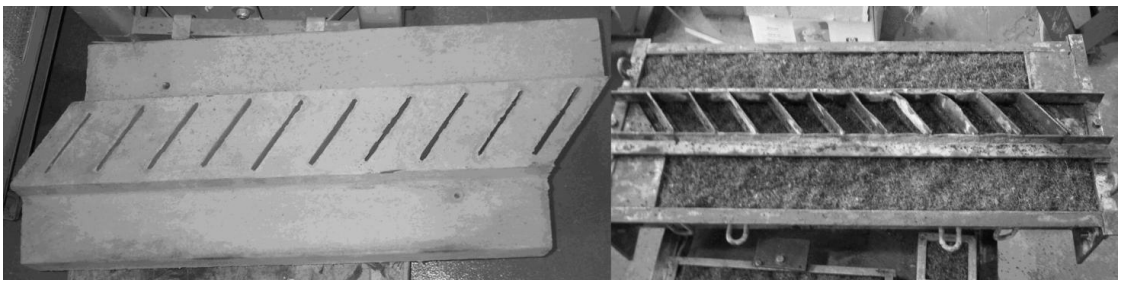

Figure 2.32 Precast cover slab for drainage channels (Pilakoutas *et al*. 2004)

By performing central-load bending tests, it is reported that the slabs satisfied the loading conditions adopted for pavements by BS-EN-124. It is also reported that the use of RSFRC in such geometrically complex elements will introduce benefits in term of simpler and faster execution of the structure and offers savings in the assembly and placing of the reinforcement.

2.6 Research and development needs

A large amount of steel as part of the cord and bead of used tyres are currently discarded in the world; so, illustrating the importance of the steel recovered from used tyres as reinforcement in concrete will be of paramount value to the world. However, the following barriers were identified on the use of RSF as much as possible in commercial applications and find a market for RSF in the construction industry:

- Problems associated with adding fibre to concrete i.e. workability, balling effect and maximum fibre ratio for RSF;
- A lack of information regarding to the shear behaviour of cementitious composites reinforced with RSF;
- Inadequate information regarding to durability performance of cementitious composites reinforced with RSF such as water absorption by immersion and by capillarity, permeability to air, chloride diffusion by migration under nonsteady state and drying shrinkage;

- The need for further research on the possible innovative systems for shear strengthening of RC beams such as thin panels reinforced with RSF as replacement for the existing strengthening systems like the ones based on steel plates and fibre reinforced polymer (FRP) systems applied according to the externally bonded reinforcement (EBR) or the near surface mounted (NSM) techniques;
- A lack of appropriate finite element modelling of RSFRC elements failing in bending and in shear, and the need to study the applicability of the existing analytical models for predicting the compressive, flexural and shear behaviour of ISFRC for developed RSFRC.

Chapter 3

3 Technology of RSFRC with rheological and mechanical properties suitable for industrial applications

3.1 Introduction

In this chapter, firstly the technological aspects for the production of Recycled Steel Fibre Reinforced Concrete (RSFRC) and the mix compositions of the experimental programs are described. Then, to assess the mechanical properties of the developed RSFRC, experimental and numerical research was performed according to the following three phases:

- the first phase (section 3.3.1) is devoted to the assessment of the flexural behaviour of the developed RSFRC. For this purpose three point notched beam bending tests with RSFRC and ISFRC were carried out according to the RILEM recommendations

(RILEM TC 162-TDF 2002). The results from these tests were analysed in terms of design parameters, such as the limit of proportionality (f_{fct}), equivalent (f_{eq}) and residual ($f_{R,i}$) flexural tensile strength parameters, and these values were compared with the ones collected in a database that includes $f_{R,i}$ values from the same type of tests executed with ISFRC specimens;

- the second phase (section 3.3.1.5) is dedicated for the obtainment of the fracture mode I parameters of the developed RSFRC by performing inverse numerical analysis with the results obtained in the three point notched beam bending tests;

- in the third phase (section 3.3.2), the compressive behaviour of the developed RSFRC was investigated by performing compression tests on RSFRC cylinders with fibre content of 60 kg/m^3, aiming to assess the Young's modulus, compressive strength and post peak behaviour of the developed RSFRC. The applicability of the existing analytical model for predicting the compressive stress-strain relationship of industrial steel fibre reinforced concrete (ISFRC) for the developed RSFRC was also assessed.

3.2 Technological aspects for the production of RSFRC

3.2.1 Mix compositions of the experimental program

The materials used in the composition of the RSFRC were: ordinary Portland cement, fly ash, limestone filler, Sika Viscocret 3005 superplastisizer, water, three types of aggregates (fine river sand, coarse river sand and crushed aggregates 5-12 mm) and steel fibres. Hooked end ISF (diameter and length equal to 0.5 mm and 30 mm, respectively) were used in the ISFRC specimens. The RSF used in the RSFRC specimens was supplied by RECIPNEU company, and were obtained from the cryogenic process of waste tyres, described in Section 2.2.1.2. Figure 3.1 shows some types of fibres used in the RSFRC.

Figure 3.1 Used recycled steel fibres

Geometric properties of recycled steel fibres have been determined on a sample of 1000 fibres by using an electronic calliper that had a precision of 0.01 mm (see Figure 3.2).

Figure 3.2 Digital calliper

The RSF diameters varied between 0.18 mm and 1.44 mm, with an average value of 0.29 mm. Six length ranges and four diameter ranges were defined and the number of fibres included in each range was counted, and the obtained results in terms of percentage of fibres in each class are represented in Figure 3.3. It should be noted that the distance between the outer ends of the fibres were considered as the fibre length. The range that included the largest number of length values was 25-35 mm (30%) followed by the class 35-45 mm (26%) and 45-65 mm (17%).

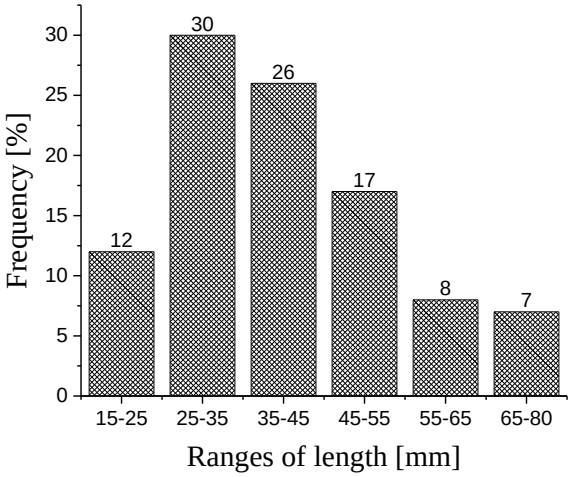

a)

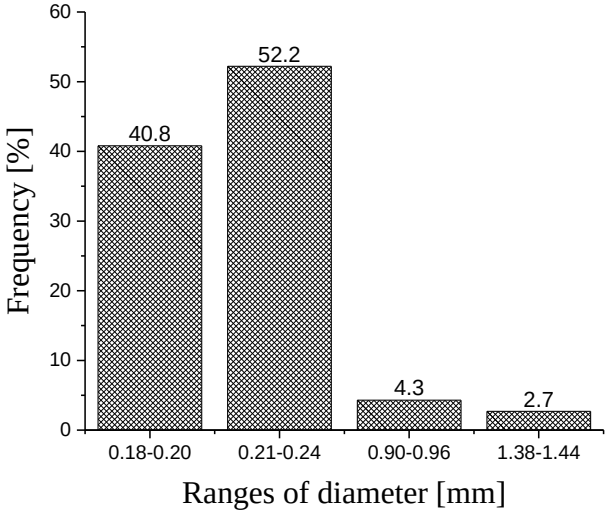

b)

Figure 3.3 a) Relative frequency of the length of the RSF; b) Relative frequency of the diameter of the RSF

Table 3.1 shows the three mix proportions used (common to RSFRC and ISFRC). Note that, for all the specimens, mixes of similar concrete strength class (40 MPa in standard cylinders) were used in order to perform a reliable comparison of the mechanical properties of RSFRC and ISFRC. In the present chapter the label M_j is used to differentiate the concrete mixes used for different dosages of fibres, where "j" identifies the content of fibres, in kg, per cubic meter of concrete, while the labels RSFRCj and ISFRCj identify RSFRC and ISFRC, respectively, with fibre content of "j" in kg/m^3.

Table 3.1 Mix proportions (Kg per cubic meter of concrete)

Mix	C	LF	W	SP	FRS	CRS	CA	FA	SF
M_45	380.5	326.2	126.8	6.09	362.6	574.6	510.1	-	45
M_60	380.5	353.0	140.0	7.83	237.0	710.0	590.0	-	60
M_90	408.0	395.0	150.0	6.26	263.0	658.0	446.0	73.0	90

C = Cement; LF = Limestone Filler; W = Water; SP = Superplasticizer; FRS = Fine River Sand; CRS = Coarse River Sand; CA = Crushed Aggregates; FA = Fly Ash; SF = Steel fibres (ISF or RSF)

When a large amount of RSF are added to the concrete, the fibres tend to ball if the mixture is not appropriately modified in order to take the high perturbation that fibres introduce in the aggregates skeleton organization (Pereira *et al*. 2008). The balling degree depends on the mix proportions and on the dosage and type of fibres used.

On the other hand, the addition of RSF to concrete has a detrimental effect on its workability, which can be captured by performing slump tests (Figure 3.4). In fact, fibres increase the internal friction of the mixture, mainly with stiff fibres, like is the case of steel ones, due to the interacting mechanisms of fibre/fibre, fibre/matrix and fibre/aggregates (Tlemat 2004).

Figure 3.4 Slump test of RSFRC specimens

To accommodate properly 45, 60 and 90 kg of RSF per cubic meter of concrete with the aimed flowability and without segregation of the constituents, an increasing content of water and superplasticizer was used with the increase of the percentage of fibres. On the other hand, to avoid the strong perturbation effect on the flowability of fresh concrete when RSF dosage is increased, in the M_90 fly ash was used, and the content of

spherical-shape fine river sand increased. In fact the spherical-shape particles of the fly ash act as micro-rollers which significantly decrease the friction and the flow resistance of the paste and, consequently, increase the workability of the concrete (Soltanzadeh *et al*. 2015, Soltanzadeh 2016).

3.2.2 Mixing strategy

There are no general rules on the order of feeding the mix components into the mixer. The order followed in this study was the one followed by Barros *et al*. (2007). The aggregates were put into the mixer in a predetermined order from the highest to the lowest aggregate dimension. First the crushed aggregates were added, then the coarse river sand and the fine river sand, and finally were mixed during one minute. Meanwhile, the aggregate saturation degree was determined. After this, it was added the necessary water quantity to saturate the aggregates, and the mixing continued again during one minute. Then, by this order, the limestone filler and cement were added, and another minute of mixing was taken. Afterwards, the superplasticizer and the water necessary to hydrate the cement were added with the mixing machine running. Finally, the steel fibres were added. In an attempt of assuring a suitable distribution of RSF during the execution of the concrete mixes, RSF were gradually added to the mixture. The concrete was mixed during about 300 seconds, until it started to exhibit good homogeneity. Then the specimens were cast directly in the size required for the tests. The specimens were removed from the moulds 24 hours after casting and were cured in natural environmental conditions of the laboratory.

3.3 Mechanical properties of the developed RSFRC

3.3.1 Flexural behaviour

3.3.1.1 Test series

To assess the potentialities of RSF for the reinforcement of concrete elements, three series of RSFRC specimens were subjected to three point notched beam bending tests.

Specimens reinforced with ISF were also considered for comparison purposes. The number of specimens for each series and the content of steel fibres are indicated in Table 3.2. Since a higher dispersion on the results was expected for the RSFRC, mainly for the two series of smaller content of RSF, the number of specimens prepared for the corresponding compositions was higher than for the concrete compositions reinforced with ISF.

Table 3.2 Designation of the series of tests of the experimental program

Series name	Mix	Type of fibres	Number of specimens	Content of steel fibres [kg / m^3]
RSFRC45	M_45	RSF	10	45
RSFRC60	M_60	RSF	10	60
RSFRC90	M_90	RSF	4	90
ISFRC45	M_45	ISF	4	45
ISFRC60	M_60	ISF	4	60
ISFRC90	M_90	ISF	4	90

3.3.1.2 Test setup and methodology

The specimen geometry, the position and dimensions of the notch sawn into the specimen, the loading and specimen support conditions, the characteristics for both the equipment and measuring devices and the test procedures to characterise the flexural behaviour of RSFRC are all given elsewhere (CEB-FIP-2010 2011, RILEM TC 162-TDF 2003) - see Figure 3.5.

Figure 3.6 presents a typical relationship between the applied load and the Crack Mouth Opening Displacement (CMOD) obtained from a three point beam-bending test. Using this type of relationship, the load at the limit of proportionality (F_L) and the residual flexural tensile strength parameters ($f_{R,i}$) can be obtained. F_L is the highest value of the load recorded up to a deflection (or CMOD) of 0.05 mm.

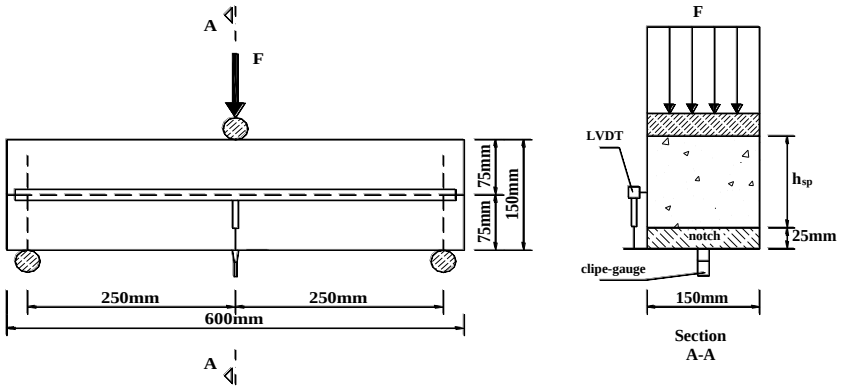

Figure 3.5 Three point beam bending test setup

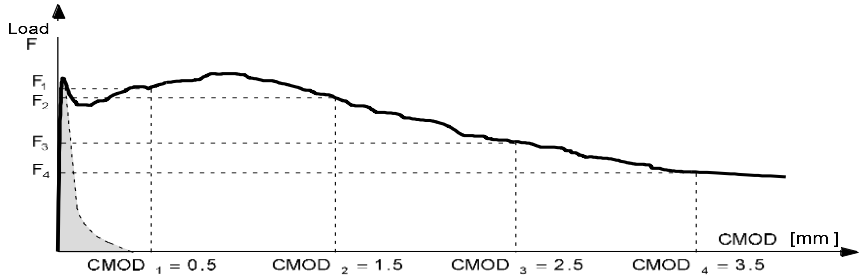

Figure 3.6 Typical load F – CMOD curve of FRC (CEB-FIP-2010 2011)

Based on the force values for the $CMOD_j$ (j = 1 to 4, see Figure 3.6) and assuming at mid span of the specimen a linear stress distribution (see Figure 3.7), the corresponding force values (F_j) are obtained, and the derived residual flexural tensile strength parameters are determined from the following equation:

$$f_{R,\mathrm{i}} = \frac{3F_j L}{2bh_{sp}^2} \tag{3.1}$$

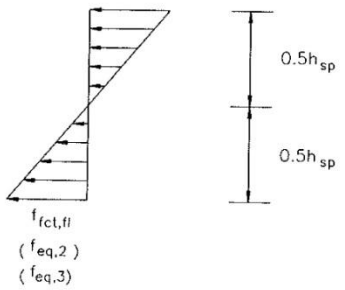

Figure 3.7 Stress distribution assumed, adopted from Vandewalle et al. (2000)

where: b = 150 mm and L = 500 mm are the width and the span of the specimen; h_{sp} = 125 mm is the distance between the tip of the notch and the top of the cross section.

The equivalent flexural tensile strength ($f_{eq,2}$) and ($f_{eq,3}$) can be determined by means of following equations:

$$f_{eq,2} = \frac{3}{2}\left(\frac{D^f_{BZ,2,I}}{0.65} + \frac{D^f_{BZ,2,II}}{0.5}\right)\frac{L}{bh^2_{sp}} \tag{3.2}$$

$$f_{eq,3} = \frac{3}{2}\left(\frac{D^f_{BZ,3,I}}{2.65} + \frac{D^f_{BZ,3,II}}{2.5}\right)\frac{L}{bh^2_{sp}} \tag{3.3}$$

where $D^f_{BZ,2,I}$, $D^f_{BZ,2,II}$, $D^f_{BZ,3,I}$ and $D^f_{BZ,3,II}$ are the contribution of steel fibres to the energy absorption capacity (see Figure 3.8).

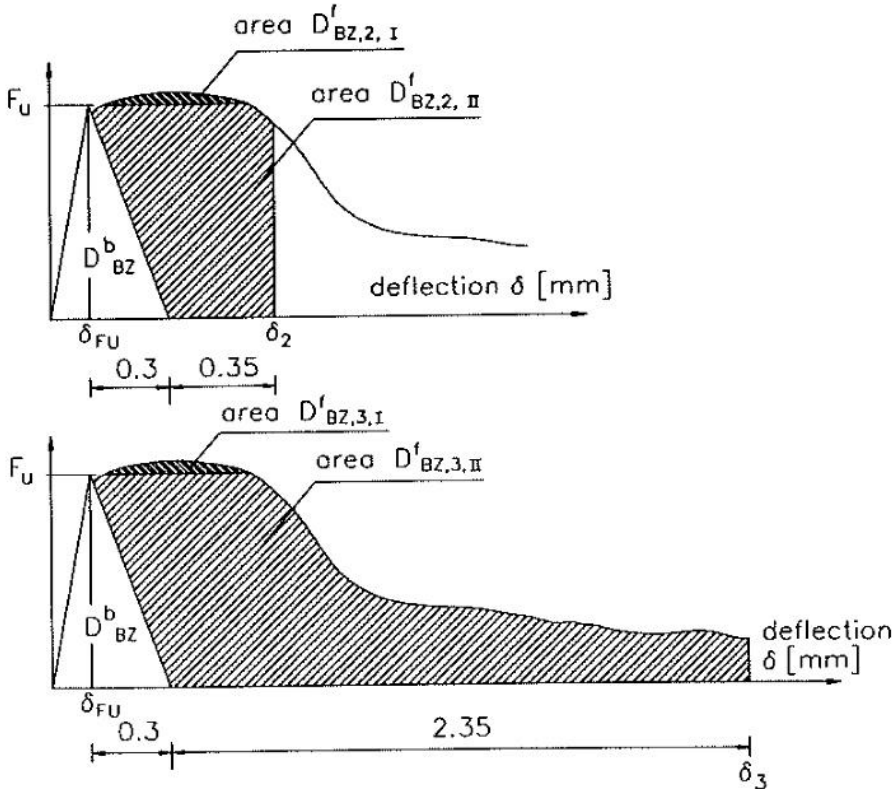

Figure 3.8 Diagrams, adopted from Vandewalle et al. (2000)

3.3.1.3 Experimental results

One of the main effects of the fibres is to control the crack propagation and maintain the crack width in the limits according to structural concrete requirements. The fibre reinforcement provides a residual strength in the post-cracking stage, which is much higher than in the corresponding plain concrete (concrete of the same strength class but without any type of reinforcement), resulting in a significant improvement of the material toughness. The level of toughness depends on the efficiency of fibre reinforcement mechanisms. Fibre pull-out should be the governing fibre failure mode in both RSFRC and ISFRC.

In Figure 3.9a average curves of flexural stress *vs*. CMOD are presented for RSFRC specimens. It is verified that the increase of the fibre content has led to an increase of the peak load and post-cracking residual strength, as expected. The flexural behaviour obtained in the three point bending tests with ISFRC specimens is illustrated in Figure 3.9b.

The comparison between the flexural behaviour of RSFRC and ISFRC are depicted in Figure 3.10. The results of three point bending tests are analysed in term of equivalent and residual flexural tensile strength parameters and corresponding coefficient of variation (COV) for RSFRC (Table 3.3) and ISFRC (Table 3.4) specimens.

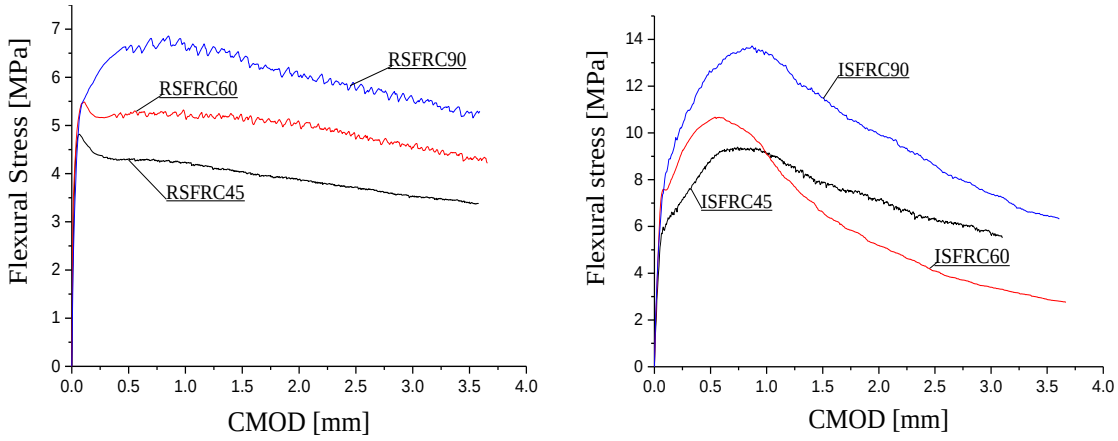

a) b)

Figure 3.9 Flexural behaviour in three point notched beam bending tests: a) RSFRC, b) ISFRC

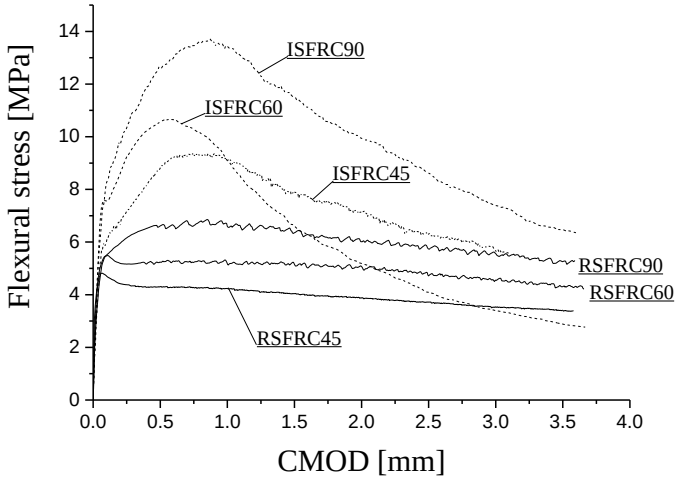

Figure 3.10 Comparison of the flexural behaviour of ISFRC and RSFRC

Table 3.3 Equivalent and residual flexural tensile strength parameters for RSFRC [MPa]

Series		$f_{fct,L}$	$f_{eq,2}$	$f_{eq,3}$	$f_{R,1}$	$f_{R,2}$	$f_{R,3}$	$f_{R,4}$
RSFRC45	Average	4.73	4.28	3.90	4.16	3.94	3.69	3.43
	COV	18.6%	28.9%	30.8%	24.6%	32.4%	33.4%	33.5%
RSFRC60	Average	5.00	5.39	5.08	5.36	5.17	4.86	4.41
	COV	11.4%	15.2%	16.8%	13.6%	17.2%	18.6%	20.7%
RSFRC90	Average	4.56	6.78	6.35	6.62	6.56	5.90	5.55
	COV	9.5%	8.3%	9.3%	7.6%	9.1%	11.9%	12.2%

Table 3.4 Equivalent and residual flexural tensile strength parameters for ISFRC [MPa]

Series		$f_{fct,L}$	$f_{eq,2}$	$f_{eq,3}$	$f_{R,1}$	$f_{R,2}$	$f_{R,3}$	$f_{R,4}$
ISFRC45	Average	5.14	8.66	7.87	8.61	8.36	6.83	5.64
	COV	4.9%	25.5%	24.3%	25.0%	23.0%	24.3%	21.9%
ISFRC60	Average	6.62	10.49	7.24	10.43	7.39	4.86	3.40
	COV	6.7%	12.8%	13.0%	13.3%	19.1%	21.7%	20.4%
ISFRC90	Average	5.99	12.75	11.31	12.37	12.00	9.71	7.38
	COV	10.5%	12.1%	22.7%	11.9%	25.3%	34.2%	37.2%

From the data it can be observed that in the RSFRC45 (45 kg of RSF per cubic meter of concrete) a larger dispersion of the results was obtained (a COV values higher than 18.5%), which can be justified by extra difficulties on assuring proper fibre distribution in the RSFRC45 specimens.

The graphical representation of the equivalent and residual flexural strength parameters for all the tested series is represented in Figure 3.11. From the obtained results it is verified that the deflection hardening phase registered in the ISFRC specimens (from crack initiation up to flexural tensile strength) was not developed in the RSFRC specimens. This indicates that fibre bridging mechanisms across the crack surfaces for relatively small crack width levels are not effective in the RSF due to the geometry and surface characteristics of these fibres. However, in the post peak stage the RSFRC specimens have almost retained the maximum flexural tensile strength up to the ultimate crack width recorded in the executed tests (3.5 mm).

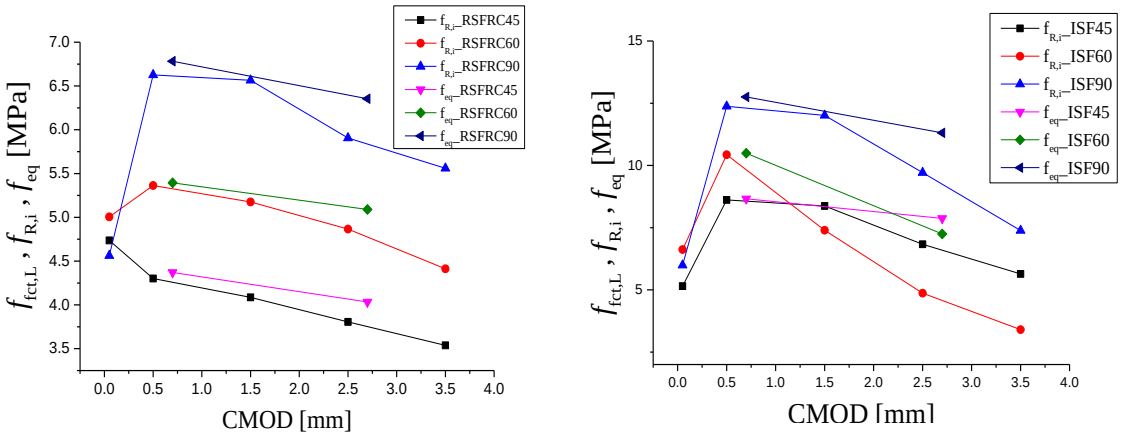

Figure 3.11 Representation of the f_{eq} and $f_{R,i}$ parameters for the series: a) RSFRC, b) ISFRC

Figure 3.12 shows the relationship between $f_{eq,2}$ and $f_{eq,3}$ obtained in RSFRC specimens. A clear linear relationship emerges between these two parameters, which is in agreement with previous research on ISFRC specimens (Barros *et al*. 2005).

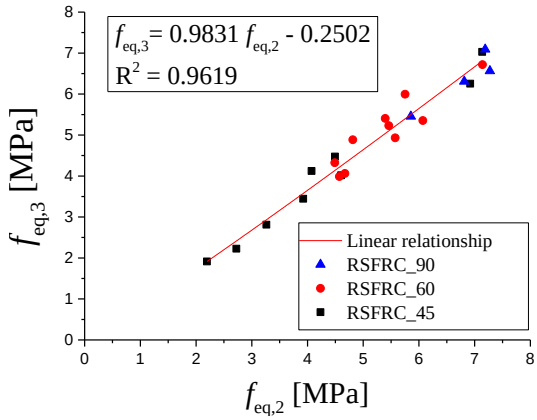

Figure 3.12 Relationship between $f_{eq,2}$ and $f_{eq,3}$

The relationships between $f_{eq,2}$ and $f_{R,1}$, and between $f_{eq,3}$ and $f_{R,4}$ are represented in Figure 3.13. Also a linear trend emerges between these parameters.

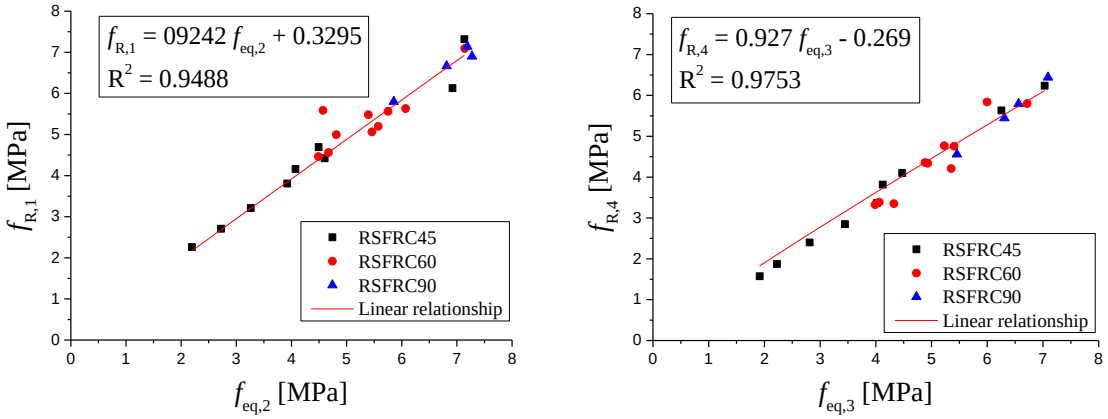

a) b)

Figure 3.13 Relationship between: a) $f_{eq,2}$ and $f_{R,1}$, b) $f_{eq,3}$ and $f_{R,4}$ for RSFRC

The characteristic values of the stress at the limit of proportionality *vs.* fibre volume percentage (V_f) and the characteristic values of the residual flexural tensile strength parameters *vs.* V_f for all tested specimens in accordance with the recommendations of RILEM TC 162-TDF (2003) and CEB-FIP-2010 (2011) are reported in Figure 3.14. The characteristic value of the different tensile strengths is determined from the following equation:

$$f_{ctk} = f_{ctms} - \frac{s_p \times t_{10(n-1)}}{\sqrt{n}} - 1.645 \times s_p \times \left(1 + \frac{s_p \times t_{10(n-1)}}{f_{ctms} \times \sqrt{n}}\right) \quad (3.4)$$

where:

n = The number of specimens;

s_p = Standard division of the test series (MPa);

f_{ctms} = Average tensile strength of the test series (MPa);

f_{ctk} = Characteristic value of the tensile strength (MPa);

$t_{10(n-1)}$ = Value of the student distribution for 10% fractile and (n-1) test results (see Table 3.5).

Table 3.5 Values for the student distribution

n	3	4	5	6	8	10	12	15	20	25	30	∞
$t_{10(n-1)}$	1.89	1.64	1.53	1.48	1.42	1.38	1.36	1.34	1.33	1.32	1.31	1.28

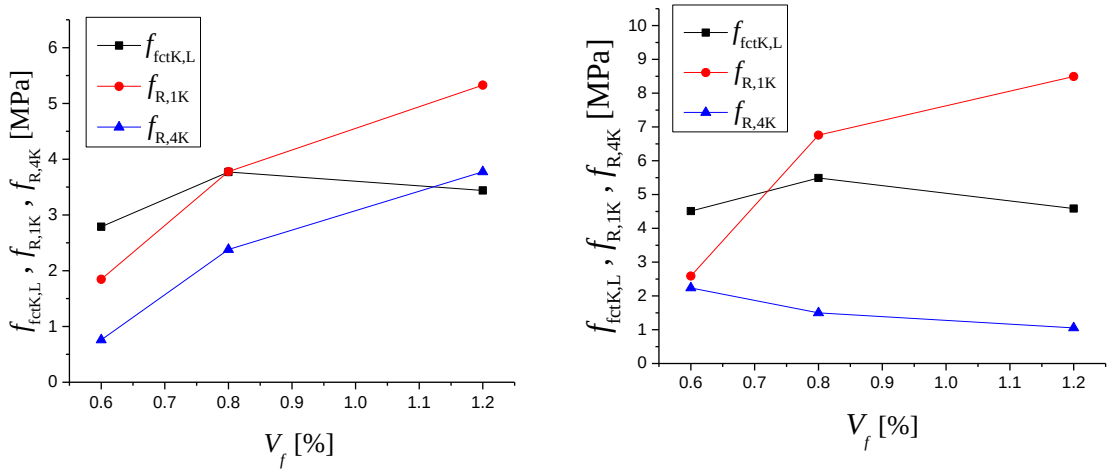

a) b)

Figure 3.14 Relationship between: $f_{fctk,L}$, $f_{R,1K}$, $f_{R,4K}$ and V_f : a) RSFRC and b) ISFRC

For a wider comparison between RSFRC and ISFRC, the database (DB) collected by Moraes Neto *et al*. (2014) in terms of $f_{R,i}$ values was used in the present work. This DB

includes $f_{R,i}$ values of ISFRC of hooked ends geometry configuration for the ISF, and presenting tensile strain softening, which is also the type of behaviour of both RSFRC and ISFRC considered in the present experimental program. Figure 3.15 compares $f_{R,1} - f_{R,3}$ and $f_{R,1} - f_{R,4}$ from the experimental results of DB with those obtained from RSFRC specimens. A similar trend emerges between the RSFRC and the DB results in terms of $f_{R,1} - f_{R,3}$ and $f_{R,1} - f_{R,4}$.

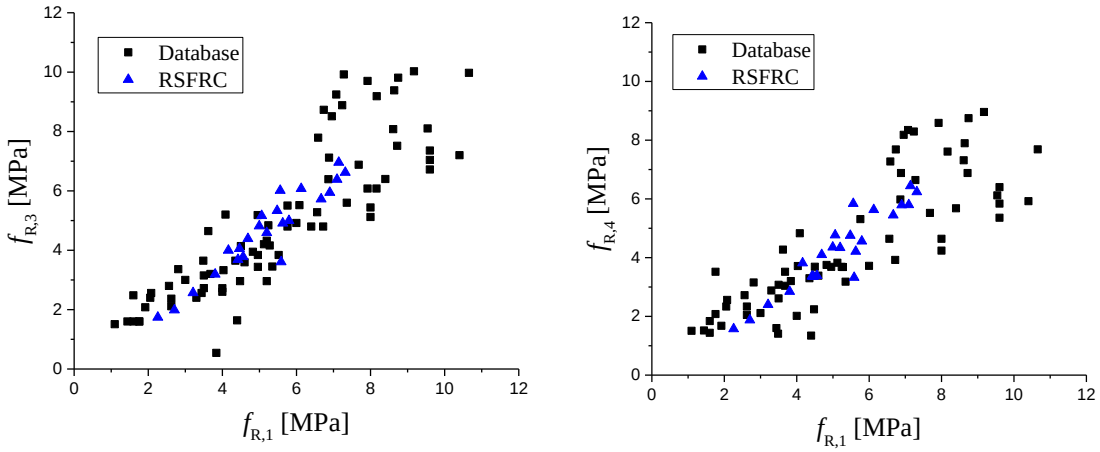

Figure 3.15 Relationship between: a) $f_{R,1}$ and $f_{R,3}$ and b) $f_{R,1}$ and $f_{R,4}$ (RSFRC and DB)

Figure 3.16 compares $f_{R,i}$ and V_f from the experimental results of the DB with those obtained from the RSFRC specimens. It is verified that the increase of the fibre volume percentage in SFRC specimens (DB) leads to a higher increase of the residual flexural tensile strength parameters, comparatively with the values obtained for RSFRC specimens, which means that, for usual SFRC compositions, the fibre reinforcement effectiveness by increasing the fibre content is higher with ISF than with RSF. However, the development of mix design strategies for the RSFRC that assure proper fibre distribution up to fibre contents used in structural applications might attenuate this different fibre reinforcement effectiveness. In any case, the $f_{R,i}$ values obtained for the developed RSFRC are sufficiently high to create good perspectives for the use of these composites in certain applications.

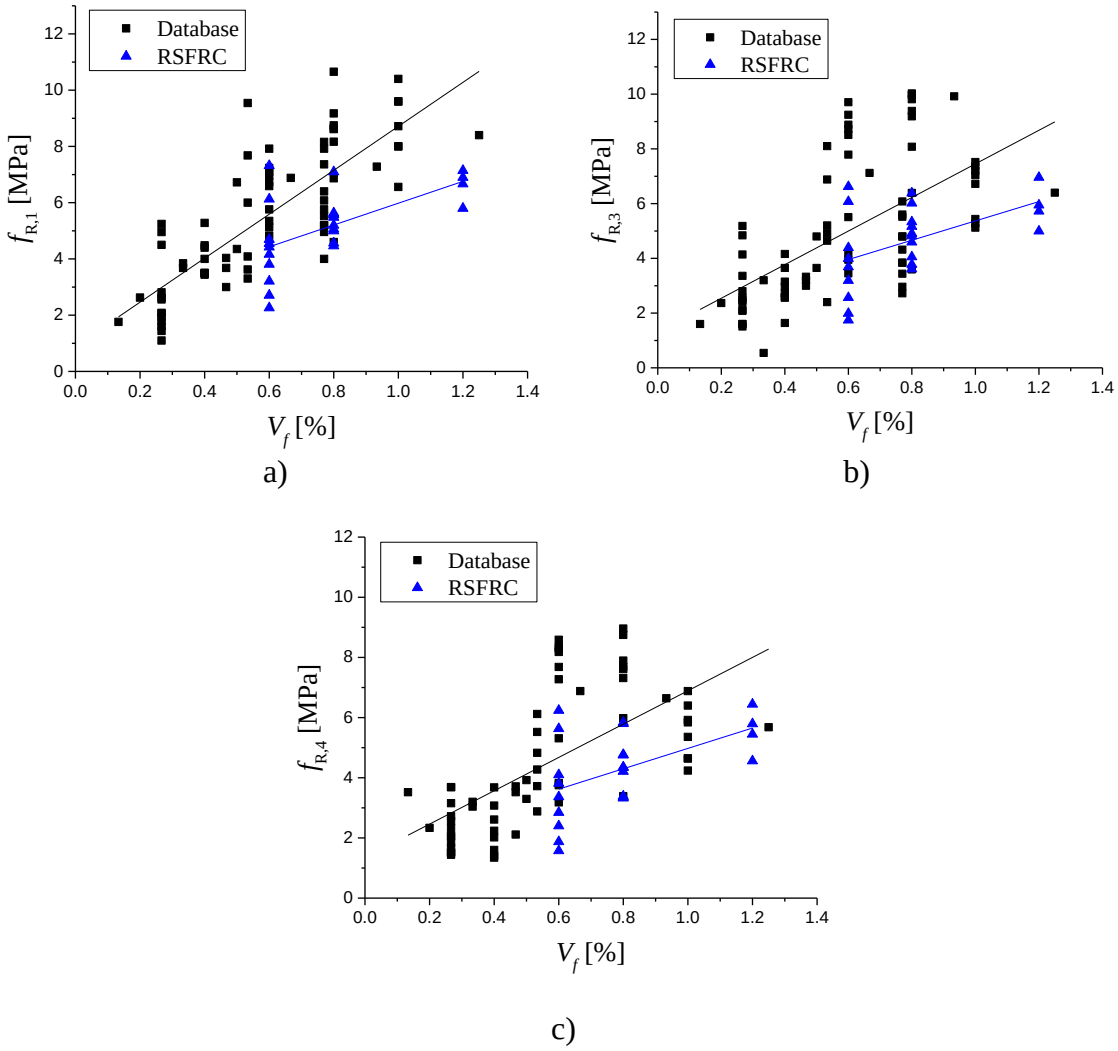

Figure 3.16 Influence of V_f on: a) $f_{R,1}$, b) $f_{R,3}$, and c) $f_{R,4}$ (RSFRC and DB)

3.3.1.4 Toughness classes

Classification is an important requirement for structural materials. When referring to regular concrete, designers choose its strength, workability or exposition classes that have to be provided by concrete producers (Prisco *et al*. 2009). When using FRC, since fibre reinforcement mechanisms are mainly activated after cracking of the concrete matrix, the residual (post-cracking) tensile strength are the parameters more influenced and must be taken into account on the FRC classifications. For structural applications with normal and high-strength concrete, the FRC classification proposed by CEB-FIP Model Code (2010)

is based on the post-cracking residual strength. For this purpose, the $f_{R,1k}$ (representing the strength interval) and a letter *a*, *b*, *c*, *d* or *e* (representing the $f_{R,3k} / f_{R,1k}$ ratio) are considered. The strength interval is defined by two subsequent numbers in the series:

1.0, 1.5, 2.0, 2.5, 3.0, 4.0, 5.0, 6.0, 7.0, 8.0 [MPa]

while the letters a, b, c, d, e correspond to the residual strength ratios:

a if $0.5 \leq f_{R,3k} / f_{R,1k} \leq 0.7$
b if $0.7 \leq f_{R,3k} / f_{R,1k} \leq 0.9$
c if $0.9 \leq f_{R,3k} / f_{R,1k} \leq 1.1$
d if $1.1 \leq f_{R,3k} / f_{R,1k} \leq 1.3$
e if $1.3 \leq f_{R,3k} / f_{R,1k}$

For instance, a material denoted as "7b" has a strength $f_{R,1k}$ ranging between 7.0 and 8.0 MPa, and the $f_{R,3k} / f_{R,1k}$ ratio ranging between 0.7 and 0.9 (Figure 3.17). This classification can also be adopted for the RSFRC. Toughness classes obtained for developed RSFRC with fibre content of 45, 60 and 90 kg/m^3 are depicted in Table 3.6.

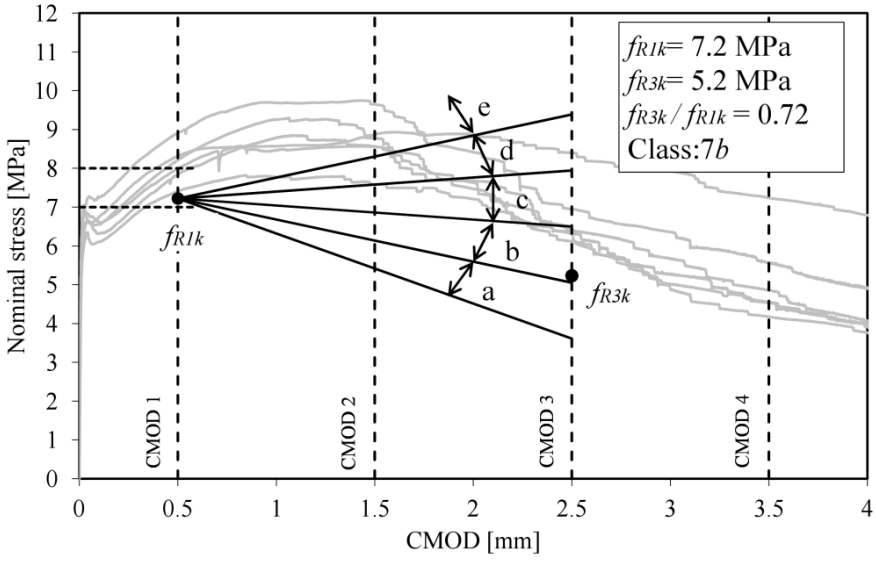

Figure 3.17 The concept of toughness class for FRC based on the relationship between the flexural stress and CMOD (CEB-FIP Model Code, 2011)

Table 3.6 Toughness class obtained for developed RSFRC specimens

Series	Toughness class
RSFRC45	1.5a
RSFRC60	3.0b
RSFRC90	5.0b

3.3.1.5 Numerical and analytical study

3.3.1.5.1 Inverse analysis with the data obtained from flexural tests

Previous research (Pereira *et al*. 2008) has indicated that fracture mode I propagation of FRC can be simulated by the trilinear softening diagram represented in Figure 3.18, whose parameters (fracture energy, G_f^I, and values of $\varepsilon_{n,\mathrm{i}}^{cr}$ and $\sigma_{n,\mathrm{i}}^{cr}$ that define the shape of the diagram that simulates the fracture mode I crack propagation) can be obtained performing inverse analysis with the force-CMOD data (or force-vertical deflection data) registered in three point notched beam bending tests.

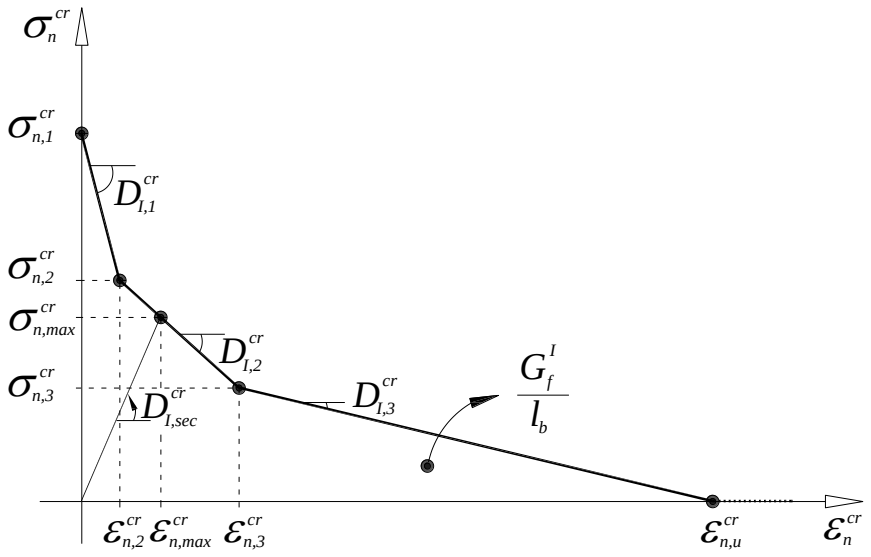

Figure 3.18 Trilinear stress strain diagram to simulate the fracture mode I crack propagation ($\sigma_{n,2}^{cr} = \alpha_1\ \sigma_{n,1}^{cr}$, $\sigma_{n,3}^{cr} = \alpha_2\ \sigma_{n,1}^{cr}$, $\varepsilon_{n,2}^{cr} = \xi_1\ \varepsilon_{n,u}^{cr}$, $\varepsilon_{n,3}^{cr} = \xi_2\ \varepsilon_{n,u}^{cr}$)

In Figure 3.18, G_f^I / l_b corresponds to the area defined by the trilinear stress-strain normal to the crack plane (σ_n^{cr} - ε_n^{cr}), where l_b is the crack band width. When using a smeared crack approach, the l_b parameter is used in order to assure that the results of the numerical simulations are not dependent of the finite element mesh refinement (Pereira *et al.* 2008). For this purpose, the l_b is assumed dependent of a geometric characteristic of the finite elements adopted in the numerical simulations. In the present case the l_b was considered equal to the square root of the area of the integration point corresponding to the integration scheme adopted for the evaluation of the stiffness matrix and stress field.

The ultimate crack strain, $\varepsilon_{n,u}^{cr}$, is defined as a function of the α_i and ξ_i parameters, fracture energy, G_f^I, tensile strength, $f_{ct} = \sigma_{n,1}^{cr}$, and crack band width, l_b, as follows (Sena-Cruz 2004),

$$\varepsilon_{n,u}^{cr} = \frac{2}{\xi_1 + \alpha_1 \xi_2 - \alpha_2 \xi_1 + \alpha_2} \frac{G_f^I}{f_{ct} l_b} \tag{3.5}$$

being $\alpha_1 = \sigma_{n,2}^{cr} / \sigma_{n,1}^{cr}$, $\alpha_2 = \sigma_{n,3}^{cr} / \sigma_{n,1}^{cr}$, $\xi_1 = \varepsilon_{n,2}^{cr} / \varepsilon_{n,u}^{cr}$ and $\xi_2 = \varepsilon_{n,3}^{cr} / \varepsilon_{n,u}^{cr}$.

The objective of the analysis is to evaluate the values of α_i, ξ_i, and G_f^I of the $\sigma_n^{cr} - \varepsilon_n^{cr}$ diagram based on the minimization of the error parameter

$$err = \frac{\left| A_{F-CMOD}^{\exp} - A_{F-CMOD}^{num} \right|}{A_{F-CMOD}^{\exp}} \tag{3.6}$$

where $A_{F-CMOD}^{\exp}$ and A_{F-CMOD}^{num} are the areas below the experimental and the numerical *F*-CMOD curves, respectively (Barros *et al*. 2004)

In this context, the specimen was modelled with a mesh of 8 node serendipity plane stress finite elements. The Gauss-Legendre integration scheme with 2×2 integration points was used in all elements, with the exception of the elements at the specimen symmetry axis, where 1×2 integration points were used in order to assure that the crack progresses along

the symmetry axis of the specimen. In the inverse analysis, the l_b was considered equal to the width of the notch (5 mm) that coincides with the width of the finite elements above the notch. Figure 3.19 shows the finite element mesh used in the inverse analysis (Sena-Cruz *et al*. 2004).

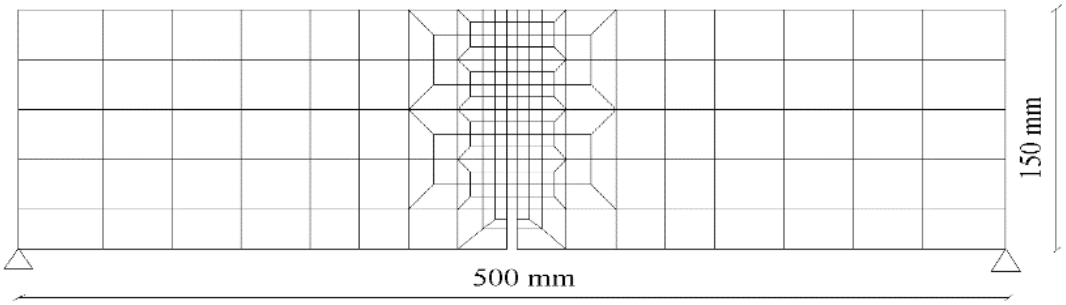

Figure 3.19 Finite element mesh adopted in the inverse analysis

An average value of E_c = 28 GPa was considered for the concrete Young's modulus. The numerical simulations were carried out with the FEM software FEMIX V4.0 (Azevedo *et al*. 2003).

The comparison between the average experimental load *vs*. CMOD and numerical load *vs*. CMOD of all tested specimens is shown in Figure 3.20.

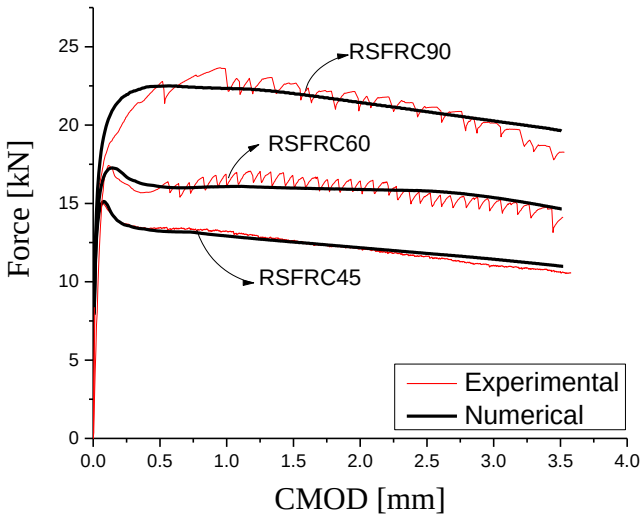

Figure 3.20 Average experimental load vs. deflection and numerical load *vs*. deflection

The values defining the $\sigma_n^{cr} - \varepsilon_n^{cr}$ diagram obtained from inverse analysis are presented in Table 3.7, and the graphical representation of these values is presented in Figure 3.21, where it is visible that the post-cracking residual strength has increased with the content of RSF.

Table 3.7 Values defining the tensile softening diagram, obtained from inverse analysis

Series	$\sigma_{n,1}^{cr}$ **[N / mm^2]**	ξ_1	α_1	ξ_2	α_2	G_f^I **[N / mm]**
RSFRC45	2.250	0.012	0.650	0.280	0.520	6.000
RSFRC60	2.300	0.032	0.750	0.350	0.730	6.300
RSFRC90	2.620	0.100	0.930	0.600	0.730	7.700

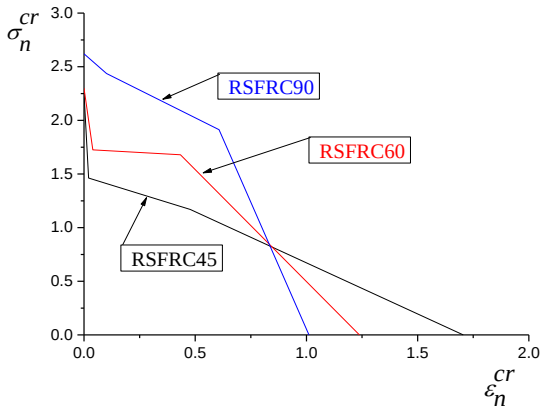

Figure 3.21 Tensile softening trilinear diagrams obtained from inverse analysis

3.3.1.5.2 Analytical investigation on applicability of stress-strain method proposed by RILEM TC 162-TDF (2003) design guideline for RSFRC

In this section it is examined an existing design guideline, developed by RILEM TC 162-TDF (2003) for ISFRC, in order to assess the applicability of the RILEM stress-strain design guideline for the flexural design of concrete reinforced with RSF. Figure 3.22 shows the stress-strain relationship adopted by RILEM for SFRC.

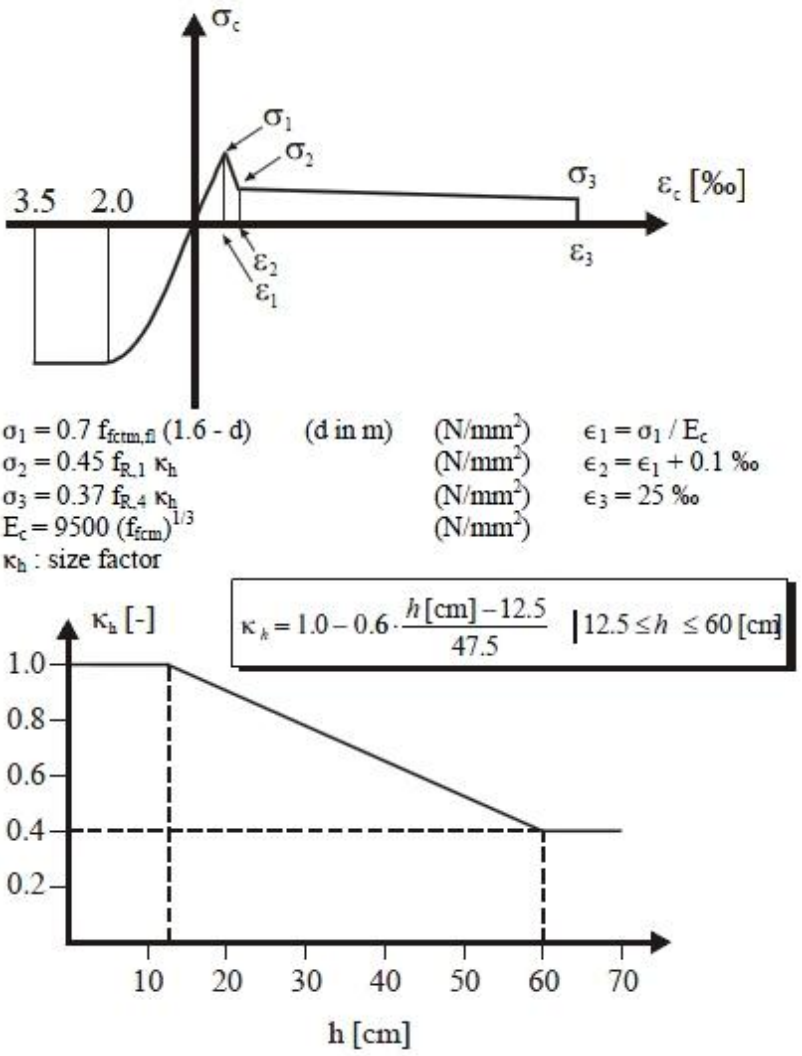

Figure 3.22 Stress-strain diagram and size factor (Recommendation of RILEM TC 162-TDF 2003)

Using the values of Table 3.3 obtained in the experimental tests and adopting the stress-strain diagram represented in Figure. 3.22, the *F*-CMOD of all series of specimens was evaluated by performing numerical simulation of the three series of the RSFRC beams. The finite element mesh adopted in the numerical simulation was the same used in the previous subsection (see Figure 3.19)

Table 3.8 represents the values of tensile softening diagram parameters (used in the finite element analysis) obtained based on the stress-strain diagram proposed by RILEM.

Table 3.8 Values defining the tensile softening diagram, obtained based on the RILEM design guideline

Series	$\sigma_{n,1}^{cr}$ **[N / mm^2]**	ξ_1	α_1	ξ_2	α_2	G_f^I **[N / mm]**
RSFRC45	4.888	0.0069	0.371	0.010	0.252	2.376
RSFRC60	5.167	0.0073	0.453	0.011	0.306	3.054
RSFRC90	4.710	0.0067	0.614	0.010	0.423	3.801

Figure 3.23 represents the tendency observed in the numerical simulation of the three series of the RSFRC beams. Each experimental curve (thick line) is the average of the Force-CMOD relationships recorded in the three point bending tests for each series.

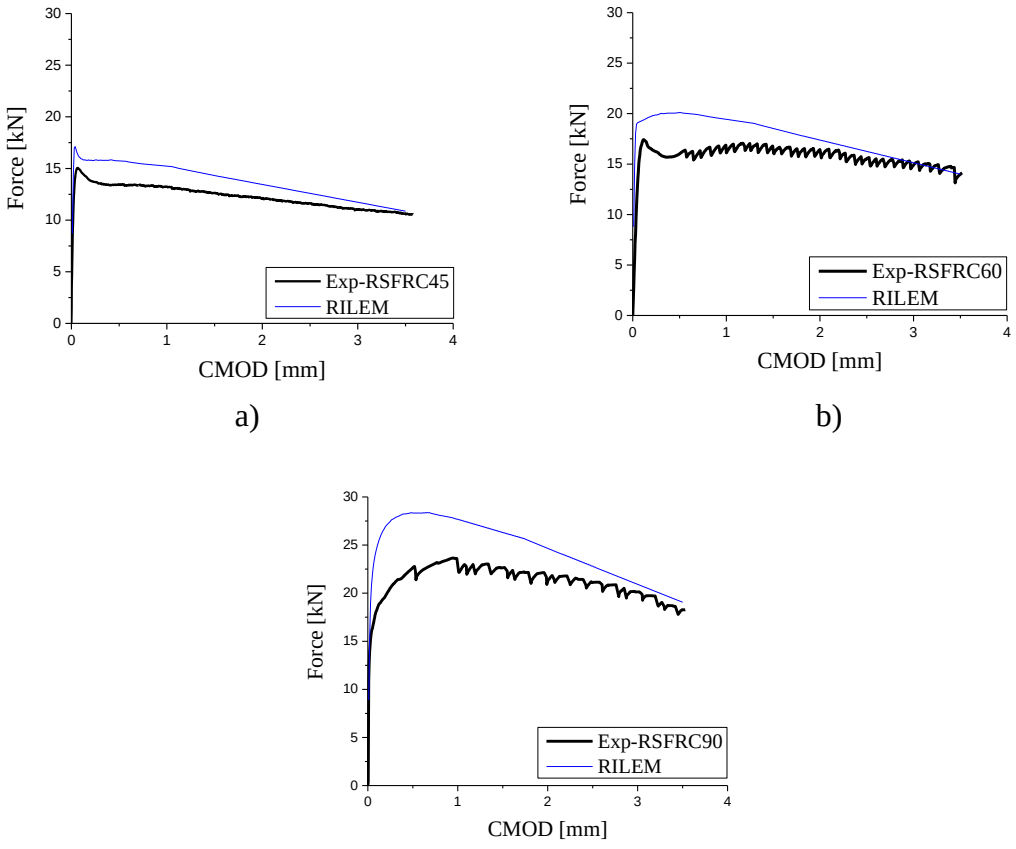

Figure 3.23 Comparison between experimental and numerical load-CMOD curves when using the $\sigma - \varepsilon$ method proposed by R1LEM TC 162-TDF

The obtained results shows that, using the stress-strain constitutive law proposed by RILEM TC 162-TDF (2003), a higher residual force was predicted up to a CMOD of about 3.5 mm and the difference between experimental and analytically obtained residual force increases with the increase of fibre dosage.

On the other hand the experimental load-CMOD curves have less steep descending in tensile strain softening branch than numerical curves. This evaluation indicates that, although the RILEM guideline is in general suitable for the flexural design of SFRC, there are some fundamental issues related to the evaluation of the tensile stress–strain behaviour of RSFRC that affect the accuracy of the guideline.

3.3.2 Uniaxial compressive behaviour

3.3.2.1 Young's modulus

Due to a higher dispersion of the flexural test results obtained for RSFRC45, and extra difficulties on assuring proper fibre distribution without fibre segregation (especially in a larger scale) in the RSFRC90 specimens, the RSFRC60 was chosen for the experimental programs regarding to the compressive behaviour (in the current chapter) and the shear behaviour (in Chapter 4) of RSFRC. The values of the modulus of elasticity or Young's modulus (E_c) of RSFRC60 were obtained with cylindrical specimens of 300 mm height and 150 mm diameter, by executing tests according to the LNEC E397 (1993). The test setup (Figure 3.24) consists of two rings installed at top and bottom central region of the specimen (here is called "test region"). The distance between the rings is 100 mm. In the top ring, three linear variation displacement transducers (LVDT) are placed around the specimen at 120° from each other to measure the axial displacement of the specimen at the test region. Figure 3.25 presents the load cycles to determine the elastic modulus of the concrete. The Young's modulus is determined from the following equation:

$$\varepsilon_c = \frac{\Delta\sigma}{\Delta\varepsilon} = \frac{\sigma_{a,n} - \sigma_{b,n}}{\varepsilon_{a,n} - \varepsilon_{b,n}} \tag{3.7}$$

where $\sigma_{a,n}$ and $\sigma_{b,n}$ are the maximum ($f_c/3$) and minimum (0.5 to 1.0 MPa) stress levels, $\varepsilon_{a,n}$ and $\varepsilon_{b,n}$ are the strains corresponding to the $\sigma_{a,n}$ and $\sigma_{b,n}$, respectively, for the applied load cycle *n*. f_c is the compressive strength of the concrete that was previously obtained from direct compressive test with a cylindrical specimen. The strain was calculated by dividing the average displacement by the length of the test region.

Figure 3.24 Test setup for determining young's modulus

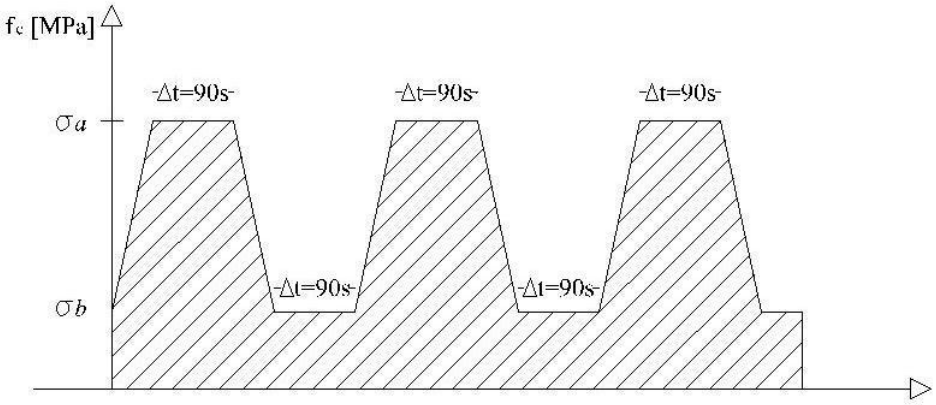

Figure 3.25 Representation of load cycles to determine the elastic modulus

Table 3.9 presents the values of specific weight and Young's modulus obtained in the tests carried out with RSFRC60 specimens.

Table 3.9 Young's modulus and specific weight of the developed RSFRC with fibre content of 60 kg / m^3

Specimen	Young's modulus [GPa]	Specific weight [kN/m^3]
RSFRC60_1	27.164	23.84
RSFRC60_2	28.234	23.61
RSFRC60_3	28.528	23.71
RSFRC60_4	28.437	23.74
average	28.090	23.72
COV (%)	2.24	0.40

3.3.2.2 Compressive strength

The compressive strength of RSFRC with fibre content of 60 kg/m^3 was assessed by performing compressive tests under displacement control with cylindrical specimens of 300 mm height and 150 mm diameter according to NP EN 12390-3 (2009) recommendations. Table 3.10 presents the compressive strength and its corresponding strain for the RSFRC60 specimens. The strain was determined by dividing the axial displacement measurements recorded by the displacement sensor of the actuator by the length of the specimen.

Table 3.10 Compressive strength and strain at peak load of RSFRC60 specimens

Specimen	Compressive strength [MPa]	Strain at peak load [%]
RSFRC60_1	48.09	0.500
RSFRC60_2	51.57	0.513
RSFRC60_3	52.70	0.485
RSFRC60_4	51.07	0.458
Average value	50.86	0.489
COV (%)	3.87	4.83

3.3.2.3 Stress-strain response

3.3.2.3.1 Strain at peak

As stated in subsection 2.3.2.1, since the main influence of the fibres is in the post peak of the compressive behaviour, it is fundamental to carry out compression tests under displacement control. Using the results obtained, a stress-strain relationship for RSFRC60 in compression was derived (Figure 3.26).

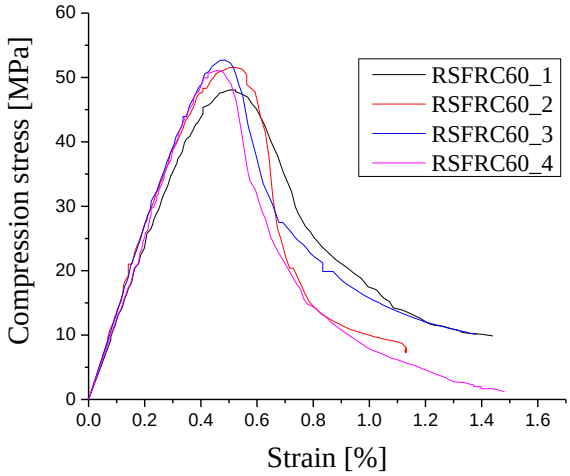

Figure 3.26 Stress-strain relationship for RSFRC60 in compression

It should be noted that the strain of the curves in Figure 3.26 is obtained from the displacement measurements recorded by the displacement sensor of the actuator and, consequently, this displacement also includes the deformation of the reaction frame of the machine, and also the initial adjustments between loading platens of the equipment and extremities of the specimen. Therefore higher strains were recorded when compared to a monitoring setup capable of reading exclusively the deformation of the material part of the specimen considered in uniaxial deformation state.

3.3.2.3.2 Applicability of existing analytical model for RSFRC

Previous work (Neves and Fernandes 2005, Barros and Figueiras 1999) has shown that the analytical model proposed by Vipulanandam and Paul (1990) suitably predicts the

stress-strain relationship of SFRC. This model was described detailed in subsection 2.3.2.1. In this section the applicability of the analytical model proposed by Vipulanandam and Paul (1990) for predicting the compressive stress-strain relationship of RSFRC60 is investigated. As stated in section 3.3.2.3.1, since higher strains and consequently lower values of Young's modulus were recorded in the compression tests (see Figure 3.26), the stress-strain curves in Figure 3.28 were rectified according to CEB-FIP 1990 (1993) in order the E_c is a value coherent with f_c by using the following equation:

$$\sigma_c = \frac{\frac{E_c}{E_{c1}}\frac{\varepsilon_c}{\varepsilon_{c1}} - \left(\frac{\varepsilon_c}{\varepsilon_{c1}}\right)^2}{1+\left(\frac{E_c}{E_{c1}}-2\right)\frac{\varepsilon_c}{\varepsilon_{c1}}} f_{cm} \tag{3.8}$$

where E_{c1} is the secant modulus from the origin to the peak compressive stress (f_{cm}). Using the values indicated in Table 3.11 the expression 2.2 (see section 2.3.2.1) was simplified and rewritten as:

$$\sigma_c = 50.86 \frac{\frac{\varepsilon_c}{0.0022}}{0.735+\left((0.264-p)\left(\frac{\varepsilon_c}{0.0022}\right)\right)+p\left(\frac{\varepsilon_c}{0.0022}\right)^{\frac{p+0.735}{p}}} \tag{3.9}$$

Table 3.11 Values used in analytical model

Property	**Value**
Young's Strength (E_c)	31425 N/mm^2
Compressive strength (f_{cm})	50.86 N/mm^2
Strain at peak load (ε_{c1})	0.0022

Assuming different values for *p*, the value of *p* that minimises the error (expression 2.6) between average experimental and analytical stress-strain curves was 0.36 (Figure 3.27).

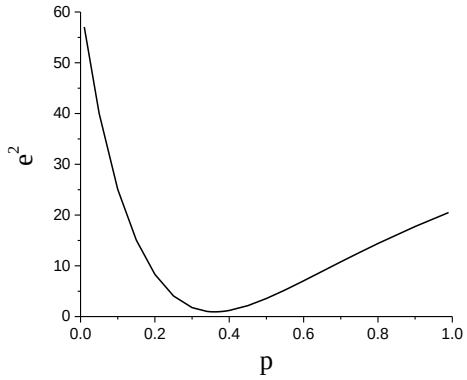

Figure 3.27 Variation of the e^2 with the p parameter

In Figure 3.28, the experimental stress-strain curves are compared with the stress-strain curve obtained analytically. From the comparison made in Figure 3.28, it could be concluded that the analytical model proposed by Vipulanandam and Paul (1990) is comparatively appropriate to simulate the post peak compressive behaviour of RSFRC60.

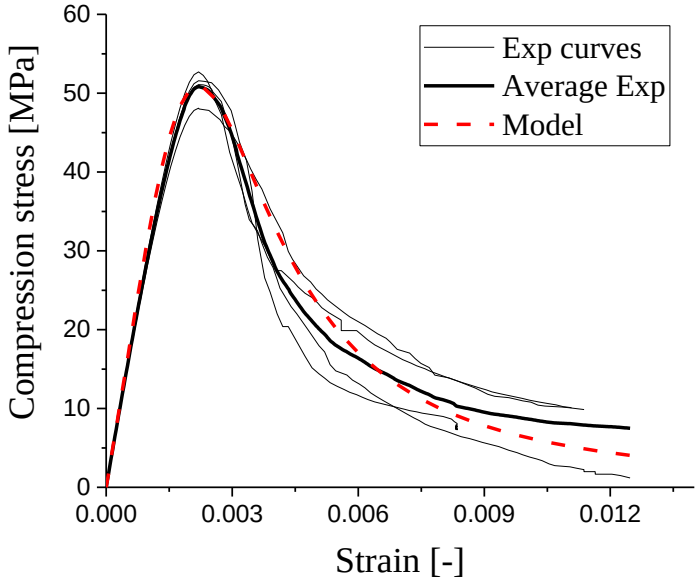

Figure 3.28 Experimental and analytical compressive stress-strain curves for RSFRC60

3.4 Conclusions

The work in this chapter was dedicated to experimental and numerical research to evaluate the mechanical properties of RSFRC. On the basis of the results presented in this work, the following concluding remarks can be highlighted:

1) From the three point notched beam bending tests results it was verified that the deflection hardening phase registered in the ISFRC specimens was not developed in the RSFRC specimens. This indicates that the fibre reinforcement mechanisms for relatively small crack width levels were not as effective in the RSF as were in the ISF, due to the geometry and surface characteristics of RSF fibres. However, the flexural strength of RSFRC specimens was almost constant and of the same order of the flexural tensile strength up to the ultimate crack width recorded in the executed tests;

2) An almost linear relationship between $f_{eq,2}$ and $f_{eq,3}$ was obtained, which was a trend already observed in ISFRC. The same tendency was also observed between the concept of residual flexural strength and equivalent flexural strength ($f_{eq,2}$ *vs.* $f_{R,1}$ and $f_{eq,3}$ *vs.* $f_{R,4}$), which was also already been registered in ISFRC. Toughness classes obtained for RSFRC45, RSFRC60 and RSFRC90 were 1.5a, 3.0b and 5.0b, respectively;

3) From a database containing the results of the characterisation of the post-cracking behaviour of ISFRC, it was verified that RSFRC results have a similar trend of the corresponding results of the ISFRC of this database ($f_{R,1} - f_{R,3}$ and $f_{R,1} - f_{R,4}$). However, the residual flexural strengthening parameters ($f_{R,\mathrm{i}}$) of ISFRC have increased more pronouncedly with the fibre volume percentage (V_f) than in the case of RSFRC, which means that for a certain post-cracking performance a higher V_f of RSF is necessary. However, the $f_{R,\mathrm{i}}$ values obtained for the developed RSFRC are sufficiently high to create good perspectives for the use of

this reinforcement in certain applications; such are the cases of concrete block foundations, slabs supported on soil or on piles;

4) From the analytical study on the applicability of stress-strain method proposed by RILEM TC 162-TDF (2003) design guideline for RSFRC, it was verified that using the stress-strain diagram proposed by RILEM TC 162-TDF, unsatisfactory predictions were obtained. A higher residual force was predicted up to a CMOD of about 3.5 mm and the difference between the experimental and the analytically obtained residual force increases with the increase of fibre dosage;

5) From the analytical study on the applicability of the model proposed by Vipulanandam and Paul (1990) for predicting the compressive stress-strain relationship of RSFRC60, it was verified that the model is comparatively appropriate model to simulate the compressive behaviour of RSFRC60.

Chapter 4

4 Assessment of the potentialities of RSFRC for RC beams failing in shear

4.1 Introduction

One of the main objectives of this thesis is to assess the potentialities of RSF for civil engineering applications. The use of ISF as shear reinforcement of RC beams has been investigated by several researchers (Amin and Foster 2016, Barros *et al*. 2013, Kwak *et al*. 2012, Ashour *et al*. 1992, Sharma 1986, Swamy and Bahia 1979); however, there is no study in the literature dealing with the use of RSF as shear reinforcement of RC beams. For this reason in this chapter the possibility of using RSF as shear reinforcement in RC beams is explored.

Three point bending tests were executed with three series of RSFRC beams with fibre

content of 60 kg per cubic meter of concrete and flexurally reinforced with a relatively high reinforcement ratio of longitudinal steel bars in order to assure shear failure for all the tested beams. The applicability of the design recommendations proposed by RILEM TC 162-TDF (2003) and CEB-FIP 2010 (2011) to estimate the contribution of RSF for the shear resistance of RC beams is also assessed. For this purpose the average values of the residual flexural tensile strength parameters of the RSFRC that were obtained from the three point bending tests in the previous chapter were used. For the analysis of RSFRC beams failing in shear, material nonlinear simulations are carried out using a computer program based on the finite element method (FEMIX V4.0). After has been demonstrated that this model is capable of predicting with high accuracy the relevant behavioural aspects of the tested beams, a parametric study is carried out for assessing the influence of fibre dosage and using ISFRC instead of RSFRC on shear reinforcement effectiveness for RC beams.

4.2 Recycled steel fibres as a shear reinforcement of flexurally reinforced concrete beams

4.2.1 Analytical formulations and predictions

According to the CEB-FIP 2010 (2011), the shear capacity of the concrete elements, V_{Rd}, comprises the shear capacity provided by SFRC, $V_{Rd,F}$, and by the steel stirrups $V_{Rd,s}$:

$$V_{Rd} = V_{Rd,F} + V_{Rd,s} \tag{4.1}$$

where

$$V_{Rd,F} = \left\{ \frac{0.18}{\gamma} \times K \left[100 \times \rho_1 \times \left(1 + 7.5 \times \frac{f_{Ftuk}}{f_{ctk}} \right) f_{ck} \right]^{1/3} + 0.15 \times \sigma_{cp} \right\} \times b_w \times d \tag{4.2}$$

In equation (4.2), γ is the partial safety factor for concrete, K is a factor related to the size effect that can be calculated according to equation (4.3), ρ_l is the longitudinal

reinforcement ratio determined from equation (4.4), d is the effective depth of the cross section and b_w is the width of the web's cross section.

$$K = 1 + \sqrt{\frac{200}{d}} \leq 2.0 \tag{4.3}$$

$$\rho_1 = \frac{A_{st}}{b_w d} \leq 0.02 \tag{4.4}$$

where A_{st} is the cross sectional area of the longitudinal bars. Also in equation (4.2), f_{ck} is the characteristic value of the FRC compressive strength, while f_{ctk} is its corresponding tensile strength that can be obtained from CEB-FIP 2010 (2011) recommendations:

$$f_{ctk} = 0.3\left(f_{ck}\right)^{\frac{2}{3}} \tag{4.5}$$

In equation (4.2) f_{Ftuk} is the characteristic value of the ultimate residual flexural tensile strength for FRC that is determined from:

$$f_{Ftuk} = f_{Ftsk} - \frac{w_u}{CMOD_3}\left(f_{Ftsk} - 0.5 f_{R,3k} + 0.2 f_{R,1k}\right) \tag{4.6}$$

where

$$f_{Ftsk} = 0.45 \times f_{R,1k} \tag{4.7}$$

and

$w_u = 1.5$ mm and $CMOD_3 = 2.5$ mm. All the parameters related to the RSFRC can be obtained from the data given in Section 3 and indicated in Table 3.

According to RILEM TC 162-TDF, the shear capacity of a SFRC beam is determined from:

$$V_{Rd,3} = V_{cd} + V_{fd} \tag{4.8}$$

where V_{cd} is the concrete contribution determined from equation (4.9)

$$V_{cd} = \left[\left(\frac{0.18}{\gamma}\right)\times K\times\left(100\times\rho_1\times f_{fck}\right)^{\left(\frac{1}{3}\right)}\right]\times b_w\times d \tag{4.9}$$

and

$$V_{fd} = 0.7K_f K\tau_{fd} b_w d \tag{4.10}$$

is the contribution of steel fibre reinforcement where:

$$K_f = 1+n\left(\frac{h_f}{b_w}\right)\left(\frac{h_f}{d}\right)\leq 1.5 \tag{4.11}$$

$$K = 1+\sqrt{\frac{200}{d}}\ \leq 2.0 \tag{4.12}$$

$$n = \frac{b_f - b_w}{h_f}\leq 3 \tag{4.13}$$

$$\tau_{fd} = \frac{0.18}{\gamma}\times f_{R,4k} \tag{4.14}$$

K_f is the factor for taking into account the contribution for the shear resistance of the flange in a T cross section beam, and τ_{fd} is the design value of the shear strength provided by the fibre reinforcement. In equation (4.11), h_f is the height of the flanges and in equation (4.13), b_f is the width of the flanges.

Table 4.1 presents the shear capacity of the tested beams (see Figure 4.1) predicted by applying the formulation proposed by CEB-FIP 2010 (2011) and RILEM TC 162-TDF, where characteristic values were adopted for the material properties (according to the equations of both formulations), and $\gamma = 1.5$. The specimen geometry and reinforcement details of the beams are all given in subsection 4.2.2. In Table 4.1 the label S_Wj was used to differentiate the tested beams, where "j" identifies the web's cross-section thickness (in mm) of the part of the beam without shear reinforcement.

Table 4.1 Shear capacity according to analytical formulations

Specimen	$V_{Rd,RILEM}$ [kN]	$V_{Rd,FIB}$ [kN]
S_W70	29.806	26.042
S_W110	45.356	41.690
S_W150	56.497	51.266

4.2.2 Experimental program

Figure 4.1 shows the geometry and reinforcement details of the beams produced for this experimental program, as well as the loading and supporting conditions. Two specimens were tested per each series.

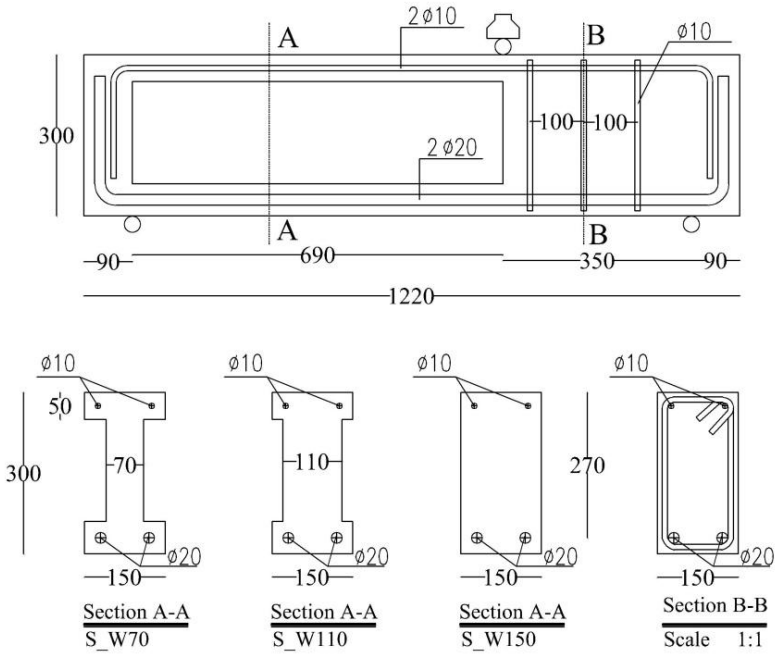

Figure 4.1 Geometry of the beams (dimensions in mm)

Based on the predictions of the shear capacity according to formulation proposed by CEB-FIP 2010 (2011) and RILEM TC 162-TDF, the RSFRC beams were flexurally reinforced with longitudinal steel bars in a percentage assumed sufficient to assure shear failure for all the beams (Figure 4.1). From tensile tests executed according to EN 10002 (1990) with coupons of the steel stirrups it was obtained an average value (of 4 coupons)

of 600.8 MPa and 754.6 MPa for the yield stress and tensile strength, respectively. Four cylinders of 150 mm of diameter and 300 mm of height were tested according to NP EN 12390 (2009) and LNEC E397 (1993) for the determination of the average compressive strength (50 MPa) and Young's Modulus (28 GPa), respectively. The Figure 4.2 shows the test setup and position of the five Linear Voltage Displacement Transducers (LVDTs). The effective depth of the cross section (*d*) is 270 mm and the shear span ratio (*a/d*) is 2.65 in order to promote the occurrence of shear failure (Zamanzadeh *et al*. 2015).

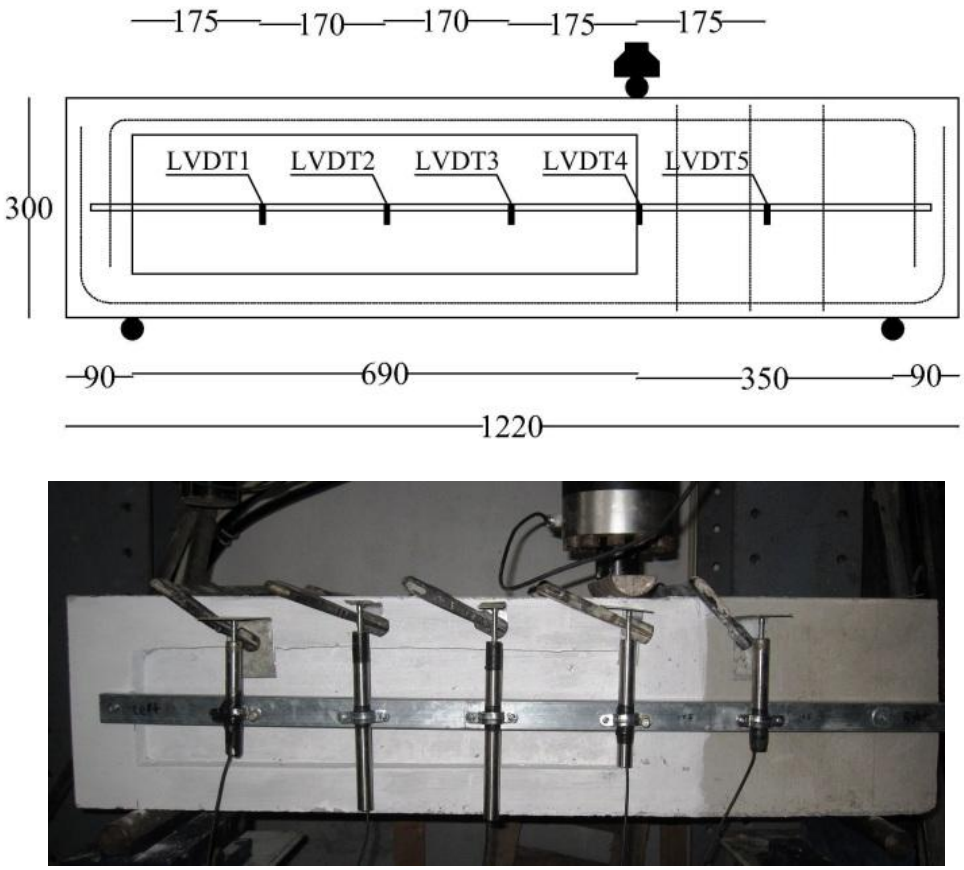

Figure 4.2 Beam configuration, test setup and position of the LVDTs (dimensions in mm)

The relationship between the applied load and the deflection at the loaded section (LVDT4) of the tested series of beams is represented in Figure 4.3. By increasing the beam web thickness the load carrying capacity has increased without affecting significantly the deflection at maximum load.

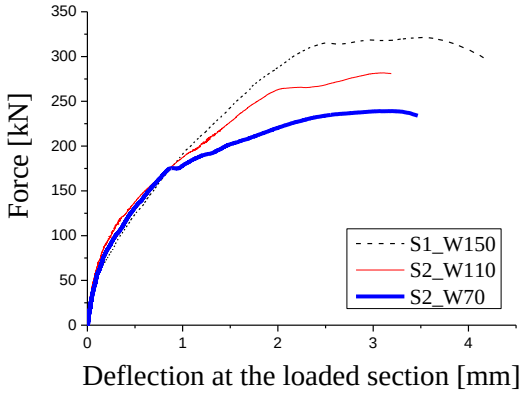

Figure 4.3 Load - deflection relationship at the loaded section for the tested series of beams

In Figure 4.6 the inversion of deflection in the last stage of the loading process of S_W110 and S_W70 beams was caused by the movement of the failure mechanism (Figure 4.4) formed at this stage in these beams and the position of the aluminium plate where it touches the piston of the LVDT3 (Figure 4.2).

a)

b)

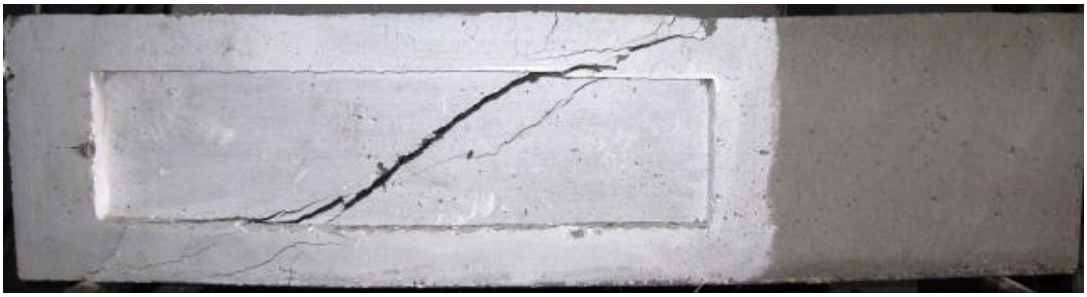

c)

Figure 4.4 Crack pattern at failure of the beams: a) S_W150, b) S_W110, c) S_W70

In fact, at the last stage of the loading process of these beams an upward relieve of deflection was experienced by the top-left part of the beam, where the aforementioned aluminium plate is bonded, leading to the registered inversion of deflection, which will be confirmed by the numerical simulations presented in next section. Table 4.2 includes the shear capacity of the tested beams, as well as the values predicted according to the RILEM TC 162-TDF and CEB-FIP 2010 (2011) formulations. The ratio between the shear capacity obtained experimentally ($V_{\exp}$) and according to the analytical formulations (V_{ana}) has decreased with the increase of the beam web thickness. Since design values are being used for the properties of the intervening materials, the $V_{\exp}/V_{Rd,ana}$ should be higher than 1.5 in order to guarantee safety predictions for the analytical approach. However, the decrease of the $V_{\exp}/V_{Rd,ana}$ with the increase of the width of the web's beam cross section (b_w) indicates that the formulations do not consider properly the favourable effect of the fibre orientation when b_w decreases. In fact, fibres become more preferentially aligned with the axis of the beam when b_w decreases due to a more pronounced wall effect, leading to more effective fibre reinforcement mechanisms in terms of arresting the crack propagation (Barros, 2011). The irregular shape of the RSF indicates that a higher tendency for this effect is expected when using ISF, due to the higher aspect ratio of these last fibres.

Table 4.2 Shear capacity according to analytical formulations and experimental tests (Zamanzadeh *et al*. 2015)

Specimen	V_{exp} [kN]	$V_{Rd,RILEM}$ [kN]	$V_{exp} / V_{Rd,RILEM}$	$V_{Rd,FIB}$ [kN]	$V_{exp} / V_{Rd,FIB}$
S_W70	81.290	29.806	2.72	26.042	3.121
S_W110	95.810	45.356	2.11	41.690	2.298
S_W150	109.172	56.497	1.93	51.266	2.129

4.2.3 Numerical simulations and discussion

A finite element mesh of 144 plane stress elements of 8 nodes was used for the simulation of the beams failing in shear. A Gauss-Legendre integration scheme with 2×2 Integration Points (IP) was used in all the concrete elements. The steel bars were simulated by perfectly bonded 82 elements of two nodes with 2 IP. In the numerical simulation of the beams the incremental approach for the crack shear stress-strain component was used and the values of the fracture mode I parameters of the smeared crack constitutive model used in the simulations were the same derived from the inverse analysis (see Table 3.10). In the incremental approach, the two stress components at each crack (crack normal stress, σ_n^{cr}, and crack shear stress, τ_{nt}^{cr}) are directly determined from their corresponding stress increments, $\Delta\sigma_n^{cr}$ and $\Delta\tau_{nt}^{cr}$. To better simulate the deformational response and the crack pattern up to the failure of structures that fail by the formation of a critical shear crack, such is the case of the tested beams, the softening crack shear stress *vs* crack shear strain relationship, represented in Figure 4.4, was adopted in the present work. The crack shear stress increases linearly until the crack shear strength is reached, $\tau_{t,p}^{cr}$, (first branch of the shear crack diagram), followed by a decrease in the shear residual strength (softening branch). The diagram represented in Figure 4.4 is defined by the following equations:

$$\tau_t^{cr}\left(\gamma_t^{cr}\right)=\begin{cases} D_{t,1}\,\gamma_t^{cr} & 0<\gamma_t^{cr}\le\gamma_{t,p}^{cr} \\ \tau_{t,p}^{cr}-\dfrac{\tau_{t,p}^{cr}}{\left(\gamma_{t,u}^{cr}-\gamma_{t,p}^{cr}\right)}\left(\gamma_t^{cr}-\gamma_{t,p}^{cr}\right) & \gamma_{t,p}^{cr}<\gamma_t^{cr}\le\gamma_{t,u}^{cr} \\ 0 & \gamma_t^{cr}>\gamma_{t,u}^{cr} \end{cases} \tag{4.15}$$

The initial shear fracture modulus, $D_{t,1}^{cr}$, is defined from equation:

$$D_{t,1}^{cr} = \frac{\beta}{1-\beta} G_c \tag{4.16}$$

where G_c is the elastic shear modulus of RSFRC and β is the shear retention factor that should be in the range]0,1[. The peak crack shear strain, $\gamma_{t,p}^{cr}$, is obtained using the crack shear strength (from the input data), $\tau_{t,p}^{cr}$, and the crack shear modulus:

$$\gamma_{t,p}^{cr} = \frac{\tau_{t,p}^{cr}}{D_{t,1}^{cr}} \tag{4.17}$$

The ultimate crack shear strain, $\gamma_{t,u}^{cr}$, depends on the crack shear strength, $\tau_{t,p}^{cr}$, on the shear fracture energy (mode II fracture energy), $G_{f,s}$, and on the crack band width, l_b:

$$\gamma_{t,u}^{cr} = \frac{2G_{f,s}}{\tau_{t,p}^{cr} l_b} \tag{4.18}$$

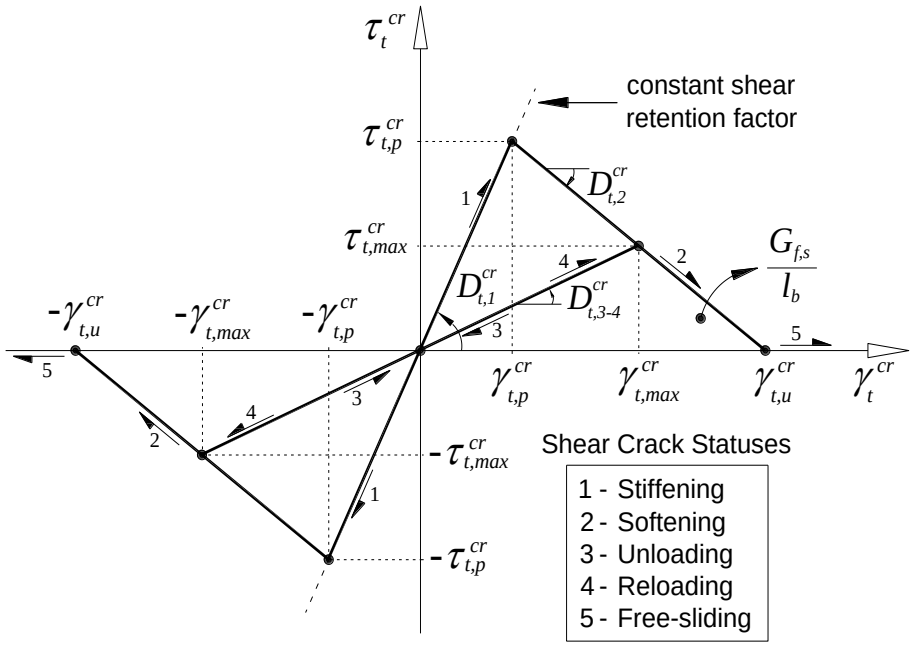

Figure 4.5 Diagram to simulate the relationship between the crack shear stress and crack shear strain component, and possible shear crack statuses

In the present approach it is assumed that the crack band width is the same for both fracture mode I and mode II processes, but specific research should be done in this respect in order to assess the influence of these model parameters on the predictive performance of the behaviour of elements failing in shear. Five shear crack statuses are proposed and their meaning is schematically represented in Figure 4.4.

The crack mode II modulus of the first linear branch of the diagram is defined by equation (4.17), while the second linear softening branch is defined by

$$D_{t,2}^{cr} = -\frac{\tau_{t,p}^{cr}}{\gamma_{t,u}^{cr} - \gamma_{t,p}^{cr}} \tag{4.19}$$

and the crack shear modulus of the unloading and reloading branches is obtained from

$$D_{t,3-4}^{cr} = \frac{\tau_{t,\max}^{cr}}{\gamma_{t,\max}^{cr}} \tag{4.20}$$

being $\gamma_{t,\max}^{cr}$ and $\tau_{t,\max}^{cr}$ the maximum crack shear strain already attained and the corresponding crack shear stress determined from the softening linear branch. Both components are stored to define the unloading/reloading branch (see Figure 4.4).

In free-sliding status ($\left|\gamma_t^{cr}\right| > \left|\gamma_{t,u}^{cr}\right|$) the crack shear modulus, $D_{t,5}^{cr}$, is null. To avoid numerical instabilities in the calculation of the stiffness matrix and in the calculation of the internal forces, when the crack shear status is free-sliding, a residual value is assigned to this term. A free-sliding status is assigned to the shear crack when $\varepsilon_n^{cr} > \varepsilon_{n,u}^{cr}$. The details about how the shear crack statuses were treated can be consulted elsewhere (Ventura Gouveia, 2011).

Table 4.3 includes the values of the model parameters adopted in the numerical simulations of the tested beams. For the concrete Young's modulus a small reduction was made following the recommendations of CEB-FIP Model Code for material nonlinear analysis (90% was assumed). To take into account the residual tensile stresses due to shrinkage, the in-situ tensile strength of the concrete, f_{ct}, is taken as $0.3\sqrt{f_{cm}}$ = 1.9 MPa. To simulate the behaviour of the longitudinal and transversal steel bars a linear stress-

strain diagram with an elasticity modulus of 200 GPa was assumed, since preliminary numerical analysis have indicated a maximum strain of 1.9‰, which is less than the yield strain of these reinforcements.

The experimental and the numerical relationships between the applied load and the deflection at the mid span section for the tested beams are compared in Figure 4.6, and the comparison of the shear capacity of the RC beams registered experimentally and obtained from numerical simulations is depicted in Figure 4.7.

Table 4.3 Values of the model parameters in the numerical simulations of the tested RC beams (Zamanzadeh *et al*. 2015)

Property	**Value**
Poisson's ratio (ν_c)	0.20
Initial Young's Strength (E_c)	25000 N/mm^2
Compressive strength (f_c)	40 N/mm^2
Trilinear tension-softening diagram	f_{ct}=1.9 N/mm^2 α_i, ξ_i, and G_f^I in Table 3.11
Crack shear stress-crack shear strain softening diagram	β = 0.1, $\tau_{t,p}^{cr}$ = 1.5 MPa, $G_{f,s}$ = 3.0 N/mm
Crack band width, l_b	Square root of the area of Gauss integration point
Threshold angle (Sena-Cruz 2004)	α_{th} = 30˚
Maximum number of cracks per integration point (Sena-Cruz 2004)	2

The model has captured with high accuracy the deformational response of the tested beams, even the inversion of deflection when the failure mechanism occurred in the S_W70 and S_W110 beams. This effect was not occurred in the S_W150 beam since the I cross shape of the other beams favour the occurrence of the aforementioned movement of the failure mechanism.

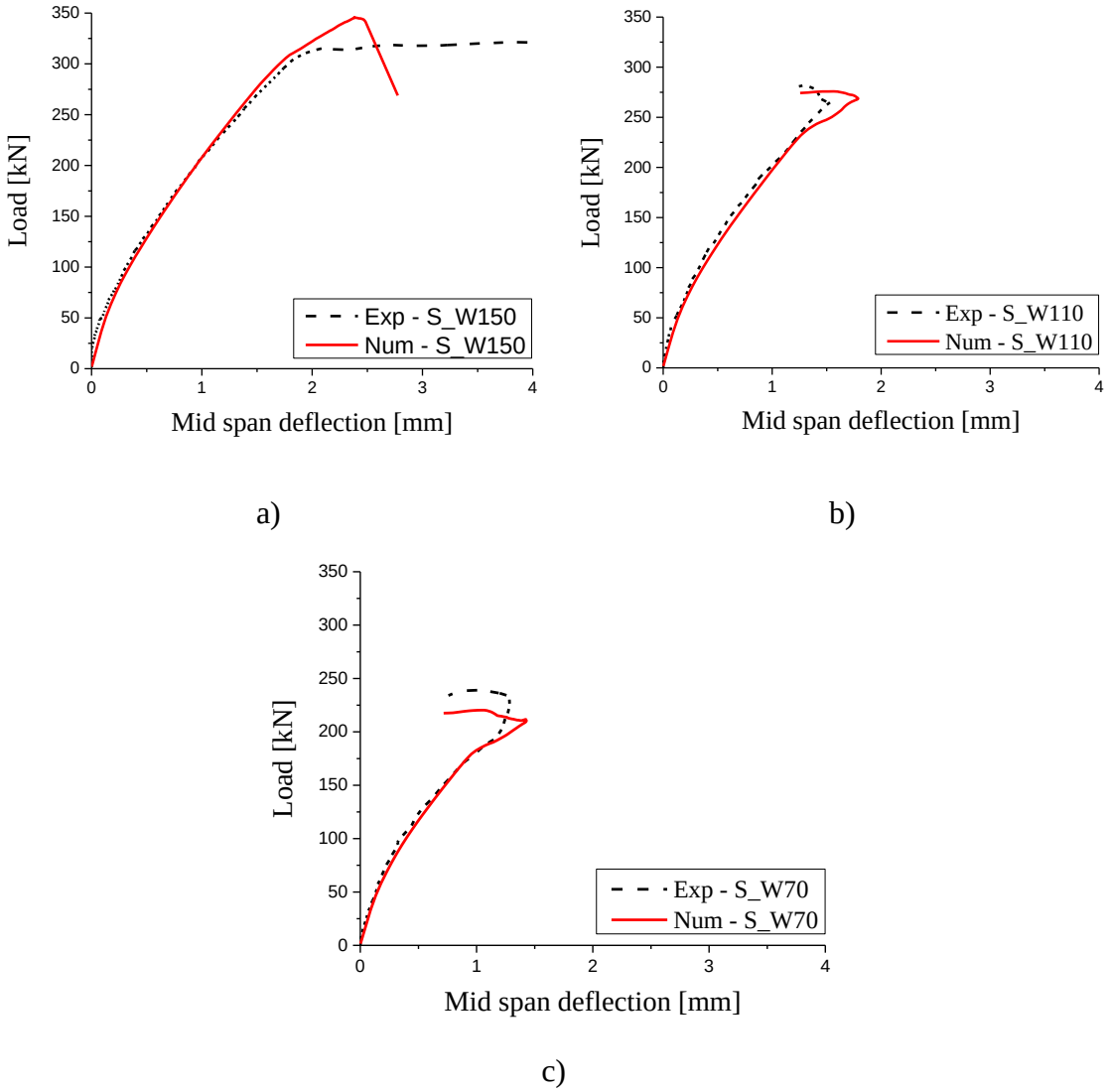

Figure 4.6 Comparison of the experimental and numerical load-deflection curves of the bending tests with I-shape beams failing in shear: a) S_W150, b) S_W110 and c) S_W70

The maximum average strain in the longitudinal steel bars of the S_W150 was 1.9‰, which indicates that these RSF have potential to convert a brittle shear failure mode in a ductile flexural failure mode for these types of structural elements if a higher post-cracking residual strength is assured for the RSFRC (Zamanzadeh *et al*. 2015).

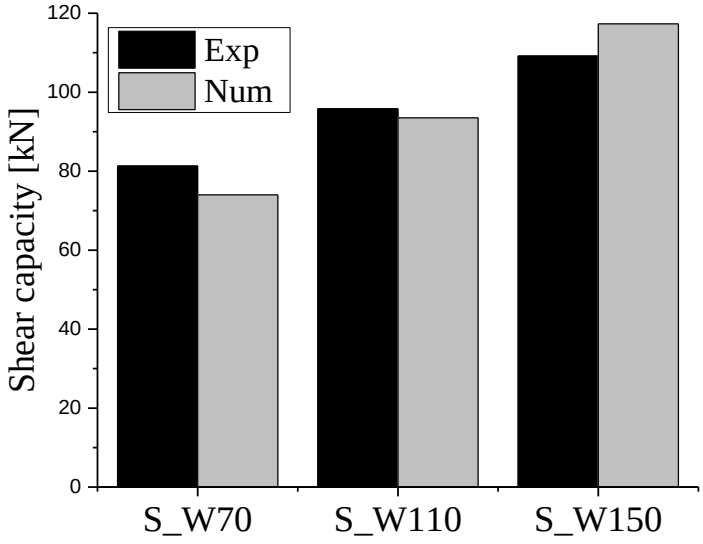

Figure 4.7 Comparison of the shear capacity of the RC beams registered experimentally and obtained from numerical simulations

4.2.4 Parametric study for assessing effectiveness of the RSF in terms of shear reinforcement

The previous numerical model, whose good predictive performance for the simulation of the behaviour of the structures under consideration was confirmed in the previous section, was adopted to perform a parametric study for the evaluation of the influence of different fibre dosages on the load carrying capacity. Furthermore the shear behaviour of the RC beams reinforced with 60 kg RSF (RSFRC60) were compared with RC beams reinforced with 60 kg ISF per cubic meter of concrete (ISFRC60).

The beams that simulated in this section have the same mesh of the S_W70; S_W110 and S_W150 beams. The arrangement of the steel reinforcement, the support and load conditions, and the finite element mesh were the same of the ones adopted in the numerical simulations of the previous section.

The following content of fibres was studied: 0 kg/m^3 (plain concrete); 45 kg/m^3; 60 kg/m^3 and 90 kg/m^3.

4.2.4.1 Influence of fibre dosage

Figure 4.8 compares the relationship between the load and mid span deflection curves obtained for three different fibre contents. The model parameters are those indicated in Table 4.3. For the fracture mode I of RSFRC beams they correspond to the values obtained from inverse analysis that are indicated in Table 3.11. As expected the load carrying capacity increases with increase of fibre dosage.

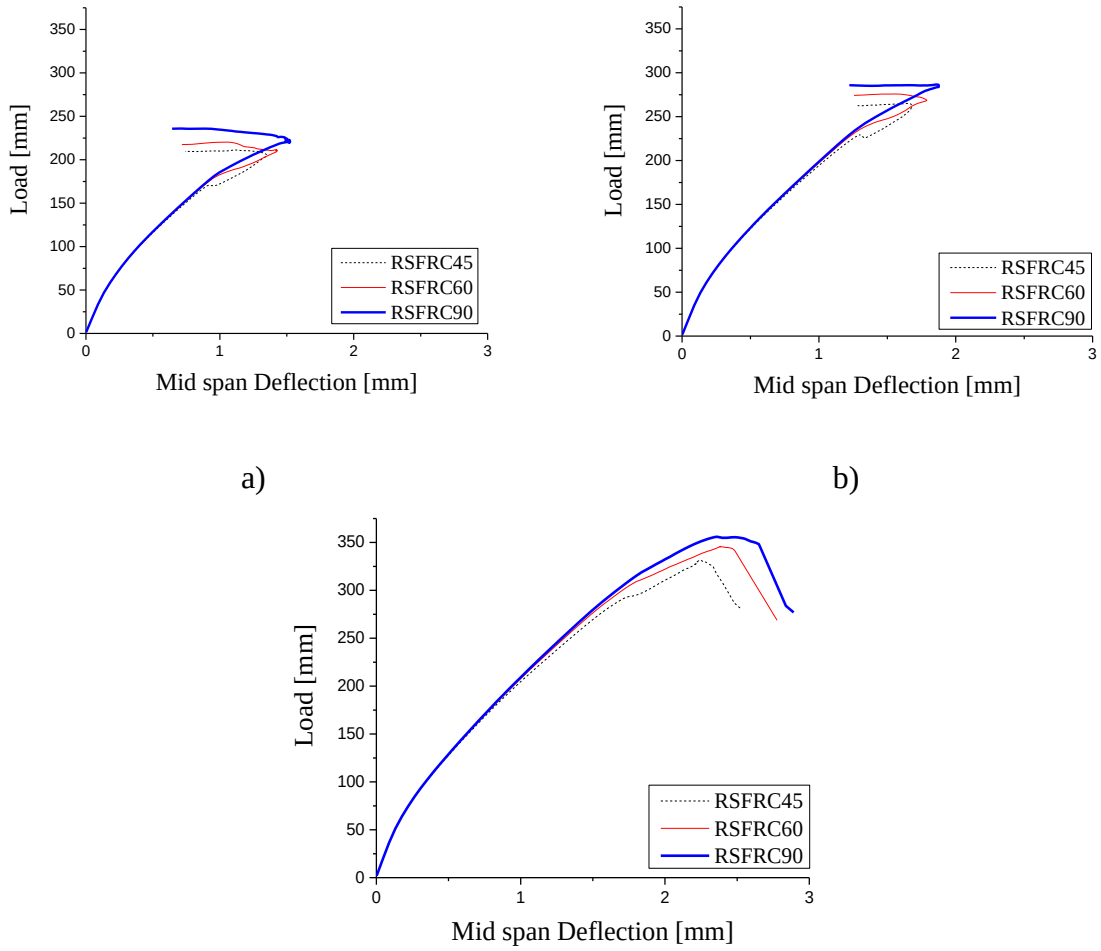

Figure 4.8 Influence of fibre dosage on the relationship between the force and the mid span deflection: a) S_W70, b) S_W110 and c) S_W150

To assess the effectiveness of the RSF in terms of shear reinforcement, the present numerical model was used for simulating the same series of RC beams but without any fibre reinforcement (plain concrete, PC). The values of model parameters adopted in the numerical simulation of the PC beams were corresponded to the values which were obtained by Baghi (2015), Barros *et al*. (2013) and the values obtained by Barros *et al*. (2013) by simulation of the experimental tests carried out by Chaallal *et al*. (2011) The average value of load carrying capacity obtained from these three models were used for comparison propose. The concrete properties in the numerical simulations are included in Tables 4.4 - 4.6.

Table 4.4 Values of the model parameters of the concrete corresponded to Baghi (2015)

Property	**Value**
Poisson's ratio (ν_c)	0.19
Initial Young's Strength (E_c)	31381 N/mm^2
Compressive strength (f_c)	32.67 N/mm^2
Trilinear tension-softening diagram	f_{ct}=2.1 N/mm^2 α_1 =0.30, α_2 =0.3, ξ_1=0.005, ξ_2 =0.1; G_f^I =0.08
Crack shear stress-crack shear strain softening diagram	β =0.6, $\tau_{t,p}^{cr}$ =1.1 MPa, $G_{f,s}$ =0.045 N/mm
Crack band width, l_b	Square root of the area of Gauss integration point
Threshold angle (Sena-Cruz, 2004)	α_{th}=30˚
Maximum number of cracks per integration point	2

Table 4.5 Values of the model parameters of the concrete corresponded to Barros *et al*. (2013)

Property	**Value**
Poisson's ratio (ν_c)	0.15
Initial Young's Strength (E_c)	33271 N/mm^2
Compressive strength (f_c)	39.7 N/mm^2
Trilinear tension-softening diagram	f_{ct}=2.2 N/mm^2 α_1 =0.30, α_2 =0.3, ξ_1=0.005, ξ_2 =0.1; G_f^I =0.086
Crack shear stress-crack shear strain softening diagram	β =0.4, $\tau_{t,p}^{cr}$ =1.1 MPa, $G_{f,s}$=0.050 N/mm
Crack band width, l_b	Square root of the area of Gauss integration point
Threshold angle (Sena-Cruz, 2004)	α_{th}=30˚
Maximum number of cracks per integration point	2

Table 4.6 Values of the model parameters of the concrete corresponded to Chaallal et al. (2015) tested beams (Barros *et al*. 2013)

Property	**Value**
Poisson's ratio (ν_c)	0.15
Initial Young's Strength (E_c)	30000 N/mm^2
Compressive strength (f_c)	25 N/mm^2
Trilinear tension-softening diagram	f_{ct}=1.8 N/mm^2 α_1 =0.25, α_2 =0.15, ξ_1=0.004, ξ_2 =0.1; G_f^I =0.09
Crack shear stress-crack shear strain softening diagram	β =0.5, $\tau_{t,p}^{cr}$ =1.2 MPa, $G_{f,s}$=0.06 N/mm
Crack band width, l_b	Square root of the area of Gauss integration point
Threshold angle (Sena-Cruz, 2004)	α_{th}=30˚
Maximum number of cracks per	2

integration point

Figure 4.9 compares the relationship between the load and mid span deflection curves obtained from numerical simulations for three different models of plain concrete.

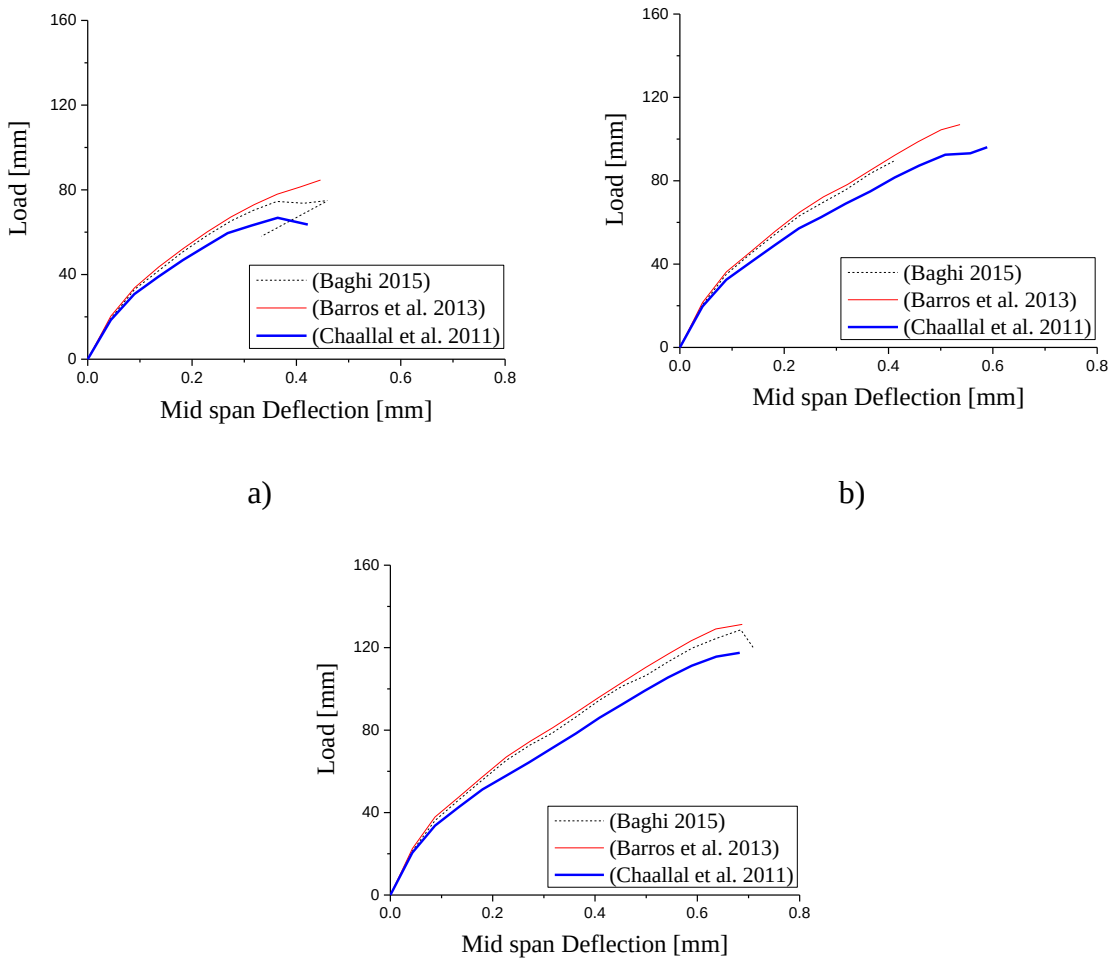

Figure 4.9 The relationship between the load and mid span deflection curves obtained from numerical simulations for three different models of plain concrete: a) S_W70, b) S_W110 and c) S_W150

From these simulations the results presented in Table 4.7 were obtained, showing that the RSF shear reinforcement efficiency increases with the decrease of the thickness of the web's cross section. For the S_W70 a maximum increase of 157% was obtained when using 90 kg/m^3 of RSF.

Table 4.7 Increase of shear capacity provided by RSF

Specimen	RSFRC45	RSFRC60	RSFRC90
S_W70	141%	147%	157%
S_W110	137%	142%	148%
S_W150	132%	137%	141%

4.2.4.2 ISFRC instead of RSFRC

In this section the previous numerical model was used to compare the shear behaviour of the RC beams reinforced with 60 kg RSF (RSFRC60) and RC beams reinforced with 60 kg ISF per cubic meter of concrete (ISFRC60). The model parameters of RSFRC60 are those indicated in Table 4.3. Table 4.8 presents the model parameters used for simulation of ISFRC60 beams which were obtained by performing inverse analysis with the force-CMOD data registered in three point notched beam bending tests for ISFRC60 beams in chapter three.

Table 4.8 Values of the model parameters of the ISFRC60 beam

Property	Value
Poisson's ratio (ν_c)	0.2
Initial Young's Strength (E_c)	27000 N/mm^2
Compressive strength (f_c)	40 N/mm^2
Trilinear tension-softening diagram	f_{ct}=1.9 N/mm^2 α_1 =1.23, α_2 =0.07, ξ_1=0.018, ξ_2 =0.1; G_f^I =6.2
Crack shear stress-crack shear strain softening diagram	β =0.1, $\tau_{t,p}^{cr}$ =1.5 MPa, $G_{f,s}$=3.0 N/mm
Crack band width, l_b	Square root of the area of Gauss integration point
Threshold angle (Sena-Cruz, 2004)	α_{th}=30˚
Maximum number of cracks per integration point	2

Figure 4.10 compares the relationship between the load and the mid span deflection obtained for RSFRC60 and ISFRC60 beams.

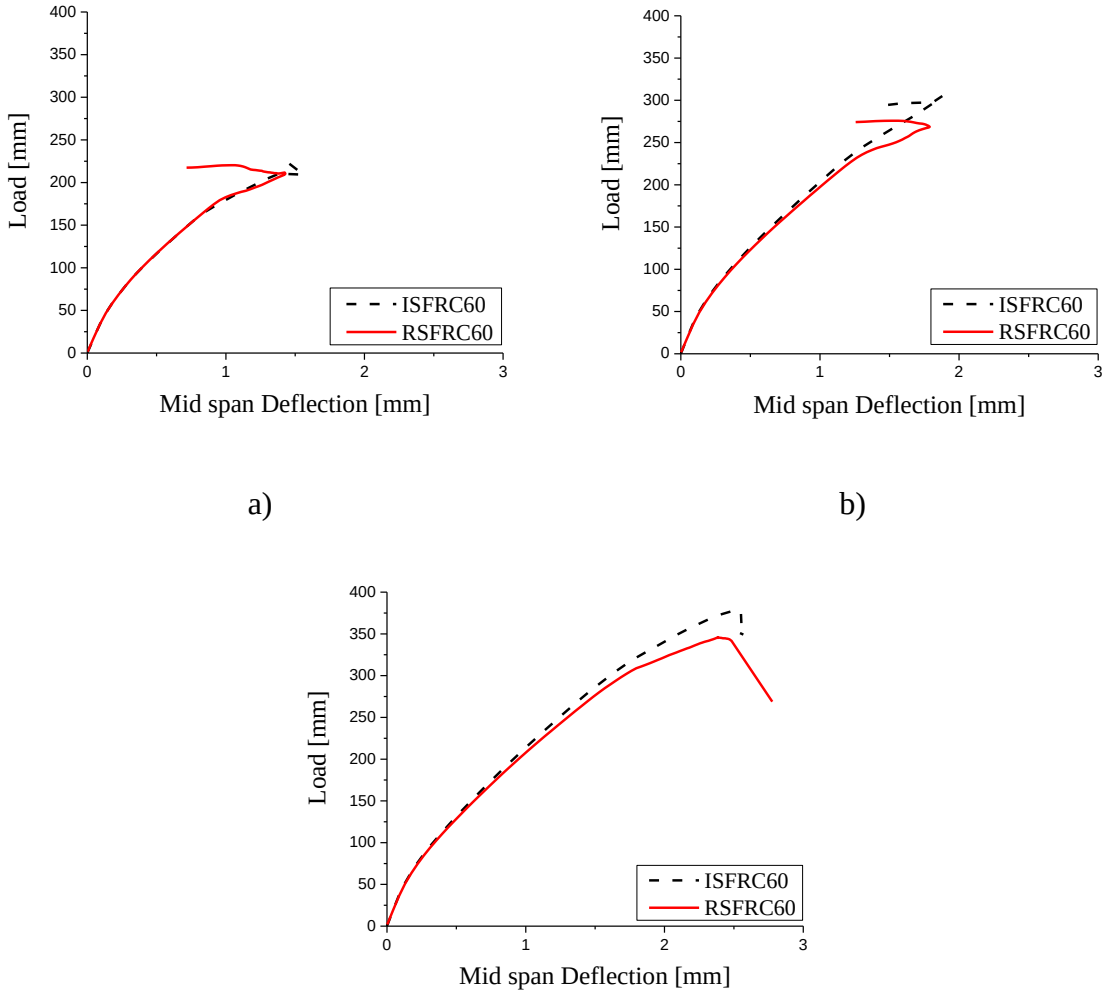

Figure 4.10 The relationship between the load and the mid span deflection obtained for RSFRC60 and ISFRC60 beams: a) S_W70, b) S_W110 and c) S_W150

Analysing the curves presented in Figure 4.10, it was verified that the load carrying capacity of ISFRC beams and their ultimate deflections have increased in comparison with RSFRC beams. The beam S_W70 failed at a load of 211 kN for a deflection of 1.41 mm, while the beams S_W110 and s_W150 failed at a load of 305 kN and 378 kN for a deflection of 1.88 mm and 2.52 mm respectively.

4.3 Conclusions

The work in this chapter was dedicated to the assessment of the benefits of RSF for the shear reinforcement of shallow RC beams failing in shear. On the basis of the results of the tests with RSFRC beams failing in shear, it was observed that the ratio of the shear capacity obtained experimentally to that calculated using RILEM and *fib* guidelines has decreased with the increase of the beam web thickness, which indicates that both formulations require some enhancements for better consider the geometry of the beam in order to more accurately simulate the fibre orientation and distribution on the effectiveness of the fibre reinforcement mechanisms.

The tests with RSFRC beams failing in shear were numerically simulated by performing material nonlinear analysis with a smeared crack model under the framework of the finite element method, where the fracture mode I parameters of the crack constitutive model was determined by executing inverse analysis with the force-CMOD data registered in three point notched beam bending tests. The good predictions in terms of load carrying and deflection capacity evidenced that this numerical strategy is suitable to predict the behaviour of RSFRC beams failing in shear.

To evaluate the influence on the beam's load carrying capacity of the fibre dosage and the advantage of ISFRC instead of RSFRC and also to assess the effectiveness of the RSF in terms of shear reinforcement an extensive parametric study was carried out.

By using this model and adopting a plain concrete, it was verified that 90 kg/m^3 of RSF provided an increase of 157%, 148% and 141% in terms of shear capacity of the beams with a web's thickness of 70, 110 and 150 mm, respectively, when the shear capacity of the reference beam (plain concrete with the same flexural reinforcing ratio) is considered for comparison purpose.

Chapter 5

5 Development of recycled steel fibre reinforced mortar panels for structural reinforcement

5.1 Introduction

Exploring the possible innovative systems for shear strengthening of RC beams such as thin panels reinforced with RSF is another important objective of this thesis. In this sense, in this chapter the use of relatively high content of RSF (higher than 2% by volume) for the production of thin mortar panels for structural reinforcement is explored. The experimental program involves the following three phases and the results are presented and discussed in this chapter:

1) Evaluate two different procedures for the production of Recycled Steel Fibre Reinforced Mortar (RSFRM) panels: vacuum infusion process; technique which is used for the production of SIFCon (Slurry Infiltrated Fibre Concrete);
2) Characterisation of RSFRM mechanical properties in terms of flexural, uniaxial compression, uniaxial tension and shear behaviour, by performing three point (centre-point) flexural tests on notched and un-notched specimens, compressive, uniaxial tensile and Iosipesco tests;
3) Characterisation of durability performance of RSFRM. The following durability indicators are evaluated: water absorption by immersion and by capillarity; permeability to air; chloride diffusion by migration under non-steady state and drying shrinkage.

5.2 Technological aspects for the production of RSFRM panels

5.2.1 Vacuum infusion process

Due to detrimental effect on the workability of cementitious composite when a large amount of RSF are added, and also the tendency of RSF to ball, it was fundamental to explore possible alternatives for producing mortar reinforced with relatively high amount of RSF (more than 2% by volume), in which the fibres are not added to the composite mix during mixing time.

In this sense, firstly one prototype of thin RSFRM panel reinforced with 3% in volume of RSF was produced by using the vacuum infusion process (Figure 5.1). In this method, rather than adding fibres to mortar mixer, firstly the fibres were dispersed into the injection mould in the desired volume fraction (V_f). Then, by using vacuum process, the high fluid cement paste was injected into the mould.

Figure 5.1 Vacuum system for producing RSFRM thin panels

Figure 5.2 shows the panel just after vacuum process finished. Due to the small diameter of the pipe and valve of the vacuum mould and also the power capacity of the vacuum machine, in some parts of the panel like the one marked in red circle, the fibres were not completely filled by the paste (Figure 5.2).

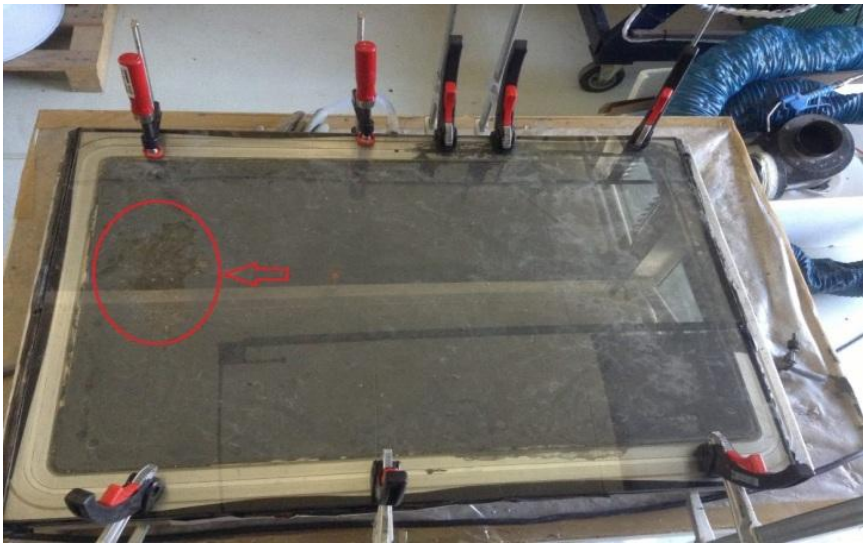

Figure 5.2 RSFRM panel after cement paste injection

5.2.2 Production of the RSFRM thin panels using SIFCon technique production

Due to the predicaments stated in the previous section, the technique which is used for the production of SIFCon was adopted for the production of RSFRM thin panels. In this

technique, after placing the RSF in the mould, the mortar is poured on fibres until the mould is filled up (Figure 5.3). An external vibration was applied during casting to ensure a good infiltration of the mortar.

Figure 5.3 The used technique for producing RSFRM panels

5.3 Mechanical properties of the developed RSFRM

5.3.1 Flexural behaviour

5.3.1.1 Mix composition

Bending test specimens were produced from three different mix compositions for mortars reinforced with RSF: M1, M2 and M3 (see Table 5.1). The mortars were composed by cement, fly ash, limestone filler, fine sand, superplasticizer and viscosity modifying admixture. In an attempt to produce as cost effective material as possible, for M3 the content of cement was decreased by being partially replaced by fly ash. Due to the better performance of M2 in terms of flexural strength and homogeneity (as will be shown in sections 5.3.1.3.1 and 5.3.2), it was used as the mix composition for developing the RSFRM (fibre content of 3.8% by volume) in the experimental programs corresponding to compressive behaviour, direct tensile, shear behaviour and durability performance.

Table 5.1 Mix compositions

Mortar	C [kg/m^3]	FA [kg/m^3]	LF [kg/m^3]	FS [kg/m^3]	VMA [kg/m^3]	SP [kg/m^3]	W [l/m^3]	W/C [l/kg]
M1	535	535	102	214	0.833	20	415	0.77
M2	546	669	----	437	1.710	11	318	0.58
M3	450	765	----	437	1.710	14	375	0.83

C = Cement; FA = Fly Ash; LF = Limestone Filler; FS = Fine Sand; VMA = Viscosity modifying admixture; SP = Superplasticizer; W = Water; W/C = Water-Cement ratio.

5.3.1.2 Mixing strategy

The cement, fly ash, limestone filler and fine sand were put into a planetary mixer with 50 l capacity and were mixed during one minute. Then, water was first mixed with the superplasticizer and, then, it was slowly added to the mixer for approximately two minutes. After this, viscosity modifying admixture was added, and the mixing continued again during two minutes. In each batch, approximately 16 litres of mortar were produced. Then, the produced mortar was poured in the moulds containing RSF with desired volume fraction. The specimens were removed from the moulds 48 hours after casting and were cured in natural environmental conditions of the laboratory.

5.3.1.3 Specimen details

Series M1 included nine similar specimens with a length of 160 mm and cross section of 40 × 40 mm^2 (Figure 5.4) with three contents of RSF (0.0%, 1.5% and 3.0% by volume).

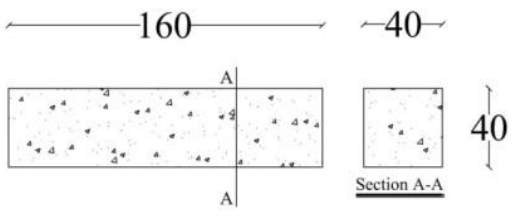

Figure 5.4 Geometry of group M1 specimens for flexural tests (dimensions in mm)

Series M2 consisted of five notched specimens with a length of 250 mm and cross section of 50 × 50 mm^2 and fibre content of 3.8% by volume, and 25 un-notched specimens with

the same geometrical dimension of notched specimens and with fibre contents of 0.0%, 2.5%, 3.0% and 3.8% by volume (Figure 5.5).

Series M3 consists of four notched specimens with a length of 250 mm and cross section of 50 × 50 mm^2 and with fibre content of 3.5% by volume.

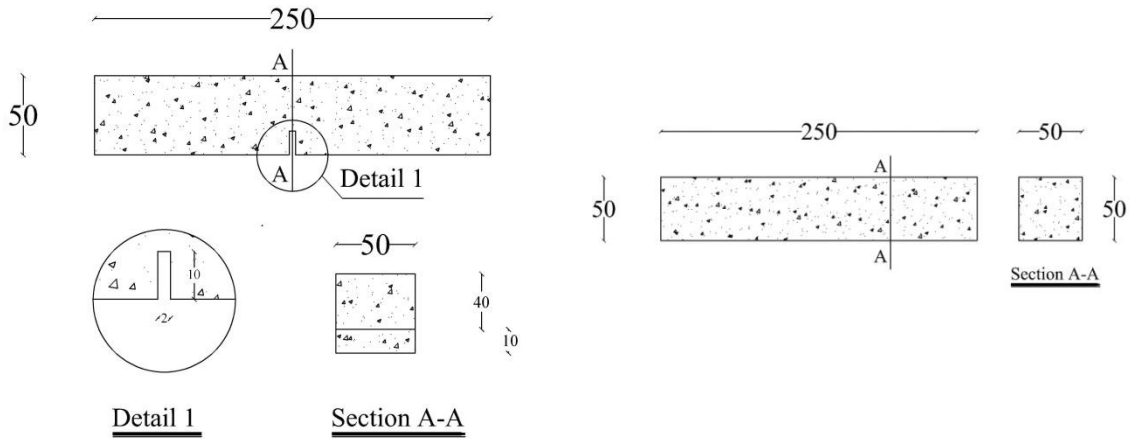

a) b)

Figure 5.5 Geometry of a) M2 and M3 series notched specimens for flexural test, b) M2 series un-notched specimens

Specific weight, fibre content and number of the tested specimens are depicted in Table 5.2. The labels Mi_j were used to differentiate the series of the tested specimens, where "Mi" identifies the type of mortar and "j" identifies the fibre volume percentage. The label Mi_jn identifies the notched beams.

Due to the existence of relatively high amount of rubber particles in the RSF that was supplied by the Biosafe company, for all the mixes (except M2_3r) an attempt was made to manually separate and take out the rubber particles as much as possible. However, in order to have an evaluation on the effect of these rubber particles in the flexural behaviour of developed RSFRM, in the mix M2_3r the RSF were used as supplied by Biosafe company.

Table 5.2 Fibre percentage, specific weight, testing time and number of specimens in each series

Specimen	Fibre percentage [%]	Specific weight [kN/m^3]	Number of specimens	Testing time [day]
M1_0	0.0	15.89	3	28
M1_1.5	1.5	16.09	3	28
M1_3	3.0	16.53	3	28
M2_0	0.0	17.91	3	14
M2_3r	3.0	19.99	5	14
M2_2.5	2.5	20.03	4	14
M2_3	3.0	20.22	5	14
M2_3.8	3.8	20.49	8	14
M2_3.8n	3.8	20.49	5	14
M3_3.5n	3.5	17.77	4	14

5.3.1.4 Flexural test procedure

Flexural tests were carried out to assess the mechanical properties of RSFRM specimens under three point bending test. To evaluate cracking moment, the corresponding deflection and also the maximum flexural stress, 35 un-notched specimens were tested. A displacement transducer (LVDT) was used in the bottom of each specimen to measure the vertical deflection of the specimen during testing (Figure 5.6).

a) b)

Figure 5.6 Test setup for three point bending test using un-notched specimens: a) M1 and b) M2 (dimensions in mm)

Nine notched specimens were used to evaluate the contribution of the RSF for the post-crack residual strength of the specimens by performing three point bending tests. A notch

of 15 mm depth and 4 mm width was made in the middle span of the specimens. An LVDT was installed at the bottom face of the specimen, close to the notch tip in order to measure the crack mouth opening displacement (CMOD) – see Figure 5.7. The results of these tests were also used to estimate the fracture energy of the composite material (energy to propagate a crack of unit area), which is designated as mode I fracture energy, and can be an indicator of the ductility of the material.

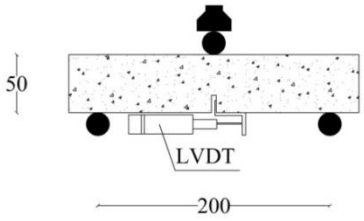

Figure 5.7 Test setup for three point bending test using notched specimens (dimensions in mm)

5.3.1.5 Experimental results

5.3.1.5.1 Three point bending test with un-notched specimens

The results of three point bending tests with un-notched prisms are used to estimate the stress at crack initiation. The cracking moment, M_{cr}, is obtained from:

$$M_{cr} = \frac{F_{cr} \times L}{4} \tag{5.1}$$

where F_{cr} is the cracking load, having been assumed as the load when a reduction of 10% in initial secant stiffness occurred. The stress at crack initiation is obtained from:

$$\sigma_{cr} = \frac{6 \times M_{cr}}{b \times h^2} \tag{5.2}$$

where b and h are the width and height of the specimen.

Figure 5.8 shows the flexural stress *vs.* mid span deflection curves of three point bending for all the un-notched specimens. The relationship between the average flexural stresses

vs. deflection for all tested specimens is depicted in Figure 5.9. The calculated values for cracking moment (M_{cr}), cracking stress (σ_{cr}) and maximum flexural stress ($\sigma_{\max}$) for all the specimens are available in the Annex "B" and the average values are presented in Table 5.3.

As expected, the failure in flexure for all specimens was due to fibres pull-out. The results in Table 5.3 show that the increase of fibre content leads to the increase of maximum flexural stress. However, this tendency was not observed for cracking stress. In fact the existence of rubber particles presents negative effect on the micro crack initiation and, consequently, on the cracking stress of the matrix. In terms of macro cracks and maximum flexural stress, the bridging effect of fibres for controlling the macro cracks is much higher than the negative effect of the existence of rubber particles. For all M2 specimens that were tested (14 days), higher values of σ_{cr} and $\sigma_{\max}$ were obtained in comparison with M1 specimens (tested at 28 days). This proves the better quality of the M2 mix with lower W/C ratio in term of flexural strength.

By comparing the average value of the experimental results obtained for M2_3r and M2_3 specimens, an increase of 53% and 12% in terms of σ_{cr} and $\sigma_{\max}$ was observed for M2_3 compared to M2_3r, which confirms the significant negative effect of the existence of rubber particles in the RSFRM on the cracking stress.

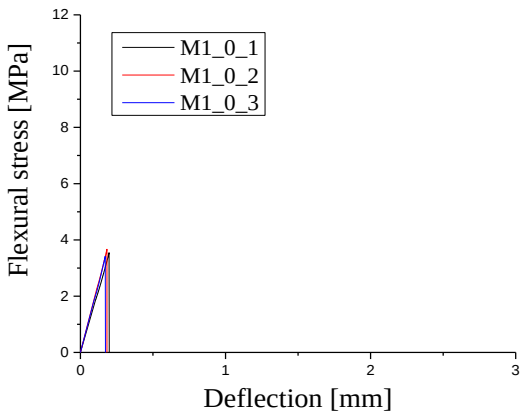

a)

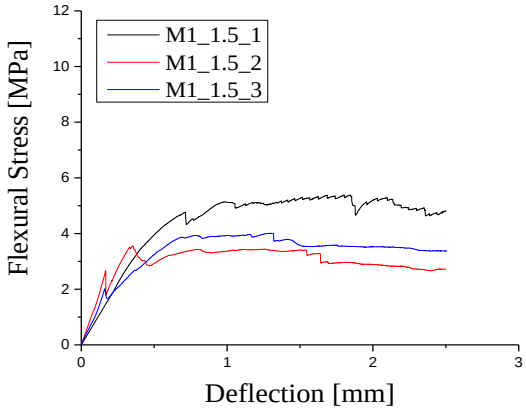

b)

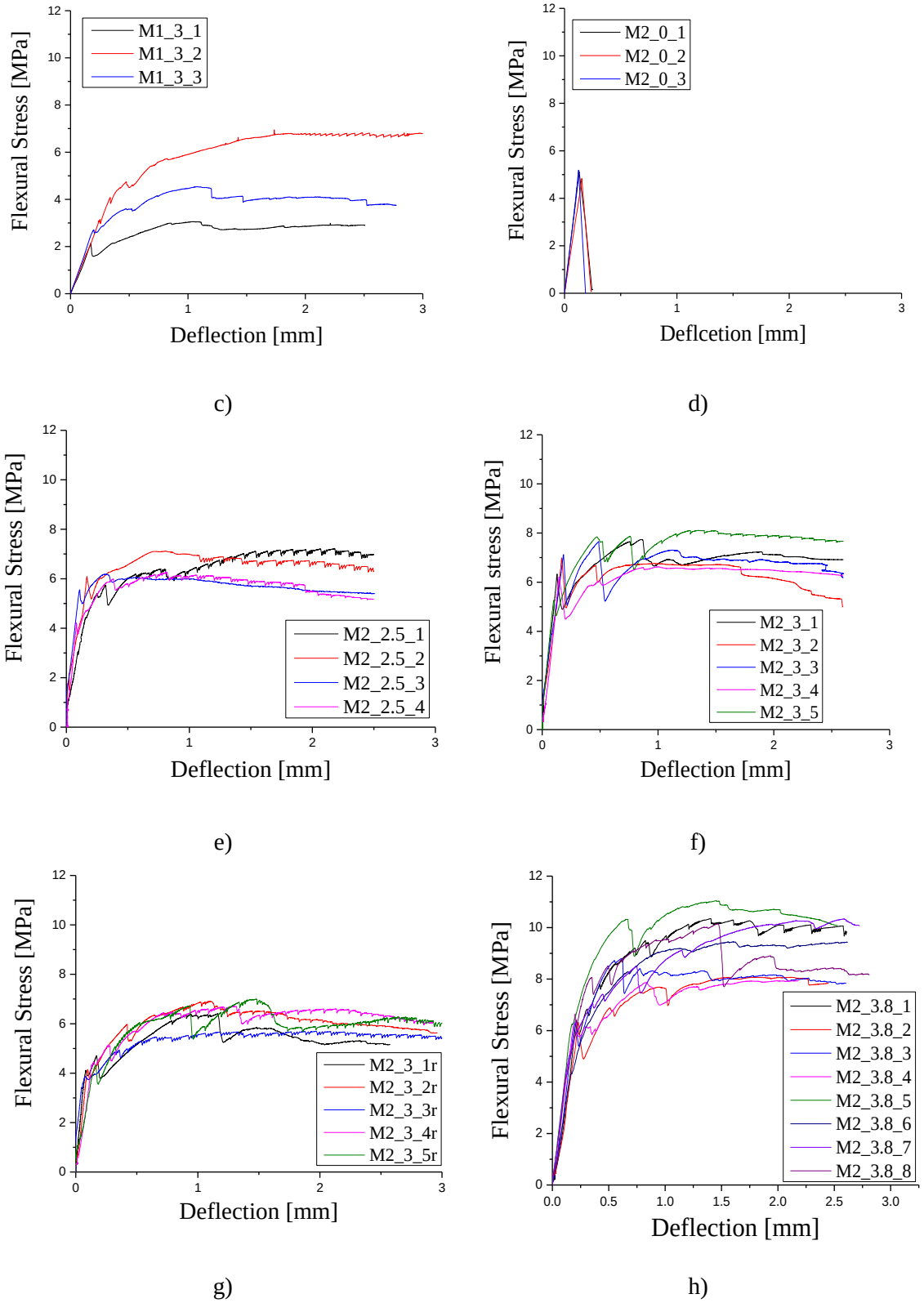

Figure 5.8 Flexural stress *vs*. mid span deflection curves of three point bending tests: a) M1_0; b) M1_1.5; c) M1_3; d) M2_0; e) M2_2.5; f) M2_3; g) M2_3r; h) M2_3.8

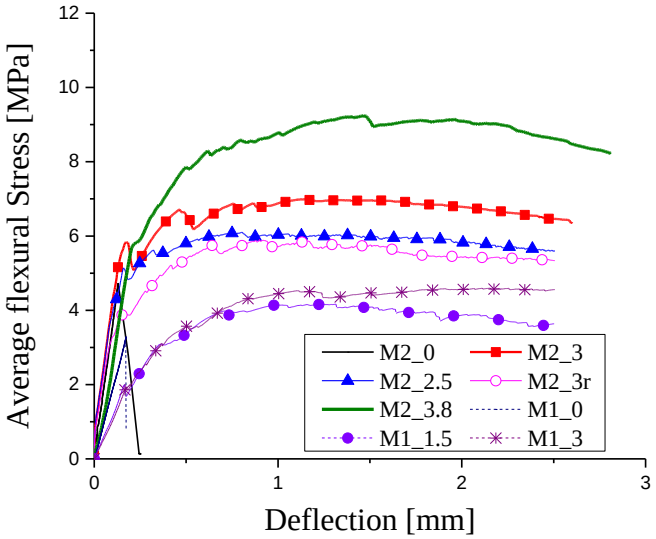

Figure 5.9 Relationship between average flexural stresses *vs*. deflection for all tested specimens

Table 5.3 Average values of cracking moment, flexural tensile strength and maximum flexural tensile stress

Specimen	M_{cr} **[kN.mm]**	σ_{cr} **[MPa]**	σ_{max} **[MPa]**
M1_0	39.00	3.58	3.58
M1_1.5	38.61	2.57	4.31
M1_3	36.25	2.63	4.89
M2_0	83.91	5.04	5.04
M2_3r	69.91	4.14	6.60
M2_2.5	88.31	5.21	6.33
M2_3	114.56	6.35	7.42
M2_3.8	121.15	6.18	9.51

5.3.1.5.2 Three point bending test with notched specimens

In Figure 5.10 the relations of flexural stress *vs*. CMOD are presented for M2_3.8n and M3_3.5n specimens. The results of three point bending tests are analysed in term of equivalent and residual flexural tensile strength and corresponding coefficient of variation (COV) for M2_3.8n and M3_3.5n series (Table 5.4).

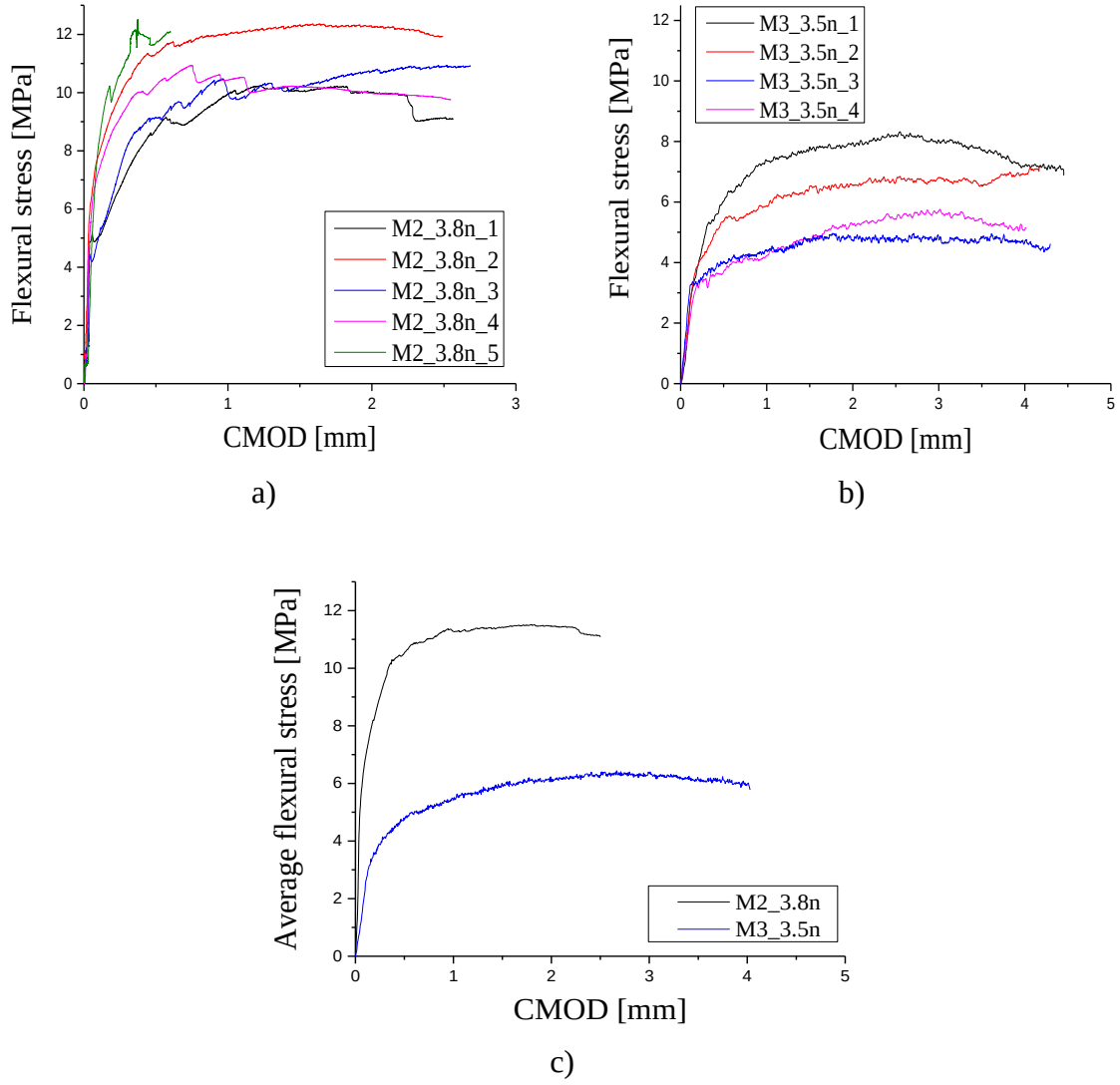

Figure 5.10 Flexural behaviour in three point notched specimen bending tests

The obtained experimental results show that flexural strength of M2 specimens (with higher content of cement) is almost two times higher than the flexural strength of M3 specimens which proves the better quality of the M2 mix with higher content of cement in term of flexural strength. For both M2 and M3 specimens, almost constant load carrying capacity was obtained up to a CMOD = 2.5 mm.

Table 5.4 Equivalent and residual flexural tensile strength parameters for M2_3.8n and M2_3.5n series

Series		$f_{fct,L}$ [MPa]	$f_{R,1}$ [MPa]	$f_{R,2}$ [MPa]	$f_{R,3}$ [MPa]	$f_{eq,2}$ [MPa]	$f_{eq,3}$ [MPa]
M2_3.8n	Average	5.12	10.23	11.14	11.20	10.54	10.34
	COV (%)	18.53	13.53	11.14	11.45	17.84	10.12
M3_3.5n	Average	1.12	4.57	5.74	6.19	5.00	5.74
	COV (%)	30.83	24.96	25.96	23.91	20.40	23.28

5.3.1.6 Inverse analysis with the data obtained from three point bending test

As stated in chapter three, the fracture mode I propagation of RSFRM can be simulated by the trilinear softening diagram represented in chapter three (see Figure 3.24), whose parameters (mode I fracture energy, G_f^I, and values of $\varepsilon_{n,\mathrm{i}}^{cr}$ and $\sigma_{n,\mathrm{i}}^{cr}$ that define the shape of the softening diagram) can be obtained by performing inverse analysis with the force-CMOD data (or force-vertical deflection data) registered in three point notched beam bending tests. In this context, the M2_3.8n specimen was modelled with a mesh of 8 node serendipity plane stress finite elements (Figure 5.11). The Gauss–Legendre integration scheme with 2 × 2 integration points was used in all elements, with the exception of the elements at the specimen symmetry axis, where 1×2 integration points were used in order to assure that the crack progresses along the symmetry axis of the specimen. In the inverse analysis, the l_b parameter was assumed equal to the square root of the area of the integration point corresponding to the integration scheme adopted for the evaluation of the stiffness matrix and stress field. The values defining the $\sigma_n^{cr} - \varepsilon_n^{cr}$ diagram obtained from inverse analysis are presented in Table 5.5.

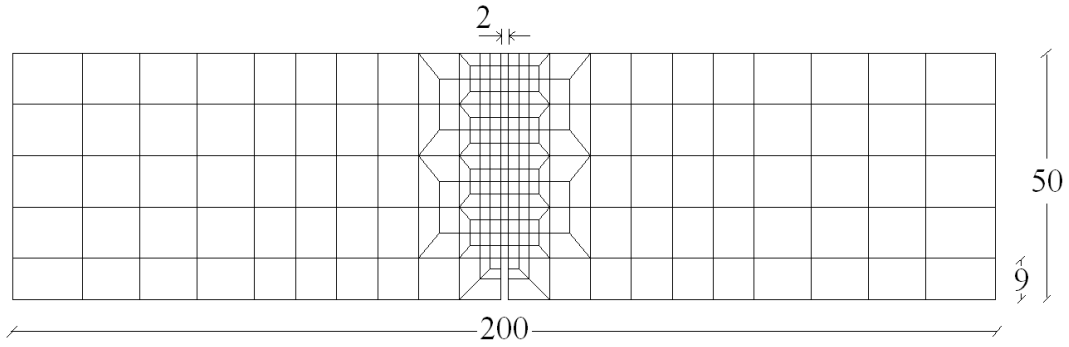

Figure 5.11 Finite element mesh adopted in the inverse analysis (dimensions in mm)

Table 5.5 Values defining the tensile softening diagram, obtained from inverse analysis

Series	$\sigma_{n,1}^{cr}$ **[N/mm²]**	$\varepsilon_{n,1}^{cr} / \varepsilon_{n,u}^{cr}$	$\sigma_{n,2}^{cr} / \sigma_{n,1}^{cr}$	$\varepsilon_{n,2}^{cr} / \varepsilon_{n,u}^{cr}$	$\sigma_{n,3}^{cr} / \sigma_{n,1}^{cr}$	G_f^I **[N/mm]**
M2_3.8n	3.000	0.070	1.200	0.600	1.130	12.000

The comparison between the average experimental load *vs*. CMOD and numerical load *vs*. CMOD of tested specimens is illustrated in Figure 5.12. The results in Figure 5.12 show that using the values presented in Table 5.5, the load *vs.* CMOD curve, predicted by FEM software FEMIX v.4.0 (Azevedo *et al*. 2003) is in good agreement with the average curve of the experimental results.

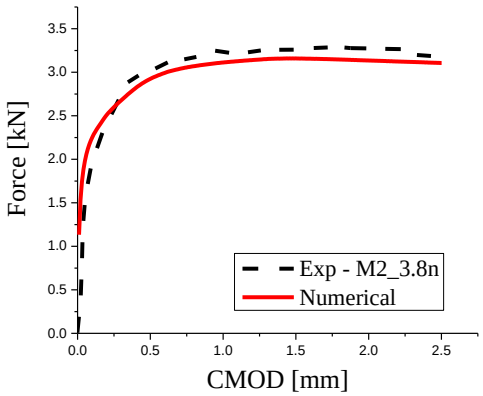

Figure 5.12 Average experimental load *vs*. deflection and numerical load *vs*. deflection

5.3.2 Homogeneity of the developed RSFRM

In a cement based composite, heterogeneity is defined as the existence of interior cracking, deteriorations, honeycombing, and variations of material compositions (ACI 544.1R. 1996).

The UPV method is suitable for the study of the homogeneity of cement based material (Lorenzi *et al*. 2007). In this method, the UPV on different spots of the sample is measured. The homogeneity of the material is identified by the level of variation in the values of UPV (Kaplan 1959). Also, the UPV test results may be influenced by a number of factors such as water-cement ratio (w/c) (Ye *et al*. 2004), admixtures (Ulucan *et al*. 2008) and volume of steel fibres.

5.3.2.1 Experimental program

In this section UPV measurements were performed on M1 and M2 specimens with different fibre contents to investigate the influence of RSF content in UPV. Moreover, in order to evaluate the homogeneity of M1 and M2 mortar matrix, the variation of the UPV obtained for M1 and M2 mortar specimens without RSF were compared.

Figure 5.13 shows the test setup used for measuring UPV value of the mortar specimens. The test instrument consists of two electro-mechanic transducers: one for producing and introducing a wave pulse into the specimen (pulse generator and transmitter); another, the receiver transducer for detecting the arrival of the pulse. In the UPV test method, an ultrasonic wave pulse is created through specimen at one point ("A", in Figure 5.13) on the surface of the specimen, and the time of its travel from point (A) to the point (B) is measured. Knowing distance between the two points ("A" and "B"), the UPV can be determined. Note that the UPV measurements were performed only through direction of the longitudinal axis, since the width and the height of the specimens were lower than the minimum path length that was recommended by the UPV test instrument manufacturer for accurate test results.

The UPV tests were executed with the bending test specimens before performing flexural tests. Therefore, the geometries of the specimens are the same indicated in the Figures 5.4 and 5.5 for M1 and M2 mortars, respectively.

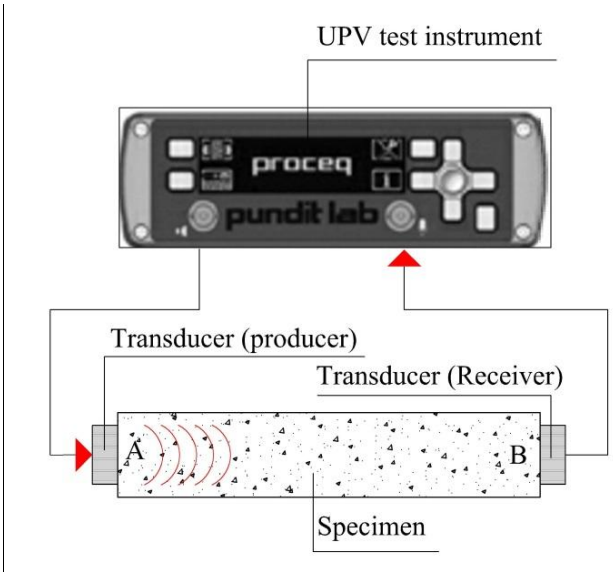

Figure 5.13 Direct ultrasonic pulse velocity test

Results of UPV tests for all M1 specimens with fibre content of 0.0%, 1.5% and 3.0% and M2 specimens with fibre content of 0.0%, 2.5%, and 3.0% by volume are presented in Figure 5.14a.

The addition of steel fibres to a cement based mortar is normally expected to increase its density due to its higher specific weight (Gebretsadik 2013), which leads to the increase of UPV, since according to the wave propagation theory, the velocity of a wave in a material increases with its density (Gebretsadik 2013). Hence, it was expected that the specimens with no fibres would have less UPV than the specimens with fibres. However, for both M1_0 and M2_0, the UPV was the highest. In fact the existence of RSF in the mortar leads to the increase of voids in the micro-structure of the mortar which causes decrease of the UPV. Analysing the relationship between the UPV and the fibre content (V_f) in Figure 5.14b, it was derived that due to the development of voids and the non-homogeneity in RSFRM, less enhancement of UPV for higher volumes of RSF was observed.

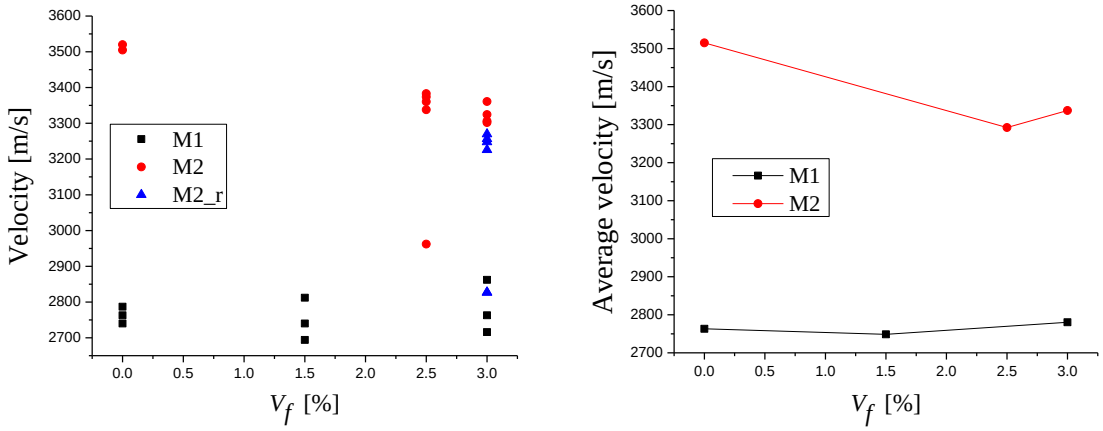

a) b)

Figure 5.14 Direct UPV test results

Higher UPV was obtained for M2 specimens with different fibre contents in comparison with the M1 specimens, which can be justified by a great role of fly ash in improving the mechanical properties of the mortar by filling its micro-pores (Khurana and Saccone 2001), since the content of fly ash in M2 mix was higher than the M1 mix.

Table 5.6 Average UPV and COV

Series	M1_0	M1_1.5	M1_3	M2_0	M2_2.5	M2_3	M2_3r
UPV [m/s]	2763	2748	2780	3515	3292	3337	3108
COV [%]	0.85	2.16	2.68	0.24	4.94	0.69	7.042

5.3.3 Compressive behaviour of RSFRM

5.3.3.1 Young's modulus

The values of the modulus of elasticity or Young's modulus (E_c) of the RSFRM were obtained with cylindrical cores of 100 mm height and 50 mm diameter, by performing tests according to the LNEC E397 (1993). The cores were extracted using a drilling machine from panels with dimensions of 600 mm × 150 mm × 100 mm and made by M2 mortar with fibre content of 3.8% by volume (Figure 5.15).

Figure 5.15 Extraction of RSFRM cores from the panel

The test setup (Figure 5.16b) consisted of two rings installed at top and bottom central region of the specimen. The distance between the rings was 33 mm. In the top ring, three LVDTs were placed around the specimen at 120° from each other. Figure 5.16a presents the load cycles to determine the value of the Young's modulus of the RSFRM. A brief description of the used method for determining the value of Young's modulus is given in the section 3.2.2.1.

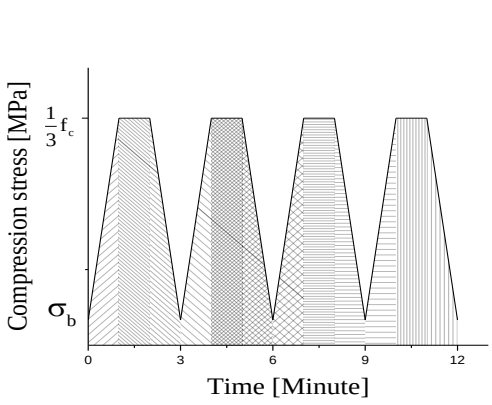

a)

b)

Figure 5.16 Determination of Young's modulus: a) Load cycles to determine the elastic modulus, b) Test setup

The values of the Young's modulus of the RSFRM were determined from the equation (3.7) and its values are presented in Table 5.7.

Table 5.7 Young's modulus of RSFRM

Specimen	E_c [GPa]
C1	17.79
C2	21.06
C3	20.92
C4	18.82
Average	19.64
COV (%)	8.17

As it can be seen in Figure 5.17, the increment of the fibre percentage in the casting direction and, consequently, the lower percentage of fibres on the top part of the specimens and fibre segregation in the bottom part of the specimens influenced the test results, leading to so high COV value for the results.

Figure 5.17 Casting direction

5.3.3.2 Compressive strength

After determining the Young's modulus, the rings were removed from the specimens and the compressive strength were determined according to NP EN 12390-3 (2009) recommendations. Table 5.8 presents compressive strength and the strain at peak load of the tested RSFRM. It should be noted that the values of strain indicated in Table 5.8 were obtained from the displacement measurements recorded by the displacement sensor of the actuator and, consequently, these displacements also includes the deformation of the reaction frame of the machine, and also the initial adjustments between loading platens of

the equipment and extremities of the specimen. Therefore higher strains were recorded when compared to a monitoring setup capable of reading exclusively the deformation of the material part of the specimen considered in uniaxial deformation state.

Table 5.8 Compressive strength of RSFRM and strain at peak load

Specimen	f_c **[MPa]**	**Strain at peak load [‰]**
C1	46.19	9.63
C2	47.10	10.5
C4	46.65	9.03
Average	46.64	9.72
COV (%)	0.97	7.60

5.3.4 Direct tensile behaviour of RSFRM

5.3.4.1 Experimental program

Tensile specimens consisted of nine rectangular coupons with dimensions of 230 mm × 50 mm × 23 mm that were extracted from two panels with dimensions of 686 mm × 188 mm × 23 mm (Figure 5.18a). Five rectangular specimens were extracted in the longitudinal direction (identified by the label "RDTT0"), and four rectangular specimens were extracted in the direction of 45 degrees (identified by the label "RDTT45"). Three specimens were also prepared using dog-bone moulds (identified by the label "DBDTT"). All tensile specimens were made by M2 mortar with fibre content of 3.8% by volume. Due to rectifying the top surface of the rectangular specimens before testing, the thickness of these specimens has been decreased to 21 mm. The top surface of the dog-bone type specimens was not rectified. Therefore, the thickness of this type of specimens was 23 mm.

Figure 5.18 shows details of the specimen, test setup, and monitoring devices to evaluate the tensile strength during test.

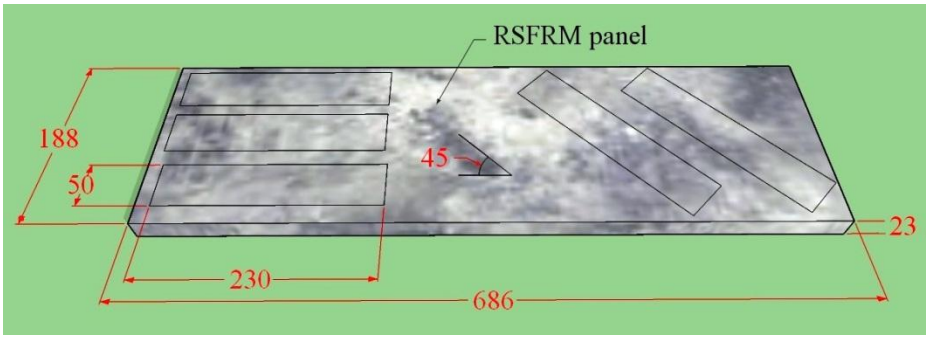

a)

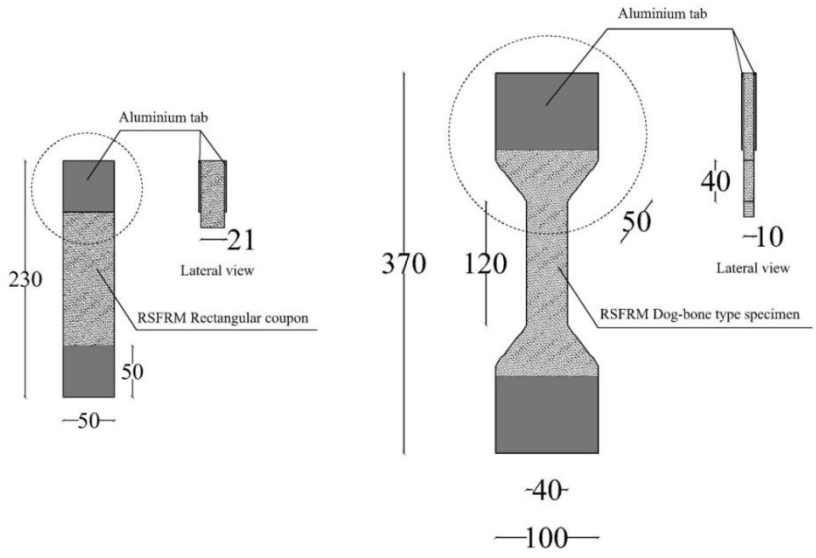

b)

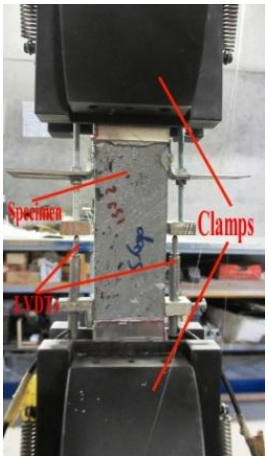

c)

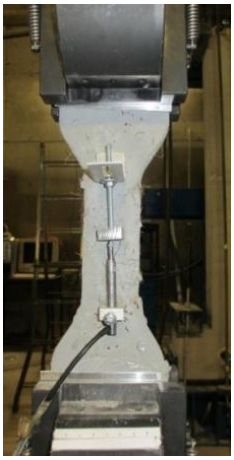

d)

Figure 5.18 Assessment of the tensile properties of RSFRM: a) Extraction configuration from RSFRM panel; b) Tensile specimens geometry and dimensions in mm; c) Test setup for RDTT0 and RDTT45 specimens; d) Test setup for DBDTT specimens

Aluminium tabs were applied to each end of the specimen by means of structural adhesive (Sikadur 32N). Then, the tabs were clamped within the wedges of the testing machine. Tensile specimens were tested under displacement control at a displacement rate of 0.5 mm/min.

5.3.4.2 Experimental results

Figure 5.19 presents crack patterns from the beginning up to the end of the test. During the strain hardening phase of RSFRM, several cracks were formed which means that the crack opening restraint provided by the fibre bridging action leads to the formation of new cracks (Mastali *et al*. 2015). The results of the tensile tests are shown in Figure 5.20. Stress values correspond to the applied load divided by the specimen's cross section area.

Figure 5.19 Crack patterns from initiation to failure

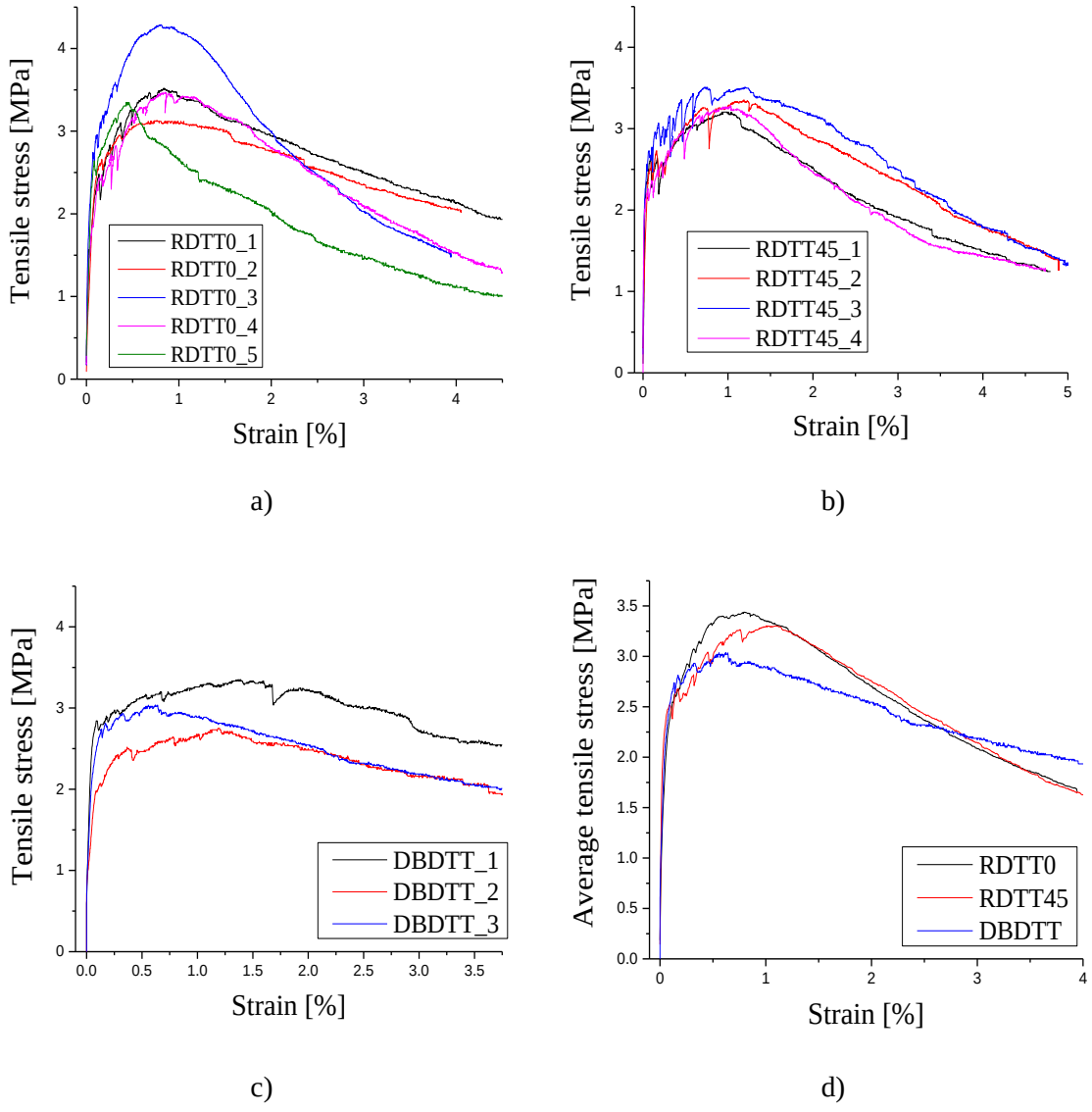

Figure 5.20 Stress–strain diagrams obtained from direct tensile tests: a) RDTT0 specimens; b) RDTT45 specimens; c) DBDTT specimens; d) Average curves

From the tensile stress–strain responses (Figure 5.20) the tensile strength, maximum tensile stress and strain at maximum tensile stress of RSFRM specimens were determined (see Table 5.9).

Table 5.9 Tensile strength, strain at maximum tensile stress and maximum tensile stress of the tested RSFRM specimens

Specimen	Tensile strength [MPa]	Strain in peak Stress [%]	Maximum stress [MPa]
RDTT0_1	2.20	0.84	3.52
RDTT0_2	2.60	0.84	3.13
RDTT0_3	2.74	0.87	4.28
RDTT0_4	2.35	0.98	3.46
RDTT0_5	2.64	0.64	3.34
RDTT45_1	2.64	1.10	3.20
RDTT45_2	2.73	1.21	3.35
RDTT45_3	2.54	0.83	3.50
RDTT45_4	2.26	1.11	3.27
DBDTT_1	2.84	1.35	3.34
DBDTT_2	2.07	1.19	2.75
DBDTT_3	2.73	0.64	3.03
Average	2.52	0.97	3.35
Std	0.247	0.227	0.365
COV (%)	9.798	23.508	10.913

Analysing the tensile stress–strain curves, three response stages are observable (Figure 5.20d). The first stage corresponds to the linear behaviour of the uncracked specimen. When the tensile strength of the composite is reached, the first crack was formed and the hardening zone started up to the peak load (second stage). The softening zone is observable after peak load as the third region. In this region (post-cracking stage during which the crack pattern has been stabilized) the frictional contribution between fibre and surrounding matrix for the debond process was visible. DBDTT have a less steep descending branch in softening zone of the tensile stress *vs*. strain curve than RDTT0 and RDTT45, leading to equal average tensile stress in the strain of 2.52% for RDTT0 and DBDTT and also in the strain of 2.83% for RDTT45 and DBDTT (see Figure 5.20d).

5.3.4.3 Numerical simulation of the direct tensile tests

The experimental direct tensile tests were simulated by performing inverse analysis with test results obtained in uniaxial tensile tests of RDTT specimens and the the fracture mode I parameters of the developed RSFRM were determined. For this purpose, FEMIX finite element analysis software (Azevedo *et al*. 2003) was used.

Figure 5.21 represents the finite element mesh used for the simulation of the specimens failing in uniaxial tension. A finite element mesh of 64 plane stress elements of 8 nodes was used. Due to the symmetry of specimen geometry, supports and loading conditions used in the direct tensile test setup, a quarter of the specimen was modeled. A Gauss-Legendre integration scheme with 2×2 Integration Points (IP) was used in all the elements. In this analysis, the l_b parameter was assumed equal to the square root of the area of the integration point.

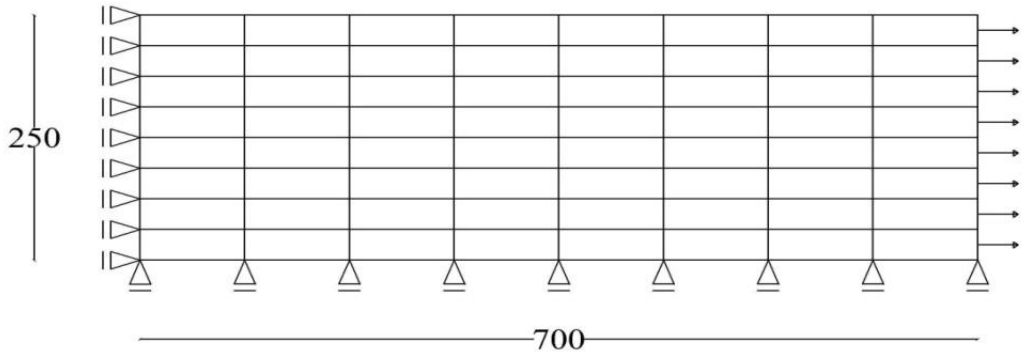

Figure 5.21 Finite element mesh of the RDDTT specimen (dimensions in mm)

The comparison between the experimental load *vs*. displacement and numerical load *vs*. displacement of the tested specimens is shown in Figure 5.22. The values defining the $\sigma_n^{cr} - \varepsilon_n^{cr}$ diagram obtained from inverse analysis are presented in Table 5.10.

Table 5.10 Values defining the tensile softening diagram, obtained from inverse analysis

Series	$\sigma_{n,1}^{cr}$ [N/mm^2]	$\varepsilon_{n,1}^{cr} / \varepsilon_{n,u}^{cr}$	$\sigma_{n,2}^{cr} / \sigma_{n,1}^{cr}$	$\varepsilon_{n,2}^{cr} / \varepsilon_{n,u}^{cr}$	$\sigma_{n,3}^{cr} / \sigma_{n,1}^{cr}$	G_f^I [N/mm]

M2_3.8n	2.450	0.004	1.390	0.019	0.700	8.000

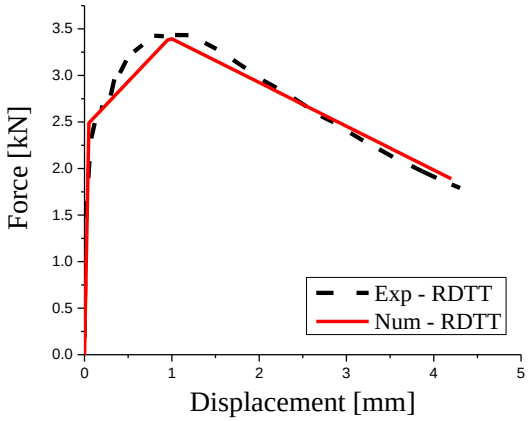

Figure 5.22 Average experimental load *vs*. displacement and numerical load *vs*. displacement

By comparing the values of the fracture energy mode I parameters obtained from inverse analysis with the results of direct tensile test and three point notched beam bending test, it is verified that the values of tensile strength and fracture energy mode I obtained from simulation of three point bending test are higher than the values obtained from simulation of direct tensile test. The difference in the values of fracture energy mode I parameters obtained from direct tensile test and three point bending test simulations could be justified by different fibre pull-out mechanisms in direct tensile and bending tests and also effect of specimen's thickness.

Unlike the direct tensile tests where pull-out of aligned fibre occurs in the crack surface, as it can be seen in Figure 5.23, in the flexural tests pull-out response of inclined fibre is observable, since after the initiation of the crack, the debonded segments of the fibre tend to bend and align with the direction of beam main axis due to increase in crack width. Spalling of the matrix in the debonded segment of the fibres also confirms the inclined fibre pull-out behaviour in the flexural tests.

In the pull-out mechanism of inclined fibre, as it is presented in Figure 5.24, the pull-out load (N) is composed of two components (N_x and N_y). Only the component on the fibre axis (N_x), contributes on the pull-out of inclined fibre generating shear bond stresses and is currently termed as the pulley effect (Shah *et al*. 1995). Therefore, for reaching a limit value of the shear bond stress which is needed for fibre pull-out occurrence, a higher pull-

out load is needed to be applied to the inclined fibre compared to the aligned fibre (with the same dimensions and embedded length). In the researches already done by Cunha *et al*. (2010) and Leung and Shapiro (1999), a higher pull-out resistance of inclined fibres for an inclination angle smaller than 30º compared to the pull-out resistance of aligned fibres were reported. On the other hand, the component N_y generates additional concentrated stresses (σ_N). Due to these concentrated stresses, the mortar between the fibre and the crack surface is pushed off and, consequently, the local spalling of the mortar occurs (Cunha 2010).

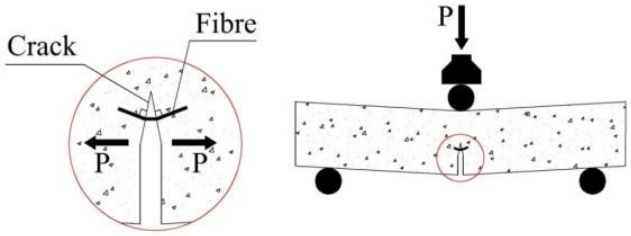

Figure 5.23 Schematic configuration of the pull-out process within the bending test

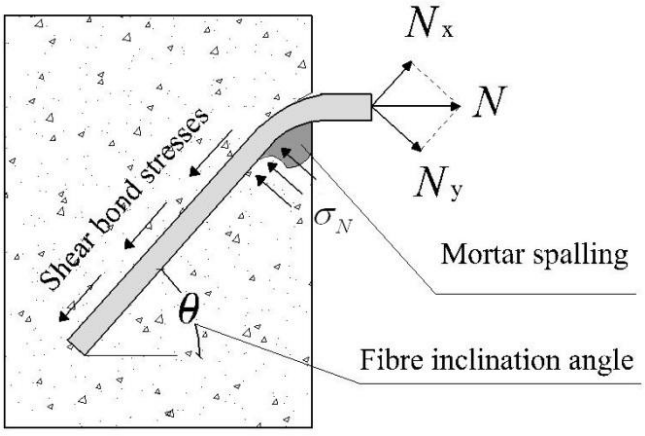

Figure 5.24 Bending and shear of an inclined fibre across a crack and the components of pull-out load (based on Leung and Geng 1998)

Moreover, the effect of fibre segregation on the tensile strength of RSFRM in lower thicknesses is not negligible. As stated in the previous subsection, the negative effect of

fibre segregation on tensile strength of RSFRM increases with the decrease of the specimens thickness. Therefore, lower tensile strength was expected for the specimens used in direct tensile tests with lower thickness compared to the specimens used in bending tests.

5.3.5 Shear behaviour of RSFRM

Due to the difficulty in developing a test setup capable of introducing a pure shear stress field, defining a test method to assess the shear behaviour of cementitious composites is still a challenge (Baghi 2015). Various researchers proposed several shear tests dealing with assessing the pure shear behaviour of materials (Boulifa *et al*. 2013, Reinhardt *et al*. 1997, Banks-Sills and Arcan 1983, Iosipescu 1967, Ohno 1957). In 1966, Iosipescu proposed a test method (Iosipescu test) for determining shear properties of metal and welded joints which was considered also appropriate for composite materials, and it was adopted by ASTM standard D-5379 (1993).

The Iosipescu specimens are loaded in an antisymmetric four points bending with a double notch in a region with high shear and low bending moment. The specimens consist of a small beam height (h_0), angle of notch root (α), and tip radius at notches (r) (Figure 5.25). This geometry of the specimen can assure a uniform shear stress zone between the notches.

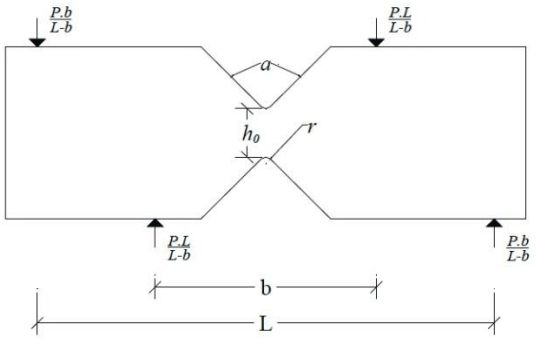

Figure 5.25 Concept of Iosipescu shear test (Baghi 2015)

5.3.5.1 Experimental program

5.3.5.1.1 Test setup and monitoring system

The shear behaviour of the RSFRM was investigated on twelve V-Double edge notched specimens made by M2 mortar with fibre content of 3.8% by volume. The device used in the scope of the research carried out in this PhD thesis is identical to the modified Iosipescu fixture (Figure 5.26a), and its details are provided elsewhere (Baghi and Barros 2016). This fixture covers the entire contact regions of the specimen.

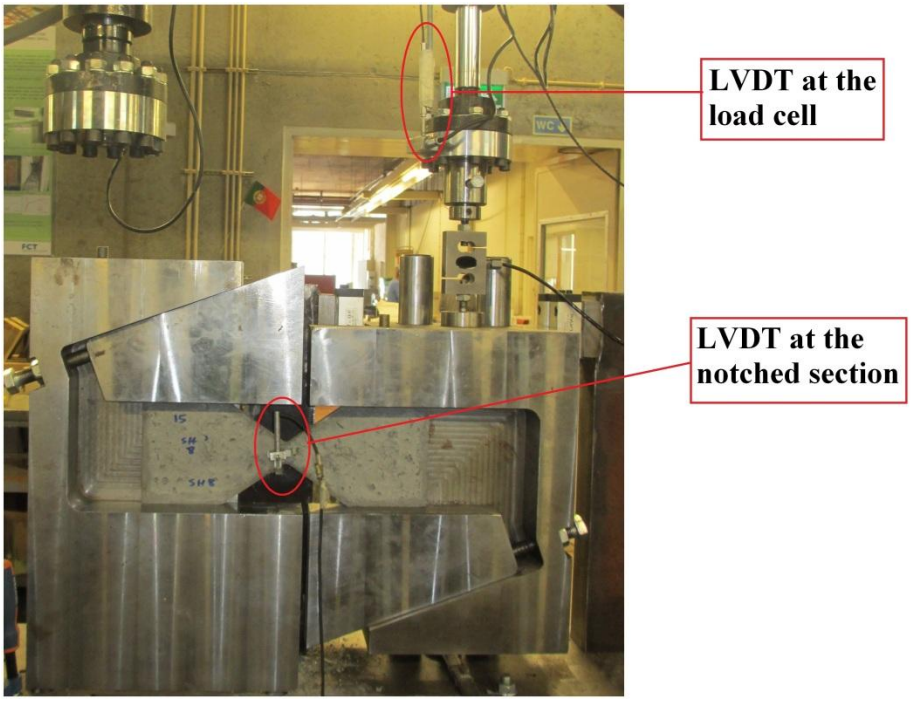

a)

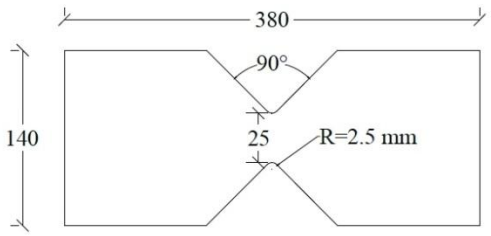

b)

Figure 5.26 Developed Iosipescu a) fixture and b) specimen at University of Minho (dimensions

in mm)

The dimensions of the specimens were 380 mm × 140 mm × 14.5 mm. The depth of the notch roots (h_0) was equal to 25 mm, the angle of notch root (α) 90°, and the tip radius at notches (r) equal to 2.5 mm (Figure 5.26b). The specimens were casted at the same time of the panels of the beams. The average tensile stress at crack initiation and average tensile strength of the RSFRM were 2.52 and 3.34 MPa, respectively. Table 5.11 presents the RSFRM material properties that were obtained in the previous sections.

Table 5.11 Values of the properties of RSFRM materials

Tensile stress at crack initiation	**Tensile strength**	**Tensile strain at tensile strength**	**Compressive strength**	**Young's modulus**
2.52 MPa	3.34 MPa	0.97 %	46.64 MPa	19.64 GPa

The load was applied (10 kN load cell) by using a servo closed loop control equipment, taking the signal read in the internal displacement transducer (LVDT) of the servo-actuator to control the test at a deflection rate of 0.005 mm/s. The value registered in the load cell was calibrated by taking into account the weight and slight friction of the movable portion of fixtur. One LDVT with the linear stroke of +/- 50 mm was installed at the loaded section to measure the displacement of the specimens (Figure 5.26a), and another one with the linear stroke of +/- 2.5 mm was installed at the notched section (as shown in Figure 5.27) to measure the sliding of the crack.

The average shear stress is determined by dividing the total applied load (P) by the area of the cross section between two notches (375 mm^2):

$$\tau_{avg} = \frac{P}{A} \tag{5.4}$$

The shear stress at crack initiation (τ_{cr}) is obtained from:

$$\tau_{cr} = \frac{F_{cr}}{A} \tag{5.5}$$

where F_{cr} is the cracking load, having been assumed as the load when a reduction of 10% in initial secant stiffness occurred.

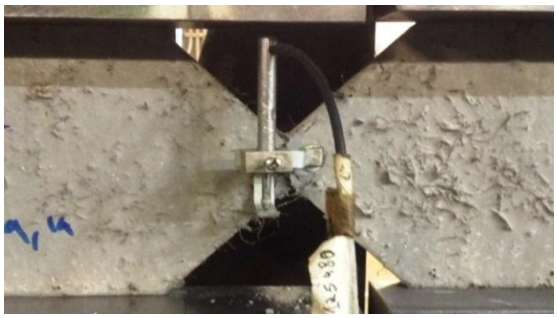

Figure 5.27 The position of the LVDT to measure sliding of the shear crack at notched section

5.3.5.1.2 Test results and discussion

The envelope and the average curve corresponding to the average shear stress *vs.* sliding relationship of the specimens are plotted in Figure 5.28. Figure 5.29 shows the typical crack patterns of these specimens.

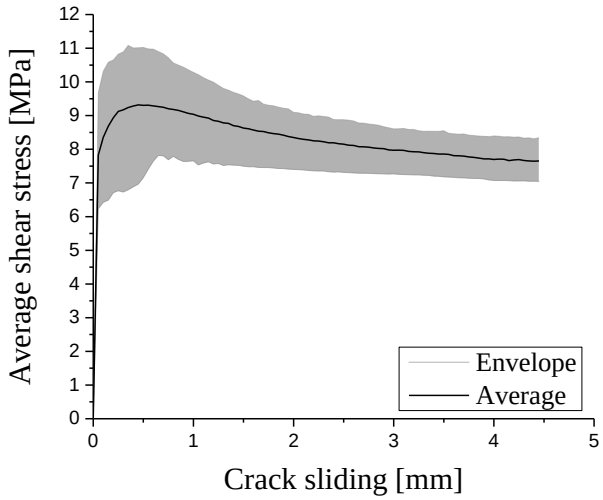

Figure 5.28 The envelope and average stress *vs*. crack sliding

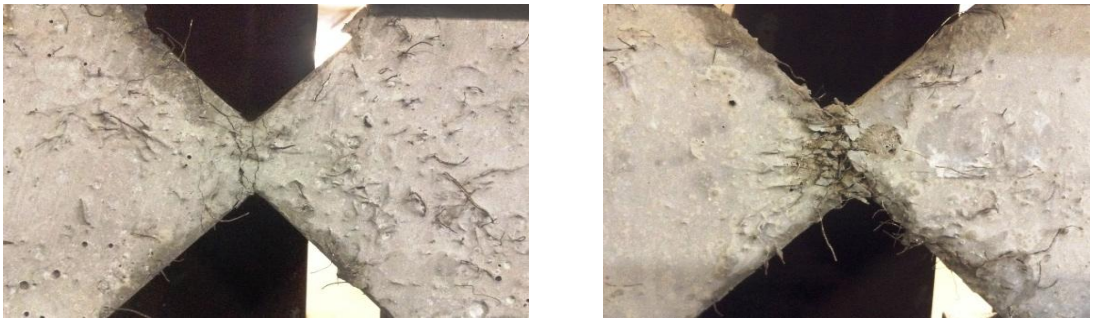

Figure 5.29 Typical crack patterns of tested Iosipescu specimens

Analysing shear stress-sliding curve presented in Figure 5.28, four individual regions are observable. The first region corresponds to the linear behaviour up to a shear stress of about 6.25 MPa (crack sliding equal to 0.02 mm) and the formation of initial vertical cracks. The second region includes the hardening zone with formation of more micro cracks simultaneously up to peak load. The first softening zone is observable after peak load as the third stage, while the micro cracks connected to each other and the load started decreasing with high slope up to a slide of about 1.5 mm. In the fourth region a lower softening slope (second softening zone) of the curve is observable above a slide of around 1.5 mm. For the average sliding of 4.45 mm, which is 9.8 times the average sliding at peak load, the RSFRM is capable of supporting 82% of the average shear strength, which confirms the high ductility of this cementitious composite when subjected to shear deformations. The average value and characteristic values of cracking shear stress was 6.25 MPa and 5.77 MPa, respectively.

5.3.5.2 Numerical simulation

The Iosipescu test was simulated by the FEM-based computer program, FEMIX (Azevedo *et al*. 2003). The two dimensional multi-directional fixed smeared crack model described in Ventura-Gouveia (2011) was used in the numerical simulation.

To simulate the crack initiation and fracture mode I propagation of RSFRM, the trilinear tension-softening diagram presented in Figure 3.18 was adopted. The values to define this diagram are indicated in Table 5.12. The RSFRM Young's modulus and compressive strength in the numerical model are the same obtained in the experimental programs in

section 5.3.3. Table 5.12 also includes the values to define shear-softening diagram presented in Figure 4.5.

Table 5.12 Values of the parameters of the RSFRM constitutive model

Property	**Value**
Poisson's ratio	0.190
Compressive strength	$46.640\,N/mm^2$
Initial Young's Strength	$19640\,N/mm^2$
Tri-linear tension softening diagram of concrete	$f_{ct}=3.300N/mm^2$, $\xi_1=0.005$, $\xi_2=0.010$, $\alpha_1=0.850$, $\alpha_2=0.610$, $G_{fn}=6.000N/mm$
Parameter defining the mode I fracture energy available to the new crack	$P_2=3$
Softening crack shear stress-strain diagram	$\sigma_{t,p}^{cr}=4.300N/mm^2, G_{fs}=1.900N/mm$, $\beta=0.600$
Crack band width	Square root of the area of Gauss integration point
Threshold angle	$\alpha_{th}=30°$

Figure 5.30 represents the finite element mesh used for the simulation of the specimens. The mesh was composed by 2015 nodes and 1920 serendipity 4 nodes plain stress elements with 2×2 Gauss-Legendre integration scheme. Figure 5.30 also shows the support and load conditions. Due to the relatively small thickness of the specimens, it is assumed that fibres are oriented primarily in the plane. The applied load, *P*, is the sum of all vertical forces in each node in contact with the movable part of the fixture. This force represents the uniform load imposed on specimens measured by the load cell in the experimental tests.

The experimental and the numerical relationship between shear stress and the sliding of the crack at the notched plane for the tested specimens are compared in Figure 5.31. The crack pattern of this specimen at the end of the analysis is represented in Figure 5.32.

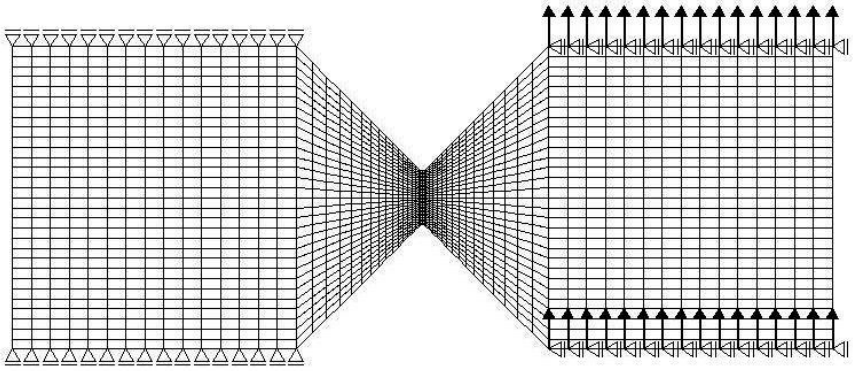

Figure 5.30 Finite element mesh of the Iosipescu specimen

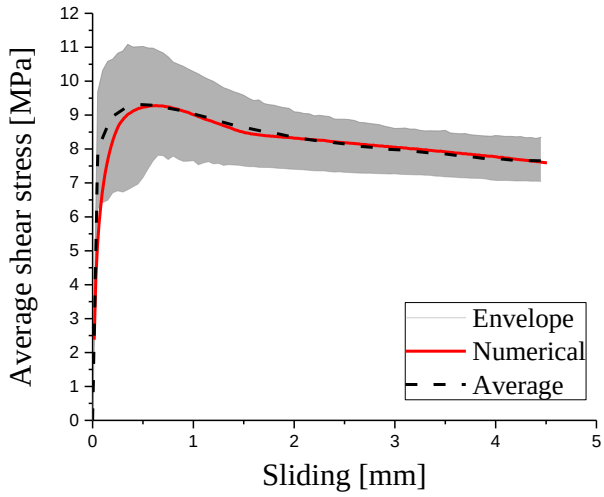

Figure 5.31 Comparison between experimental and numerical shear stress *vs*. sliding relationship

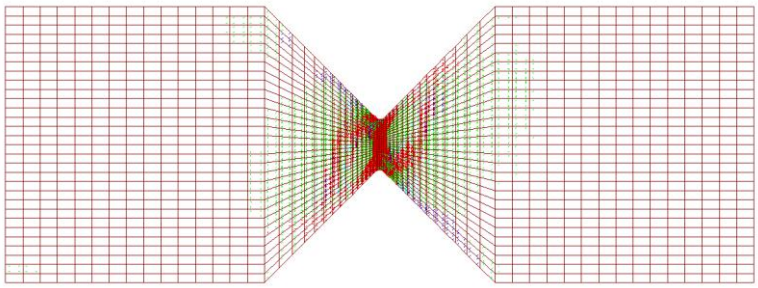

Figure 5.32 Crack pattern type of the specimens

5.3.5.3 Parametric study

By using the previous numerical model whose good predictive performance for the simulation of the shear behaviour of the specimens was evidenced, a parametric study was performed to evaluate the influence of the following parameters on the shear stress-sliding response: shear retention factor, fracture energy mode II and crack shear strength that define the crack shear softening diagram, tensile strength and fracture energy mode I that define the trilinear tension-softening diagram. The advantage of using RSFRM instead of Plain Cementitious Material (PCM) was also studied. The finite element mesh, support, and load conditions were the same adopted in the numerical simulation of the specimens in previous section.

5.3.5.3.1 Influence of β parameter (first branch of the $\tau_t^{cr} - \gamma_t^{cr}$ diagram)

The influence of β parameter on the shear stress *vs.* sliding response of the specimen is illustrated in Figure 5.33. The values of 0.10, 0.60 and 0.99 were adopted in the numerical model for this parameter. The first one was lower and the last one was higher than the value adopted in the analysis of the specimen. All the remaining parameters were maintained as the same values considered in the previous analysis. The results show that, from 0.05 mm sliding (that corresponds to the formation of first shear crack at the notched plane) up to sliding of about 4.43 mm, the shear stress capacity of the specimens slightly increases with the increase of the value of β (Figure 5.33). The crack shear strain ($\gamma_{t,p}^{cr}$) increases when the value of β decreases which means that the crack enters in its shear softening stage at larger crack shear strain (Figure 5.34). The crack shear strain ($\gamma_{t,p}^{cr}$) in Figure 5.34 was determined from the equation (4.17).

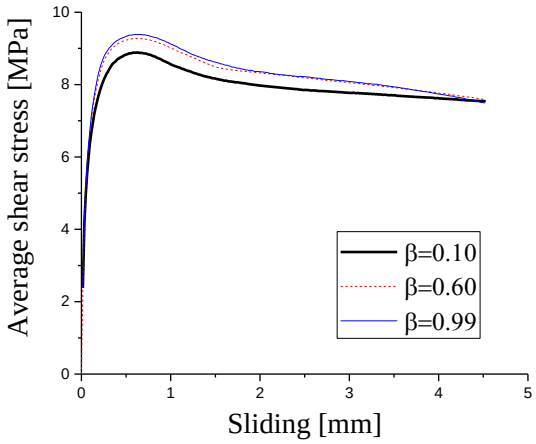

Figure 5.33 Influence of shear retention factor on average shear stress

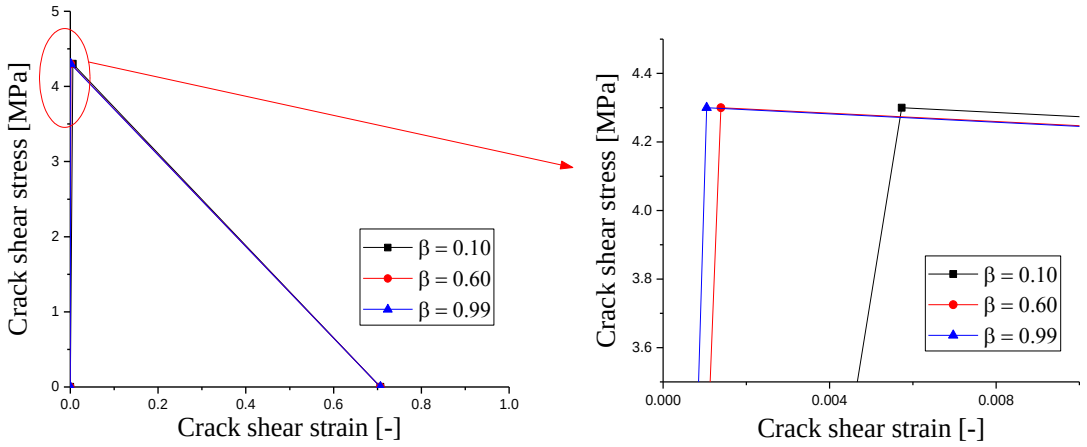

Figure 5.34 Representation of the crack shear stress-crack shear strain diagram for β equal to 0.1, 0.6 and 0.99

5.3.5.3.2 Influence of fracture energy mode II

In order to evaluate the effect of the shear fracture energy mode II ($G_{f,s}$) on the shear stress *vs.* sliding response of the specimen, the values of shear fracture energy, 0.1, 1.9 and 5.0 N/mm were adopted in the numerical model, while of all the remaining model parameters were maintained as the same values considered in the previous analysis. The first value was lower and the last value was higher than the shear fracture energy

considered in the analysis of the experimentally tested specimen (1.9 N/mm). Figure 5.35a compares the shear stress *vs*. sliding responses for three different parameters of the fracture energy mode II. The results show that the decrease of the fracture energy mode II leads to the increase of the slope of the first softening zone with abrupt shear stress decay for shear stress *vs*. sliding curve corresponding to $G_{f,s} = 0.1$. However, this tendency is not observable for the second softening zone. Furthermore, the increase of fracture energy mode II leads to the increase of the ultimate crack shear strain, since the crack shear strength was the same in the three simulations (Figure 5.35b).

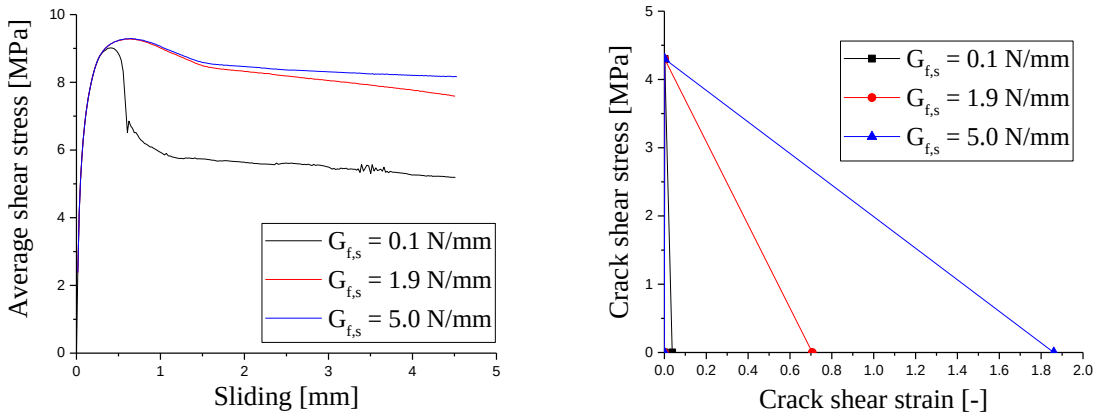

a) b)

Figure 5.35 a) Influence of the fracture energy mode II on average shear stress-sliding relationship; b) Crack shear stress-crack shear strain diagram for the fracture energy mode II equal to 0.1, 1.9 and 5.0 N/mm

5.3.5.3.3 Influence of crack shear strength

To study the influence of crack shear strength ($\tau_{t,p}^{cr}$) on the shear stress *vs*. sliding response of the specimens, the values of crack shear strength, 1.00, 4.30 and 6.00 MPa were adopted in the numerical model, while the values of all the remaining model parameters were maintained as the same values considered in the analysis of the experimentally tested specimen. The first value was lower and the last value was higher than the crack shear strength considered in the analysis of the experimentally tested specimen (4.30 MPa). Figure 5.36a compares the shear stress *vs*. sliding responses for

three different values of the crack shear strength ($\tau_{t,p}^{cr}$). From the obtained results it is derived that the increase of the value of $\tau_{t,p}^{cr}$ leads to the increase of the shear strength, since the entrance in the crack shear softening stage is postponed for later stages of the sliding process (Figure 5.36b). However, the ultimate crack shear strain decreases with the increase of $\tau_{t,p}^{cr}$, since the fracture energy mode II was the same in the three simulations (Figure 5.36b).

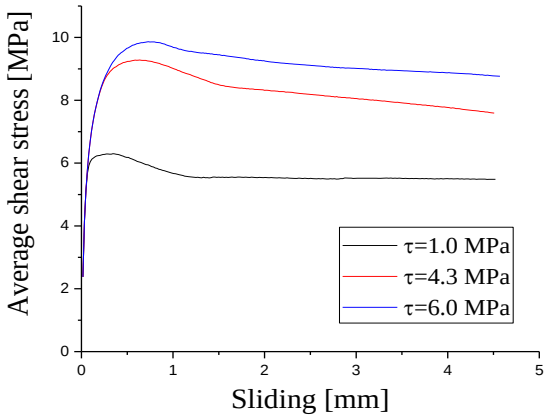

a)

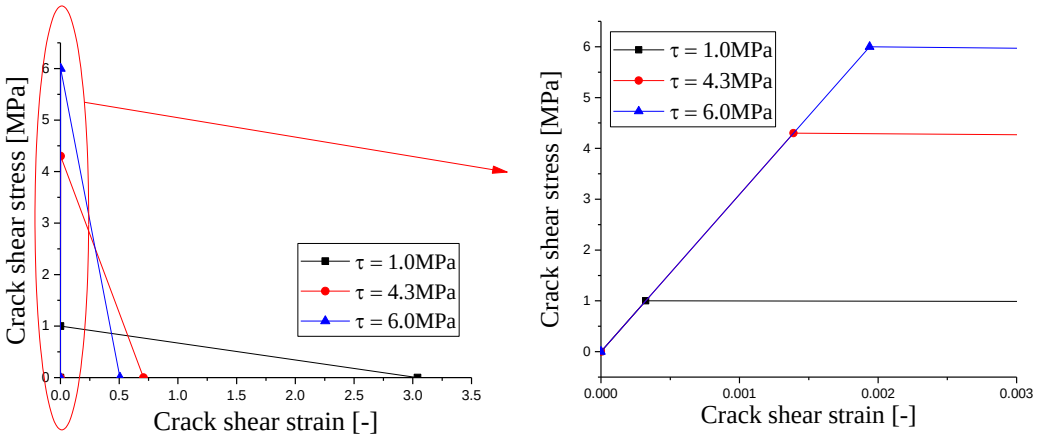

b)

Figure 5.36 a) Influence of crack shear strength on shear stress-sliding relationship; b) The crack shear stress vs. crack shear strain diagram for the crack shear strength equal to 0.1, 4.3 and 6.0 MPa

5.3.5.3.4 Influence of tensile strength

The influence of tensile strength (f_{ct}) on the shear stress *vs*. sliding response of the specimen is studied in this section. The following values of tensile strength, 2.0, 3.3 and 5.0 MPa were adopted in the numerical model, while the values of all the remaining model parameters were maintained the same. The first value was lower and the last value was higher than the tensile strength considered in the analysis of the experimentally tested specimen (3.3 MPa). Figure 5.37 compares the shear stress *vs.* sliding responses for three different values of the tensile strength. The results show that the increase of the value of tensile strength leads to the increase in both shear strength and slope of the softening zone, so that at the sliding of 3.18 mm, the curves corresponding to the tensile strength equal to 3.3 and 5.0 MPa have the same shear stress.

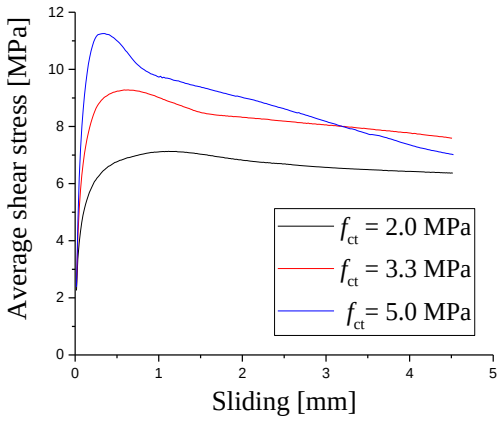

Figure 5.37 Influence of the tensile strength on shear stress-sliding relationship

5.3.5.3.5 Influence of fracture energy mode I

In Figure 5.38 the influence of G_f^I parameter on the shear stress *vs.* sliding response of specimens is depicted by adopting the values 1.0, 6.0 and 12.0 for this parameter. The obtained results show that for the G_f^I less than 6.0 N/mm the shear strength significantly increases with the increase of the fracture energy mode I. However, for the value of G_f^I

between 6.0 N/mm and 12.0 N/mm, the shear strength slightly increases with the increase of G_f^I.

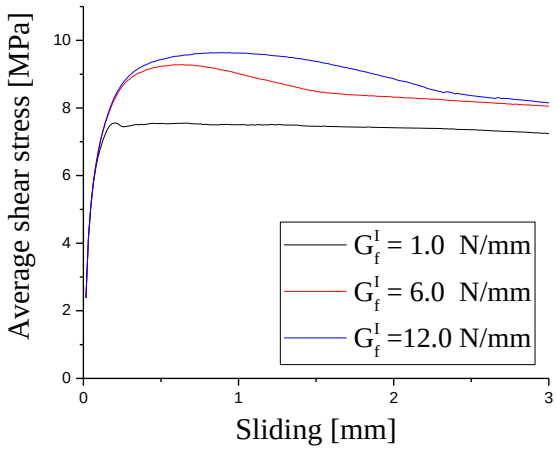

Figure 5.38 Influence of the fracture energy mode I on shear stress-sliding relationship

Table 5.13 includes the values of shear strength and corresponding sliding for the fracture energy mode I equal to 1.0, 6.0 and 12.0 N/mm. The results in Table 5.13 show that the increase of the G_f^I leads to the increase of the sliding corresponding to the shear strength.

Table 5.13 Shear strength and sliding at shear strength obtained by adopting three different values of fracture energy mode I

G_f^I **[N/mm]**	**Shear strength [MPa]**	**Sliding at shear strength [mm]**
1.0	7.55	0.20
6.0	9.28	0.63
12.0	9.63	0.90

5.3.5.3.6 Plain cementitious material

Figure 5.39 compares the shear stress *vs.* sliding relationship obtained when the specimen is made by a plain cementitious material (PCM) and a RSFRM. The material properties of the PCM are presented in Table 5.14 (Baghi and Barros 2016). Apart the properties of

these two materials, the remaining simulation conditions (geometry, loading and supports) were the same in the both analysis.

Table 5.14 Values of the parameters of the PCM constitutive model (Baghi and Barros 2016)

Property	**Value**
Poisson's ratio	0.100
Compressive strength	$31.600\,N/mm^2$
Initial Young's Strength	$14000\,N/mm^2$
Tri-linear tension softening diagram of concrete	$f_{ct}=1.800N/mm^2$, $\xi_1=0.005$, $\xi_2=0.100$, $\alpha_1=0.300$, $\alpha_2=0.300$, $G_f^I=0.080N/mm$
Parameter defining the mode I fracture energy available to the new crack	$P_2=3$
Softening crack shear stress-strain diagram	$\sigma_{t,p}^{cr}=1.000N/mm^2$, $G_{fs}=0.045N/mm$, $\beta=0.600$
Crack band width	Square root of the area of Gauss integration point
Threshold angle	$\alpha_{th}=30°$

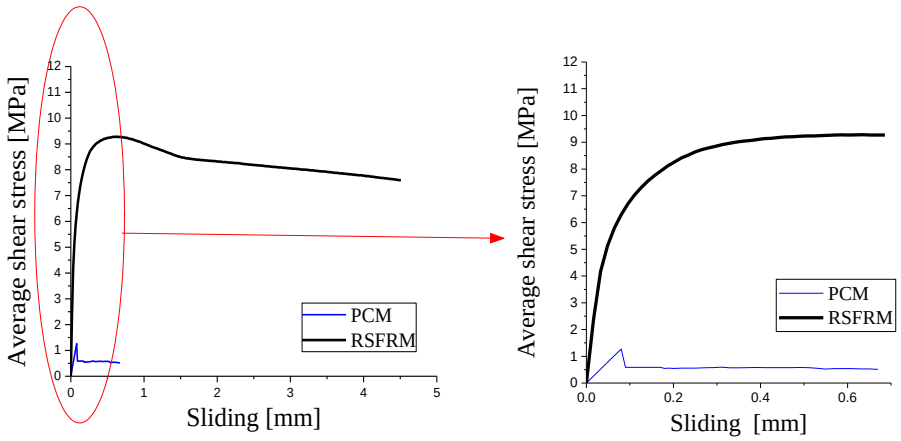

Figure 5.39 Shear response of a specimen made by RSFRM and Plain Cementitious Material (PCM)

The RSFRM specimen failed at 7.3 times higher shear strength than the PCM specimen. Unlike the shear stress *vs.* sliding response of the RSFRM with an obvious nonlinear stage up to the peak load, followed by a relatively smooth softening response with high ductility behaviour, the PCM specimen had a brittle behaviour, with abrupt load decay just after peak load.

5.4 Durability performance

Durability of concrete is defined as the ability to resist weathering action, chemical attack, and abrasion while maintaining its desired engineering properties during its expected service life. In a service life of structure, beside the ability of the structure to resist mechanical actions, it must be able to resist the physical and chemical aggressions (Chintalapudi and Rama 2016). So, durability is one of the most important aspects of cementitious composites that must be taken into account due to its fundamental incidence in the serviceability life of structures (Frazão *et al*. 2015).

In this part of the experimental program dealing with the development of RSFRM panels, durability performance of RSFRM specimens was studied. Five different durability tests were performed, applied to RSFRM made by M2 mortar with fibre content of 3.8% by volume in order to evaluate its durability indicators normally used for plain concrete, namely: water absorption by immersion and by capillarity, permeability to air, chloride diffusion by migration under non-steady state and drying shrinkage. For comparison purpose, the recent research dealt with durability of Steel Fibre Reinforced Self-Compacting Concrete (SFRSCC) that was conducted by Frazão (2015) was also considered.

5.4.1 Water absorption by immersion

The water absorption by immersion is a characteristic that evaluates the material existing porosity (Evangelista and Brito 2004). The water absorption by immersion was determined according to the Portuguese Standard LNEC E394:1993. To measure the water absorption by immersion, first the core specimens with the diameter of 44 mm and height of 40 mm were dried to constant mass in a ventilated oven at a temperature of

105 ± 5 ºC. The dry mass was called M_d. Afterwards the samples were placed in a vacuum chamber which was connected by a hose to a rotary vacuum pump (Figure 5.40). The chamber (and therefore the specimens) was evacuated and pumping was continued for three hours. The hose was then clamped, disconnected from the vacuum pump and immersed in a tank containing water. When the clamp was released, water was drawn into the vacuum chamber. When the specimens have become fully immersed, the hose was removed from the water tank and air allowed to enter the vacuum tank so that atmospheric pressure forces water into the evacuated pores of the material. The specimens were immersed in water until the change in mass during 24 hours was less than 0.1%. The obtained saturated mass was called M_s.

a) b)

Figure 5.40 Water absorption by immersion: a) specimens used; b) vacuum chamber

The water absorption by immersion (W_i) was calculated from the following equation:

$$W_i = \frac{M_s - M_d}{M_s - M_h} \times 100 \qquad (5.6)$$

where M_h is the hydrostatic mass of the specimen immersed in water. Table 5.15 presents the test results of water absorption by immersion.

Comparing the average value of 30.1 % for the open porosity of RSFRM (RSF content of 3.8% by volume) with the value of 11.3 % that was obtained by Frazão *et al.* (2015) for SFRSCC (fibre content of 0.8% by volume) allows concluding that addition of RSF to cementitious composite significantly increases its open porosity due to air attraction on the surface of fibres containing rubber crumb on their surface.

Table 5.15 Water absorption by immersion test results

Specimen	M_d **[g]**	M_s **[g]**	M_h **[g]**	**Open porosity [%]**
OP1	203.05	235.11	128.10	29.954
OP2	203.38	235.61	129.46	30.354
OP3	190.00	221.90	118.08	30.720
OP4	220.47	252.40	142.42	29.026
OP5	183.89	214.30	115.35	30.724
OP6	208.76	240.64	133.36	29.708
			Average	30.081
			COV (%)	2.18

5.4.2 Water absorption by capillarity

The water absorption coefficient due to capillary action was measured using RSFRM prism specimens with dimensions 80 mm × 40 mm × 40 mm at atmospheric pressure according to the Portuguese Standard LNEC E393:1993. For this purpose, prisms with dimensions 160 mm × 40 mm × 40 mm were prepared and were broken into two halves (Figure 5.41). After drying to constant mass at the age of 28 days, one face of the specimens was immersed in 5 ± 1 mm of water and the velocity of water absorption in no saturated specimens was measured during 34 days. The water absorbed by capillarity, W_c, was determined by the ratio between the increase of the mass specimen by the area of the lower surface of the specimen, Ω_i that was in contact with the water, according the following equation:

$$W_c = \frac{M_i - M_0}{\Omega_i} \tag{5.7}$$

where M_i is the mass of the specimen in contact with water for different times of reading ($\sqrt{t_i}$) and M_0 is the dry mass of the specimen at 40 ± 5 °C.

Figure 5.41 Water absorbed by capillarity

The results in terms of the amount of water absorbed per unit area *vs.* square root of time are presented in Figure 5.42. The coefficient of water absorption by capillarity action, which corresponds to the slope of these curves during the initial 4 hours of testing, was 0.2153 $mg/mm^2/\min^{0.5}$ which is nearly two times greater than the amount of coefficient of water absorption by capillarity action ($0.0941\, mg/mm^2/\min^{0.5}$) that was obtained by Frazão (2015) for SFRSCC (fibre content of 0.8% by volume). This means that the developed RSFRM is not as capable as SFRSCC to prevent penetration of deteriorating agents.

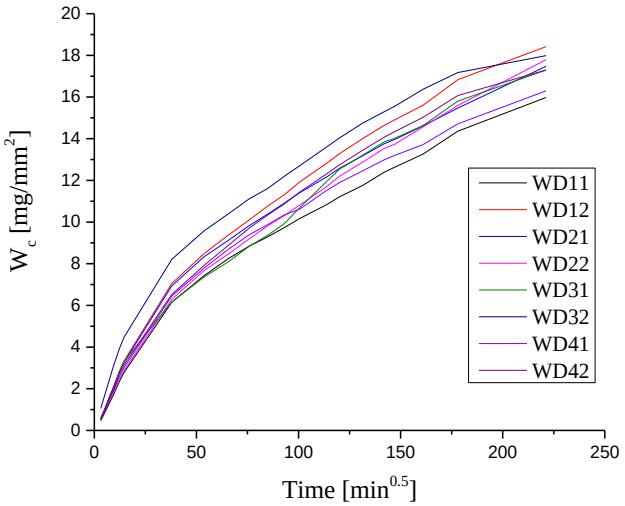

Figure 5.42 Water absorption by capillarity of RSFRM

5.4.3 Air permeability

The air permeability of RSFRM was determined with cylindrical cores of 40 mm height and 45 mm diameter by using Leeds cell device. This device ensures that the specimen is subjected to a steady state flow of the fluid that passes perpendicularly through a known area under a prescribed air pressure differential between the two surfaces of the sample during a certain period of time (see Figure 5.43).

Figure 5.43 Leed cell in air permeability test

For gases, the coefficient of permeability, K_G is determined based on the modified D'Arcy law, according with the following equation, which considered the compressibility and the viscosity of the fluid.

$$K_G = \frac{4.04vL \times 10^{-16}}{A(P_1^2 - 1)} \tag{5.8}$$

where ν is gas flow, L is the thickness of the specimen cross section crossed by the gas (40 mm), A is the cross section of specimen crossed by the gas (0.0016 mm^2), P_1 is the absolute pressure gas inlet (adopted 3 bar).

Figure 5.44 shows the obtained values of air permeability coefficients for RSFRM specimens. The average of air permeability coefficient values was 0.61×10^{-16} m^2, which was 1.4 times higher than the average value obtained by Frazão (2015) for SFRSCC (0.443×10^{-16} m^2). However, lower variation of the test results was observed for RSFRM (COV = 6.3%) compared to SFRSCC (COV = 8.3%).

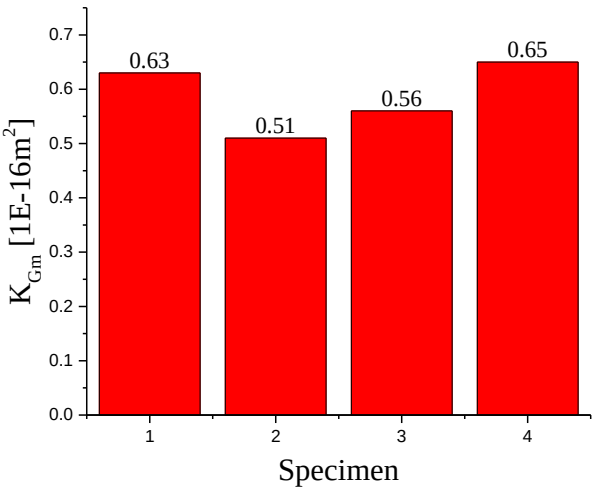

Figure 5.44 Air permeability coefficients for RSFRM specimens

5.4.4 Diffusion of chlorides by migration under non-steady state

To study the resistance of RSFRM against chloride penetration, an accelerated non-steady state migration test method was used according to the recommendation of NT BUILD 492 (1999). Five RSFRM cylindrical specimens with a diameter of 100 mm and a thickness of 50 mm were tested. In this test, an external electrical potential was applied axially across the specimen, by forcing the chloride ions outside to migrate into the specimen (Figures 5.45 and 5.46). After 24 hours of test duration, the specimen was axially split and a silver nitrate solution was sprayed on to one of the freshly split sections.

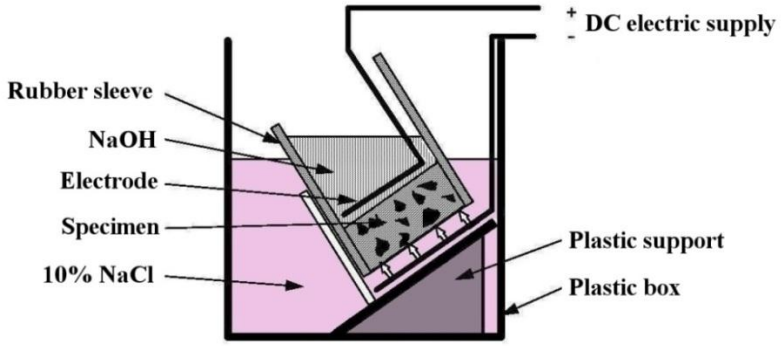

Figure 5.45 Chloride migration test setup (based on NT BUILD 492, 1999)

a) b)

Figure 5.46 Chloride migration test of RSFRM: a) at the beginning; b) at the end of test

The chloride penetration depth was measured from the visible white silver chloride precipitation and the chloride migration coefficient was calculated from this penetration depth. The catholyte solution is 10% NaCl (2 N) by mass in tap water and the anolyte

solution is 0.3 N NaOH in tap water. The determination of the chloride migration coefficient D_{nssm} is given by the following equation:

$$D_{nssm} = \frac{RT}{zFE} \times \frac{x_d - \alpha\sqrt{x_d}}{t} \tag{5.9}$$

where:

$$E = \frac{U - 2}{L}$$

$$\alpha = 2\sqrt{\frac{RT}{zEF}} \times erf^{-1}\left(1 - \frac{2c_d}{c_0}\right)$$

D_{nssm}: non-steady state migration coefficient, m2/s;

z: absolute value of ion valence, for chloride, z = 1;

F: Faraday constant, F = 9.648 ×10^4 J/(V·mol);

U: absolute value of the applied voltage, V;

R: gas constant, R = 8.314 J/(K·mol);

T: average value of the initial and final temperatures in the anolyte solution, K;

L: thickness of the specimen, m;

x_d: average value of the penetration depths, m;

t: test duration, seconds;

erf^{-1}: inverse of error function;

c_d: chloride concentration at which the colour changes, $c_d \approx 0.07\ N$;

c_0: chloride concentration in the catholyte solution, $c_0 \approx 2\ N$.

Since $erf^{-1}\left(1 - \frac{2 \times 0.07}{2}\right) = 1.28$, the following simplified equation can be used:

$$D_{nssm} = \frac{0.0239(273+T)L}{(U-2)t}\left(x_d - 0.0238\sqrt{\frac{(273+T)Lx_d}{U-2}}\right) \quad (5.10)$$

where D_{nssm} is non-steady state migration coefficient, $\times 10^{-12}$ m^2/s.

The values of the non-steady state chloride migration coefficient, D_{nssm}, for RSFRM specimens are presented in Table 5.16. By comparing the results indicated in Table 5.16 with the average value of D_{nssm} that was obtained by Frazão (2015) for SFRSCC (D_{nssm} = 11.61×10^{-12} m^2/s), it was verified that a higher value of chloride migration coefficient was obtained for RSFRM. Figure 5.47 shows RSFRM specimens after chloride migration test. During the test, it was possible to observe the formation of corroded material in the cathode solution of the tests, which was increased with the duration of the test.

Figure 5.47 RSFRM specimens after chloride migration test

Table 5.16 Results of chloride migration test

Specimen	D_{nssm} **[$\times10^{-12}$ m^2/s]**
D1	14.67
D2	15.03
D3	15.58
D4	15.34
D5	14.83
Average	15.09
COV (%)	2.45

5.4.5 Drying shrinkage

Drying shrinkage is a typical occurrence in almost every cementitious product caused by evaporation of internal water in hardened cementitious material. However, volume change in drying concrete is not equal to volume of water evaporated. The change in volume of unrestrained cement paste during hydration is approximately equal to loss of water layer of one molecule thick from the surface of all gel particles. Though it is a multidimensional contraction, the drying shrinkage of cementitious materials is normally measured in the largest dimension of the body (Malathy and Rao 2002).

The selected method to evaluate the RSFRM shrinkage was based on the American standard ASTM C 151. Mortar bars of 25 mm × 25 mm × 250 mm with inserted stainless steel studs partially embedded coaxial with the bar on each top were used to measure the drying shrinkage. This method also requires a measuring device composed by a steel frame containing a dial gauge and also a reference bar of stainless steel (Figure 5.48).

a) b) c)

Figure 5.48 RSFRM shrinkage test: a) Measurement device; b) Reference bar; c) Used specimens

The RSFRM bar specimens 48 hours after casting were demoulded and were immediately measured with one of the faces positioned to the operator, annotating the value provided by the comparator. Afterwards, by rotating the specimens the values for all the other faces were registered. Soon after measuring the initial length, the specimens were maintained in an environment under controlled temperature and moisture. This process was repeated

during 25 days after demoulding to allow for registration of mortars shrinkage over time. Before each measurement, the reference bar was also tested always in the same position. The continuously measurement of this reference bar permits to take into account possible maladjustment of the inserted studs into steel support and even of the measuring equipment (entering directly to the shrinkage calculation). The values of drying shrinkage over time are presented on Figure 5.49.

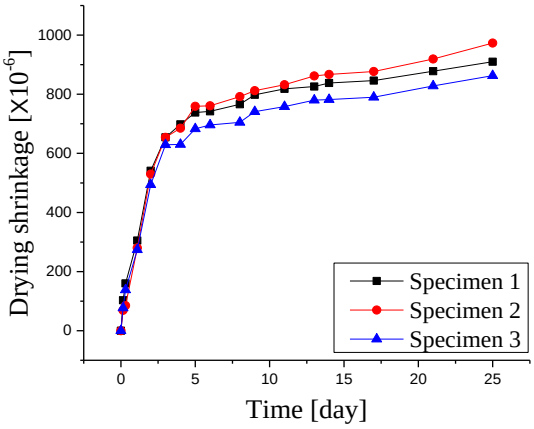

Figure 5.49 Specimens shrinkage over time

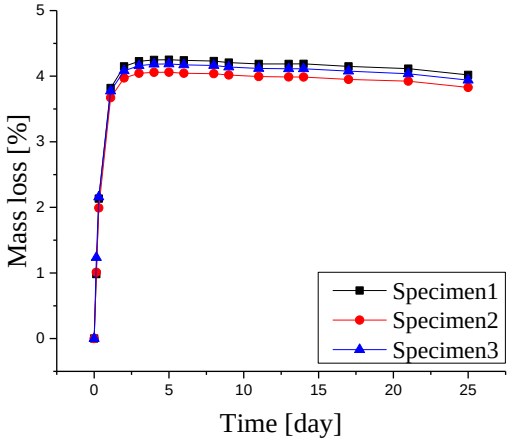

Figure 5.50 Mass loss of specimens over time

Analysing the curves presented in Figure 5.49, it was verified that the bigger part of drying shrinkage occurred on early ages (4 days), which was expectable once that drying shrinkage is intimately connected to moisture loss for the external environment (Carrajola 2006, Ribeiro *et al*. 2006, Lange *et al*. 2005) and it was on the early ages that a higher loss of water occurred.

In parallel to the RSFRM shrinkage test, mass loss over time for each RSFRM specimens used in the shrinkage tests was also determined considering drying shrinkage is intimately related to water loss to the external surrounding environment. Before each reading of length, the specimens were weighted on balance with precision of 0.001 g, placed in the same room where the shrinkage measurement was performed. Figure 5.50 presents the obtained mass loss results over time of all specimens. As it was acceptable, a higher mass loss on early ages (2 days) for all of the specimens was observed.

5.5 Conclusions

In the present chapter experimental work and numerical simulations were performed to characterise the mechanical properties and the durability performance of the developed Recycled Steel Fibre Reinforced Mortar (RSFRM). On the basis of the results obtained, the following concluding remarks can be made:

- The increase of RSF dosage in the developed cementitious composite leads to the decrease of the UPV due to presence of the rubber particles in RSF and development of voids.
- Flexural test results presented in this chapter showed that the increase of the fibre content leads to the increase of the maximum flexural stress. Furthermore, the flexural strength of RSFRM specimens is almost constant and of the same order of the flexural tensile strength up to the ultimate crack width recorded in the executed tests (2.5 mm). On the other hand it was verified that, taking out rubber particles from RSF, it provided an increase of 53% and 12% in terms of σ_{cr} and $\sigma_{\max}$, respectively;
- Based on the results obtained from direct tensile tests, a higher average tensile strength for RDTT specimens (thickness = 21 mm) compared to DBDTT specimens (thickness = 10 mm) was obtained. On the other hand, higher values of tensile strength and fracture energy mode I obtained from simulation of the flexural tests compared to the values obtained from simulation of the direct tensile tests was justified on the basis of different fibre pull-out mechanisms in direct tensile and bending tests and also effect of specimen's thickness;
- The shear behaviour of the RSFRM was investigated by Iosipescu shear test method. It was verified that after reaching the crack shear strength, by increasing the load, an obvious nonlinear stage up to the peak load, followed by a relatively smooth softening response with high ductility behaviour is observable. The capability of a FEM-based computer program to predict the behaviour of this type of structures up to its failure was studied. The shear crack softening diagram available in the multi-directional fixed smeared crack model implemented in the FEMIX computer program, allowed to simulate the shear behaviour of the

Iosipescu specimen. After has been demonstrated that this FEM-based computer program is capable of predicting with high accuracy the shear behaviour of the tested specimens, an extensive parametric study is carried out for assessing the influence of shear retention factor, fracture energy mode II, crack shear strength, tensile strength and fracture energy mode I on shear stress-sliding response of RSFRM. It was concluded that: i) from 0.05 mm sliding (that corresponds to the formation of first shear crack at the notched plane) up to sliding of about 4.43 mm, the shear stress capacity of the specimens slightly increases with the increase of the value of shear retention factor, ii) the decrease of the fracture energy mode II leads to the increase of the slope of the first softening zone, iii) the increase of the values of tensile strength and crack shear strength leads to the increase of the shear strength. For the values of G_f^I between 1.0 to 6.0 N/mm, shear strength significantly increases with the increase of G_f^I. Furthermore, the advantage of RSFRM versus mortar was also studied and it was verified that the RSFRM specimen failed at a 7.3 times higher shear stress than of the plain cementitious material (PCM) specimen;

- Based on the results obtained from durability tests the following conclusion remarks were made: i) a higher average non-steady state chloride migration coefficient and air permeability coefficient was obtained for RSFRM compared to SFRSCC, ii) addition of RSF to cementitious composite significantly increases its open porosity due to air attraction on the surface of fibres containing rubber crumb on their surface. On the other hand, relatively higher value of coefficient of water absorption by capillarity was obtained for the RSFRM compared to the value that was already obtained for SFRSCC, which confirms that the developed RSFRM is not as capable as SFRSCC to prevent penetration of deteriorating agents, iii) from drying shrinkage tests it was verified that the bigger part of drying shrinkage occurred on early ages (4 days) and it was on the early ages that a higher loss of water occurs.

Chapter **6**

6 Assessment of the potentiality of RSFRM for the shear strengthening of RC beams

6.1 Introductions

Recently, a good potentiality of using thin plates of Strain Hardening Cementitious Composites (SHCC) with Carbon Fibre Reinforced Polymer (CFRP) laminates to increase the flexural capacity of Reinforced Concrete (RC) beams and also the energy dissipation of beam-column joints has been reported (Baghi *et al*. 2016, Esmaeeli and Barros 2015, Baghi 2015). On the other hand, an extensive experimental program and analytical study have been performed by Baghi *et al*. (2016) to assess the influence of the Hybrid Composite Plates (HCP) on the shear strengthening and repairing of RC beams.

In this chapter, the assessment of the thin panels of Recycled Steel Fibre Reinforced Mortar (RSFRM) for the shear strengthening of RC beams is investigated. To examine the efficiency of RSFRM panels (developed in the previous chapter) as a shear strengthening solution for RC beams, these panels were applied in the lateral faces of RC beams of "I" cross section shape (Figure 6.1) deficiently reinforced in shear, and flexurally reinforced with a relatively high reinforcement ratio of longitudinal steel bars.

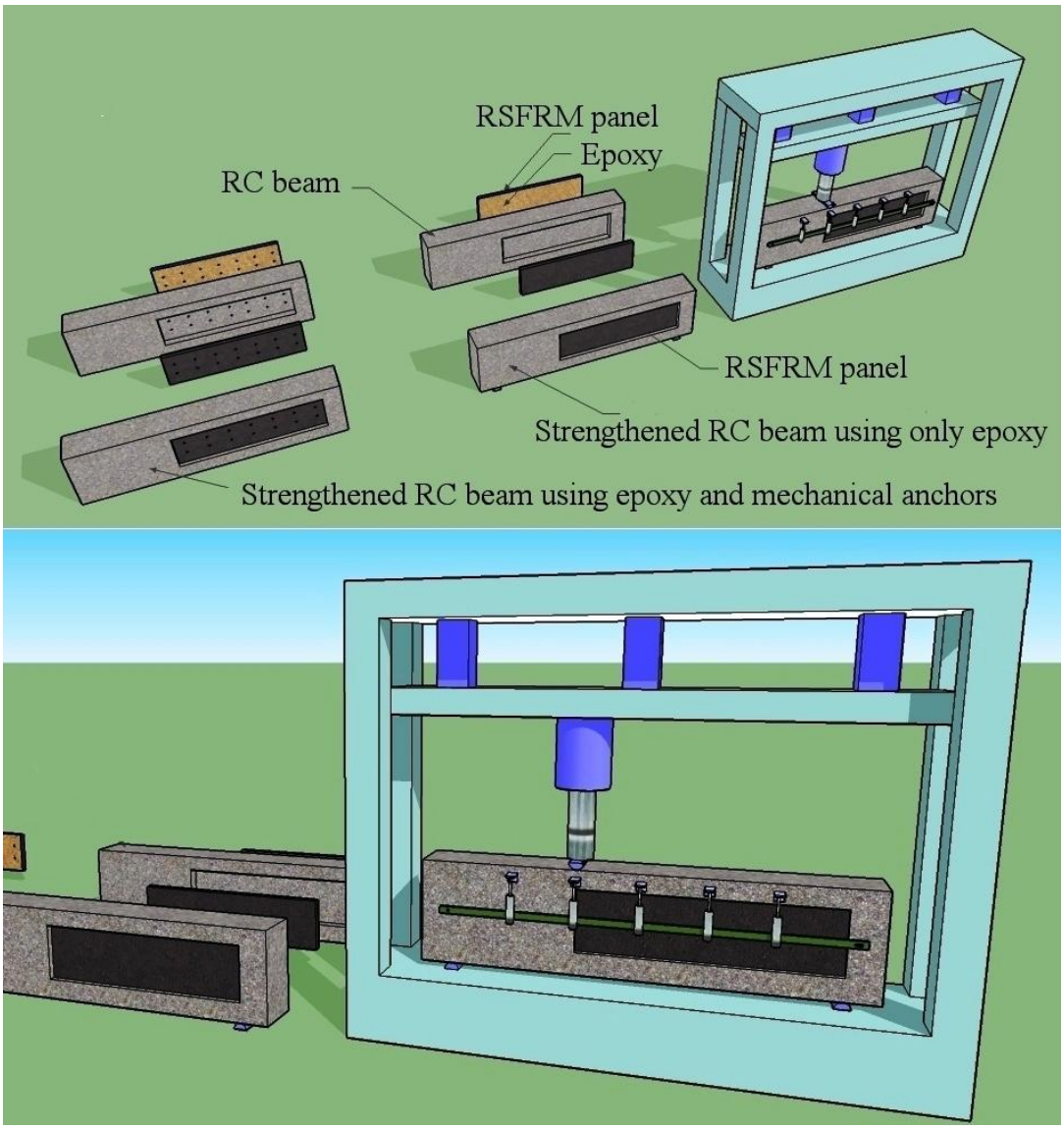

Figure 6.1 Overview of the assessment of the RSFRM for the shear strengthening of RC beams.

By adopting the analytical formulation developed by Baghi *et al*. (2016) to predict the shear capacity of RC beams strengthened with HCP, the applicability of this formulation for estimating the contribution of RSFRM panels for the shear resistance of RC beams is assessed. Also, a new shear design approach was developed combining the SMCFT with the formulation of RILEM TC 162-TDF. For the analysis of strengthened beams failing in shear, material nonlinear simulations are carried out using FEMIX finite element based computer program.

6.2 Experimental program

6.2.1 Beams and test setup

The beams of this experimental program had a length of 1250 mm, and 1040 mm clear span and were composed of rectangular and I-shape cross sections (see Figure 6.2). The longitudinal steel reinforcement consisted of $2\phi 20$ laid at the bottom, and $2\phi 10$ at the top as tensile and compression reinforcement, respectively, giving to the beam's cross section an effective depth (d) of 260 mm. To prevent premature anchorage failure and sliding, the steel bars were anchored at the section of the supports with 90° hooks. In order to promote the occurrence of shear failure in only one of the shear spans, a three point bending test setup with different length of the shear spans was selected with a shear span to effective depth ratio (a/d) of 2.65 (Figure 6.2). The monitored shear span had an I-shape cross section with the length of 690 mm and without any transverse reinforcement in an attempt of assuring shear failure mode for this span. The other span had a rectangular cross section and, to avoid shear failure occurrence in this span, a relatively high percentage of steel stirrups ($\phi 10$@100 mm) was applied. Figure 6.2 shows the test setup and position of the five Linear Voltage Displacement Transducers (LVDTs) used to measure the beam's deflection.

RSFRM panels with the dimensions of 686 mm × 186 mm × 23 mm were produced (see figures 6.3a,b), and they were bounded in the lateral faces of the beams by using the two following strategies: bonded to the concrete substrate of the beam´s lateral faces by

applying exclusively epoxy adhesive (SB-E series); besides epoxy adhesive, mechanical anchors were applied in an attempt of increasing the shear strengthening effectiveness provided by the RSFRM panels due to the extra concrete confinement promoted by these anchors (SB-EM series). Control beams without any type of shear reinforcement and strengthening (SB-C series) were also tested for comparison purpose.

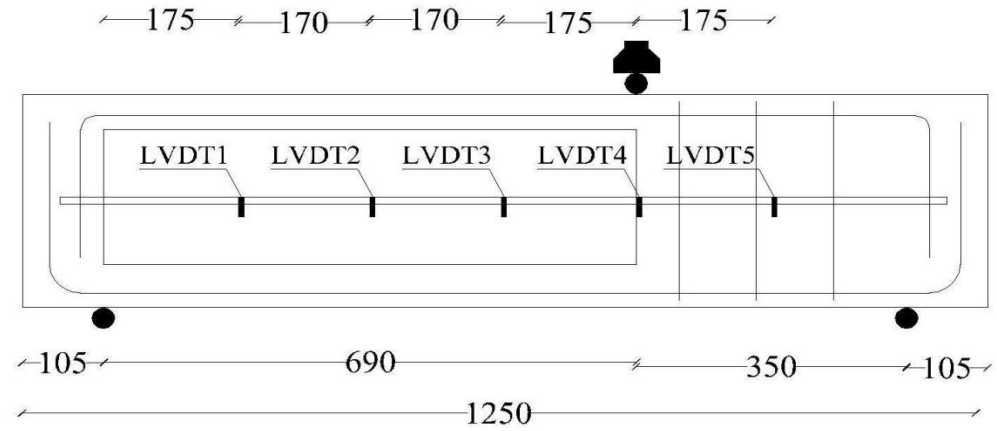

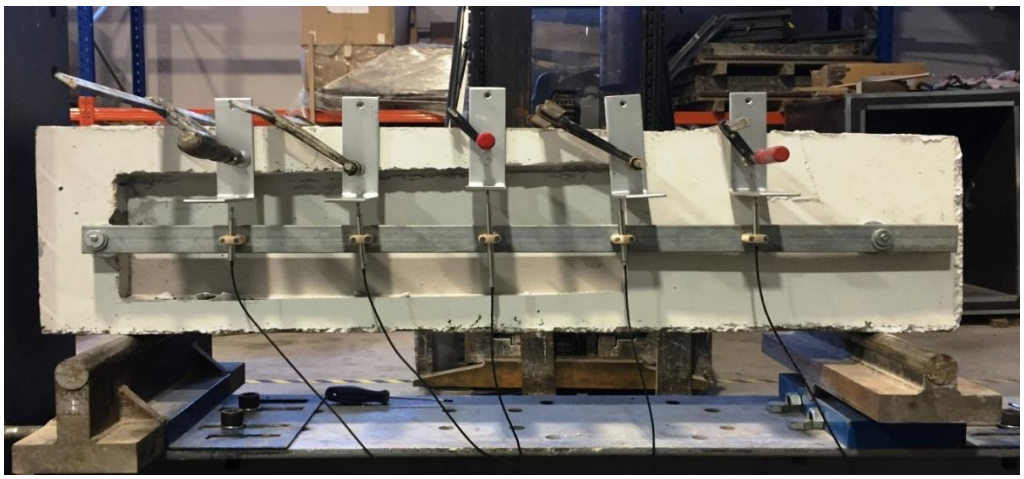

Figure 6.2 Beam's configuration, test setup and position of the LVDTs (dimensions in mm)

To apply the RSFRM panels to the lateral faces of the beams, firstly the surfaces of the beams were cleaned by compressed air and then an epoxy adhesive (S&P220) layer of a thickness of about 1 mm was homogenously applied on the surfaces of the concrete beam to be in contact with the panels, as well as on the interior face of the panels (Figure 6.3d). Mechanical clamps were used to maintain the panels pressed against the lateral surfaces

of the beam up to the time that the epoxy resin developed sufficient bond strength to allow their removable.

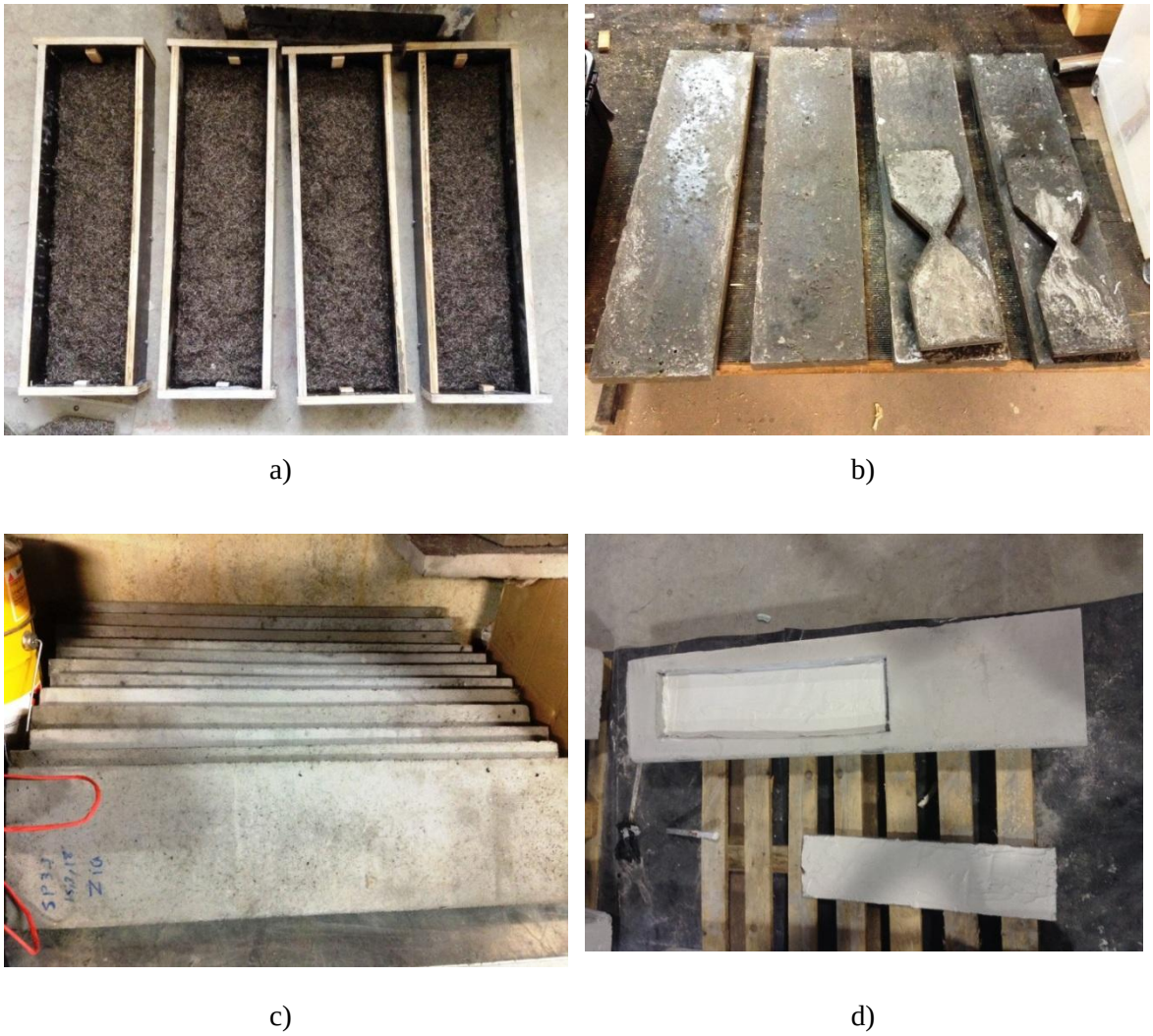

a) b)

c) d)

Figure 6.3 a) RSF placed in the moulds; b) RSFRM panels after demoulding; c) RSFRM panels before bonding to the beams; d) Application of epoxy adhesive on the surfaces of the concrete beams and panels

Two weeks after applying the RSFRM panels to the lateral faces of the beams, ten holes were drilled through both panels and web of the SB-EM beams with a diameter of 10 mm for the installation of mechanical anchors, as illustrated in Figure 6.4. Then, The RSFRM panels were confined to the concrete substrate of these beams with ten mechanical fasteners composed of bolts and nuts, by applying a torque of 20 N.m in the nuts on both sides of the beams.

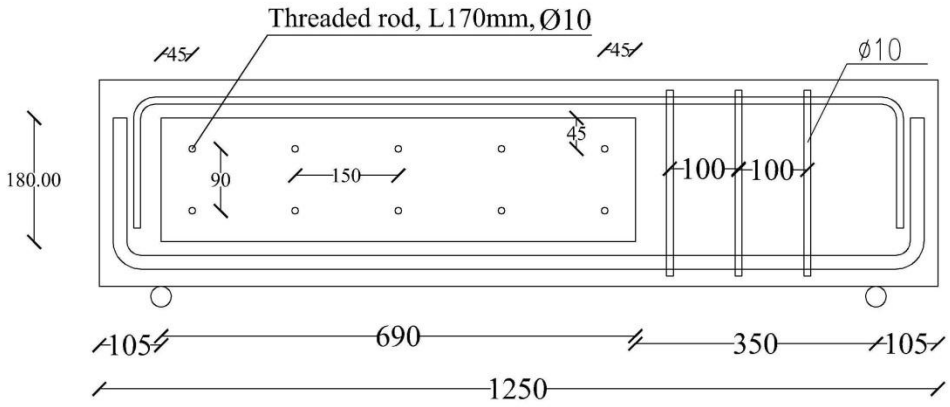

Figure 6.4 Position of mechanical anchors (dimension in mm)

Figures 6.5, 6.6 and 6.7 show the geometry and reinforcement details of the three series of beams produced for this experimental program, as well as the loading and supporting conditions. The values of tensile properties of the steel bars were the same mentioned in section 4.2.2.

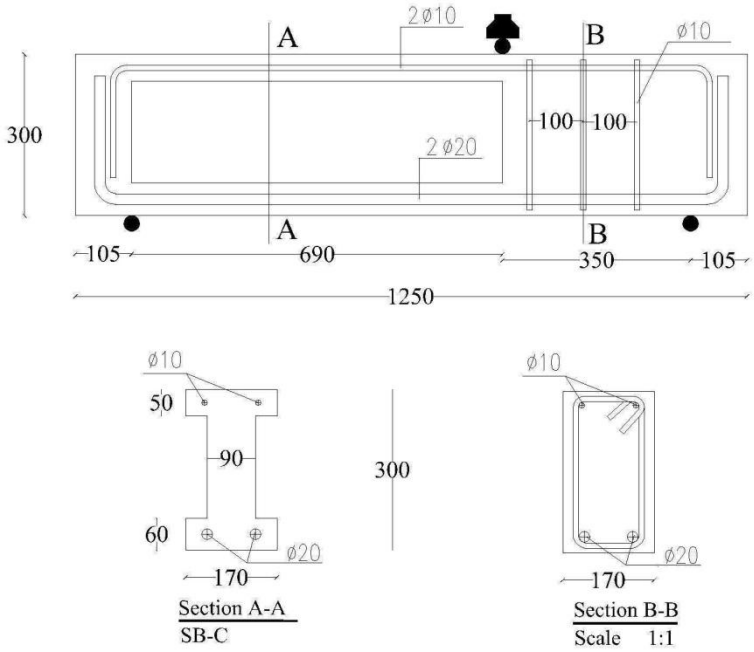

Figure 6.5 Geometry of the SB-C beams (dimensions in mm)

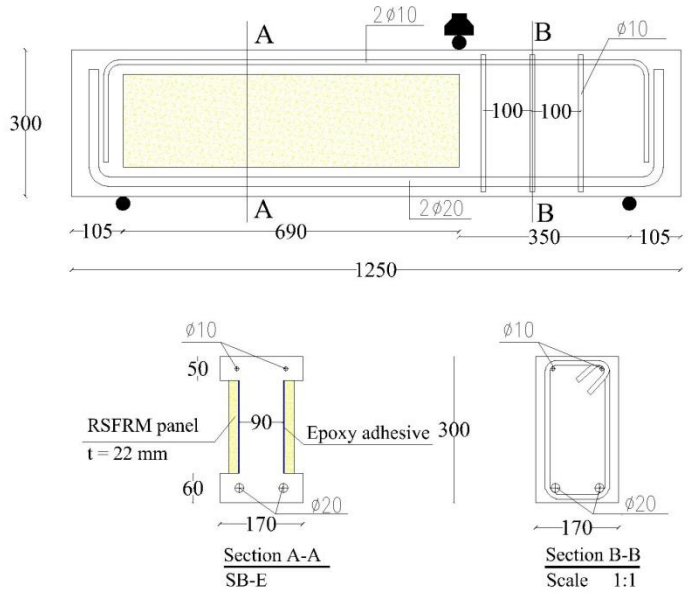

Figure 6.6 Geometry of the SB-E beams (dimensions in mm)

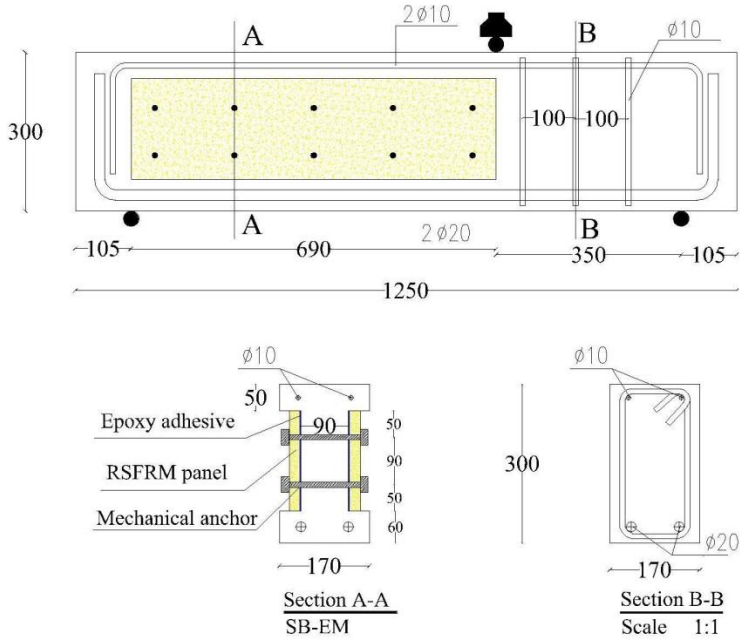

Figure 6.7 Geometry of the SB-EM beams (dimensions in mm)

In the first experimental program three beams (one beam from each series) were tested. Since the beams SB-E1 and SB-EM1 unexpectedly failed at the support section before shear failure occurrence of the beam, in the second experimental program, a confinement system by using steel plates was applied to the beam's support sections (Figure 6.8). The labels SB-C2, SB-E2 and SB-EM2 identify RC beams tested in the second experimental program. The details of the plates used in confinement system are provided in Annex C. In the third experimental program, the effectiveness of this technique was explored for shear repairing of pre-damaged RC beams (PSB-E). For this purpose, firstly the control beam in the first experimental program (SB-E1) was loaded up to failure load and then fully unloaded. Then, the RSFRM panels were bonded to the damaged SB-C1 beam using epoxy adhesive, and the beam was tested again.

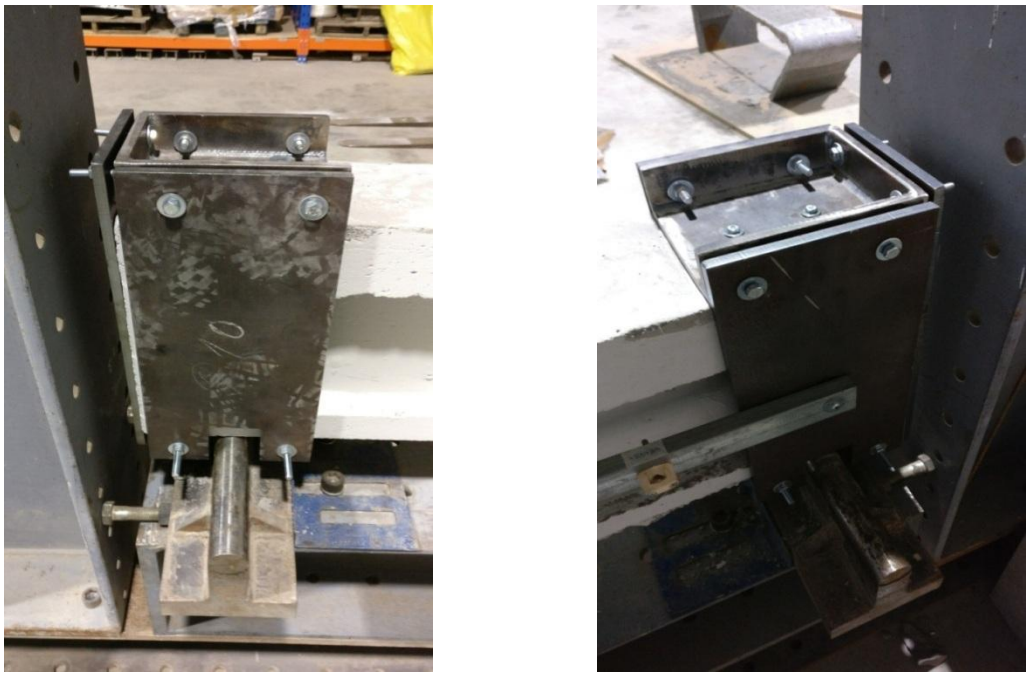

Figure 6.8 Confinement system applied to the support sections

6.2.2 Experimental results

The relationship between the applied load and the mid span deflection (LVDT3) of the tested series of beams is represented in Figure 6.9 and the crack patterns at failure of the

tested beams are illustrated in Figure 6.10. As it can be seen in Figure 6.10, only SB-C1, SB-C2 and SB-EM2 beams were failed in shear at monitored shear span.

Due to deficient execution of the anchorage length of the longitudinal reinforcement in the SB-E1 and SB-EM1 beams, these beams unexpectedly failed at both support section and shear span (Figure 6.10b,c). Thus, it was not possible to accurately estimate the real shear efficiency of the strengthening technique for these beams. In any case, all the strengthened and repaired beams presented higher load carrying capacity than the control beams (SB-C1 and SB-C2).

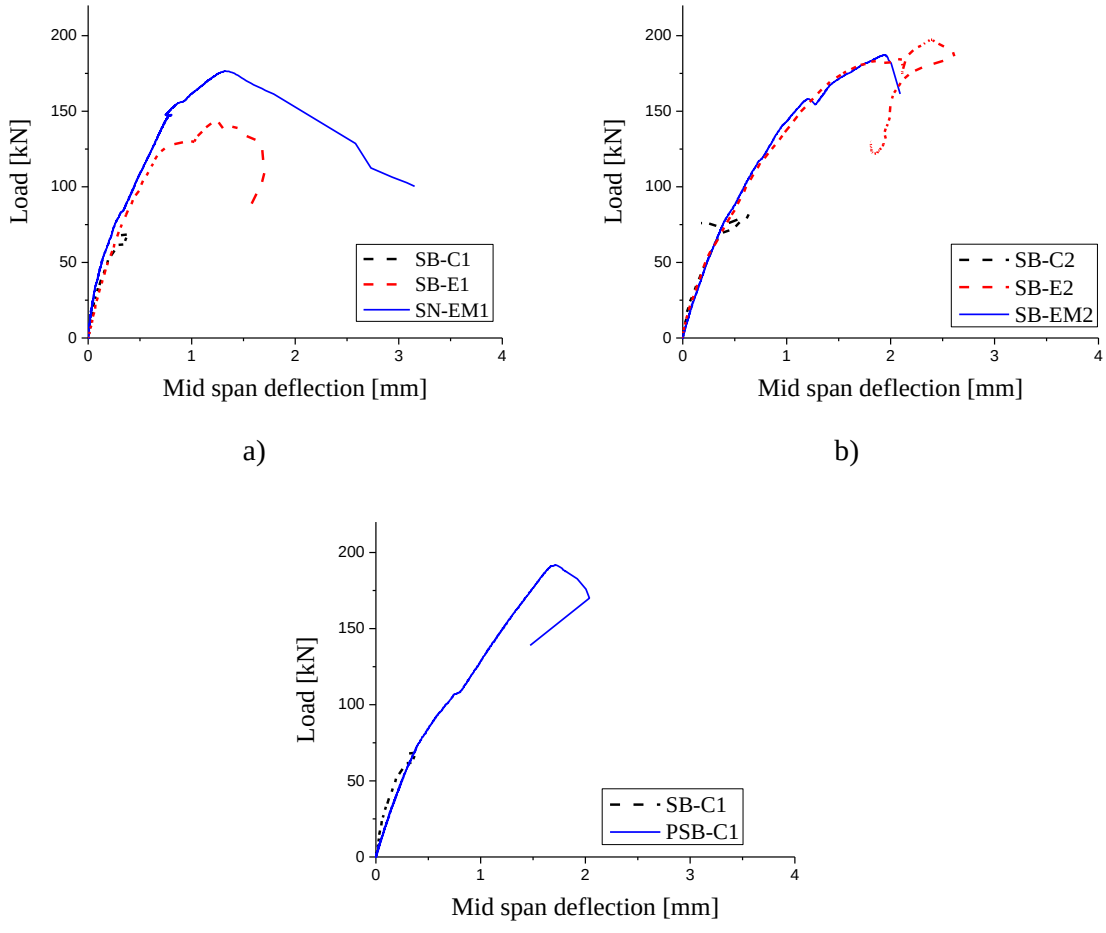

Figure 6.9 Load – deflection relationship at the loaded section for the tested beams in the: a) First experimental program; b) Second experimental program; c) Third experimental program with pre-damaged beam

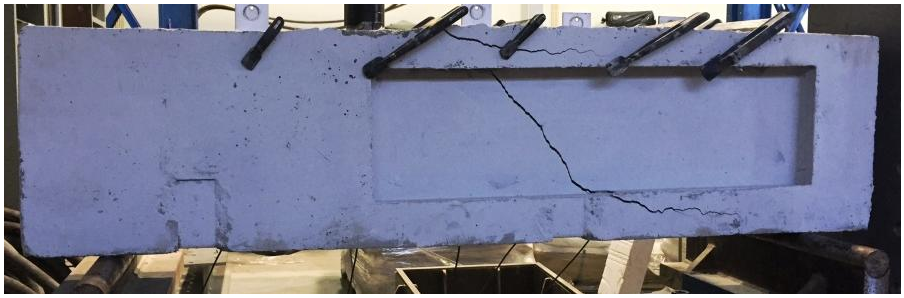

a)

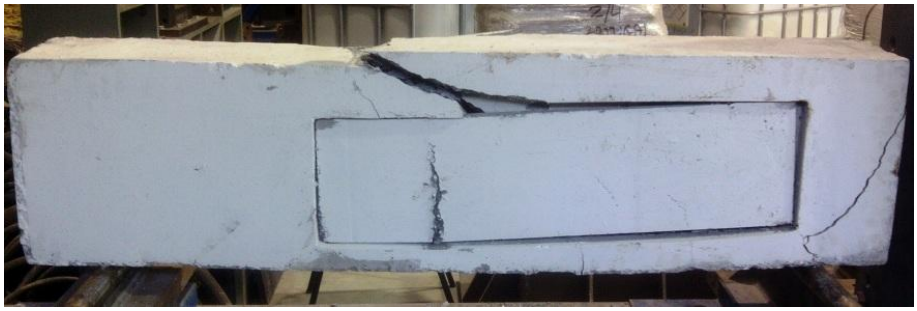

b)

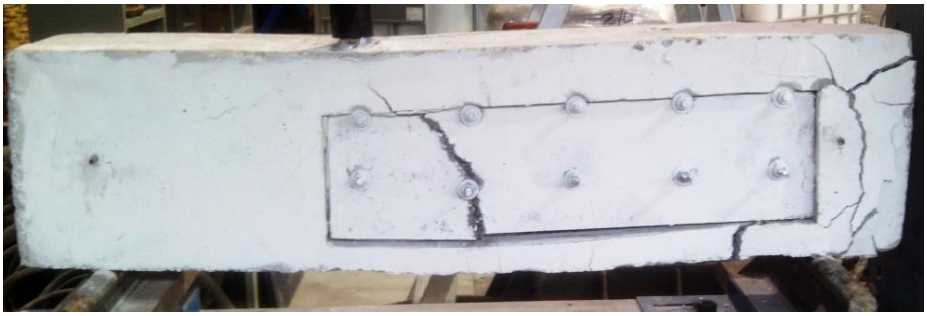

c)

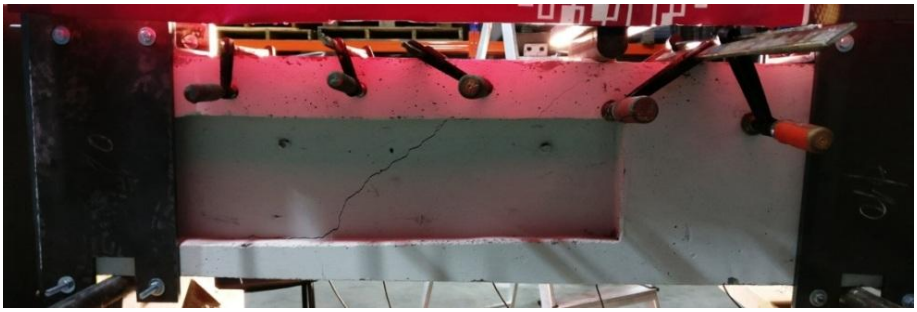

d)

e)

f)

g)

Figure 6.10 Crack pattern at failure of the tested beams: a) SB-C1, b) SB-E1, c) SB-EM1, d) SB-C2, e) SB-E2, f) SB-EM2, g) PSB-E1

From the obtained results the maximum load capacity of the tested beams (F_{max}) and their corresponding deflection (Δ_u) are indicated in Table 6.1. In Table 6.1, F_{max}^{SB-Ci} and Δ_u^{SB-Ci} are the maximum load capacity and corresponding mid span deflection of the SB-C

beams. The values of the $\frac{F_{max}}{F_{max}^{SB-Ci}}$ ratio are also presented in Table 6.1, where F_{max} is the maximum load capacity of the beam strengthened with RSFRM panel. The beam SB-E2 failed at a load level higher than the maximum load registered in SB-EM2 beam (see Table 6.1). The SB-E2 beam failed due to concrete spalling at the loading section without shear failure at the shear span (Figure. 6.10e), while SB-EM2 developed a shear failure at the shear span (Figure. 6.10f). This means that the use of mechanical anchors has negligible effect in the adopted shear strengthening technique in this series of beams. Also, this negligible effect will be confirmed by the numerical simulations presented in next section. However, further experimental program with more tested beams is still needed to be performed for addressing various issues related to the effectiveness of the mechanical anchors on the adopted shear strengthening technique.

Table 6.1 Relevant results in terms of maximum load capacity and corresponding mid span deflection

Beam designation	**Mid span deflection Δ_u [mm]**	F_{max} **[kN]**	$\frac{\Delta_u}{\Delta_u^{SB-Ci}}$	$\frac{F_{max}}{F_{max}^{SB-Ci}}$
SB-C1	0.36	69.10	-	-
SB-E1	1.22	143.18	3.40	2.07
SB-EM1	1.32	176.50	3.66	2.55
SB-C2	0.63	82.54	-	-
SB-E2	2.38	197.34	3.77	2.39
SB-EM2	1.93	187.50	3.06	2.27
PSB-E1	1.70	191.75	4.72	2.77

From the results presented in Table 6.1, the maximum mid span deflection, at peak load, of the SB-E1 and SB-EM1 beams was 3.40 and 3.66 times higher than the corresponding deflection of the SB-C1 beam, respectively. The maximum load capacity of the SB-E1 and SB-EM1 beams was 2.07 and 2.55 times higher than the maximum load capacity of the control beam (SB-C1 beam). On the other hand, the maximum load capacity of the

SB-E2 and SB-EM2 beams was 2.39 and 2.27 times higher than the maximum load capacity of the control beam tested in the experimental program (SB-C2 beam). Furthermore, the obtained results for PSB-E1 beam (see Table 6.1) reveal that, this beam failed at 2.77 and 2.32 times higher than the maximum load carrying capacity of the BS-C1 and BS-C2 beams, respectively, which reveals the shear strengthening effectiveness of the RSFRM panels for the overall behaviour of this type of beams.

6.3 Numerical simulations and discussion

For a better understanding of the effectiveness of the shear strengthening technique with RSFRM panels, material nonlinear simulations were carried out using a computer program based on the finite element method (FEMIX V4.0). Figure 6.11 represents the finite element mesh adopted for the simulation of the BS-C beams.

Taking advantage of the symmetry of the beams, in order to reduce the computational time of the numerical simulations, only half of the full size beam was modelled. Serendipity 8 nodes solid elements with 2×2×2 Gauss-Legendre integration scheme were used for the simulation of both the concrete and RSFRM panel (three degrees-of-freedom per node). The steel stirrups and longitudinal steel bars were modelled with 3D embedded cables of 2 nodes (one degree-of freedom per node), by using a 2 Gauss-Legendre integration scheme, and perfect bond to the surrounding medium was assumed. The tested beams showed that no slip occurred between concrete substrate and RSFRM panels, so perfect bond between substrate and RSFRM panel was assumed.

The three dimensional multi-directional fixed smeared crack model, briefly described in section 4.2.3, was used in the numerical simulations of the beams. To simulate the crack initiation and the fracture mode I propagation of plain concrete and RSFRM, the tri-linear tension softening diagram represented in Figure 3.18 was used.

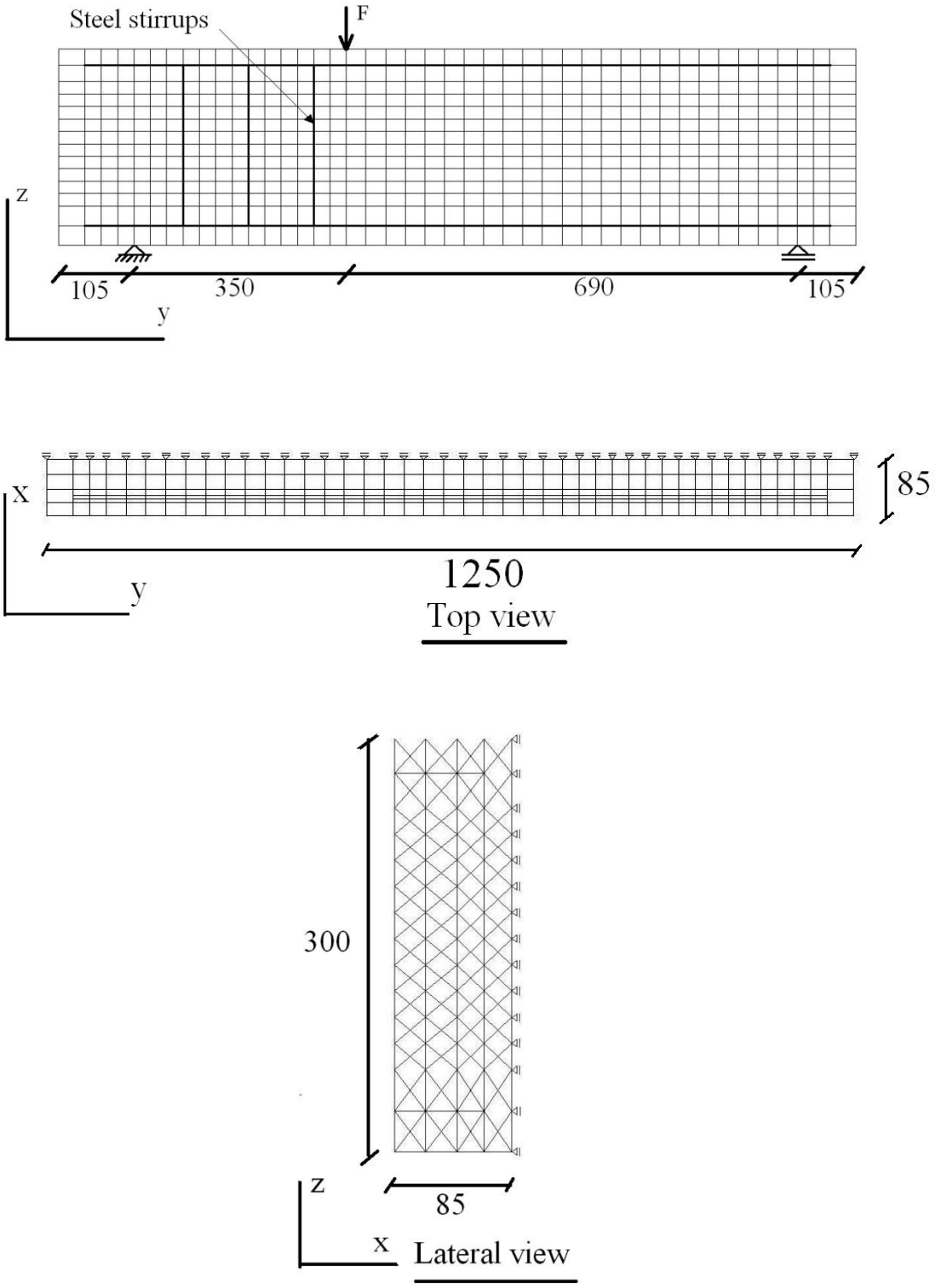

Figure 6.11 Geometry, mesh and support condition of the beam SB-C (dimensions in mm)

The bolts in the SB-EM2 beam were modelled with 3D two-node truss elements, and torque was simulated by applying a temperature decrease of -25.5°C in these elements, evaluated according to the following equations:

$$F = \frac{\tau}{r} \tag{6.1}$$

$$\sigma = \frac{F}{A} \tag{6.2}$$

$$\varepsilon = \frac{\sigma}{E} = T.\alpha \tag{6.3}$$

where τ is the applied torque (N.m), and r, A, and E are the radius, cross sectional area, and elasticity modulus of the bolt (5 mm, 78.5 mm^2, and 200 GPa), respectively. In these equations T and α are the temperature variation and the coefficient of thermal expansion, respectively. The same strategy was used for modelling the confinement system of the support section.

By simulating the tested beams in the second experimental program and performing inverse analysis, the values defining the crack shear softening diagram of the adopted multi-directional fixed smeared crack constitutive model were derived.

Table 6.2 includes the values of the model parameters adopted in the numerical simulations of the tested beams. The values defining the shear softening diagram of plain concrete were determined by fitting as best as possible the force-deflection relationship registered in the tested control beam (SB-C2), while for the RSFRM, they correspond to the values obtained from inverse analysis on the results obtained by Iosipescu shear tests (as it was explained in Chapter 5).

Table 6.2 Values of the parameters of the constitutive model for the concrete

Property	**Value**
Poisson's ratio (ν_c)	0.19
Initial Young's Strength (E_c)	22000 N/mm^2
Compressive strength (f_c)	25 N/mm^2
Trilinear tension-softening diagram	f_{ct}=1.8 N/mm^2 α_1 =0.30, α_2 =0.3, ξ_1=0.004, ξ_2 =0.1; G_f^I =0.08
Crack shear stress-crack shear strain softening diagram	β = 0.6, $\tau_{t,p}^{cr}$ = 1.0 MPa, $G_{f,s}$ = 0.1 N/mm
Crack band width, l_b	Cubic root of the volume of Gauss integration point
Threshold angle (Sena-Cruz 2004)	α_{th} = 30°
Maximum number of cracks per integration point (Sena-Cruz 2004)	2

Table 6.3 Values of the parameters of the constitutive model for the RSFRM

Property	**Value**
Poisson's ratio (ν_c)	0.19
Initial Young's Strength (E_c)	19640 N/mm^2
Compressive strength (f_c)	44.370 N/mm^2
Trilinear tension-softening diagram	f_{ct}=3.3 N/mm^2 α_1 =0.85, α_2 =0.61, ξ_1=0.005, ξ_2 =0.01; G_f^I =6.0
Crack shear stress-crack shear strain softening diagram	β = 0.6, $\tau_{t,p}^{cr}$ = 4.3 MPa, $G_{f,s}$ = 1.9 N/mm
Crack band width, l_b	Cubic root of the volume of Gauss integration point
Threshold angle (Sena-Cruz 2004)	α_{th} = 30°
Maximum number of cracks per integration point (Sena-Cruz 2004)	2

The experimental and the numerical relationships between the applied load and the mid span deflection for the tested beams are compared in Figure 6.12, where it shows that the numerical model is able to capture with good accuracy the deformational response of the

beams. It should be noted that criterion adopted for ending the numerical simulations was lack of convergence.

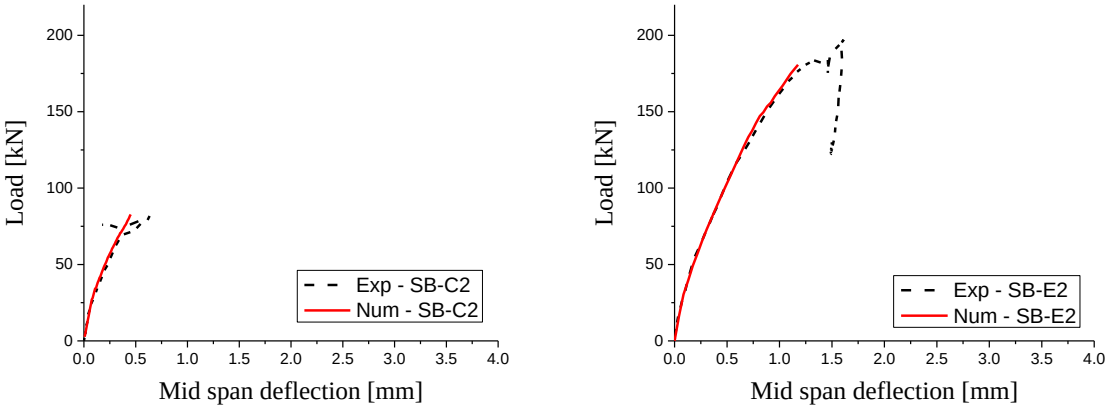

a) b)

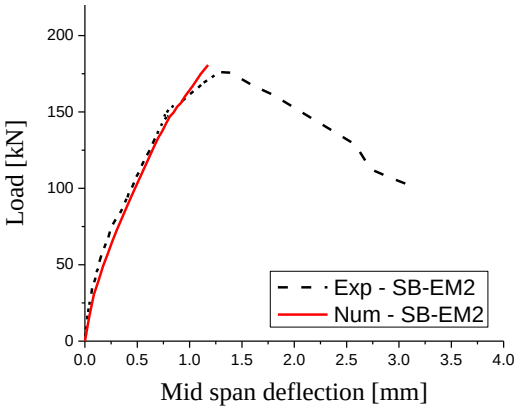

c)

Figure 6.12 Comparison of the experimental and numerical load *vs*. mid span deflection relationships: a) SB-C2, b) SB-E2 and c) SB-EM2

6.4 Analytical study

In this section the applicability of the analytical formulation developed by Baghi *et al*. (2016) based on the Simplified Modified Compression Field Theory (SMCFT) is

evaluated for predicting the contribution of RSFRM panels for the shear resistance of RC beams. In the following section a brief description of the model is provided, since the detailed exposition can be found elsewhere (Baghi *et al*. 2016). Furthermore, to predict the enhanced shear capacity of RC beams strengthened with RSFRM panels, a new shear design approach was developed combining the SMCFT with the formulation of RILEM TC 162-TDF. By using this approach, parametric studies were carried out to assess the influence of relevant parameters on the shear strengthening effectiveness of this technique.

6.4.1 Assessment of the applicability of analytical approach proposed by Baghi *et al*. (2016) for predicting the shear capacity of RC beams strengthened with RSFRM panels.

The analytical approach adopted by Baghi *et al*. (2016) is supported on the SMCFT developed by Bentz *et al*. (2006) by adapting it to the proposed strengthening technique. According to this approach, the shear capacity of a RC beam shear strengthened with RSFRM panels (v) is obtained from the following equation:

$$v = v_c + v_s + v_{panel} \tag{6.4}$$

where v_c, v_s and v_{panel} are the shear strength due to concrete, steel stirrups, and RSFRM panels, respectively. Since the monitored shear span did not include steel stirrups, in the equation (6.4), $v_s = 0$.

In the SMCFT model suggested by Bentz *et al*. (2006), the shear strength of a section is a function of two parameters: the tensile stress factor in the cracked concrete (β) (equation 6.5) and the inclination of the diagonal compressive stress in the web of the section (θ) (equation 6.6).

$$\beta = \frac{0.4}{1+1500\varepsilon_x} \cdot \frac{1300}{1000+s_{xe}} \tag{6.5}$$

$$\theta = (29 + 700\varepsilon_x).(0.88 + \frac{s_{xe}}{2500}) \leq 75^{\circ} \tag{6.6}$$

In the equations (6.5) and (6.6), ε_x and s_{xe} are the longitudinal straining of the web and crack spacing parameter, respectively, and can be determined by equations (6.7) and (6.8), respectively:

$$\varepsilon_x = \frac{\nu.\cot\theta - \nu_c / \cot\theta}{E_s \rho_{sx}} \tag{6.7}$$

$$s_{xe} = \frac{35S_x}{a_g + 16} \geq 0.85S_x \tag{6.8}$$

where S_x, a_g, E_s and ρ_{sx} are vertical distance between longitudinal reinforcement (see Figure 6.13), maximum concrete aggregate size, modulus of elasticity of longitudinal reinforcement and longitudinal steel reinforcement ratio. In equation (6.7), the longitudinal steel reinforcement ratio is determined by the following equation:

$$\rho_{sx} = \frac{A_{sx}}{A_c} \tag{6.9}$$

where, A_c is the area of the concrete cross section.

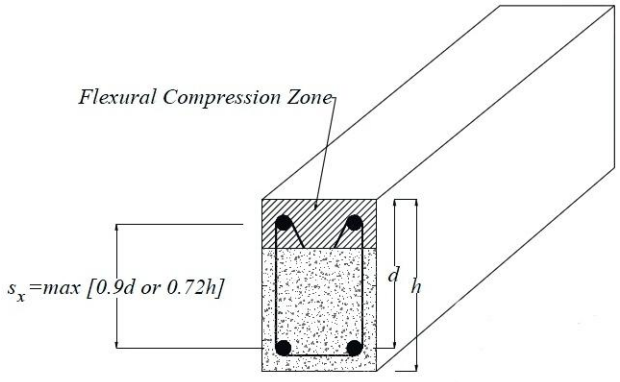

Figure 6.13 Concept of S_x (Collins and Mitchell 1991, Kuchma *et al*. 2008)

In a rectangular non-cracked section the maximum shear stress in the cross section can be determined by equation (6.10) (Blanksvärd 2009, Blanksvärd 2007):

$$\tau_{\max} = \frac{VQ}{It} = \frac{3V}{2A} \tag{6.10}$$

where V is the total shear force, Q and I are the first and second moment of area, respectively, and t is the thickness of the cross section of area A. Shear resistance of the RSFRM panel by assuming perfect bond between RSFRM panel and concrete substrate can be expressed as:

$$V_{panel} = 2\left(\frac{2}{3} t_{panel} h_{panel} \tau_{avg}\right) \tag{6.11}$$

where t_{panel} and h_{panel} are the thickness and height of the RSFRM panel, respectively. In equation (6.11), τ_{avg} is the crack shear stress, which is assumed as the value adopted in the inverse analysis with the data obtained from Iosipescu tests (4.3 MPa). Note that the factor 2 originates from that the RSFRM panels are applied on both sides of the beam (Baghi *et al*. 2016). The shear strength of a RC beam strengthened with RSFRM panel can be determined by following equation:

$$v = v_c + v_{panel} = \beta\sqrt{f_c'} + \frac{4 t_{panel} h_{panel} \tau_{avg}}{3(b_w + 2t_{panel})d} \tag{6.12}$$

where b_w and f_c' are the width of the beam's cross section and concrete compressive strength, respectively. The solution procedure to calculate the shear strength of the concrete beams, according to the SMCFT adapted to the strengthening technique by RSFRM panel (Figure 6.14) starts by assuming the initial value of 1.0×10^{-3} for ε_x (Bentz *et al*. 2006). Considering the maximum aggregate size (a_g) was 12 mm in all beams and using for the s_{xe} the value of 281 mm (equation 6.8), the values of β and θ are

estimated equal to 0.1623 (equation 6.5) and 35.73 degrees (equation 6.6), respectively. Then, the ε_x will be equal to 3.869×10^{-4} (equation 6.7).

Since 3.869×10^{-4} does not equal the assumed value of 1.0×10^{-3}, a new estimate of ε_x needs to be made and the calculations should be repeated until convergence is reached ($\left|\varepsilon_x-\varepsilon_x^{est}\right|\le10^{-6}$).

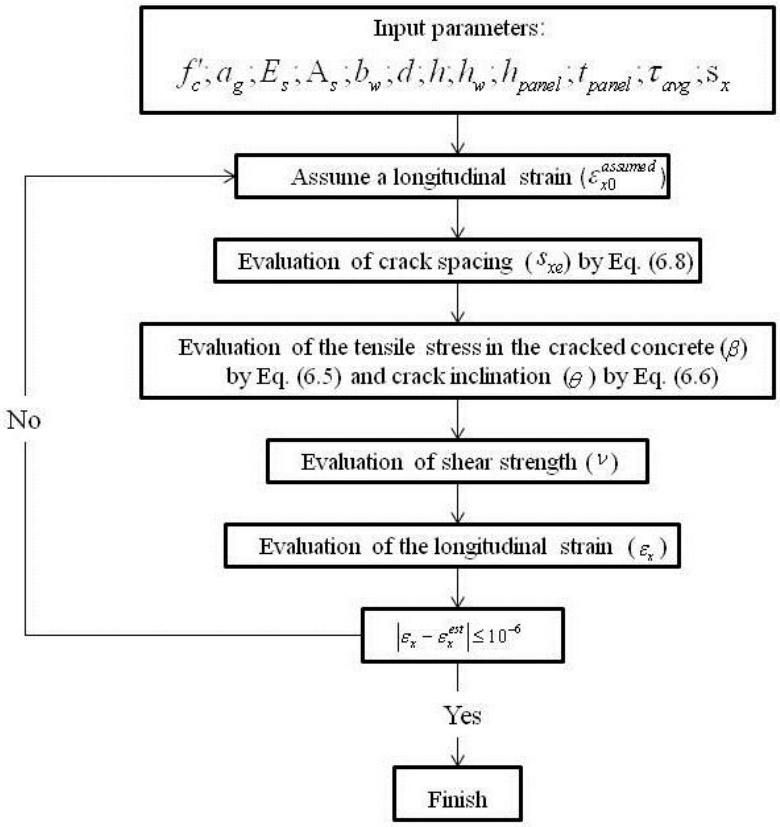

Figure 6.14 Calculation procedure of SMCFT adapted for the strengthening technique with RSFRM panels

Finally, it should be checked that the longitudinal reinforcement can transmit the required stresses across the cracks without exceeding its yield stress. According to Bentz *et al.* (2006), the transmitted stress in the longitudinal reinforcement at cracks (f_{sxcr}) is determined by:

$$f_{sxcr} = \frac{(\nu + \nu_c)\cot\theta}{\rho_x} \tag{6.13}$$

It should be noted that before evaluating the shear strength of the RC beams strengthened with RSFRM panels, compressive strength of the concrete of RC beams (f_c') was derived equal to 19 MPa by performing back analysis with the same calculation procedure on the results of BS-C beams, while the shear strength due to RSFRM panel was neglected.

Table 6.4 includes the results of the tested SB-C1, SB-C2 and SB-EM2 beams, as well as the values predicted according to the analytical formulations. Since the other beams were not failed in shear, these beams are not included in the analytical evaluation. The average ratio between experimental to predicted shear resistance of the BS-EM2 beam was 0.99, which does not guarantee safety predictions for this analytical approach. Hence, in order to have conservative estimates of shear strength for RC beams strengthened with RSFRM panels, it may be more appropriate to propose new analytical approaches based on toughness class of the material used in panels as it will be discussed in the next section.

Table 6.4 Analytical *vs*. experimental results of the strengthened beams with RSFRM panels

Specimen	ε_x **[‰]**	F_{exp} **[kN]**	F_{ana} **[kN]**	f_{sxcr} **[MPa]**	F_{exp} / F_{ana}
BS-C1	0.247	70	83	151	0.84
BS-C2	0.247	83	83	151	1.00
BS-EM2	0.408	188	190	167	0.99

From the results presented in Table 6.4, since the values of f_{sxcr} for all of the beams are less than the yield stress of the longitudinal reinforcement, the longitudinal steel rebars are predicted not to yield at the cracks.

6.4.2 New approach to determine shear capacity of RC beams strengthened with RSFRM panels

To predict the shear capacity of RC beams strengthened with RSFRM panels, a new shear design approach is developed based on combining the SMCFT with the formulation of RILEM TC 162-TDF. In this approach, the same calculation procedure described in Figure 6.14 is followed, while by assuming perfect bond between RSFRM panel and concrete substrate, the shear capacity of the RSFRM panel is determined according to RILEM TC 162-TDF from the following expression:

$$\nu_{panel} = 0.7K \times \tau_{fd} \tag{6.14}$$

where K is a factor related to the size effect that can be calculated according to equation (6.15) and τ_{fd} is the design value of the increase in shear strength due to fibre reinforcement determined from equation (6.16).

$$K = 1 + \sqrt{\frac{200}{h_{panel}}} \leq 2.0 \tag{6.15}$$

$$\tau_{fd} = \frac{0.18}{\gamma} \times f_{R,4k} \tag{6.16}$$

where $f_{R,4k}$ is the characteristic value of the residual flexural tensile strength parameter corresponding to the CMOD equal to 3.5 mm (8.13 MPa).

Adapting the SMCFT to the proposed strengthening technique is performed by adding the formulation of RILEM TC 162-TDF to the simplified MCFT, leading to:

$$\nu = \nu_c + \nu_{panel} = \beta\sqrt{f_c'} + 0.7K \times \tau_{fd} \times \rho_{panel} \tag{6.17}$$

where ν and ν_c are the predicted shear strength of the RC beam strengthened with RSFRM panel and shear strength due to concrete, respectively. The expressions for β

and θ are provided by equations (6.5) and (6.6). In equation (6.17), ρ_{panel} is the RSFRM panel reinforcement ratio that can be determined from equation (6.20).

$$\rho_{panel} = \frac{2t_{panel} \times h_{panel}}{b_w \times d} \tag{6.18}$$

Table 6.5 presents the results of the tested SB-C2 and SB-EM2 beams, as well as the values predicted according to the proposed analytical formulations.

The ratio between experimental to predicted shear resistance for BS-EM2 beam was 1.53, which reveals that proposed analytical approach gives a conservative estimate of shear strength for RC members strengthened with RSFRM panels.

Table 6.5 Proposed analytical and experimental results of the strengthened beams with RSFRM panels

Specimen	F_{exp} **[kN]**	F_{ana} **[kN]**	f_{sxcr} **[MPa]**	F_{exp} / F_{ana}
BS-C2	83	83	151	1.00
BS-EM2	188	123	154	1.53

6.4.2.1 Parametric study

By using the proposed analytical approach for predicting the shear capacity of RC beams strengthened with RSFRM panels, a parametric study was performed to evaluate the following parameters involved in this type of strengthening application on their strengthening effectiveness: strength class of the concrete of the RC beam to be strengthened and $f_{R,4k}$ value of RSFRM. The advantage of using RSFRM panel instead of panel made of Plain Cementitious Material (PCM) is also studied. Furthermore, minimum value of the longitudinal steel reinforcement ratio without yielding of the longitudinal reinforcement was evaluated.

6.4.2.1.1 Influence of strength class of the concrete of the RC beam to be strengthened

The influence of f_c' on the shear capacity of the RC beams strengthened with RSFRM panels is illustrated in Figure 6.15. The values of 5.0, 19.0 and 50.0 MPa were adopted in the proposed analytical model for this parameter. The first value was lower and the last value was higher than the value adopted in the analysis of the specimen (19.0 MPa). All the remaining parameters were maintained as the same values considered in the previous analysis. As expected the increase of f_c' leads to increase the shear capacity of the RC beams.

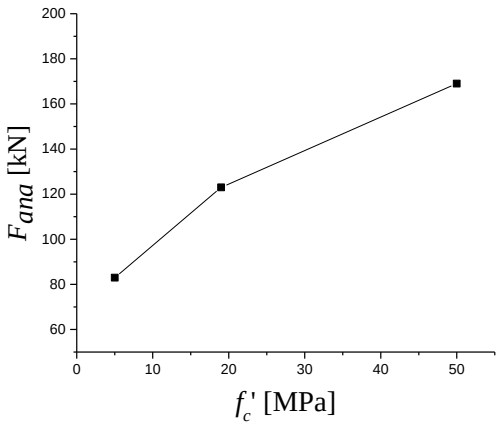

Figure 6.15 Relationship between f_c' and F_{ana}

6.4.2.1.2 Influence of $f_{R,4k}$ value of RSFRM

In order to evaluate the influence of the $f_{R,4k}$ on the shear capacity of the RC beams strengthened with RSFRM panels, the values of $f_{R,4k}$, 2.0, 8.13 and 15 MPa were adopted in the proposed analytical model, while all of the remaining model parameters were maintained as the same values considered in the previous analysis. The first value was lower and the last value was higher than the one considered in the analysis of the

experimentally tested specimen (8.13 MPa). The values of F_{ana} and corresponding ε_x predicted by the proposed model for three different values of $f_{R,4k}$ are presented in table 6.6 and the graphical representation of these values are presented in Figure 6.16. The results presented in Figure 6.16 show that shear capacity of the beams increases linearly with $f_{R,4k}$.

Table 6.6 Influence of $f_{R,3k}$ on the shear capacity of the RC beams strengthened with RSFRM panels

$f_{R,4k}$ [MPa]	F_{ana} [kN]	ε_x [‰]
2.00	103	0.170
8.13	123	0.234
15.00	147	0.304

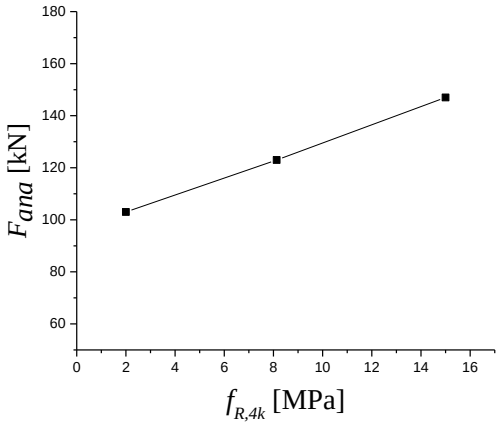

Figure 6.16 Relationship between $f_{R,4k}$ and F_{ana}

6.4.2.1.3 Minimum value of the longitudinal steel reinforcement ratio without yielding of the longitudinal reinforcement

To evaluate the minimum value of the longitudinal steel reinforcement ratio without yielding of the longitudinal reinforcement, randomly assumed values of longitudinal reinforcement ratio presented in table 6.7 were adopted in the proposed model. Table 6.7 presents the predicted values of F_{max} and f_{sxcr} for assumed values of reinforcement ratio.

The graphical representation of the results is illustrated in Figure 6.17. For the longitudinal reinforcement ratio of around 0.0038, the stress transmitted by the longitudinal steel reinforcement cross the cracks exceeds its yield stress.

Table 6.7 Predicted values of f_{sxcr} for assumed values of reinforcement ratio

ρ_{sx} [-]	A_s [mm^2]	f_{sxcr} [MPa]
0.0021	50	830
0.0038	86	599
0.0049	115	501
0.0064	150	423
0.0085	200	351
0.0128	300	266
0.0171	400	217
0.0214	500	184
0.0256	600	160
0.0280	666	147

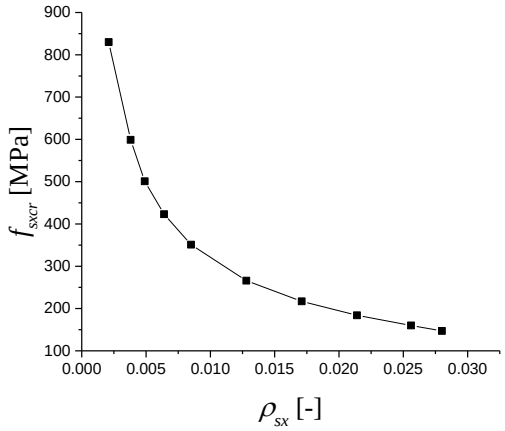

Figure 6.17 Relationship between longitudinal reinforcement ratio and f_{sxcr}

6.4.2.1.4 Influence of RSFRM instead of Plain cementitious mmaterial

In order to evaluate the advantage of using RSFRM panel instead of panel made by Plain cementitious material (PCM), the proposed analytical approach was used for prediction of the shear capacity of the RC beams strengthened with PCM panel. It is assumed the PCM panel has the same dimensions, and also it has the same material properties of the concrete substrate. As expected, lower value of F_{max} was estimated for the beam consisted of PCM panel (96 kN) in compare with the one estimated for the beam strengthened with RSFRM panel (123 kN).

6.5 Conclusions

The work in this chapter was dedicated to the assessment of the benefits of thin panels of RSFRM for the shear strengthening of RC beams failing in shear. Furthermore, the effectiveness of this strengthening technique was explored for the shear repairing of pre-damaged RC beams. On the basis of the results it was observed that the maximum load capacity of the beams strengthened with RSFRM panels was 2.07 to 2.55 times higher than the maximum load capacity of the control beam. The maximum mid span deflection, at peak load, of the beams strengthened with RSFRM panels was 3.06 to 3.77 times higher than the corresponding deflection of the control beam, which reveals the shear strengthening effectiveness of the RSFRM panels for the overall behaviour of this type of beams.

The tests with three series of RC beams were numerically simulated by performing material nonlinear analysis with three dimensional multi-directional fixed smeared crack model under the framework of the finite element method. The good predictions in terms of load carrying and deflection capacity evidenced that this numerical strategy is suitable to predict the shear behaviour of RC beam strengthened with RSFRM panels.

by applying the analytical formulation developed by Baghi *et al*. (2016) based on Simplified MCFT to the beams strengthened with RSFRM panels, it was concluded that

the obtained value of F_{max} / F_{ana} does not guarantee safety predictions for this analytical approach. A new shear design approach was developed combining the SMCFT with the formulation of RILEM TC 162-TDF and it was concluded that the proposed approach gives a conservative estimate of shear strength for RC members strengthened with RSFRM panels.

Chapter 7

7 Conclusions and future perspectives

7.1 General conclusions

The first part of the present work was dedicated to assess the potentialities of recycled steel fibres from the recycling process of post-consumed tyres as a shear reinforcement system of reinforced concrete beams. An experimental program was conducted on a series of RC beams of different cross section web's thickness reinforced with RSF. This experimental program also included the characterisation of the post-cracking properties of the developed concretes reinforced with RSF (RSFRC) and concrete reinforced with industrial steel fibres (ISFRC) in order to compare the reinforcement performance of RSF. The experimental results were also used to determine the fracture mode I

constitutive law of the developed RSFRC, which was taken as the fundamental requisite to simulate the contribution of the RSF for the crack propagation under the framework of the material nonlinear simulations of the experimental tests carried out with RSFRC beams failed in shear.

The second part of this work was dedicated to explore the use of thin cement based (mortar) panels reinforced with relatively high content of RSF for structural strengthening. The mechanical properties and the durability performance of this recycled steel fibre reinforced mortar (RSFRM) were characterised. The panels were produced by using the mixing technique which is used for the fabrication of SIFCon. Then, their potentialities as a shear strengthening solution for RC beams deficiently reinforced in shear were investigated by performing three point bending tests with RC beams of "I" cross section shape shear strengthened with this type of panels. Advanced numerical simulations and an analytical study were carried out to contribute for a better understanding of the effectiveness of the shear strengthening technique with RSFRM panels.

7.1.1 RSFRC failing in bending and in shear

On the basis of the results presented in the first part of the thesis, the following concluding remarks can be highlighted.

RSF are stiff and do not easily accommodate to the dynamically changing shape of the bulk paste located between particles constituting the granular skeleton structure. Consequently, RSF must be gradually added to the mixture to improve the distribution of fibres within the concrete. As expected, these difficulties increase with the content of RSF that can be overcome by increasing the content of paste in the composition. For sustainable and cost competitive RSFRC it is recommended to use fly ash in relatively high percentages and fine aggregates derived from the recycling industry.

Fibre pull-out was the governing failure model in three point notched beam bending tests. From the comparison of the equivalent and residual flexural strength parameters for all the tested series, it was verified that the deflection hardening phase registered in the

ISFRC specimens was not developed in the RSFRC specimens. This indicates that the fibre reinforcement mechanisms for relatively small crack width levels were not so effective in the RSF due to the geometry and surface characteristics of these fibres. However, the flexural strength of RSFRC specimens was almost constant and of the same order of the flexural tensile strength up to the ultimate crack width recorded in the executed tests.

It was also verified that an almost linear relationship exist between $f_{eq,2}$ and $f_{eq,3}$, which indicates a linear dependency between the energy absorption in the fracture process of the RSFRC with the CMOD for the interval of CMOD of 0.5 mm to 2.5 mm, which is a trend already observed in ISFRC. A linear relationship between the concept of residual flexural strength and equivalent flexural strength ($f_{eq,2}$ *vs.* $f_{R,1}$ and $f_{eq,3}$ *vs.* $f_{R,4}$) was also observed, which had already been registered in ISFRC.

For a more enlarged comparison between RSFRC and ISFRC, a database containing the results of the characterisation of the post-cracking behaviour of ISFRC was also used in the present work. It was verified that RSFRC results have a similar trend of the corresponding results of the ISFRC of this database ($f_{R,1} - f_{R,3}$ and $f_{R,1} - f_{R,4}$). However, the residual flexural strengthening parameters ($f_{R,\mathrm{i}}$) of ISFRC have increased more pronouncedly with the fibre volume percentage (V_f) than in the case of RSFRC, which means that for a certain post-cracking performance a higher V_f of RSF is necessary, which can be a sustainable and competitive solution if the adjustments in the composition of the RSFRC to support this V_f do not compromise these requisites, but further research in this respect must be done. In any case, the $f_{R,i}$ values obtained for the developed RSFRC are sufficiently high to create good perspectives for the use of this reinforcement in certain applications, such are the cases of concrete block foundations, slabs supported on soil or on piles.

From the analytical study on the applicability of stress-strain method proposed by RILEM TC 162-TDF (2003) design guideline for RSFRC, it was verified that using the stress-strain diagram proposed by RILEM TC 162-TDF, unsatisfactory predictions were

obtained. A higher load carrying capacity was predicted up to a CMOD of about 3.5 mm, and the difference between the experimental and the analytically results increases with the fibre dosage.

From the analytical study on the applicability of the model proposed by Vipulanandam and Paul (1990) for predicting the compressive stress-strain relationship of RSFRC60, it was verified that the model is capable of simulating the compressive behaviour of RSFRC60.

On the basis of the results of the tests with RSFRC beams failing in shear, it was observed that the ratio of the shear capacity obtained experimentally to that calculated using RILEM and *fib* guidelines decreased with the increase of the beam web thickness, which indicates that both formulations require some enhancements for better consider the geometry of the beam in order to more accurately simulate the fibre orientation and distribution on the effectiveness of the fibre reinforcement mechanisms. In any case, however, safe predictions were obtained for all the studied cases by using the formulations proposed by these guidelines.

The tests with RSFRC beams failing in shear were numerically simulated by performing material nonlinear analysis with a smeared crack model under the framework of the finite element method, where the fracture mode I parameters of the crack constitutive model was determined by executing inverse analysis with the force-CMOD data registered in three point notched beam bending tests carried out according to the RILEM TC 162-TDF recommendations. For modelling the crack shear stress versus crack shear strain a softening diagram was used. The good predictions in terms of load carrying and deflection capacity evidenced that this numerical strategy is suitable to predict the behaviour of RSFRC beams failing in shear. By using this model and adopting a plain concrete, it was verified that 90 kg/m^3 of RSF provided an increase of 157%, 148% and 141% in terms of shear capacity of the beams with a web's thickness of 70, 110 and 150 mm, respectively, when the shear capacity of the reference beam (plain concrete with the same flexural reinforcing ratio) is considered for comparison purpose.

7.1.2 Development of RSFRM panels for structural reinforcement

On the basis of the results presented in the second part of the thesis, the following concluding remarks can be highlighted.

The increase of RSF dosage in the developed cementitious composite leads to the decrease of the UPV value due to presence of the rubber particles in RSF and development of voids and the non-homogeneity in RSFRM.

Flexural tests results showed that the increase of the fibre content leads to the increase of the maximum flexural stress. Furthermore, the flexural strength of RSFRM specimens is almost constant and of the same order of the flexural tensile strength up to the ultimate crack width recorded in the executed tests (2.5 mm). On the other hand it was verified that, taking out rubber particles from RSF, it provided an increase of 53% and 12% in terms of σ_{cr} and $\sigma_{\max}$, respectively.

Based on the results obtained from the simulations of the direct tensile tests and flexural tests, higher values of tensile strength and fracture energy mode I were obtained from the simulations of the flexural tests compared to the values obtained from the simulations of the direct tensile tests. This was justified on the basis of different fibre pull-out mechanisms in direct tensile and bending tests, and also on the effect of specimen's thickness.

The shear behaviour of the RSFRM was investigated by Iosipescu shear test method. It was verified that after reaching the crack shear strength, by increasing the load, a nonlinear shear-sliding stage has occurred up to the peak load, followed by a relatively smooth softening response with high ductility behaviour. The capability of a FEM-based computer program to predict the behaviour of this type of specimens up to a relatively shear damage was demonstrated. In fact, the shear crack softening diagram available in the multi-directional fixed smeared crack model implemented in the FEMIX computer program, allowed to simulate the shear behaviour of the Iosipescu specimen. After has been demonstrated that this FEM-based computer program is capable of predicting with high accuracy the shear behaviour of the tested specimens, a parametric study was carried out for assessing the influence of shear retention factor, fracture energy mode II, crack

shear strength, tensile strength and fracture energy mode I on shear stress-sliding response of RSFRM. It was concluded that: i) from 0.05 mm sliding (that corresponds to the formation of first shear crack at the notched plane) up to sliding of about 4.43 mm, the shear stress capacity of the specimens slightly increases with the increase of the value of shear retention factor, ii) the decrease of the fracture energy mode II leads to the increase of the slope of the first softening zone (more brittle behaviour), iii) the increase of the values of tensile strength and crack shear strength leads to the increase of the shear strength. For the values of G_f^I between 1.0 to 6.0 N/mm, shear strength significantly increases with G_f^I. Furthermore, the advantage of RSFRM versus mortar was also studied and it was verified that the RSFRM specimen failed at a 7.3 times higher shear stress than of the plain cementitious material (PCM) specimen.

Based on the results obtained from durability tests the following conclusion remarks were made: i) a higher average non-steady state chloride migration coefficient and air permeability coefficient was obtained for RSFRM compared to SFRSCC, ii) addition of RSF to cementitious composite significantly increases its open porosity due to air attraction on the surface of fibres containing rubber crumb on their surface. On the other hand, relatively higher value of coefficient of water absorption by capillarity was obtained for the RSFRM compared to the value that was already obtained for SFRSCC, which confirms that the developed RSFRM is not as capable as SFRSCC to prevent penetration of deteriorating agents, iii) from drying shrinkage tests it was verified that the bigger part of drying shrinkage occurred on early ages (4 days) and it was on the early ages that a higher loss of water occurs.

On the basis of the results of the tests with RC beams strengthened with RSFRM panels, it was verified that the RSFRM panels were capable of increasing the load carrying and deflection capacity of the tested RC beams.

The tests with three series of RC beams strengthened with RSFRM panels were numerically simulated by performing material nonlinear analysis with three dimensional multi-directional fixed smeared crack model under the framework of the finite element method. The good predictions in terms of load carrying and deflection capacity evidenced

that this numerical strategy is suitable to predict the shear behaviour of RC beams strengthened with RSFRM panels. On the other hand, by applying the analytical formulation developed by Baghi *et al*. (2016) based on Simplified MCFT to the beams strengthened with RSFRM panels, it was concluded that the obtained value of F_{max} / F_{ana} does not guarantee safety predictions for this analytical approach. A new shear design approach was developed combining the SMCFT with the formulation of RILEM TC 162-TDF and it was concluded that the proposed approach gives a conservative estimate of shear strength for RC members strengthened with RSFRM panels.

7.2 Recommendations for future research

In the following, some recommendations are proposed for future research:

- For a more comprehensive assessment of the shear reinforcement effectiveness of RSF in RC beams, real scale beams should be tested in order to avoid a detrimental impact of the scale effect on the results;
- Regarding to the analytical studies carried out using RILEM and *fib* guidelines in the present thesis, it should be pointed out that for better consider the geometry of the beam in order to more accurately simulate the fibre orientation and distribution on the effectiveness of the fibre reinforcement mechanisms, some enhancements should be applied for both formulations;
- The distribution of steel fibres along the height of the cross section should be studied precisely. For this purpose, the fibres segregation degree parameter, and the number of fibres in different layers of the section should be obtained by an image analysis technique;
- The influence of the percentage of existing steel stirrups on the effectiveness of the proposed strengthening technique should be evaluated;
- Further experimental program with more tested RC beams strengthened with RSFRM panels is needed to be performed for addressing various issues related to the effectiveness of the mechanical anchors on the adopted shear strengthening system.

- The use of the proposed strengthening technique for the increase of the load carrying capacity and ductility performance of masonry type structures should be explored.

References

ACI 318, (2008), "*Building code requirements for structural concrete and commentary*." appendix A, strut-and-tie models ed. s.l.: American Concrete Institute.

ACI 544.1R (1996), "*State-of-the-Art Report on Fibre Reinforced Concrete*", American Concrete Institute, Farmington Hills, Michigan.

ACl 544 (1988), "*Measurements of properties of fibre reinforced concrete*." ACI Materials Journal, 85(6), pp:583-593.

ACI 544.2R (1987), "*Measurement of Properties of Fibre Reinforced Concrete*." ACI Journal.

Aiello, M.A., Leuzzi F., Centonze G. & Maffezzoli A. (2009), "*Use of steel fibres recovered from waste tyres as reinforcement in concrete: Pull-out behaviour, compressive and flexural strength*" Waste Management 29(6), pp:1960-1970.

AMAT. (2003). "Advanced molecular agitation technology", from www.amat-ltd.com.

Amin, A. & Foster, S., (2016), "*Shear strength of steel fibre reinforced concrete beams with stirrups*" Engineering Structures 111(15), pp:323–332.

Aoude, A. F., Belghiti, M., cook, W.D. & Mitchell, D., (2012), "*Response of steel fibre-reinforced concrete beams with and without stirrups.*" ACI Structure Journal, 109(3), pp:359-368.

Ashour, S.A., Hassanain, G.S. & Wafa, F.F. (1992), "*Shear behaviour of high-strength fibre reinforced concrete beams.*" *ACI Structure Journal, 89,* pp:176–184.

ASTM C1018-94b (1995), *Standard test method for flexural toughness and firstcrack strength of fibre-reinforced concrete (using beam with third-point loading).* American society of testing and materials, ASTM Annual Book of Standards 4.02, Philadelphia, USA. pp:509-516.

ASTM C157 / C157M (2014), Standard "*Test Method for Length Change of Hardened Hydraulic-Cement Mortar and Concrete*" American society of testing and materials.

ASTM C596 - 09e1 Standard "*Test Method for Drying Shrinkage of Mortar Containing Hydraulic Cement*" American society of testing and materials.

ASTM D5379 (1993), "*Standard Test Method for Shear Properties of Composite Materials by the V-Notched Beam Method*" American society of testing and materials.

Azevedo, A.F.M., Barros, J.A.O. and Sena-Cruz, J.M., Ventura-Gouveia, A. (2003), "*Software in teaching and design of structures*" III Conference Luso-Mozambican of Engineering, pp:81-92, 19-21. (in Portuguese)

Athira, Rossli, S. & Syahrizal, Ibrahim, I. (2012), "*Mechanical Properties of Recycled Steel tyire Fibres in Concrete*" technical report Faculty of Civil Engineering, University Technology Malaysia.

Azevedo, A.F., Barros, J.A.O., Sena-Cruz, J.M., & Gouveia, A.V. (2003), "*Software no ensino e no projecto de estruturas (Software in structural engineering education and design)*" III Portuguese-Mozambican Conference of Engineering, pp:81-92.

Baghi, H. (2015), "*Shear strengthening of reinforced concrete beams with SHCC-FRP panels*" PhD thesis, University of Minho.

Baghi, H. & Barros, J.A.O. (2016), "*Shear Properties of the Strain Hardening Cementitious Composite Material*" Journal of Materials in Civil Engineering. ISSN (online):1943-5533.

Baghi, H., Barros, J.A.O. Barros & Menkulasi, F. (2016) "*Shear strengthening of reinforced concrete beams with Hybrid Composite Plates (HCP) technique: Experimental research and analytical model*" Engineering Structures 125, pp:504–520

Baghi, H. Barros, J.A.O. & Ventura-Gouveia, A. (2016), "*Shear strengthening of reinforced concrete beams with hybrid composite plates.*" Adv Struct Eng 2016. http://dx. doi.org/10.1177/1369433215622873

Balouch, S., Forth, J. & Granju, J. (2010), "*Surface corrosion of steel fibre reinforced concrete,*" Cement and Concrete Research, 17, pp:410-414.

Banks-Sills, L. & Arcan, M. 1983, "*An Edge Crack Mode II Fracture Specimen*" Experimental Mechanics, 23(3), pp:257-261.

Barr, B., Gettu, R., AI-Oraimis, K.A. & Bryars, L.S. (1996), "*Toughness measurement-the need to think again.*" Cement and Concrete Composites, 18 (4), pp:281-297.

Barros, J.A.O., "*Behaviour of fibre reinforced concrete – experimental analysis and numerical simulation*" PhD thesis, FEUP, 1995. (in Portuguese)

Barros, J.A.O., "*Technology, design and applications of steel fibre reinforced self-compacting concrete*", 6th International Conference Fibre Concrete 2011 Technology, Design, Application, CTU in Prague, Masarykova kolej, 8 and 9 September 2011. (Invited Keynote Lecturer)

Barros, J.A.O., Baghi, H., Dias, S.J.E.A. & Ventura-Gouveia A. (2013), "*A FEM-based model to predict the behaviour of RC beams shear strengthened according to the NSM technique*" Journal of engineering structures, 56 pp:1192-1206.

Barros, J.A.O., Cunha, V. M., Ribeiro, A.F. & Antunes, J.A., (2005), "*Post-cracking behaviour of steel fibre reinforced concrete*" Materials and Structures, 31(1), pp: 47-56.

Barros, J.A.O., Gettu, R. & Barragan, B.E. (2004), "*Material nonlinear analysis of steel fibre reinforced concrete beams failing in shear*". Proceeding of 6th International RILEM Symposium on fibre reinforced - BEFIB 2004, Edts. M. di Prisco, R. Felicetti, G.A. Plizarri, 1, pp:711-720.

Barros, J.A.O. & Figueiras, J.A. (2001), "*Nonlinear analysis of steel fibre reinforced concrete slabs on grade*", Composite Structures J., 79(1), pp:97-106.

Barros, J.A.O. & Figueiras, J. (1999), "*Flexural Behaviour of SFRC: Testing and Modeling.*". Materials in civil engineering, 11(4), pp:331-339.

Barros, J.A.O. & Figueiras, J.A. (1998), "*Experimental behaviour of fibre concrete slabs on soil*", Journal Mechanics of Cohesive-frictional Materials, 3, pp277-290.

Barros, J.A.O., Lourenço, L. A., Soltanzadeh, F. & Taheri, M. (2014), "*Steel fibre reinforced concrete for elements failing in bending and in shear*." European Journal of Environmental and Civil Engineering, 18(1), pp:33-65.

Barros, J.A.O., Moraes-Neto, B.N., Melo, G.S.S.A. & Frazão, C.M.V. (2015), "*Assessment of the effectiveness of steel fibre reinforcement for the punching resistance of flat slabs by experimental research and design approach*", Composites Part B Journal, 78, pp:8-25.

Barros, J.A.O., Pereira, E.B. and Santos, S.P.F. (2007), "*Lightweight panels of steel fiber reinforced self-compacting concrete*" ASCE Materials in Civil Engineering Journal, 19(4), pp:295-304.

Barros, J.A.O., Zamanzadeh, Z., Mendes, P.J.D. & Lourenço, L.A.P. (2013), "*Assessment of the potentialities of recycled steel fibres for the reinforcement of cement based materials*" The New Boundaries of Structural Concrete Session C – New Scenarios for Concrete, Bergamo Italy.

Bdour, N. & Al-Khalayleh, A. (2010), "*Innovative Application of Scrap-tyre Steel Cords in Concrete Mixes*" Jordan Journal of Civil Engineering, 4(1), pp:55-61.

Bentz, E.C., Vecchio, F.J. & Collins, M.P. (2006), "*Simplified modified compression field theory for calculating shear strength of reinforced concrete elements*" ACI Struct Journal, 103(4), pp:614–624.

Blanksvärd, T. (2007), "Strengthening of concrete structures by the use of mineral based composites." Master Thesis. Luleå University of Technology.

Blanksvärd, T. (2009), "Strengthening of concrete structures by the use of mineral based composites." PhD Thesis. Luleå University of Technology.

Boulifa, R., Laid-Samami, M. & benhassine, M.T., (2013), "*A New Technique for Studying the Behaviour of Concrete in Shear,*" Journal of King Saud University, 25(2), pp:149-159.

Buratti, N., Mazzotti, C. & Savoia, M. (2011), "*Post-cracking behaviour of steel and macro-synthetic fibre-reinforced concretes*" Construction and Building Materials, 25(5), pp:2713–2722.

Caggiano, A., Cremona, M., Faella, C., Lima, C. & Martinelli, E. (2012), "Fracture behaviour of concrete beams reinforced with mixed long/short steel fibres" Construction and Building Materials, 37, pp:832-840.

Carrajola, A. (2006) "*The Influence of shrinkage reducing admixtures on the cracking control of concrete*," Instituto Superior Técnico, Master Dissertation, Portugal in Portuguese.

Carreira, D. & Chu, K. (1985), "*Stress-strain relationship for plain concrete in compression*." AO Journal, 1985, 83, No. 6, pp:797-804.

CEB-*fib* Model Code 2010, CEB and FIP, 2011.

CEB-*fib* Model Code 1990, Design code, 1993.

Cengiz, O. & Turanli, L. (2004), "*Comparative evaluation of steel mesh, steel fibre and highperformance polypropylene fibre reinforced shotcrete in panel test*." Cem Concr Res, 34, 1357–1364.

Centonze, G., Leone, M & Aiello, M.A. (2012), "*Steel fibres from waste tyres as reinforcement in concrete: A mechanical characterisation*" Construction and Building Materials 36, pp:46-57.

Chaallal, O., Mofidi, A., Benmokrane, B. & Neale, K. (2011), "*Embedded through-section FRP rod method for shear strengthening of RC beams: performance and comparison with existing techniques*." Journal of Composites for Construction 15(3) pp:374–383.

Charles Lawrence Recycling Ltd (2004) http://recycling.clgplc.co.uk

Chintalapudi, K. & Rama, M. (2016) "*Properties of Bacterial-based Self-healing Concrete- A review*" International Journal of ChemTech Research CODEN (USA): IJCRGG ISSN: 0974-4290 Vol.9, No.02 pp:182-188.

CNR-DT (2006, 2007), "*Guide for the Design and Construction of Fibre-Reinforced Concrete Structures.*" 204, Italian National Research Council, Italy.

Collins, M.P. and Mitchell, D. (1991), "*Prestressed concrete structures*", New Jersey:Prentice-Hall.

Colombo, M., di Prisco, M. & Mazzolen,i L. (2009), "*Sprayed tunnel linings: a comparison between several reinforcement solutions.*" Materials & Structures, 42, pp:1295–311.

Commission E. (1999), Council directive 1999/31/EC of 26 April 1999 on the landfill of waste. Off J Eur Commun: pp:1-19.

Cucchiara, C., Mendola, L. & Papia, M. (2004), "*Effectiveness of stirrups and steel fibres as shear reinforcement.*" Cement & Concrete Composites, 26(7), pp:777-786.

Cunha, V. (2010), "*Steel Fibre Reinforced Self-Compacting Concrete (From Micro-Mechanics to Composite Behaviour)*" PhD Thesis, Civil Engineering Department - School of Engineering, University of Minho.

Cunha, V.M.C.F., Barros, J.A.O. & Sena-Cruz, J.M. (2010), "*Pullout Behaviour of Steel Fibres in Self-Compacting Concrete.*" Journal of Materials in Civil Engineering, 22(1), pp:1-9.

De Montaignac, R., Massicotte, B. & Charron, J.P. (2012), "*Design of Sfrc Structural Elements: Flexural Behaviour Prediction.*" Materials and Structures, 45(4), pp:623-636.

Ding, Y. & Kusterle, W. (1999), "*Comparative study of steel fibre-reinforced concrete and steel mesh-reinforced concrete at early ages in panel tests*." Cement and Concrete Research, 29 pp:1827–1834.

Drdlová, M., Buchar, J., Krátký, J. & Řídký, R. (2015), "*Blast resistance characteristics of concrete with different types of fibre reinforcement*" Structural Concrete, 16, pp:508-517.

EFNARC (1996), European Federation of Producers and Applicators of Specialist Products for Structures. European specification for sprayed concrete.

EN 10002-1:1990. Metallic materials-Tensile testing. Part 1: Method of test (at ambient temperature). CEN, Brussels, Belgium, 35.

Esmaeeli, E. Barros, J.A.O. 2015), "*Flexural strengthening of RC beams using hybrid composite plate (HCP): experimental and analytical study*." Compos Part B J 79, pp:604–20.

European Committee for Standardisation, *BS EN 124 - Dully tops for vehicular and pedestrian areas- design requirements, type testing, marketing, quality control*. BSI, London, 1994.

Eurocode 2, (2004), Design of concrete structures - Part 1-1: General rules and rules for buildings. Brussels: Comité Européen de Normalisation (CEN), EN 1992-1-1:2004.

Evangelista, R. & Brito, J. (2004), "*Criteria for the Use of Fine Recycled Concrete Aggregates in Concrete Productio*n" Conference: Conference on the Use of Recycled Materials in Building and Structures, RILEM, Barcelona, Spain.

Frazão, C., Camões A., Barros, J.A.O. & Gonçalves, D. (2015), "Durability of steel fibre reinforced self-compacting concrete", Constr. Build. Mater. 80 pp:155–166, http://dx.doi.org/10. 1016/j.conbuildmat. 2015.01.061.

Gebretsadik, B.T. (2013), "*Ultrasonic Pulse Velocity Investigation of Steel Fibre Reinforced Self Compacted Concrete.*" UNLV Theses/Dissertations/Professional Papers/Capstones. Paper 1828.

Gopalaratnam, V., Gettu, R., Carmona, S. & Jamet, D. (1995), "*Characterisation of toughness of fibre reinforced concretes using the lod-CMOD response"* Fracture Mechanics of Concrete Structures, Proceedings FRAMCOS-2, edited by Folker H. Wittmann, AEDIFICATIO Publishers, D-79104 Freiburg.

Graeff, A., Pilakoutas, K., Lynsdale, C. & Neocleous, K. (2009), "*Corrosion Durability of Recycled Steel Fibre Reinforced Concrete*" Intersections 6, pp:77-89.

Graeff, A.G., Pilakoutas, K., Neocleous, K. & Vania N.N. Peres, M. (2012), "*Fatigue resistance and cracking mechanism of concrete pavements reinforced with recycled steel fibres recovered from post-consumer tyres*" Engineering Structures, 45, pp:385-395.

Granju, J.L. & Balouch, S.U. (2005), "*Corrosion of steel fibre reinforced concrete from the cracks.*" Cement and Concrete Research 35, pp:572-577.

Grzybowski M. & Shah, S. P. (1990), "*Shrinkage cracking of fibre reinforced concrete*." ACI Mat. J., 87(2), pp:138–148.

Hai, H. (2009), "*Shear behaviour of steel fibre reinforced concrete beams withou stirrup reinforcement.*" A dissertation submitted in partial fulfillment of the requirements of the degree of Ph.D, University of Michigan.

Hsu, L. & Hsu, C-T. (1994), "*Stress-strain behaviour of steel-fibre high strength concrete under compression*", Structural Journal, 91(4), pp:448-457.

Hylands, K.N. & Shulman, V. (2003), "*Civil engineering applications of tyres*." Crow Thorne, Transport Research Laboratory,. Viridis Report VR5.

INTEC, R. (2003), INTEC'S high technology plant for the production of ultra fine rubber powders.

Iosipescu, N., (1967), "*New accurate method for single shear testing of metals,*" Journal of Materials, 3, pp:537- 566.

Janusz, P. (1983), "*The splitting test applied to steel fibre reinforced concrete.*" The international Journal of Cement Composites and Lightweight Concrete, 5(1), pp:49-53.

Japan Society of Civil Engineers, JSCE-SF1 (1994), "*Recommendation for design and contraction steel fibre reinforced concrete*" JSCE Concrete Library, 3. pp:5-29.

Japan Society of Civil Engineers, JSCE-SF4 (1994), *Methods of tests for flexural strength andflexural toughness of steel fibre reinforced concrete. Concrete Library of JSCE,* pp:58-61.

Kakay, S., Omdal, R., Sæstad, A., Refsland, K. & Gudmestad, O.T. (2015), "*Effects of Using Fibres on Cracks and the Ductility of Lightweight Concrete*" WIT Transactions on Engineering Sciences, 90 pp:133-147.

Kaplan, M.F. (1959) "*The effects of age and water to cement ratio upon the relation between ultrasonic pulse velocity and compressive strength of concrete*" Magazine of Concrete Research, 11(32), pp:85-92.

Kohler, R. (1996), "*Cryogenic processing of scrap tyres*." Polymer Recycling No. 2: pp:83-88.

Kosa, K. & Naaman, E. (1990), "*Corrosion of steel fibre reinforced concrete*." ACI Materials Journal 87, pp:27-37.

Krstulovic-Opara, N. & AI-Shannag, M.J. (1999), "*Slurry infiltrated mat concrete (SIMCON)-based shear retrofit of reinforced concrete members.*" ACI Structural Journal, 96 (1), pp:105-114.

Kuchma, D.A.M., Hawkins, N., Kim, S., Sun, S., and Su Kim, K. (2008). "*Simplified shear provisions of the AASHTO LRFD Bridge Design Specifications*." PCI Journal, pp:53-73.

Kwak, Y.K., Eberhard, M.O., Kim, W.S. & Kim, J. (2012), "*Shear strength of steel fibre reinforced concrete beams without stirrups.*" ACI Structure Journal, 99, pp:530–538.

Lange, D.A., D'ambrosia, M.D. & Grasley, Z.C (2005). "*Drying stress and internal relative humidity in concrete*", Material Science of Concrete, Wiley, USA.

Lankard, D.R. (1985), "*Preparation, Properties and Applications of Concrete- Based Composites Containing 5 % to 20 % Steel Fibre*", Steel Fibre Concrete, US - Sweden Joint Seminar, pp:199-217.

Lee, M. L. (2003), "*A State of the Art Review on HPFRCC*". Sustainable Advanced Materials, Report for Sub-Task 15, Sustainable Advanced Materials for Road Infrastructure (SAMARIS).

Lee, M.K. & Barr, B.LO. (2003), "*Strength and fracture properties of industrially prepared steel fibre reinforced concrete*" Cement and Concrete Composites, 25, pp:221-332.

Lee, S., Cho, J. & Vecchio, F. J., (2011), "*Diverse Embedment Model for Fibre-Reinforced Concrete in Tension: Model Development.*" ACI Materials Journal, 108(5), pp:516-525.

Leung, C.K.Y. & Geng, Y.P. (1998), "*Micromechanical modeling of softening behaviour in steel fibre reinforced cementicious composites*." Int. Journal Solids Strucutres, 35(32), pp:4205-4222.

Leung, C.K.Y. & Shapiro, N. (1999) "*Optimal steel fibre strength for reinforcement of cementitious materials,*" Journal of Materials in Civil Engineering, 11(2) pp:116-123.

Lion, Y. (2012), "*Mechanical properties of recycle steel fibre reinforced concrete*" A report submitted in partial fulfilment of the requirements for the award of the degree of Master of Engineering (Civil-Structure) Faculty of Civil Engineering Universiti Teknologi Malaysia

LNEC E393, "*Concrete. Determination of water absorption by capillarity*," Lisbon: LNEC, p.2 (1993)

LNEC E394, *Concrete. Determination of water absorption by immersion – test at atmospheric pressure*, Lisbon:LNEC, p.2 (1993).

LNEC E397-1993:1993. Concrete – *Determination of the elasticity young modulus under compression.* Portuguese specification from LNEC.

Lorenzi, A., Tisbierek, F. & Filho, L. (2007), "*Ultrasonic Pulse Velocity Analysis in Concrete Specimens*" IV Conferencia Panamericana de END Buenos Aires – Octubre 2007.

Lourenço, L., Barros, J.A.O. & Alves, J., (2011), "*Fibre reinforced concrete of enhanced fire resistance for tunnel segments.*" ACI SP-276-4, Durability enhancements in concrete with fibre reinforcement, Editors: Corina-Maria Aldea and Nur Yazdani, March.

Malathy, R. & Rao, G.A. (2002). "*Drying shrinkage of cementitious composites incorporated with silica fume*" 27th Conference on Our World In Concrete & Structures, Singapore, pp:235-241.

Mangat, P. & Gurusamy, K. (1987), "*Chloride diffusion in steel fibre reinforced marine concrete.*" Cement and Concrete Research 17, pp:385-396.

Mansur, M., Chin, M. & Wee, T. (1999), "*Stress-strain relationship of high-strength fibre concrete in compression*", Journal of Materials in Civil Engineering, 11(1), pp:21-29.

Mastali, M., Valente, I.B., Barros, J.A.O. & Gonçalves, D.M.F. (2015), "*Development of innovative hybrid sandwich panel slabs: Experimental results*" Composite Structures 133 (2015) pp:476–498.

Micelli, F., Leone, M, Centonze, G & Aiello M.A. (2015), "*Go Green: Using Waste and Recycling Materials*" Published by OMICS Group eBooks. 731 Gull Ave, Foster City, CA 94404, USA.

Mindess, S. & Young, J.F. (1981), Concrete, Prentice-Hall, Englewood Cliffs, N.J.

Moraes-Neto, B.N., Barros, J.A.O., Melo, G.S.S.A. (2014) "*A model to simulate the contribution of fibre reinforcement for the punching resistance of RC slabs*" ASCE Journal of Materials in Civil Engineering, 26(7).

Morris, J.W., Glazer, J. & Chan, J.W. (1990), "Metallurgical determinants of toughness at cryogenic temperature" Advances in Cryogenic Engineering 36 part B: pp:777-785.

Neocleous, K., Tlemat, H. & Pilakoutas, K., (2006), "*Design Issues for Concrete Reinforced with Steel Fibres, Including Fibres Recovered from Used Tyres.*" Materials in Civil engineering, 18(5), pp:677–685.

Neves, R.D. & Fernandes, J.C.O., (2005), "*Compressive behaviour of steel fibre reinforced concrete*" Journal of Structural Concrete 6(1) pp:1-8.

Nordstrom, E. (2000), "*Steel fibre corrosion in cracks. Durability of sprayed concrete*." Licentiate Thesis, Lulea University of Technology.

NP EN 12390-3:2009. Testing hardened concrete. Part 3: Compressive strength of test specimens.

NT BUILD-492 (1999) "*Chloride migration coefficient from non-steady-state migration experiments*" Nordtest Method, UDC 691.32/691.53/691.54.

NZS4203, (1992), General structural design and design loadings for buildings, standard published 12/14/1992 by Standards New Zealand.

Ohno, K. (1957), "*Shear Tests of Reinforced Concrete Beam by Special Type of Loading,*" Transactions of the Architectural institute of Japan pp:581-584.

Olivito, R.S. & Zuccarello, F. (2010), "*An experimental study on the tensile strength of steel fibre reiforced concrete.*" Composites Part B Engineering 41(3), pp:246-255.

Papakonstantinou, C.G. & Matthew, J.T. (2006), "*Use of waste tire steel beads in Portland cement concrete.*" Cement and Concrete Research 36, pp:1686–1691.

Pereira, E.B., Barros, J.A.O. & Camões, A.F. (2008), "*Steel fibre reinforced self-compacting concrete–experimental research and numerical simulation*" Structural engineering, 134(8), pp:1310-1321.

Pilakoutas, K., Neocleous, K. & Tlemat, H. (2004), "Reuse of tyre steel fibres as concrete reinforcement." Proceedings of the ICE: Engineering Sustainability: pp:131-138.

Pilakoutas, K. & Strube, R. (2001), "*Reuse of tyre fibres in concrete, in Recycling and Reuse of Used Tyres*" Proceedings of the International Symposium, Dundee

Prisco, M., Felicetti, R. & Plizzari, G (eds), (2004), "*Fibre- Reinforced Concrete*". In: RILEM Proceedings of the 6th RILEM Symposium (BEFIB 2004), PRO39, BEFIB 2004. RILEM Publications S.A.R.L., Bagneux, France.

Reinhardt, H.W., Ozbolt, J., Xu, S. & Dinku, A. (1997), "*Shear of Structural Concrete Members and Pure Mode II Testing,*" Advanced Cement Based Materials 5, pp:75-85.

Ribeiro, A.B., Gonçalves, A., & Carrajola A. (2006), "*Effect of shrinkage reduction admixtures on the pore structure properties of mortars*." Materials and Structures, 39, pp:179-187.

RILEM TC 162-TDF, (2003), "*Test and design methods for steel fibre reinforced concrete: σ-ε design method - Final Recommendation*." Materials and Structures, Volume 36, pp:560-567.

RILEM TC 162-TDF (2002), "*Test and Design Methods for Steel Fibre Reinforced Concrete, Design of steel fibre reinforced concrete using the $\sigma-\omega$ method: principles and applications*", Materials and Structures, 35, pp:262-278.

Rodriguez, I.M., Lasesgoiti, M.F., Cabrero, M.A., Torres, A., Chomon, M.J. & Caballero, (2001). "*Pyrolysis of scrap tyres*." Fuel Processing Technology 72(1), pp:9-22.

Rossi, P.Les Bétons de FibresMétalliques. Presses ENPC, 1998.

Safeer, H., Ahmed, M. & Moncef, L. (2004), "*Experimental study on settlement and punching behaviour of full-scale RC and SFRC precast tunnel lining segments.*" Engineering Structures, 72(1), pp:1-10.

Sena-Cruz, J.M. (2004), "*Strengthening of concrete structures with near-surface mounted CFRP laminate strips*" PhD Thesis, Department of Civil Engineering, University of Minho, http://www.civil.uminho.pt/composites.

Sena-Cruz, J.M., Barros, J.A.O., Fernandes, A.R., Azevedo, A.F.M. & Camıes, A. (2004), "*Stress crack opening relationship of enhanced performance concrete.*" 9th Portuguese Conference on Fracture, ESTSetúbal, Portugal,. s.l., s.n., pp:395-403.

Sharma, A.K. (1986), "*Shear strength of steel fibre reinforced concrete beams*." *ACI J. Proc., 83*, pp:624–628.

Soltanzadeh, F. (2016), "*High performance fibre reinforced concrete for the replacement of shear stirrups*" PhD thesis, University of Minho.

Soltanzadeh, F., Barros, J.A.O. and Santos, R.F.C. (2015), "*High performance fiber reinforced concrete for the shear reinforcement: experimental and numerical research*", Journal of Construction and Building Materials. 77, pp:94-109.

Susetyo, J., Gauvreau, P. & Vecchio, F.J. (2011), "*Effectiveness of Steel Fibre as Minimum Shear Reinforcement.*" ACI Structural Journal, 108(4), pp :488-496.

Swamy, R.N. & Bahia, H.M. (1979), "*Influence of fibre reinforcement on dowel resistance to shear.*" ACI J. Proc. 76, pp:327–355.

SYEP (2001), *Dealing with waste lyres. South Yorkshire environmental partnerships,* http://www.syep.org.uk

Thomas, J. & Ramaswamy, A. (2007), "*Mechanical properties of steel fibre reinforced concrete.*" Journal of Materials in Civil Engineering, ASCE (May 2007), pp:385–392.

Tlemat, H. (2004), "*Steel fibre from waste tyres to concrete; testing, modeling and design*" Phd thesis, Department of Civil and Structural Engineering, University of Sheffield.

Tlemat, H., Pilakoutas, K. & Neocleous, K. (2006), "*Stress-strain characteristic of SFRC using recycled fibres*" Material and Structures 39(3), pp:365-377.

Tlemat, H., Pilakoutas, K. & Neocleous, K. (2003), "*Pullout behaviour of steel fibres recycled from used tyres*", Proceedings of International Symposia on Celebrating Concrete: People and Practice (in Role of Concrete in Sustainable Development), Dundee UK, Sept. 2003, Thomas Telford Ltd London, pp:175-184.

Tlemat, H., Pilakoutas, K. & Neocleous, K. (2004), "*Demonstrating steel fibres from waste tyres as reinforcement in concrete.*" Material characterisation, Proceedings of the First International Conference on Innovative Materials and Technologies for Construction and Restoration.

Toutanji, H.A. & EI-Korchi, T. (1994), "*Uniaxial Tensile Strength of Cementitiouse Composites*." Journal Testing and Evaluation, ASTM, 22(3), pp:226-232.

Ulucan, Z.Ç., Türk, K. & Karata, M. (2008), "*Effect of mineral admixtures on the correlation between ultrasonic velocity and compressive strength for self-compacting concrete*." Russian Journal of Nondestructive Testing, 44(5), pp:367–374.

UNI 11039, (2003), "*Steel fibre reinforced concrete*", Italy.

Used tyre Working Group (2004), Sixth report of the used tyre working group.

Van Mier, J.G.M., Stang, H. & Ramakrishnan, V. (1996), "*Practical structural applications of FRC and HPFRCC.*" Proceedings of the second international RlLEM workshop on high performance fibre reinforced cement composites. pp:450-459.

Vanaerschot, A., Lomov, S., Moens, D. & Vandepitte, D. (2015). "*Variability in composite materials properties"* Applied Mechanics & Materials, 807, pp:23-33.

Vandewalle, L. et al. (2000) "Design method for steel fiber reinforced concrete proposed by RILEM TC 162-TDF" Fifth International RILEM Symposium on Fibre-Reinforced Concrete (FRC), pp:51-64.

Ventura-Gouveia, A., (2011), "*Constitutive models for the material nonlinear analysis of concrete structures including time dependent effects*". PhD Thesis, Department of Civil Engineering, University of Minho.

Ventura-Gouveia, A., Barros, J.A.O. & Azevedo, A.F. (2011), "*Crack constitutive model for the prediction of punching failure modes of fibre reinforced concrete laminar structures.*" Computers and Concrete, 8(6), pp:735-755.

Vipulanandan, C. & Paul, E. (1990), "*Performance of epoxy and polyester polymer concrete.*" Materiais Journal, 87(3), pp:241-251.

Voo, J.Y. & Foster, S.J. (2003), "*Variable Engagement Model for Fibre Reinforced Concrete in Tension*." Proceedings Advanced Materials for Construction of Bridges, Buildings, and Other Structures III Sydney, Australia: The University of New South Wales. Published by ECI Digital Archives 8(6), pp:735-755.

Wang, Y., Wu, H.C. & L. V.C. (2000), "*Concrete reinforcement with recycled fibres.*" journal of materials in civil engineering, 12(4), pp:314-319.

Wu, H.C., Lim, Y.M. & Li, V.C. (1994), "*Shrinkage behaviour of cementitious composites with recycled fibres.*" Proc., 2nd Annu. Great Lakes Geotech./Geoenvir. Conf. on Waste Mat. and Their Geotech./ Geoenvir. Applications.

Wu, H.C., Lim, Y.M., Li, V.C. & Foremsky, D.J. (1996a), "*Utilization of recycled fibres in concrete.*" Proc., Mat. Engrg. Conf., K. Chong, ed., ASCE, New York, pp:799–808.

Wu, H.C., Lim, Y.M. & Li, V.C. (1996b), "*Application of recycled tyre cord in concrete for shrinkage crack control.*" J. Mat. Sci. Lett., 15, pp:1828–1831.

Ye, G., Lura P., Van Breugel, K. & Fraaij, A.L.A. (2004), "*Study on the development of the microstructure in cement-based materials by means of numerical simulation and ultrasonic pulse velocity measurement.*" Cement and Concrete Composites, 26(5), pp:491-497.

Yip, W. (1998), "*Generic form of stress-strain equations for concrete*" Cement and Concrete Research, 28(4), pp:499-508.

Zamanzadeh, Z., Lourenço, L.A.P. & Barros, J.A.O. (2015), "*Recycled steel fibre reinforced concrete failing in bending and in shear*" Journal of Construction and Building Materials. 85, pp:195-207.

Annex A

Numerical simulation of compression test

For better understanding the effect of rubber particles on the compressive strength of RSFRC, the compression test on concrete cubic specimen containing rubber particles were numerically simulated. For this purpose, the Femix finite element software was used (Azevedo *et al*. 2003). A finite element mesh of 900 plane stress elements of 8 nodes was used for the simulation of the specimen. Due to the symmetry of specimen geometry, supports and loading conditions used in the compression test setup, one eighth of the specimen was modelled. A Gauss-Legendre integration scheme with 2×2 Integration Points (IP) was used in all the concrete elements. The rubber particles modelled with 2-noded perfect bonded embedded cable elements (one degree-of-freedom per each node) and the elastic properties of rubber were attributed to these elements. Figure 1A shows the crack patterns of this specimen obtained from numerical simulation. Rubber elements are presented in green colour. As it can be seen in Figure1A, the cracking in the concrete elements surrounding rubber elements was formed.

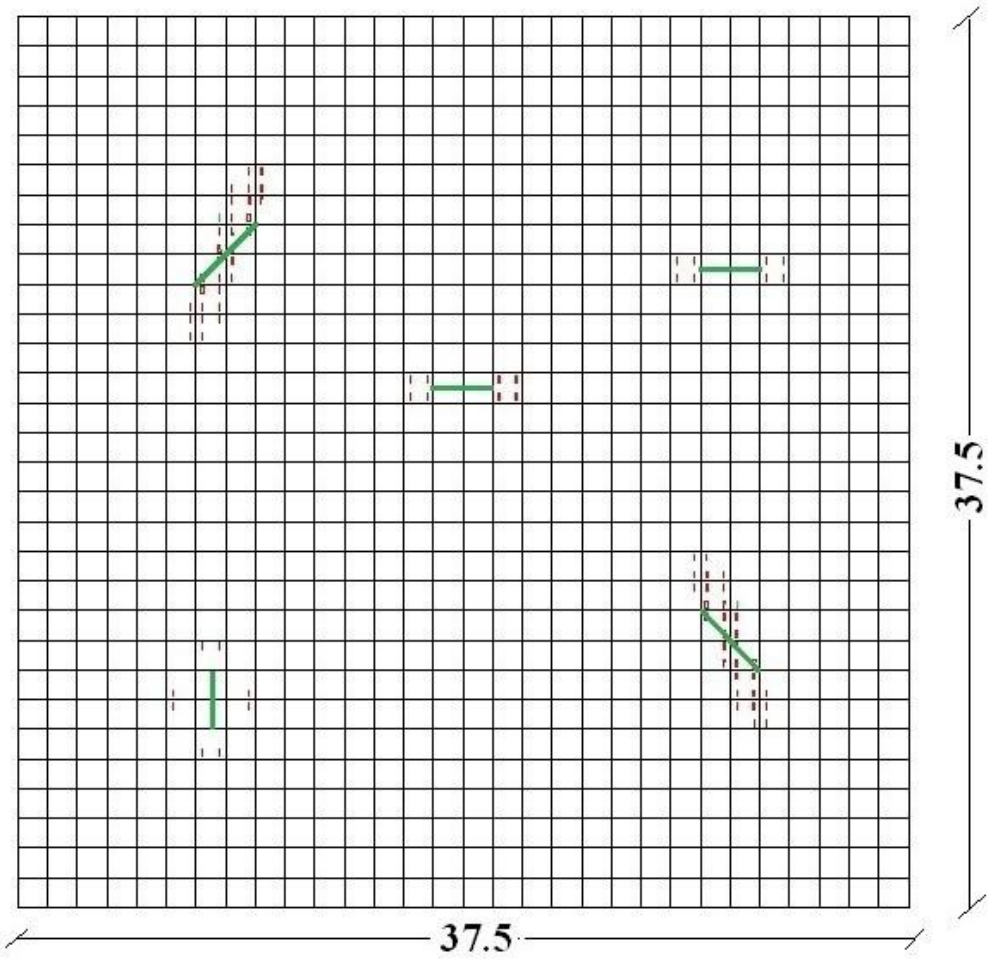

Figure A1 Crack patterns of the specimen

Annex B

Results of three point bending tests with un-notched specimens

Table B1 Results of three point bending test with un-notched M1_0 specimens

Specimen	D_{cr} [mm]	M_{cr} [kN.mm]	σ_{cr} [MPa]	$\sigma_{\max}$ [MPa]
M1_0_1	0.302	38.50	3.54	3.54
M1_0_2	0.291	41.50	3.81	3.81
M1_0_3	0.295	37.00	3.40	3.40
Average	0.296	39.00	3.58	3.58
STD	0.005	2.291	0.21	0.210
COV	1.881	5.875	5.87	5.875

Table B2 Results of three point bending test with un-notched M1_1.5 specimens

Specimen	D_{cr} [mm]	M_{cr} [kN.mm]	σ_{cr} [MPa]	$\sigma_{\max}$ [MPa]
M1_1.5_1	0.37	33.33	3.20	5.38
M1_1.5_2	0.167	26.92	2.61	3.55
M1_1.5_3	0.165	39.27	1.92	4.00
Average	0.23	38.61	2.57	4.31
STD	0.167	11.369	0.640	0.953
COV (%)	0.16	29.44	24.86	22.12

Table B3 Results of three point bending test with un-notched M1_3 specimens

Specimen	D_{cr} [mm]	M_{cr} [kN.mm]	σ_{cr} [MPa]	$\sigma_{\max}$ [MPa]
M1_3_1	0.174	22.43	2.15	3.05
M1_3_2	0.240	48.63	3.038	7.09
M1_3_3	0.198	37.68	2.711	4.53
Average	0.204	36.25	2.63	4.89
STD	0.033	13.155	0.449	2.047
COV (%)	16.37	36.28	17.05	41.83

Table B4 Results of three point bending test with un-notched M2_0 specimens

Specimen	D_{cr} [mm]	M_{cr} [kN.mm]	σ_{cr} [MPa]	$\sigma_{\max}$ [MPa]
M2_0_1	0.184	58.95	5.11	5.11
M2_0_2	0.153	93.00	4.83	4.83
M2_0_3	0.125	99.80	5.18	5.18
Average	0.154	83.91	5.04	5.04
STD	0.029	21.887	0.185	0.185
COV (%)	19.16	26.08	3.67	3.67

Table B5 Results of three point bending test with un-notched M2_3r specimens

Specimen	D_{cr} [mm]	M_{cr} [kN.mm]	σ_{cr} [MPa]	$\sigma_{\max}$ [MPa]
M2_3r_1	0.085	75.40	4.09	6.40
M2_3r_2	0.102	65.55	4.06	6.91
M2_3r_3	0.088	66.90	3.79	5.69
M2_3r_4	0.147	71.75	4.44	6.99
M2_3r_5	0.165	69.95	4.33	6.99
Average	0.117	69.91	4.14	6.60
STD	0.0363	3.924	0.255	0.563
COV (%)	30.98	5.612	6.15	8.54

Table B6 Results of three point bending test with un-notched M2_2.5 specimens

Specimen	D_{cr} [mm]	M_{cr} [kN.mm]	σ_{cr} [MPa]	$\sigma_{\max}$ [MPa]
M2_2.5_1	0.158	86.65	4.90	4.90
M2_2.5_2	0.167	103.15	6.09	7.11
M2_2.5_3	0.105	85.25	5.50	6.18
M2_2.5_4	0.082	71.40	4.21	6.25
M2_2.5_5	0.254	95.10	5.38	7.21
Average	0.153	88.31	5.21	6.33
STD	0.066	11.878	0.702	0.931
COV (%)	43.46	13.45	13.45	14.70

Table B7 Results of three point bending test with un-notched M2_3 specimens

Specimen	D_{cr} [mm]	M_{cr} [kN.mm]	σ_{cr} [MPa]	$\sigma_{\max}$ [MPa]
M2_3_1	0.129	116.60	6.33	7.73
M2_3_2	0.169	112.80	6.99	6.99
M2_3_3	0.185	141.55	7.07	7.65
M2_3_4	0.145	114.35	6.21	6.62
M2_3_5	0.104	87.50	5.18	8.10
Average	0.146	114.56	6.35	7.42
STD	0.032	19.157	0.760	0.599
COV (%)	21.87	16.72	11.95	8.06

Table B8 Results of three point bending test with un-notched M2_3.8 specimens

Specimen	D_{cr} [mm]	M_{cr} [kN.mm]	σ_{cr} [MPa]	$\sigma_{\max}$ [MPa]
M2_3.8_1	0.215	127.15	6.35	10.35
M2_3.8_2	0.231	126.20	6.31	8.072
M2_3.8_3	0.205	127.25	6.36	8.80
M2_3.8_4	0.203	132.05	6.60	7.93
M2_3.8_5	0.180	130.15	6.24	11.04
M2_3.8_6	0.247	87.65	4.38	9.45
M2_3.8_7	0.215	89.80	5.20	10.34
M2_3.8_8	0.352	149.00	8.05	10.14
Average	0.231	121.15	6.18	9.51
STD	0.052	21.311	1.063	1.147
COV (%)	22.83	17.58	17.18	12.05

Annex C

Details of the plates used in confinement system for support sections in the second experimental program

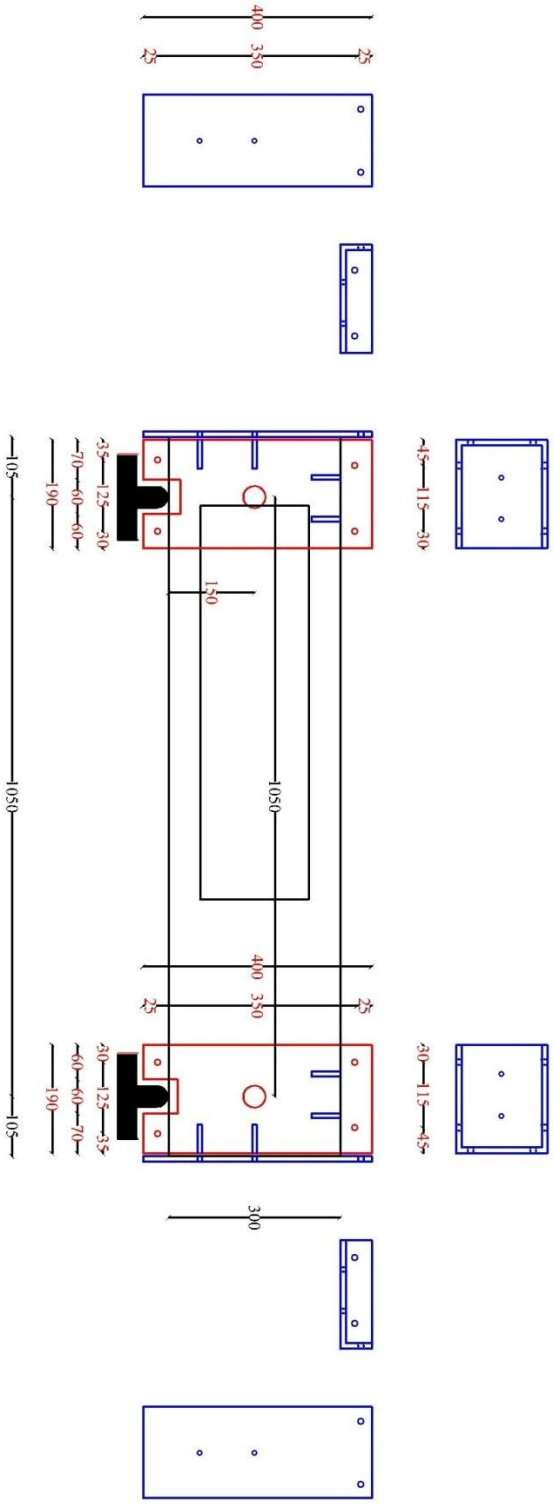

Plate 1- Amount: 2

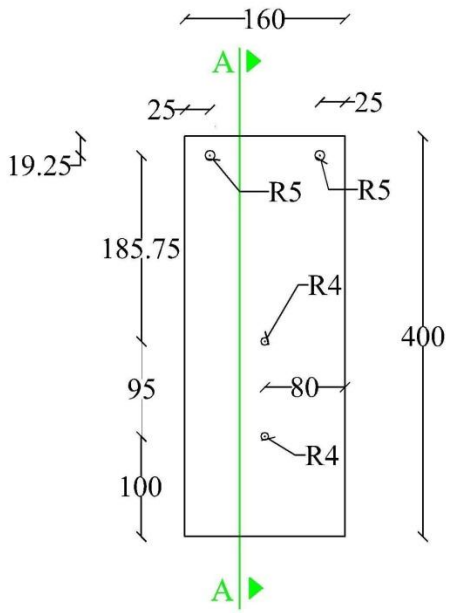

Top View
Scale 1:1

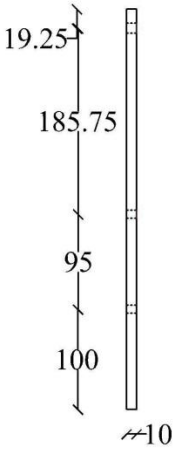

Section A-A
Scale 1:1

Plate 2 - Amount : 1 **Support A**

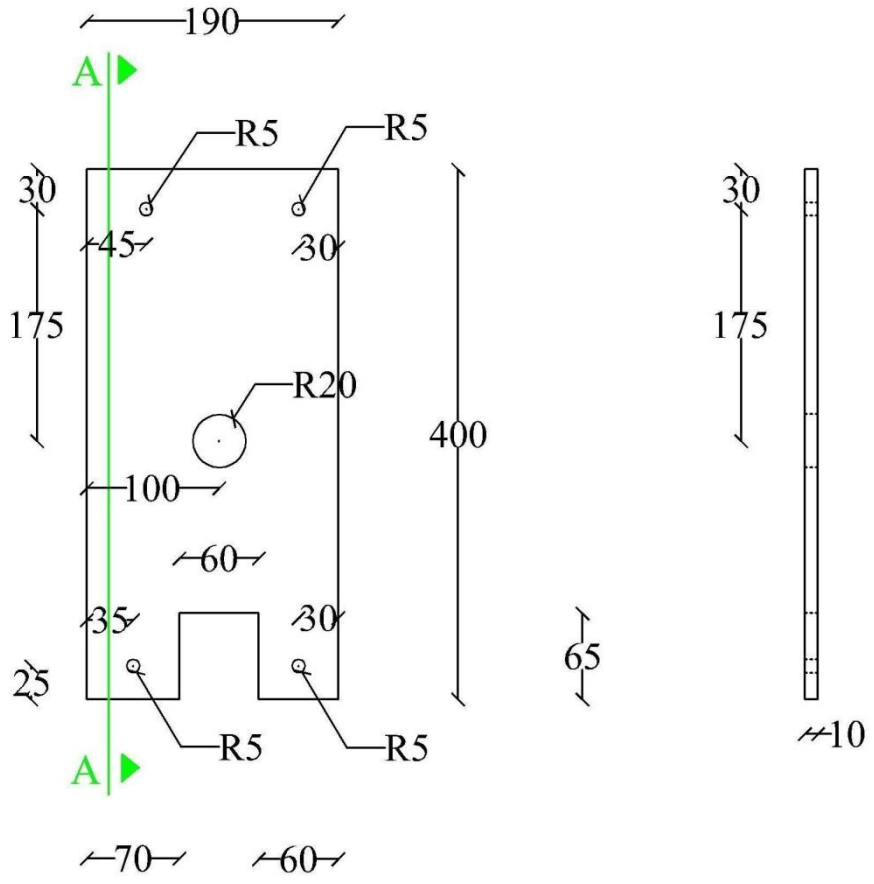

Top View
Scale 1:1

Section A-A
Scale 1:1

Plate 3 - Amount : 1 Support A

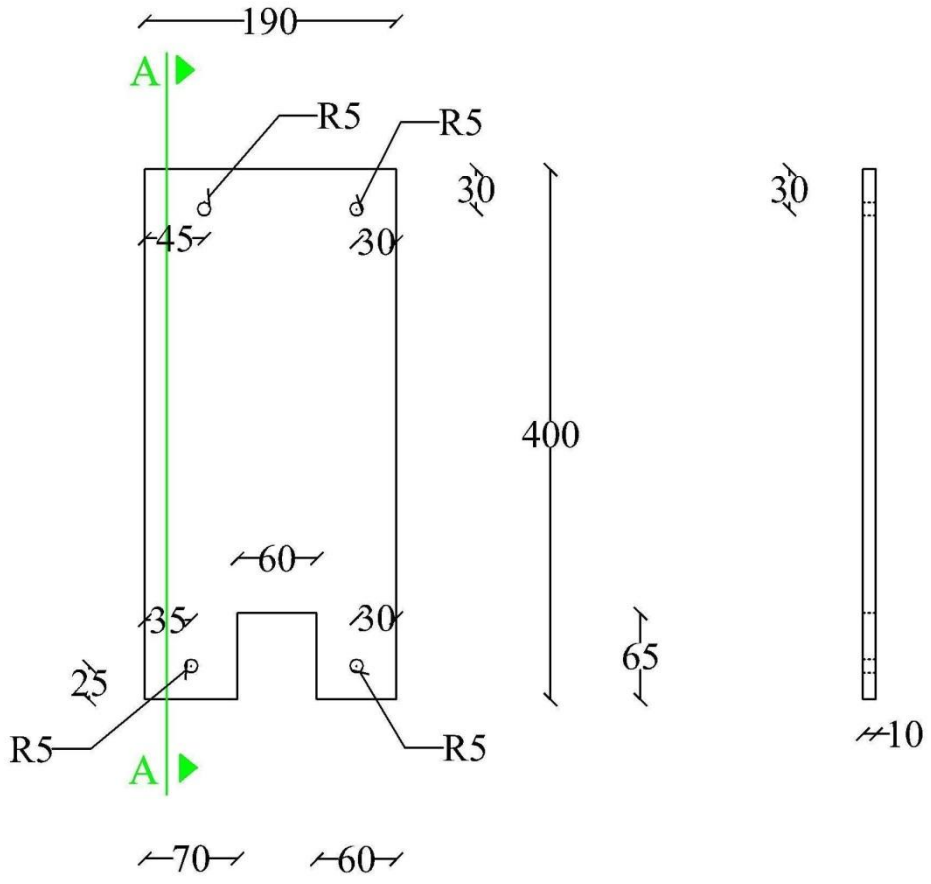

Top View
Scale 1:1

Section A-A
Scale 1:1

Plate 4 - Amount : 1

Support A

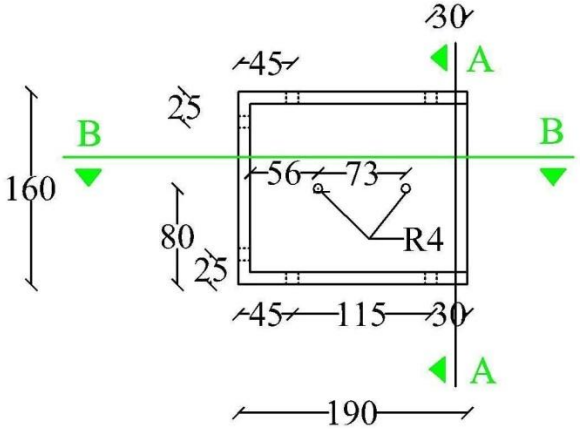

Top View

Scale 1:1

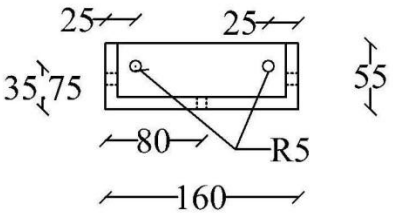

Section A-A

Scale 1:1

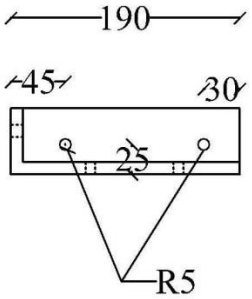

Section B-B

Scale 1:1

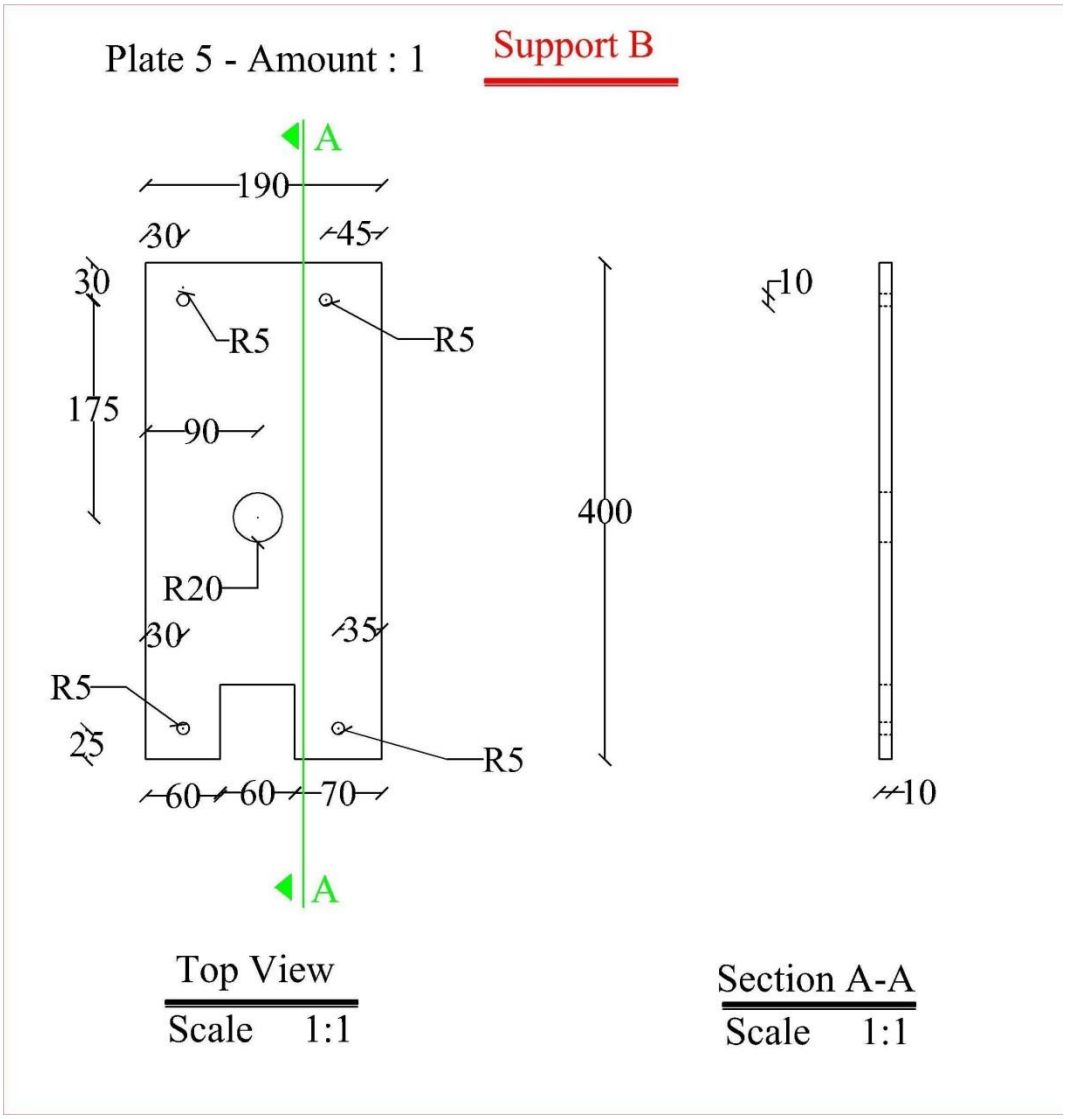
Plate 5 - Amount : 1
Support B
A
190
30
45
30
R5
R5
175
90
R20
30
35
R5
25
R5
60
60
70
A
400
10
10
Top View
Scale 1:1
Section A-A
Scale 1:1

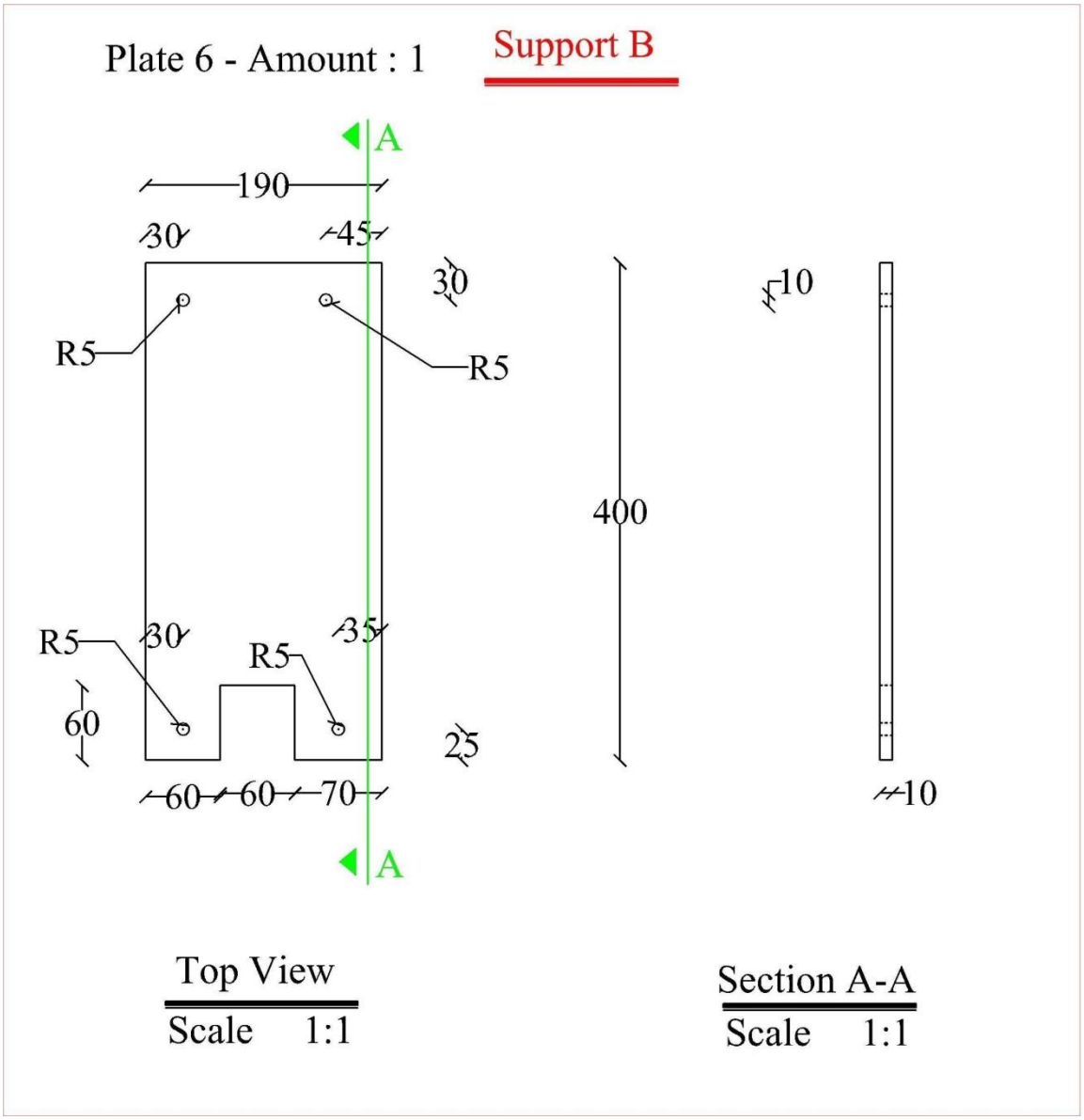
Plate 6 - Amount : 1
Support B
A
190
30
45
30
R5
R5
400
10
R5
30
35
R5
60
25
60
60
70
10
A
Top View
Scale 1:1
Section A-A
Scale 1:1

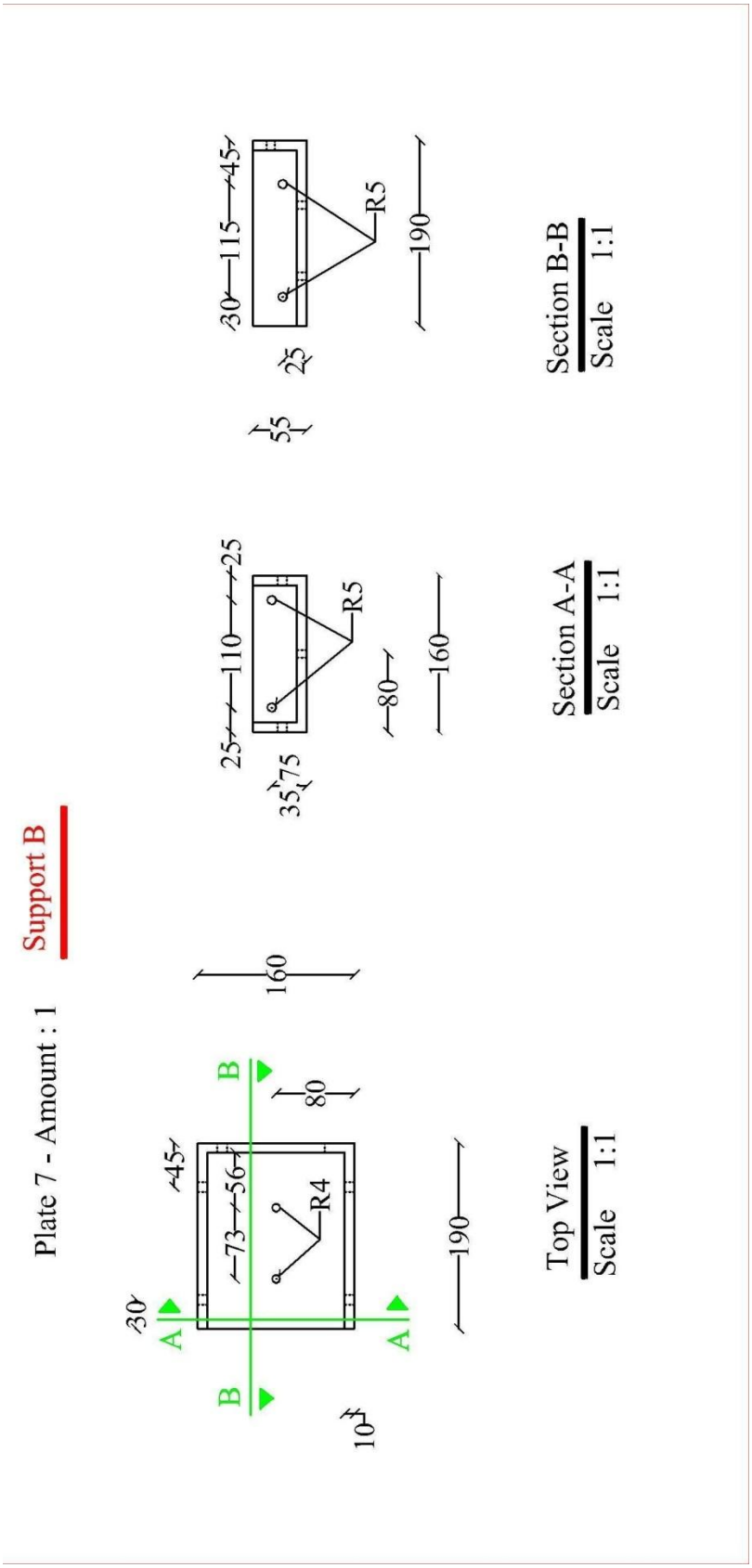
Plate 7 - Amount : 1
Support B
30
A
B
45
73
56
R4
80
B
A
10
190
160
Top View
Scale 1:1
25
110
25
35
75
R5
80
160
Section A-A
Scale 1:1
30
115
45
25
55
R5
190
Section B-B
Scale 1:1